UNIVERSIDAD
DE MÁLAGA

TESIS DOCTORAL 2021

Spectroscopic and DFT study of molecular
and supramolecular parameters governing
charge transport in imide-based
semiconductors

ALEXANDRA HARBUZARU HARBUZARU

DIRECTORAS:

Mª CARMEN RUIZ DELGADO Y ROCIO PONCE ORTIZ

PROGRAMA DE DOCTORADO:

Química y Tecnologías Químicas, Materiales y Nanotecnología

FACULTAD DE CIENCIAS:

Departamento de Química-Física

ALEXANDRA HARBUZARU HARBUZARU

TESIS DOCTORAL 2021

UNIVERSIDAD
DE MÁLAGA

AUTOR: Alexandra Harbuzaru Harbuzaru

https://orcid.org/0000-0003-2434-3182

DECLARACIÓN DE AUTORÍA Y ORIGINALIDAD DE LA TESIS PRESENTADA PARA OBTENER EL TÍTULO DE DOCTOR

D./Dña ALEXANDRA HARBUZARU HARBUZARU

Estudiante del programa de doctorado QUIMICA Y TECNOLOGÍAS QUÍMICAS, MATERIALES Y NANOTECNOLOGÍA de la Universidad de Málaga, autor/a de la tesis, presentada para la obtención del título de doctor por la Universidad de Málaga, titulada: SPECTROSCOPIC AND DFT STUDY OF MOLECULAR AND SUPRAMOLECULAR PARAMETERS GOVERNING CHARGE TRANSPORT IN IMIDE-BASED SEMICONDUCTORS

Realizada bajo la tutorización de Mª CARMEN RUIZ DELGADO y dirección de Mª CARMEN RUIZ DELGADO Y ROCIO PONCE ORTIZ

DECLARO QUE:

La tesis presentada es una obra original que no infringe los derechos de propiedad intelectual ni los derechos de propiedad industrial u otros, conforme al ordenamiento jurídico vigente (Real Decreto Legislativo 1/1996, de 12 de abril, por el que se aprueba el texto refundido de la Ley de Propiedad Intelectual, regularizando, aclarando y armonizando las disposiciones legales vigentes sobre la materia), modificado por la Ley 2/2019, de 1 de marzo.

Igualmente asumo, ante a la Universidad de Málaga y ante cualquier otra instancia, la responsabilidad que pudiera derivarse en caso de plagio de contenidos en la tesis presentada, conforme al ordenamiento jurídico vigente.

En Málaga, a 27 de SEPTIEMBRE de 2021

Fdo.: ALEXANDRA HARBUZARU HARBUZARU Doctorando/a	Fdo.: Mª CARMEN RUIZ DELGADO Tutor/a
Fdo.: Mª CARMEN RUIZ DELGADO Y ROCIO PONCE ORTIZ Director/es de tesis	

D. Juan Carlos Otero Fernández de Molina, Catedrático de la Universidad de Málaga y Director del Departamento de Química Física de la Universidad de Málaga,

Certifica:

Que la memoria presentada por Alexandra Harbuzaru Harbuzaru bajo el título SPECTROSCOPIC AND DFT STUDY OF MOLECULAR AND SUPRAMOLECULAR PARAMETERS GOVERNING CHARGE TRANSPORT IN IMIDE-BASED SEMICONDUCTORS para optar al grado de Doctor en Ciencias Químicas, ha sido realizada bajo la dirección de los Doctoras Dª. María del Carmen Ruiz Delgado y Dª. Rocío Ponce Ortiz en el Departamento de Química Física de la Universidad de Málaga.

Y para que conste, firman el presente certificado en Málaga a 27 de Septiembre de 2021

Fdo.: Juan Carlos Otero Fernández de Molina

Dª María del Carmen Ruiz Delgado, Profesora Titular del Departamento de Química-Física de la Universidad de Málaga y Dª Rocío Ponce Ortiz, Profesora Titular del Departamento de Química Física de la Universidad de Málaga,

Certifican:

Que la memoria presentada por Alexandra Harbuzaru Harbuzaru bajo el título SPECTROSCOPIC AND DFT STUDY OF MOLECULAR AND SUPRAMOLECULAR PARAMETERS GOVERNING CHARGE TRANSPORT IN IMIDE-BASED SEMICONDUCTORS para optar al grado de Doctora en Ciencias Químicas, ha sido realizada bajo nuestra dirección en los laboratorios del Departamento de Química Física y en el Servicio de Espectroscopía Vibracional del Servicio Central de Apoyo a la Investigación de la Universidad de Málaga.

Considerando que constituye una Tesis Doctoral, autorizamos mediante este escrito la presentación y defensa de la misma en la Facultad de Ciencias de la Universidad de Málaga.

Y para que conste, firman el presente certificado en Málaga a 27 de Septiembre de 2021

Fdo.: Mª C. Ruíz Delgado   Fdo.: R. Ponce Ortiz

Para comenzar me gustaría agradecer a mis directoras de Tesis, Mª Carmen y Rocío. He sido muy afortunada de poder aprender de las mejores. Gracias a ellas he aprendido a disfrutar de la investigación, a crecer profesionalmente y a estar orgullosa de lo que hago.

Después me gustaría darles las gracias a todas las personas que, de alguna manera, me han ayudado durante este periodo predoctoral y para ello, seguiré el orden en el que los fui conociendo desde que entré en el grupo.

Quiero agradecer especialmente a Iratxe. No puedo ser más afortunada de haberla conocido en el Máster. Gracias por todo lo que me enseñaste en mis comienzos, primero para realizar el trabajo fin de máster y después para la Tesis Doctoral. Tenía un poco de miedo antes de empezar, pero ahora puedo decir que ha sido la etapa más bonita de mi vida, en la que he aprendido muchísimo y de la que ahora estoy muy orgullosa. Gracias a ti ha ocurrido todo esto.

Gracias a Víctor por mandarme con las 'niñas', como él dice, mis directoras de tesis, porque ahora miro atrás y no puedo estar más contenta por ello. He aprendido mucho de ti estos años. También quiero dar las gracias a Teo por darme la oportunidad de realizar la Tesis Doctoral en el grupo y por confiar en mí.

A Rafa por explicarme tan bien, con sus seminarios, cómo hacer cálculos teóricos, por animarme y por ayudarme cada vez que lo necesitaba. A María por toda su gran ayuda durante estos años.

Quiero agradecer a mis compañeros por hacer más amenos los años de tesis. A Irene y Sergio G. por resolver todas mis dudas. Perdón por entrar a vuestro despacho con tanta energía siempre que me surgía alguna duda. Tengo muchas vivencias con vosotros que recordaré

siempre como las más bonitas durante este periodo predoctoral. Samara, mi compañera de despacho, por resolver mis inquietudes, por ayudarme siempre que lo he necesitado y también por las risas de alguna que otra tarde, y también a mi otro compañero de despacho Sergio M. A Abel, por ayudarme en el laboratorio siempre, por explicarme cómo usar algún equipo que él dominaba muy bien, por los ratos de charlas y risas, y por alegrarme el día desde muy temprano con su saludo. A Sara, por todos los viales que me proporcionaba cuando no encontraba por ningún sitio cuando más me hacían falta, así como algún que otro disolvente. A Guzmán por ayudarme en mis comienzos, por resolver mis dudas muchas veces, y por explicarme cómo usar los equipos del laboratorio de OFETs así cómo fabricar los dispositivos. A Raúl, por su gran ayuda en mi último año de tesis. A aquellos que me han ayudado y ya no están en el grupo, como Nadia y Ana Claudia.

A Zafra y Cristina C. por hacer que los experimentos en el laboratorio de Espectroscopía Vibracional del SCAI resulten mucho más fáciles. Gracias por resolver todas mis dudas, por responder a cada pregunta, siempre con buena cara y dispuestos a ayudar, por explicarme cómo funciona cada equipo y por qué las cosas se hacen así. Por hacer de psicólogos muchas veces, escuchando mis problemas y dándome consejos, y por muchas más cosas que hacen la lista interminable. Por ayudarme desde que he entrado en el grupo con el trabajo fin de máster, desde entonces he aprendido y he madurado mucho gracias a vosotros.

A los técnicos del Departamento, Cristina L. y José, por ayudarme siempre que lo he necesitado y también a Lourdes por su ayuda en todo lo relacionado con el papeleo. A los técnicos del SCAI, Cristina R., José María, Laura y Estefanía, por todas las medidas que hicieron para mi, a veces con mucha bulla para alguna publicación.

Me gustaría también agradecer a los grupos que han sintetizado los compuestos que dan forma a esta Tesis. Especialmente al Prof. José Luis Segura y a su estudiante Matías. Gracias también al Prof. Xugang Guo por sus compuestos *ladder-type* que componen el 75% de los resultados de esta Tesis Doctoral.

Quiero agradecer también al grupo del Prof. Mario Caironi del Istituto Italiano di Tecnología (IIT) donde durante mi estancia aprendí mucho sobre OFETs, además de conseguir muy buenos resultados.

Quiero mencionar también a Helena, que, aunque su estancia fue corta, he aprendido mucho de ella. Gracias por el ánimo en el mes previo a depositar la tesis.

En cuanto al ámbito personal, quiero dar especialmente las gracias a Antonio, mi marido y compañero. A ti te debo mucho. Gracias a ti he conseguido mucho en mi vida personal y profesional. Gracias cariño por confiar en mí, por hacerme ver que podía conseguir las cosas si me lo proponía, por ilusionarte al igual que yo con mis logros, por ser mi gran apoyo estos años. Por tu paciencia cuando echaba muchas horas trabajando, o cuando salía con los compañeros y volvía muy tarde. Gracias por ese niño que viene en camino, y por esperarme hasta que yo tuviera las cosas más encaminadas. Tengo claro que vas a ser un super papá y que me apoyarás para poder compaginar mi vida profesional con la familiar.

A mis padres por intentar hacer que tengamos un mejor futuro.

I. INTRODUCTION

I.I. Electrical materials

Based on the electrical conductivity (σ), the materials can be classified as conductors, semiconductors, or insulators (dielectrics). Semiconductors are materials with electrical conductivities in between those of conductors (metals) and dielectrics (glass, plastics).

The conductivity phenomenon can be readily explained by making use of the energy band theory, according to which, in the solid state the energy levels of the electrons shared between neighboring atoms are close to each other rather that the discrete energy levels of electrons in isolated atoms. This closely spaced set of energy levels is called the energy band, known as the valence band for the lowest occupied energy levels and the conduction band for the higher unoccupied energy levels[1]. The energy separation between the bands is known as the forbidden gap, energy gap or the band gap (Figure I.1).

The width of the band gap determines the conduction properties of any material. Thereby, in the case of conductors, there is no energy gap between the two bands, namely, the valence band overlaps the conduction band and electrons can easily move in response to an external stimulus from the valence to the conduction band giving rise to conduction. On the other extreme, the insulators present a large gap between the valence and the conduction bands[2]. Finally, in the case of the semiconductors, the valence band which is completely filled with valence electrons, and the conduction band, which contains no electrons at 0 K, are separated by a small gap (~ 1 eV).
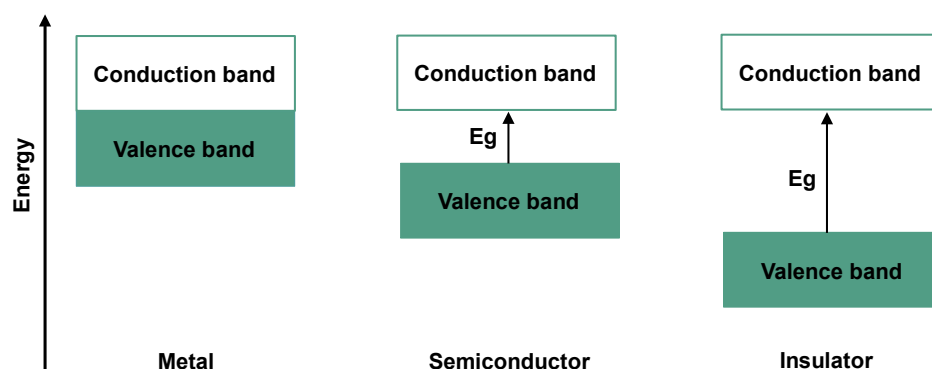
Figure I.1. Schematic representation of energy bands for solids.

I.II.   Organic semiconductors

Various classes of materials are qualified as semiconductors. Besides inorganic semiconductors, the organic semiconductors have attracted enormous attention because of their physical properties, mechanical flexibility, environmental-friendly, large-scale production, and abilities to be processed at low temperatures and to be modified via chemical methods in unlimited fashions, therefore, providing a large availability of new materials. The key advantage of organic molecular semiconductors over traditional inorganic semiconductors is their processability[3].

The organic molecular solids are characterized by weak intermolecular forces (Van der Waals and electrostatic type), in contrast to inorganic semiconductors (Se, Ge) which are characterized by covalent bonds[4–6]. This is a key difference that impacts their properties and processability. Whereas the inorganic compounds require extreme processing conditions, such as temperature and vacuum, the weak bonding present in organic materials allows for processing at/or around room temperature and at ambient pressure via ink-jet printing, laser printing, or other simple methods. This allows the organic semiconductor devices to be built on a

variety of unconventional substrates, such as glass, polymer foils, cloth, and paper, which opens new prospects for semiconductor applications[3,6–14].

I.II.I. A brief overview on the first organic semiconductors

Historically, organic materials were used as insulators. However, in the middle of the last century, different findings demonstrated that organic materials could present electrical conductivity[15]:

- In 1948, thermal activated conductivity was observed in metal-free and copper phthalocyanines and, some years later, photoconductivity and electroluminescence properties were found in organic molecular crystals[16]. However, because of their poor performance and stability, these early devices had no practical interest and did not attract much attention. By then, organic materials were mostly considered exotic materials with little potential for applications.

- In the 1970s, two important discoveries spurred a significant research interest in the area of organic semiconductors. The first important discovery was in 1973, when Anderson *et al.* observed that the tetrathiafulvalene-tetracyanoquinodimethane[17,18] complex (TTF-TCNQ, Figure I.2) exhibited metallic conductivity at room temperature, and the second one was in 1977, when the group of scientists formed by Alan J. Heeger, Alan G. MacDiarmid and Hideki Shirakawa discovered that the conductivity of the polyacetylene (Figure I.2) could be modulated from a dielectric to a conductor character by chemical doping with oxidant species such as I_2, Br_2 or Cl_2[19,20]. This report recognized that a key feature of conducting polymers is the presence of a backbone consisting of alternating single and double bonds, resulting in a conjugated system. This, in turn, led to a relatively small energy gap, enabling the appearance

of both semiconducting (undoped) and metallic properties[21]. They were awarded the Nobel Prize in 2000 for 'the discovery of conductive polymers'[22–24], being the pioneering work promoting the development of a new fascinating research field called organic electronics.

TTF   **TCNQ**   **Polyacetylene**
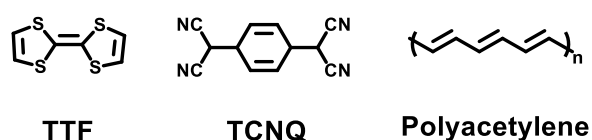
Figure I.2. TTF-TCNQ complex and polyacetylene organic semiconductors.

I.II.II. Molecular structure of organic semiconductors

Organic semiconductors are mainly based on carbon atoms and other elements such as hydrogen, oxygen, nitrogen, sulfur, or fluorine atoms, among others. These materials can be divided into polymers and small molecules (Figure I.2) and they structurally consist of systems with highly delocalized π-conjugation which provides them with unique electrical and optical properties. The π-conjugation delocalization is attributed to the p_z-orbitals of sp^2-hybridized carbon atoms in the molecules, as can be seen in Figure I.3(a). In this case, the three sp^2 orbitals are arranged in a coplanar structure around each carbon atom, and they overlap yielding bonding and antibonding molecular σ and σ* orbitals (Figure I.3(b)). On the other hand, the remaining atomic p_z orbitals are orthogonal to the plane of the sp^2 orbitals (Figure I.3(a)), and they overlap yielding bonding and antibonding molecular π and π* orbitals; these orbitals represent the frontier orbitals of the molecule (Figure I.3(b)).
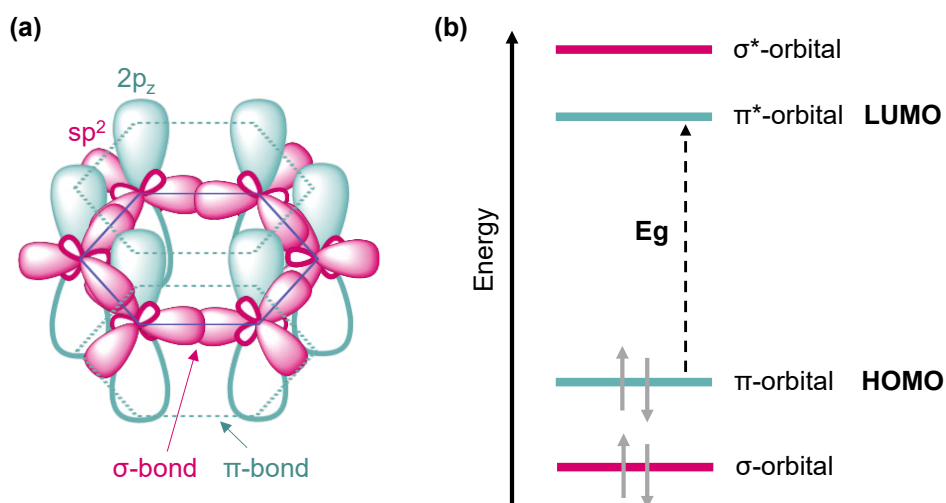
Figure I.3. (a) Schematic illustration of sp^2 hybridization. sp^2 orbitals lie on the same plane and form σ-bonds while p_z orbitals are orthogonal to the plane and form π-bonds. Formation of σ and π bonds in benzene and (b) energy level diagrams of molecular orbitals in benzene[25].

The π-conjugated systems consist of the alternation of single (σ) and double (σ+π) bonds along their backbone, as can be seen in the case of benzene molecule (C_6H_6, Figure I.3(a)). The formed π-bonds are significantly weaker than the σ ones and are highly delocalized on the molecule, allowing charge transport through the materials. In the particular case of benzene, the π-bonding orbitals represent the highest occupied molecular orbital (HOMO) and is analogous to the valence band in solids, whereas the π-antibonding orbitals represent the lowest unoccupied molecular orbital (LUMO) which is analogous to the conduction band (Figure I.3(a)). The energy difference between the HOMO and LUMO orbitals defines the band-gap energy (E_g), as shown in Figure I.3, and for organic molecular semiconductors, these values are in the range of 1.5–3.0 eV, resulting in strong optical activity in the visible range[5]. The optical

bandgap of π-conjugated systems depends on structural factors, such as effective conjugation length, planarity, aromaticity and the presence of electron-withdrawing or electron-donor groups[26]. However, the organic material properties are not only determined by intramolecular factors, but also by supramolecular interactions, and thus, both must be investigated in order to obtain promising molecular materials for their application in electronic devices with outstanding performances[27].

I.III. Relationship between chemical structure and electronic properties

The relationship between chemical structure and the electronic properties of the thin films in electronic devices is complex and not fully understood, so continued efforts are required to develop design rules for new materials in order to elucidate the mechanisms involved in the device functioning[3].

From a molecular point of view, a π-conjugated system can have four constituting structural components: the conjugated backbone, heteroatoms, substituents (electron donating or withdrawing atoms/groups) and side chains (i.e., solubilizing groups)[28]. Among these components, the conjugated backbone is unequivocally the dominant factor dictating most of the optoelectronic properties, including energy levels, band gap, inter- and intramolecular interactions, and solubility. Moreover, it has a great influence on the molecular packing. However, heteroatoms, substituents and side chains also have sizeable influence on the optoelectronic properties of conjugated systems, in particular, in the solid state where morphological features (aggregation, molecular packing/stacking, solubility, etc.) are significantly affected by the choice of these structural components. Some representative examples to illustrate

the role of molecular design on charge transport properties are shown in the following content.

(i) Conjugated backbone: effect of π-conjugation extension and aromaticity

Linear acenes, which are aromatic hydrocarbons systems composed of ladder-like fused benzene rings (Figure I.4), present a high aromaticity and have been widely used in the design of organic semiconductors with improved charge transport properties.

Anthracene   **Tetracene**   **Pentacene**

Hexacene
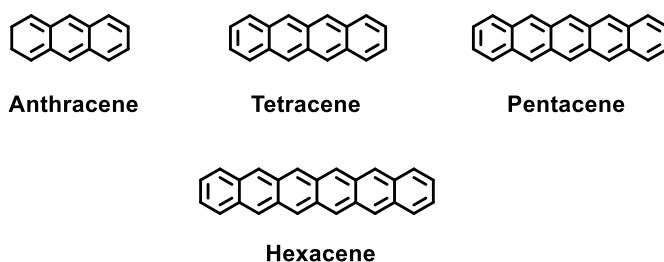
Figure I.4. Chemical structures of some representative acenes.

The electronic properties of acenes strongly relay on their molecular packing structures. It has been seen that, the theoretical charge mobility in these systems, increases with the number of benzene rings as a result of lower reorganization energies and higher transfer integrals. However, in practical applications, the mobility depends on the choice of the acene core length, which must be a combination of theoretical performance limit, chemical stability, and ease of processing. As the conjugation length increases, the HOMO level is destabilized, going from -5.7 eV for anthracene to -4.96 eV for hexacene, indicating higher tendency to oxidation in air for longer acenes.

The thin film morphology is also strongly dependent on the molecular size, therefore, shorter acenes tend to have more three-dimensional growth while very large acenes tend to give small grains[29]. Moreover, the larger acenes need more insulating solubilizing groups to rend them soluble, which may reduce their charge mobility.

Therefore, the combination of conjugation extension and aromaticity is an effective way to achieve high charge mobilities for fused ring systems with good stability.

(ii) Conjugated backbone substitution with heteroatoms

Heteroatom substitution (Figure I.5) constitutes an effective way to tune electronic properties, solubility, and molecular packing[30–34].

Pentathienoacene

Benzoannulated penthathienoacene

TIPS-TAP
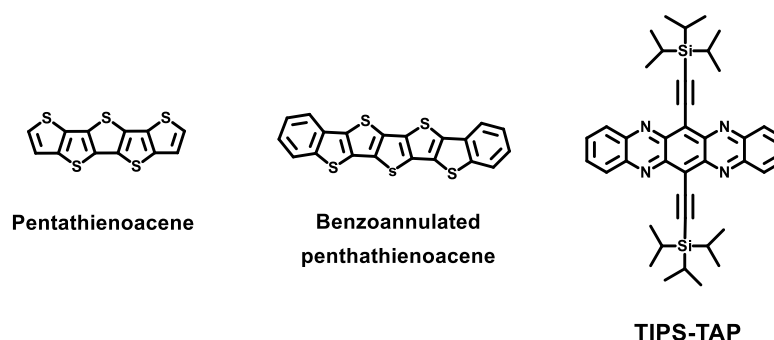
Figure I.5. Representative heteroatom substitution in organic semiconductors.

The replacement of benzene rings with aromatic thiophene rings increases the benzenoid character of the ladder π-conjugated system, thus lowers the HOMO levels and increases HOMO-LUMO gaps. Therefore, this modification usually enhances chemical stability[32,33,35–37].

In addition, the charge transport properties of organic semiconductors can be modulated by using this strategy, therefore, depending on the heteroatom use, n-type (electron transport), p-type (hole transport) or ambipolar (both electron and hole transport) charge transport properties can be obtained. For example, the substitution of a sp^2 carbon, in a conjugated skeleton, with a nitrogen atom can lead to n-type charge transport properties[30,31] (TIPS-TAP in Figure I.5).

(iii) Conjugated backbone substitution with electron withdrawing groups

Electron withdrawing groups, such as F, Cl, Br, and CN (Figure I.6), can remove electron density from a π-conjugated system, both by resonance and inductive effects.

TIPS-FTCT

TCIT

PDIF-CN$_2$
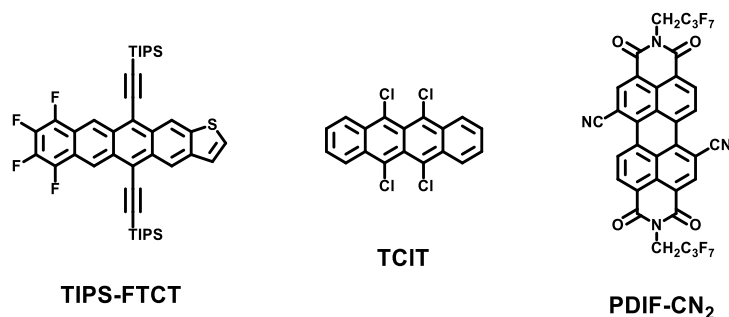
Figure I.6. Representative halogenated organic semiconductors.

The substitution on the conjugated skeleton with this kind of groups generally leads to enhanced molecular stability toward oxidation, promotes ambipolar or electron transport, as well as modifies molecular packing[38–40].

Regarding the energy levels, the electron withdrawing groups can lower the LUMO energy level (below -3.8 eV) increasing the

semiconductors stability against air[41–43]. On the contrary, electron-rich substituents, such as alkoxy or alkyl thioether, can elevate the energy level of the conjugated backbone, reducing the semiconductors stability against air[28].

(iv) Alkyl side chains substitution

The main function of alkyl side chains as substituents in the π-conjugated skeleton is to act as solubilizing groups to improve the processability of organic semiconductors in solution. These alkyl chains are considered insulating materials and do not contribute to charge transport directly. However, these alkyl side chains were recognized, over the years, to have a substantial impact on charge transport properties due to their influence on molecular packing and thin film morphology in solid state[44–48].

In the case of acenes, alkylation or arylation of *peri*-positions (Figure I.7) has been introduced to improve stability against oxidation and prevent dimerization of the molecules. These substitutions also changed packing motifs from herringbone to face-to-face π-stacking by diminishing C-H···π interactions[49–51,28].
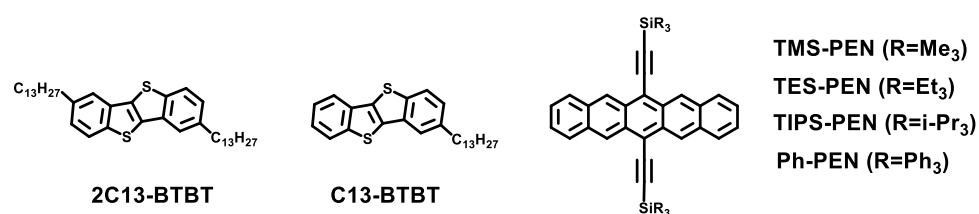
Figure I.7. Representative alkyl side chain substitutions in organic semiconductors.

On the other hand, it has been found that the alkyl chain sizes play also a significant role on the formation of 2D and 3D polycrystallites, which directly affects charge mobility[52].

I.IV. Impact of intra- and intermolecular semiconductor properties on charge transport

Intramolecular conformational order and intermolecular packing are closely related properties, and both account for the molecular order in a sample.

Taking the organic field effect transistor devices (OFETs, see Section I.VI.I.) as an example, there are many factors related to the organic semiconductors which influence the properties of these kind of devices. Some of these factors are (i) HOMO and LUMO energy levels of the organic semiconductor, (ii) packing mode of the organic molecules in the solid state, and (iii) morphology of the organic thin films. All these factors are now discussed below.

(i) HOMO and LUMO energy levels

The whole motion process of charge carriers in the semiconducting materials involves two critical processes which affect the device functioning: i) charge injection which takes place at the semiconductor-electrode interface and ii) charge transport, which takes place at the semiconductor-dielectric interface[53].

The HOMO and LUMO energy levels have a large influence on the charge carrier injection process. This process can be effective when the HOMO and LUMO orbitals of the molecules at the semiconductor-

electrode interface, are at levels where holes/electrons can be injected/extracted at accessible applied electric fields.

Once the charges are injected in the thin film at the corresponding interface, charge transport occurs at the semiconductor-dielectric interface. Efficient charge transport in π-conjugated organic and polymeric semiconductors is one of the most important requirements for the development of high-performance devices[54,55]. Significant progress has been made towards improved understanding of intrinsic charge-transport phenomena in these materials, and although it is difficult to associate a charge transport mechanism to a system, two extreme different transport models can be differentiated: the band transport for delocalized charges and the hopping transport for localized charges[56–58].

The band-like transport model is expected in high quality organic crystals, due to the strong delocalization of charge carriers that can move through a continuum of energy levels in the solid. On the other hand, hopping transport is commonly associated to amorphous or highly disordered organic semiconductors. This model is described by the Marcus theory[59] which assumes that the charge carrier hop from an occupied localized site to an adjacent unoccupied localized site due to a phonon-assisted mechanism that permit to overcome the energy barrier. According to this theory, the electronic transport is controlled by two parameters: i) the transfer integral (t), which indicates the interaction between the HOMOs or LUMOs of two adjacent molecules and ii) the reorganization energy which consists of both intra- and intermolecular contributions. The former one (λ) represents the energy that considers the conformational changes that the molecules suffer due to the acceptance or release of a charge, while the latter one reflects the changes in the polarization of the adjacent molecules. Usually, a combination of large

transfer integral and small reorganization energy, leads to higher charge carrier mobility[28].

(ii) Packing mode of the organic molecules in the film state

The packing mode of the organic semiconductors in the thin films also have an important influence on the OFETs functioning. In addition, the reorganization energy due to intermolecular contributions and especially the transfer integral are strongly dependent on the molecular packing mode[60], therefore, they are very important for the analysis of the charge transport between molecules. In order to facilitate charge transport between molecules, a highly dense and ordered molecular packing motif is required that results in large transfer integrals.

There are four different packing motifs as shown in Figure I.8:

(a) Herringbone packing (face-to-edge) without π - π overlap (face-to-face) between adjacent molecules.

(b) Herringbone packing with π-π overlap between adjacent molecules,

(c) Lamellar packing, one-dimension (1-D) π -stacking, and

(d) Lamellar packing, two-dimension (2-D) π -stacking.

This last packing motif is believed to be the most efficient for charge transport because it can increase the transfer integrals to the maximum and transport the charge carriers through an almost straight line (namely, the shortest route).
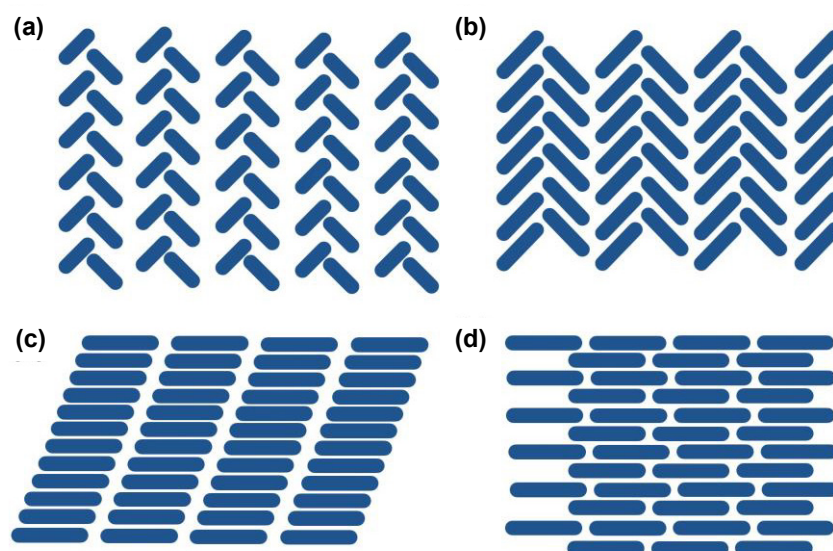
Figure I.8. Typical crystal packing found in organic semiconductors: (a) herringbone packing without π - π overlap, (b) herringbone packing with π - π overlap, (c) 1D π-stacking, (d) 2D π-stacking.

(iii) Morphology of the organic thin films

Morphology of the organic semiconductor is also an important factor which affects both injection and charge transport processes. Depending on how the molecules pack together to form a film, the organic semiconductors can exhibit a wide range of morphologies from completely amorphous to crystalline morphology, however greater electrical performances are achieved when films morphologies with crystalline domains cover the area between source and drain electrodes, with the semiconductor preferentially oriented in the way where π-π interactions go in the charge transport direction[3,61–63].

I.V. Characterization of organic semiconductors

In order to achieve a better understanding of the relationship between chemical structure and optoelectronic properties of the thin films in electronic devices, a detailed characterization of organic semiconductors is required. To this end, the most versatile class of characterization techniques is optical spectroscopy, which is able to make use of all kinds of light-matter interactions including absorption, emission, and various types of scattering, to provide a direct probe of many optoelectronic properties of organic semiconductors, with additional sensitivity to the thin film morphology.

In this thesis, the most used spectroscopic techniques are the electronic absorption spectroscopy (UV-Vis/NIR) and vibrational Raman spectroscopy. These techniques have been widely used to characterize many different classes of π-conjugated oligomers and polymers[3,64–90]. In particular, Raman spectroscopy is able to provide us information from both molecular and supramolecular levels, but also from interfaces as will see below.

The fact that Raman spectroscopy is particularly suitable for the study of conjugated molecules is because of the well-accepted effective conjugation coordinate (ECC) model developed by Zerbi *et al.*[51,91–95]. In this model a new vibrational coordinate is defined, Я, which describe the evolution of the structure from the ground state to the excited state. Namely, Я coordinate describes the direction along which the electron-phonon coupling is most effective, and the Raman active normal vibrational modes with strong contributions along Я, result in the strongest peaks in the Raman spectra, leading to quite simple Raman spectral

profiles for the π-conjugated materials, even for those with very complex molecular structures[96,97].

As stated in this model, Raman dispersion is described by the effective force constant, $F_Я$, which depends on the effective conjugation length. Thus, increased conjugation leads to lower $F_Я$ values, which means that, in a given series of oligomers, the totally symmetric C=C/C-C stretching modes undergo sizeable dispersion both in frequency and relative intensity. In addition, when π-conjugated heteroaromatic systems become doped by either chemical or electrochemical oxidation/reduction, various types of quinoid-like chain defects are created, which are evidenced by a significant red shift of the strongest Raman bands associated to the π-conjugated path, due to the softening of the C=C bonds[3,82,95]. The evolution of the Raman spectral profile between the neutral and the different doped states is a useful tool for elucidating the type of charge carrier created upon oxidation or reduction[94,98,99].

In addition, DFT calculations is a very useful tool to interpret the Raman spectra, since it has been demonstrated to give accurate values for vibrational mode energies of conjugated molecules (using appropriate methods and scaling factors)[100,101] helping to identify the specific nature of the vibrational modes and establish structure-properties relationships.

To highlight the versatility of Raman spectroscopy, in the following section we present a selection of a few representative published studies in which Raman spectroscopy technique was used for the study of different properties of π-conjugated systems, as shown in Figure I.9.
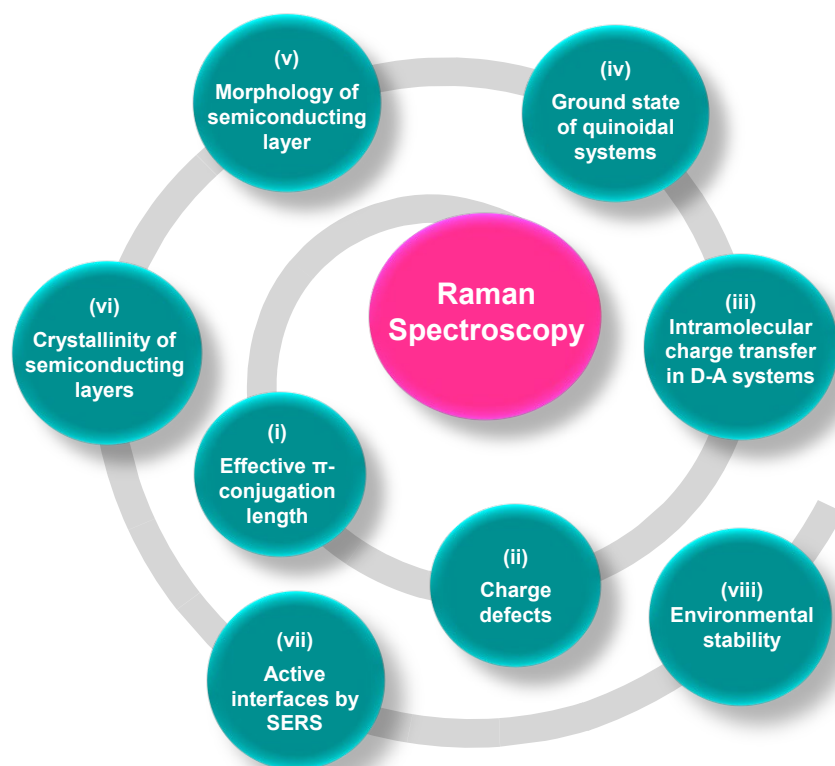
Figure I.9. Raman spectroscopy as a tool for the study of π-conjugated systems properties. D-A (donor-acceptor).

(i) Estimating the effective π-conjugation length.

Raman spectroscopy has demonstrated to be a useful tool to estimate the effective π-conjugation length within a series[82,83,90,102,102–112] of molecules and our group has a vast experience of over 20 years on the use of Raman spectroscopy to probe the degree of π-conjugation. Thus, an example is the study of a series of α, α'-dimethyl end-capped oligothiophenes with increasing chain length from three to six thiophene units[108,112–115] (DMnT, Figure I.10).
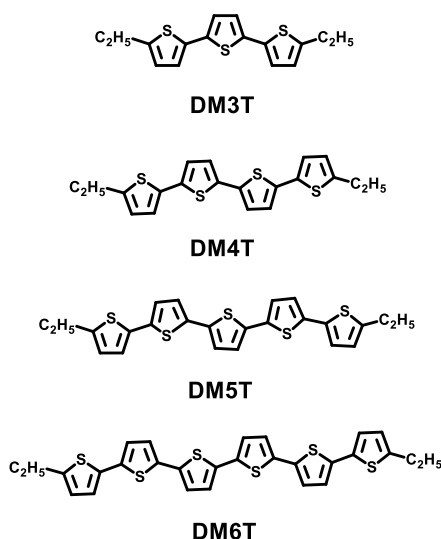
Figure I.10. Chemical structures of the series α, α'-dimethyl end-capped oligothiophenes DMnT (n = 3-6).

In this series, it has been demonstrated, a gradual downshift of the so-called ECC mode of oligothiophenes, indicating that the π-conjugation extension increases when the number of thiophene rings vary from 3 to 6 units. The gradual downshifts also indicate that the limit of π-conjugation was not yet reached for the hexathiophene system.

(ii) Characterizing different types of charge defects.

About 30 years ago, Furukawa et al., demonstrated that Raman spectroscopy is a useful tool in the characterization of conjugational defects in π-conjugated materials[107,109,116]. In this context, it is also worth mentioning the studies carried out by our group.[110,111,117], in which they investigated the electronic and vibrational structures of charged defects in two alkyl end-capped oligothiophenes (DM5T and DM6T, Figure I.11), induced by doping.
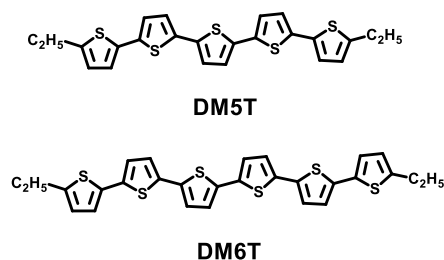
DM5T

DM6T

Figure I.11. Chemical structures of DM5T (α, α'-dimethylquinquethiophene) and DMT6 (α, α'-dimethylsexithiophene).

In this case, it has been demonstrated, focusing on the ECC mode, that the π-conjugation extension increases upon oxidation, which can be understood in terms of variations of the oligomer backbone from a heteroaromatic to a heteroquinoid structure, where the double C=C bonds are weakened, while the single C-C bonds are strengthened (Figure I.12).

Heteroaromatic   **Heteroquinoid**
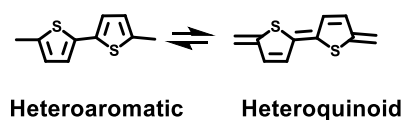
Figure I.12. Chemical structures of aromatic and quinoidal oligothiophenes.

(iii) Analyzing the efficiency of the intramolecular charge transfer (ICT) in donor-acceptor systems.

Raman spectroscopy was also used to evaluate the effectiveness of the ICT from the electron-donor to the electron-acceptor end groups in both polar (namely, push-pull) and non-polar systems[118,118–123]. As an example, our group[122] has previously studied a series of polar donor-acceptor systems containing a dithienothiophene (DTT, Figure I.13) unit as electron relay, the same donor group, and acceptors with different

strengths, by using Raman spectroscopy complemented with UV-Vis/NIR absorption and IR spectroscopy.
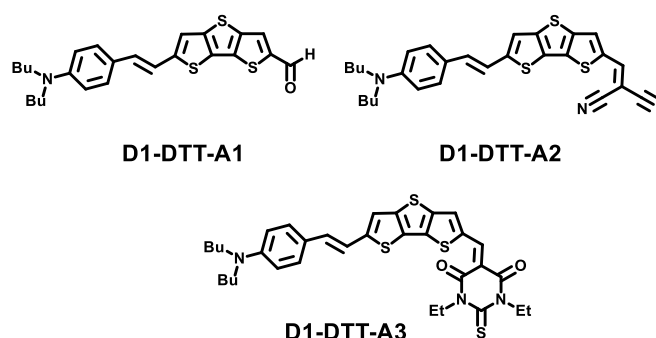
Figure I.13. Chemical structures of donor-acceptor systems containing DTT units.

In this case, it has been demonstrated that Raman spectroscopy, combined with IR spectroscopy, is able to analyze the presence of an effective ICT in these systems.

(iv) Analyzing the ground state of quinoidal systems.

In general, the ground state of quinoidal systems with small HOMO-LUMO gaps, where electrons can be easily promoted from the HOMO to the LUMO orbital, may present increasing radical character as the HOMO-LUMO gap decreases. Therefore, the singlet ground state (S_0) of these compounds is proposed to be represented by the resonance of a closed-shell quinoid Kekulé structure and a biradical form (see the example in Scheme 1.1), being the relative weight of these two forms who determine the biradical contribution to the electronic ground state. However, it is also important to consider the existence of a magnetically active triplet state (T_1) that is proposed to be in thermal equilibrium with the S_0 state and, therefore, could be energetically populated at room

temperature (Figure I.14). Raman spectroscopy has been shown to be efficient in elucidating the ground state of quinoidal systems[72,77,124–126].
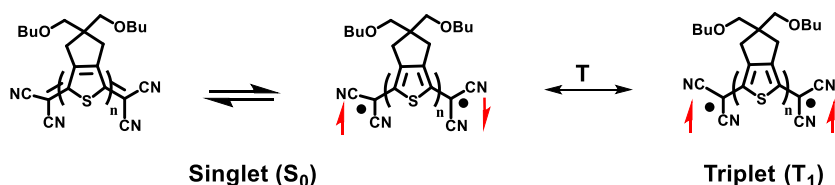
Figure I.14. Quinoidal closed-shell (left) and diradical (middle) resonant structures proposed for the singlet ground state of quinoidal systems (Qn) in equilibrium with the triplet species[77].

In this sense, as an example, it is worth mentioning the study of a series of dicyanomethylene end-capped quinoidal oligothiophenes, Qn (n=2-6, Figure I.14), with increasing chain length from dimer to hexamer[77]. In this study, Raman spectroscopy indicated an inversion of ECC mode tendency as the oligothiophene chain increases, thus, highlighting the open-shell structure of systems longer that Q4.

In addition, resonant and temperature dependent Raman spectroscopies were demonstrated to provide more information on the ground and excited states electronic structures. Resonant Raman spectroscopy consists of choosing the excitation laser wavelength to fit with a particular electronic transition. Thus, it is possible to register and analyze both singlet and triplet species separately. Finally, by using temperature dependent Raman spectroscopy, the increase population of T_1 with increasing temperature, at the expense of S_0, was demonstrated.

(v) Morphological study of semiconducting layers

Many published studies have applied Raman spectroscopy to probe morphological changes in samples consisting of an organic semiconductor[127–132] or a mixture of different components[133,134], which is very interesting for solar cells.
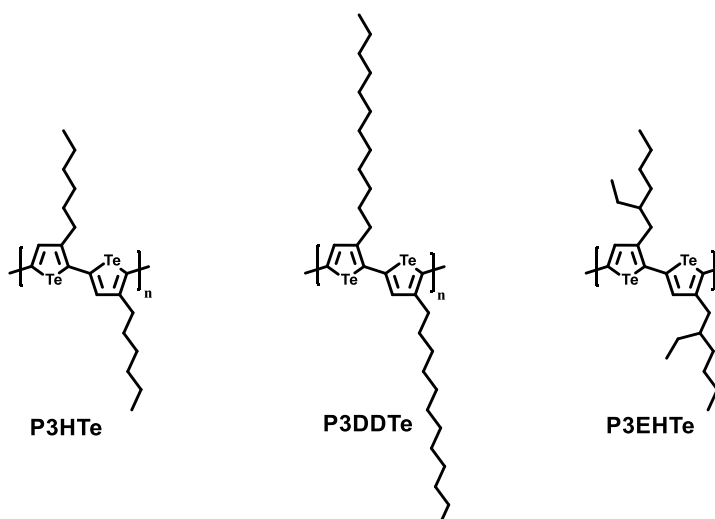
Figure I.15. Chemical structures of P3HTe (with a standard linear hexyl chain), P3DDTe (with a long linear dodecyl chain) and P3EHTe (with a branched 2'-ethylhexyl chain).

In this context, it is worth mentioning the study, carried out by Kim et al.[134], in which they made use of absorption spectroscopy and resonant Raman spectroscopy to investigate the impact of the heavy tellurium atom, different side chains and processing conditions on the molecular order of three polytellurophenes, depicted in Figure I.15.

In this case, it was demonstrated that P3Hte has a remarkable Raman spectrum with clearly defined vibrational peaks associated with ordered, which exhibit a much narrower distribution of highly planar

conformations, and disordered polymer phases, which exhibits a broad range of twisted conformations. In addition, it was observed that the substitution of sulfur atom in P3HT by tellurium, leads to a more planar backbone which is evidenced by the shift of the C=C vibrational peak to lower wavenumbers and the smaller optical band gap. On the other hand, it was also demonstrated that increasing the length of the linear side chain from hexyl to a dodecyl moiety introduces a greater proportion of disordered phases at room temperature due to kinetic hindrance; however, both P3Hte and P3DDTe can achieve a similar high degree of molecular order at higher processing temperatures. In contrast, by using a branched 2-ethylhexyl side chain, an inherently greater conformational disorder through steric hindrance is introduced, which is still present at higher processing temperatures, explaining the poorer charge carrier mobility found in OFETs for this polymer.

(vi) Analyzing the degree of crystallinity of semiconducting layers

In organic molecular materials, the molecules are generally flexible and held together by weak non-directional Van der Waals forces, therefore they are expected to exhibit different crystalline domains, leading to polymorphism. As an example, Brillante et al.[135], used micro-Raman spectroscopy to study polymorphism in crystals, and then, the results were extrapolated to analyze thin film polymorphism. To this end, they investigated the Raman spectra in the region of lattice phonons (~ 10-150 cm^{-1}), whose frequencies probe intermolecular interactions and are hence very sensitive to different molecular packing motifs.

(vii) Spectroscopic characterization of active interfaces by using SERS

Surface-enhanced Raman spectroscopy (SERS) is of particular interest, since it can be an efficient technique for the characterization of

active interfaces in OFETs, interfaces that are in principle hidden with other experimental techniques[136,137]. As an example, Zhenan Bao et al.[137], were able to analyze the order and molecular orientation of molecules derived from pentacene, both at the semiconductor-dielectric interface and at the electrode-semiconductor interface in an OFET, by using SERS.

Another example is the exhaustive study of the chemical composition and molecular order at the interface of donor-acceptor mixtures for solar cells by using SERS, carried out two years later by Kim et al.[136].

These two representative examples indicate the great potential of Raman spectroscopy to analyze buried interfaces, inaccessible for most experimental techniques.

(viii) Study of environmental stability

Raman spectroscopy can also support the study of the stability of semiconductors in OFETs[138,139]. For instance, Di Fabrizio et al.[139], analyzed the different interactions of pentacene film with oxygen, nitrogen, and moisture by using micro-Raman spectroscopy.

I.VI. Applications of organic semiconductors

I.VI.I. Organic electronic devices: OFETs

The main potential applications of organic semiconductors include organic light-emitting diodes (OLEDs)[140–149], organic field effect transistors (OFETs)[150–154] and organic photovoltaic cells (OPVs)[145,155–159], among others. Owing to the large efforts of both academic and industrial research laboratories during the last 30 years, organic light-emitting diodes (OLEDs) have been already incorporated in commercial products, while

organic photovoltaic cells (OPVs) and organic field effect transistors (OFETs) have already shown important advances and promising features.

This thesis is mainly focused in OFET devices, therefore in the following section a detailed description of these organic devices will be made.

The organic field-effect transistors (OFETs) are the main logic units in electronic circuits, where they usually work as either amplifiers or on/off switches[28,152]. These devices share the same structural and operational principle with the traditional transistors, however in this case the inorganic semiconducting material is replaced by an organic semiconductor.

The OFETs are technologically attractive since all their layers can be deposited at low temperature (above 120 ºC *versus* 900 ºC in inorganic semiconductors) which make them compatible with a variety of substrates including flexible plastics, and allowing the coverage of large areas, for example by printing, at low cost[6,160–164]. These properties allow their possible use in electronic paper or in flexible displays, in electronic skin, in sensors and in low-cost memory devices and radiofrequency identification (RFIDs) tags.

Furthermore, OFETs can be excellent platforms for answering intriguing scientific questions about charge transport in organic semiconductor materials, with a fine control of the charge density in the semiconductor layer[6].

I.VI.II. A brief overview on OFETs

The first OFET was fabricated by Tsumura et al. in 1986[165] using electrochemically polymerized polythiophene as the active semiconducting material (10^{-5} cm^2 V^{-1} s^{-1}, I_{ON}/I_{OFF} = 10^2- 10^3).

Subsequently, small molecules such as phthalocyanines[166] and sexithiophene[151] were used as semiconducting materials in OFETs. However, these devices exhibited rather low charge mobility with poor storage and operation stability, far from meeting the requirements for realistic applications.
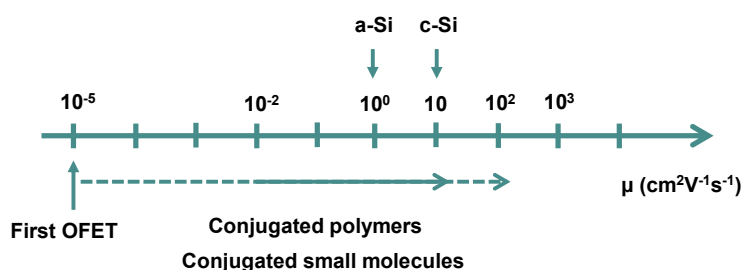
Figure I.16. Scale of charge carrier mobility at room temperature of semiconducting materials.

From that moment, the performance of OFETs has radically improved due to a better understanding of the impact of the chemical and solid-state structures of the organic semiconductors on charge transport, as well as factors related to the device structure[6,28,167], which are explained in detail in section I.VI.III.).

Nowadays, the performance of OFETs is already surpassing that of amorphous silicon (a-Si) FETs with field effect mobilities of 0.1-1 $cm^2 V^{-1} s^{-1}$ (Figure I.16) and is approaching that of polycrystalline silicon (c-Si) FETs (Figure I.16) with field effect mobilities higher than 10 $cm^2 V^{-1} s^{-1}$. The state-of-the-art charge carrier mobilities for thin film OFETs are 17.2 $cm^2 V^{-1} s^{-1}$ in the case of vacuum-deposited small molecules[168], 31.3 $cm^2 V^{-1} s^{-1}$ for solution-processed small molecules[169], and 10.5 $cm^2 V^{-1} s^{-1}$ for conjugated polymers[170]. For bulk single crystal devices, mobility as high as 15-40 $cm^2 V^{-1} s^{-1}$ has been reported[171–174].

I.VI.III. OFET structure and operation

(i) Device geometry

An OFET is a three-terminal device, in which a voltage applied to a gate electrode controls the current flow between the source and drain electrodes via an imposed voltage. The basic scheme is shown in Figure I.17, where V_{GS} and V_{DS} are the voltages applied to the gate and drain electrodes, respectively. The source electrode is normally grounded.
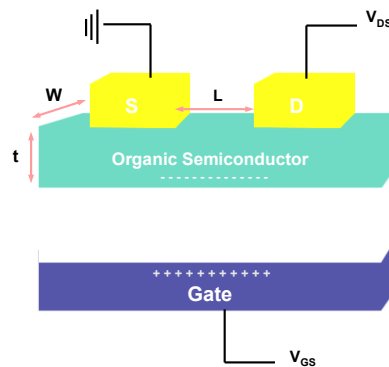
Figure I.17. Schematic illustration of top contact – bottom gate organic field effect transistor. *L* is the channel length; *W* is the channel width and *t* is the thickness of the semiconductor layer.

As can be seen in Figure I.17, an OFET is based on three fundamental components:

Contacts: also known as gate, source and drain electrodes as shown in Figure I.17. The voltage is usually applied to the gate (V_{GS}) and drain (V_{DS}) electrodes, while the source electrode (V_S) is normally grounded ($V_S = 0$ V). Source and drain electrodes are usually based on gold, while the gate electrode is based on doped silicon. Aluminum is also employed as contact electrodes.

Dielectric or **insulator**: can be a metal oxide, being SiO_2 the most often used, which is thermally grown on top of the gate electrode. Polymers are also potential materials as dielectrics because of their native insulator properties and are widely used. Typical examples of these polymers are polyimide (PI), polymethylmethacrylate (PMMA), polyvinyl alcohol (PVA) or polyvinyl phenol (PVP).

Organic semiconductor layer: Both polymers and small molecules are used as semiconducting materials. Depending on the type of the charge carriers they transport, these materials can be further sub-categorized as semiconductors that allow for p-type, n-type, and ambipolar transport channels when incorporated in OFETs. The most common organic semiconductors are explained in detail in the section I.VII.)

Depending on the order in which these layers are deposited during the device fabrication, four device structures can be built up, as shown in Figure I.18. These device architectures are: bottom contact – bottom gate (BCBG, Figure I.18(a)), top contact – bottom gate (TCBG, Figure I.18(b)), bottom contact – top gate (BCTG, Figure I.18(c)) and top contact – top gate (TCTG, Figure I.18(d)). In all the geometries the semiconductor layer must be connected with source and drain electrodes[175] and the dielectric layer to the gate electrode.

	Bottom Contact	**Top Contact**
Bottom Gate	Source · Organic Semiconductor · Drain · Dielectric · Substrate (Gate) — **(a) BCBG**	Source · Drain · Organic Semiconductor · Dielectric · Substrate (Gate) — **(b) TCBG**
Top Gate	Gate · Dielectric · Source · Organic Semiconductor · Drain · Substrate — **(c) BCTG**	Gate · Dielectric · Source · Organic Semiconductor · Drain · Substrate — **(d) TCTG**
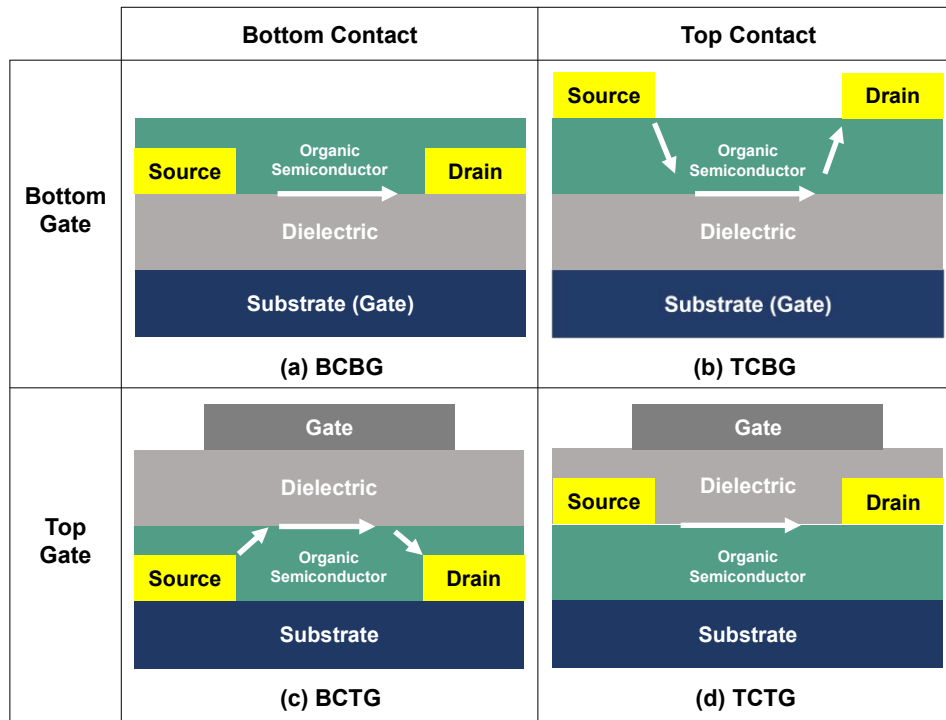
Figure I.18. The schematic representations of the four OFET configurations: (a) bottom contact – bottom gate (BCBG), (b) top contact – bottom gate (TCBG), (c) bottom contact – top gate (BCTG) and (d) top contact – top gate (TCTG).

These four geometries can be lumped in two groups: *coplanar* (Figure I.18(a) and (d)), when the source and drain electrodes are in the same plane as the conducting channel and *staggered* (Figure I.18(b) and (c)), when the source and drain electrodes are offset from the plane of the conducting channel. The white arrows in Figure I.18 represent the charge carrier pathways from source to drain electrodes. In a coplanar structure the charges are injected directly from the source electrode to the semiconductor/dielectric interface, while in the staggered geometry, the charges are injected into the bulk of the undoped semiconductor and need to travel through several tens of nanometers of undoped semiconductor before they reach the semiconductor/dielectric interface.

The different geometries can have a significant effect on the final performance[176–178] of the OFET. For instance, TCBG and BCTG (Figure I.18(b) and (c)) usually give better performances than those of BCBG and TCTG (Figure I.18(a) and (d)). This is attributed to the improved contact between the organic semiconducting layer and the electrodes. BCBG configuration allows for quick examination of new semiconductor materials and processing methods because the gate dielectric, insulator, and source and drain contacts can be prefabricated, and the semiconductor is deposited in the last step of the process. Another advantage of this structure is that the semiconductor-dielectric interface is maintained pristine as no additional steps are required after the deposition of the semiconductor. However, this structure leaves the organic semiconductor exposed to air and is easily penetrated by oxygen, water and other factors and therefore, the performance of this kind of devices often degrades during storage. In contrast, in BCTG and TCTG configurations, the active layer is encapsulated by the gate dielectric layer and the gate electrode, and therefore the device stability is significantly improved. However, in this case, the dielectric must be chosen carefully to preserve the integrity of the semiconductor[6,179,180].

In this thesis, the most used configurations were the top contact - bottom gate (TCBG) and bottom contact - top gate (BCTG), which are described in detail in the methodology chapter.

It is well known that interface engineering is one of the most widely investigated approaches to improve the device performance. Both electrode/organic layer and the dielectric/organic layer interfaces are involved in the whole motion process of charge carriers in the semiconducting material, and therefore, they have a huge impact on the device characteristics.

The electrode/organic layer interface has a key influence on the carrier injection process, while the dielectric/organic layer interface determines the carrier transport process and device stability. Many methods are used to modify the electrode/organic layer interface in order to improve carrier injection. A very common approach is the introduction of a buffer layer between the source-drain electrode and the organic layer, which reduces the energy barrier and prevents the penetration of metal atoms into the organic layer. The dielectric/organic layer interface dominates charge carrier transport and affects the device stability in three different ways[181]. First, the trap density on the dielectric layer surface affects the device performance dramatically, especially for n-type OFETs[179,182]. Second, the dielectric layer can influence the morphology and crystallinity of the organic semiconductor layers which in turn severely impact the performance and device stability. The third way is the influence of this interface on the aggregation of organic semicrystalline grains.

Hence, higher order and continuous thin films with lamellar packing are required to obtain high mobility and stability. This leads to better molecular orbital overlap between neighboring molecules, and which in turn favors carrier transfer, as well as inhibit the charge carrier trapping under ambient conditions by H_2O or O_2, and/or impurities of the atmosphere. This can be achieved by optimizing both electrode/organic semiconductor and dielectric/organic semiconductor interfaces, which are an effective way to obtain high performance devices with excellent stability[43,182,183].

(ii) Device operation

In the case of an ideal device, when no V_{GS} is applied, there is no charge accumulation at the semiconductor-dielectric interface, and the device is turned 'off'.

Assuming a n-channel OFET (Figure I.17), where the majority of charge carriers are electrons, the application of a positive V_{GS} polarizes the dielectric causing the accumulation of negative charge carriers at the semiconductor-dielectric interface and the transistor is 'on'. If there is no V_{DS} applied to the drain electrode, the negative charge density at the semiconductor-dielectric interface will be uniform across the channel. However, when a positive V_{DS} is applied, the accumulated charge carriers flow from source to the drain electrode where a drain current I_D is measured. The charge density in the transistor channel and, thus, the current, are modulated by the magnitude of the field applied, V_{GS}, hence the 'field-effect' terminology.

In a real device, a small positive V_{GS} is often required first, to fill charge traps at the dielectric-semiconductor interface before free charge carriers are accumulated in the conduction channel. This trap filling potential is known as the threshold voltage V_{Th} and can result from sources like crystal deffects, interfacial roughness and impurities.
The operating mode of an OFET produces two typical curent-voltage characteristics as shown in Figure I.19.

- the output or I_D-V_{DS} curves, which are obtained by holding V_{GS} constant and sweeping V_{DS} (Figure I.19(a)).
- the transfer or I_D-V_{DS} curves, which are obtained by holding V_{DS} constant and sweeping V_{GS} (Figure I.19(b)).
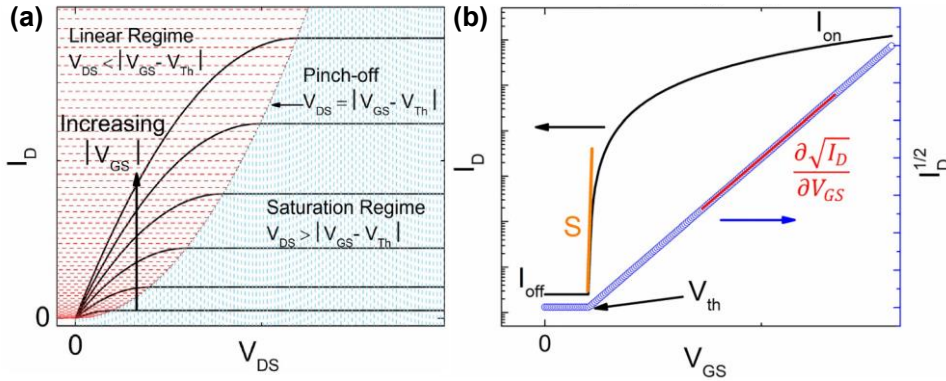
Figure I.19. (a) Output and (b) Transfer representations of n-channel OFETs in saturation regime[6]. Copyright © 2021, AIP Publishing.

As long as $V_{DS} \ll (V_{GS} - V_{Th})$, the current flowing to the transistor channel (I_D) obeys the Ohm's law, namely, it increases linearly with V_{DS}. This is referred to as the linear regime (Figure I.20(a)). However, when the V_{DS} is further increased to become equal to $V_{GS} - V_{Th}$, the concentration of mobile charge carriers reduces to zero near the drain electrode, which means that the channel is pinched-off (P in Figure I.20(b)). Further increasing the source-drain voltage does not substantially increase the current but leads to the expansion of the depletion region and therefore a slight shortening of the conduction channel. In this situation the transistor is operating in saturation regime[184,185] (Figure I.20(c)).
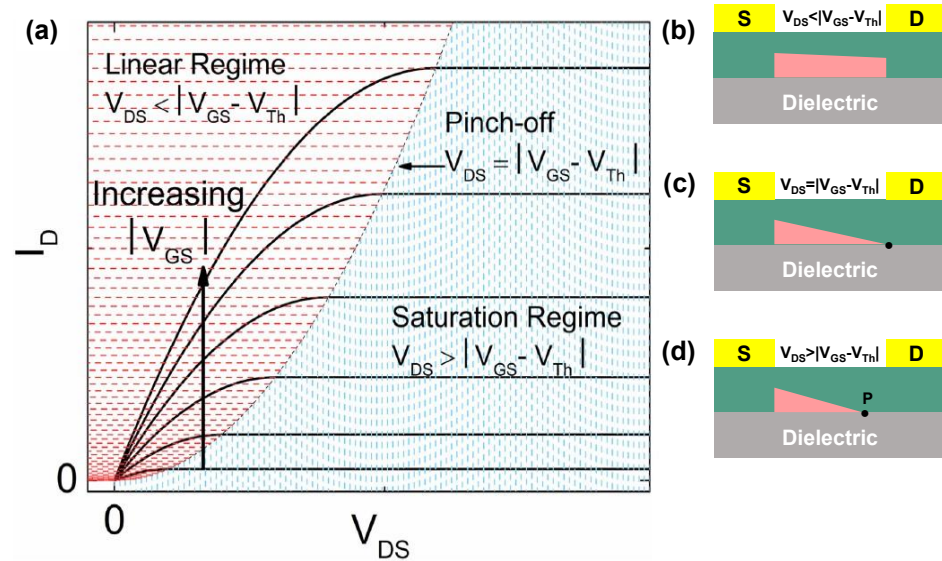
Figure I.20. (a) Ideal OFET output characteristics, (b)-(d) TCBG structures with the conduction channel in light pink, (b) In linear regime, (c) at pinch-off, and (d) in the saturation regime[6]. Copyright © 2021, AIP Publishing.

From the transfer characteristics (Figure I.19(b)), various parameter can be extracted which characterize the performance of an OFET:

Charge transport mobility (μ) is the drift velocity of carriers per unit of electric field strength. Depending on the nature of the semiconductor and electrodes used, the formed channel can be p-type or n-type.

On/off current (I_{ON}/I_{OFF}) is the ratio between the maximum *on*-state current and the minimum *off*-state current.

Threshold voltage (V_{Th}) is the minimum gate voltage required to turn on the transistor.

The performance parameters were extracted from I_D-V_{DS} response plots (transfer curves) in the saturation regime by using the assumptions of conventional transistor formalism ([Eq I.1]. These parameters include field-effect mobility µ, threshold voltge V_{Th}, and current on/off ratio (I_{ON}/I_{OFF}).

$$I_{D,sat} = \frac{W}{2L} \mu C_{diel} (V_{GS} - V_{Th})^2 \quad \text{[Eq. I. 1]}$$

Where $I_{D,sat}$ is the drain current in the saturation regime, W the channel width, L the channel length, C_{diel} the capacitance per unit area of the insulator layer, and V_{GS} the gate voltage.

I.VII. Organic semiconductor materials for OFETs

As mentioned above, there are two major groups of organic semiconductor materials for electronic devices: π-conjugated polymers and small-molecule semiconductors.

An important difference between these two classes of materials lies in the way they are processed to form thin films. Whereas small molecules are usually deposited by evaporation, conjugated polymers can only be processed from solution e.g., by spin-coating or printing techniques. Additionally, a number of low-molecular materials can be grown as single crystals allowing intrinsic electronic properties to be studied on such model systems.

According to their charge transport polarity, these materials can be further sub-categorized as (i) p-type, where the majority of carriers are positive charges or holes, (ii) n-type, where the main carriers are negative

charges or electrons, and (iii) ambipolar semiconductors, where both hole and electron charge carriers can be transported.

It is well known that the charge injection and charge transport processes are highly influenced by the HOMO and LUMO energy levels of semiconducting materials, which also determines their stability in ambient conditions[182,186,187]. The charge injection process occurs at the metal/semiconductor layer interface and in order to be effective, the HOMO/LUMO energies of the organic semiconductor must be at levels where both holes and electrons can be extracted and injected, respectively at accessible applied electric fields. Once the charges are injected in the organic thin film, charge transport process occurs at the dielectric/semiconductor layer interface, and this can be effective when highly ordered molecules are present at this interface since they can provide enough molecular orbital overlap to allow efficient charge transfer between consecutives molecules[54].

The frontier molecular orbitals can be modified in three principal ways[188]: (i) enlarging the π-conjugated systems (ii) incorporating planar fused aromatic ring systems or quinoidal systems, and (iii) incorporating alternating donor/acceptor functional units. These methods are very effective for reducing HOMO-LUMO gaps, however options (i) and (ii) have the adverse effect of increasing HOMO energy levels, thus reducing ambiental stability. This problem is overcome by option (iii) in which both electron-rich and electron-deficient molecular groups are integrated into the semiconductor, providing a local acceptor character that stabilizes both HOMO and LUMO levels. This combined donor-acceptor (D-A) strategy is widely used to design efficient polymer photovoltaic materials.

Ladder-type heteroarene systems, which are molecules composed of fused aromatic rings connected via sharing two or more adjacent

atoms, represent a very attractive class of high performance small-molecule semiconductors or building blocks for the construction of polymeric semiconductors as they meet most of the above-mentioned requirements[189]. These molecules contain locked and planar π-electronic systems and are clearly distinguishable from linear conjugated molecules where the aromatic rings are interconnected via carbon-carbon bonds. Thus, several of the distinctive merits offered by the fusion of heteroaromatic rings into ladder-type heteroarenes are: i) extended π-conjugation lengths and improved electron delocalization within the molecules, as a result of their highly planar backbone structures, which lead to reduced HOMO-LUMO gaps[190]; ii) reduced reorganization energies due to their greatly suppressed rotational freedom through the fusion of adjacent aromatic rings, which therefore, result in enhanced intrinsic intramolecular charge transport[191]; and iii) closer π-stacking between neighboring molecules, due to the stronger intermolecular electron couplings induced by the larger π-conjugation systems of ladder-type heteroarenes, which further benefits intermolecular charge transport[103].

Many ladder-type heteroarenes, implemented in OFETs, present comparable charge carrier mobilities to those of amorphous silicon[167,194–198] (Figure I.21). However, most ladder-type molecules typically exhibit electron-rich characteristics (hole-transporting or p-type semiconductors), while the synthesis of electron-deficient analogues (electron-transporting or n-type semiconductors) is far more challenging given the existence of a high-density π-electron cloud within the aromatic skeleton. Nevertheless, the development of electron-deficient ladder-type π-conjugated systems is essential to obtain donor-acceptor semiconductors exhibiting ambipolar performances required for the achievement of low-power consumption complementary organic circuits (CMOS).

In the following section, a brief summary of the most outstanding ladder-type heteroarene-based organic semiconductor is made, including hole- and electron-transporting molecular semiconductors, as well as ladder-type conjugated polymers with application in OFETs.

I.VII.I. p-type ladder-type heteroarenes

The most promising p-type ladder-type organic semiconductors are large acenes, in which multiple benzene rings are linearly fused, such as rubrene, pentacene[45,173,199] and TIPS-pentacene[200–202] (Figure I.21), among others. These molecules present extended conjugation lengths and efficient π-orbital overlaps, leading to extraordinary hole mobility in the range of 10 to 40 $cm^2\ V^{-1}\ s^{-1}$, which suggests the great promise of ladder-type organic semiconductors to realize high-performance electronic devices[171,203]. Notwithstanding, larger acenes, such as hexacenes and heptacenes show poor ambient stability due to their high-lying HOMO energy levels, which dramatically limits their applications in organic electronics[28,204–206].
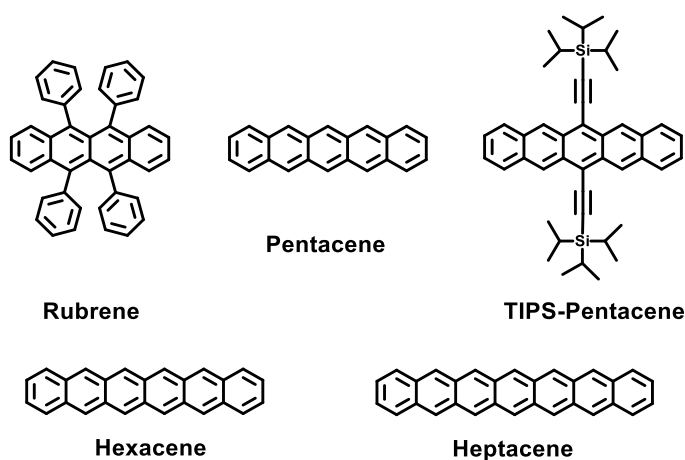
Figure I.21. Chemical structures of benchmark acenes derivatives used as p-type semiconductors in OFETs**.**

Another kind of ladder-type semiconductors with improved ambient stability[207,208] are the [n]-thienoacenes consisting of fused thiophenes in a ladder-type manner[35–37,209–212] (Figure I.22). In these systems, the incorporation of heteroatoms into the fused aromatic rings leads to the stabilization of the frontier molecular orbitals, as well as to enhanced molecular packing modes, which in turn leads to improved charge transport[28]. However, even though an improved stability is achieved for [n]-thienoacenes, significantly lowered hole mobilities compared with that of acene compounds are observed.

Tetrathienoacene   **Pentathienoacene**   **Hexathienoacene**

Heptathienoacene   **Octathienoacene**
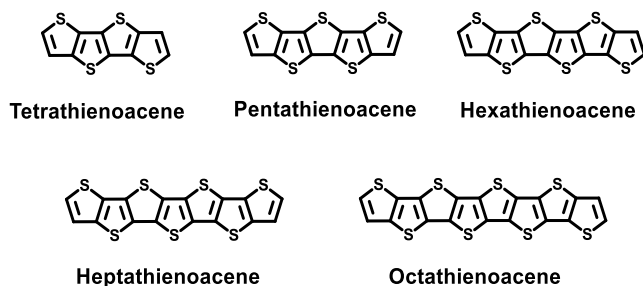
Figure I.22. Chemical structures of [n]-thienoacenes used as p-type semiconductors in OFETs.

Therefore, the combination of acenes and [n]-thienoacenes gives rise to ladder-type benzothiophene heteroarenes such as benzothienobenzothiophene (BTBT)[213–217], dinapthothienothiophene (DNTT)[218,219], dibenzothiophenothienothiophene (DBTTT)[220,221], and dianthrathienothiophene (DATT)[204] (Figure I.23), which exhibit remarkable mobilities with excellent OFET stability. These benzothiophene heteroarenes are qualified among the best performing organic semiconductor materials, with a charge carrier mobility on the order of 10 $cm^2\,V^{-1}\,s^{-1}$. In 2014, Bao et al[214] demonstrated hole mobilities up to value of up to 43 $cm^2\,V^{-1}\,s^{-1}$ for OFET devices built with 2C8-BTBT (Figure I.23)

as the active layer by using an off-center spin-coating method for device fabrication.
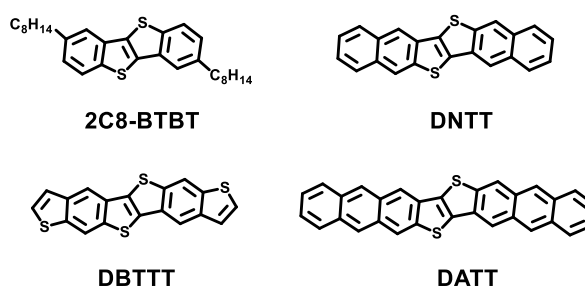
Figure I.23. Chemical structures of benchmark heteroarenes used as p-type semiconductors in OFETs.

I.VII.II. n-type ladder-type heteroarenes

As mentioned above, there are fewer accounts of n-type[41] organic semiconductors when compared to p-type, primarily because of their lower intrinsic stability in ambient conditions but also due to the difficulty of synthesizing organic semiconductors with low LUMO energy levels.

Previous studies suggested that the substitution of high-performance hole-transporting semiconductors with electron-withdrawing groups such as F, Cl, Br and CN is an efficient approach to obtain electron-transporting organic semiconductors[28]. Thus, the perfluorinated pentacene[40] (Figure I.24) showed electron-transporting behavior, with electron mobilities up to 0.11 cm^2 V^{-1} s^{-1}. On the other hand, the introduction of cyano groups into fluorene oligomers (Figure I.24) also leads to n-type semiconductors.

Perfluoropentacene   Indenofluorenedicyanovinylene
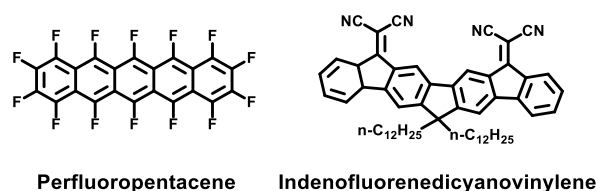
Figure I.24. Examples of representative ladder-type electron-transporting molecular semiconductors constructed by functionalizing p-type organic semiconductors with electron-withdrawing atoms or groups.

However, a straightforward modification of hole-transporting materials with strong electron-withdrawing groups remains a great challenge, mainly due to the reduced chemical reactivity and unfavored steric hindrance created by typical electron-withdrawing substituents.

The most promising and extensively investigated air-stable n-channel organic semiconductors are perylene diimide (PDI) and naphthalene diimide (NDI) derivatives[28,40,222] (Figure I.25).

NDI   PDI
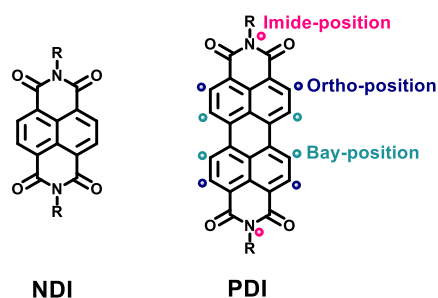
Figure I.25. Chemical structures of imide-functionalized derivatives used as n-type semiconductors in OFETs.

Their remarkable electron-transporting performance is mainly attributed to factors such as: (i) the strong electron-withdrawing ability of the imide/amide groups which lower the LUMO energy levels, thus

facilitating and stabilizing electron injection; (ii) their core planarity which enhances the π-conjugation, therefore improving intramolecular charge transport; (iii) solubilizing ability offered by alkyl substitution at the N-imide, which enables excellent solution processability and fine-tuned film morphology; (iv) N-alkyl chains that are distant from the aromatic core, which minimize the steric hindrance; therefore, the n-channel semiconductors can achieve close intermolecular π-π stacking for efficient charge carrier intermolecular hopping, and (v) facile synthetic modifications.

Moreover, the addition of highly electron-withdrawing groups such as CN and F, to these already electron-deficient molecules, lowers the LUMO levels resulting in higher electron mobilities and ambient stability[41]. Thus, Cl_2-NDI[223] and PDIF-CN_2[224–228] (Figure I.26) stand out from the crowd because they exhibit mobility values, in ambient conditions, up to 8 and 3 $cm^2 V^{-1} s^{-1}$, respectively. On the other hand, Wang et al.[189,229], reported in 2012, the ladder-type chlorinated perylene bisimide (PBI), C12-4CldiPBI (Figure I.26) which consists of two PDI units which are triply linked at their bay and alpha position (see Figure I.25). This semiconductor exhibits a low-lying LUMO energy level down to -4.22 eV, which made it one of the most electron-deficient n-type organic semiconductors at the time. In fact, single-crystal OFET devices fabricated with C12-4CldiPBI[229] showed remarkable air-stable electron-transporting characteristics with a high charge carrier mobility of up to 4.65 $cm^2 V^{-1} s^{-1}$.
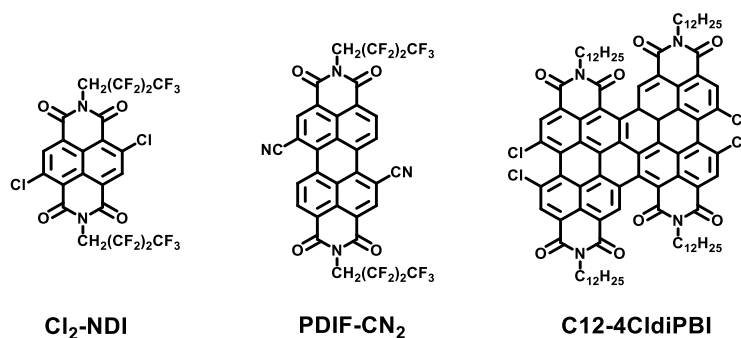
Figure I.26. Chemical structures of benchmark NDI and PDI based derivatives used as n-type semiconductors in OFETs.

Bithienoimides (BTI, Figure I.27) are another type of promising imide-functionalized heteroarenes, which combine the planarity and the efficient π-π stacking of the bithiophene unit with the electron-withdrawing capacity of the imide functionality. The BTI unit was first synthesized as an electron-deficient unit by Marks et al.,[230] and its incorporation into polymers afforded a series of semiconductors with remarkable performance in OFETs[148] and OPVs[233]. In 2017, Guo et al.,[231] synthesized a series of highly electron-deficient BTI-based ladder-type heteroarenes with up to five imide groups and 15 rings fused into their molecular backbones (Figure I.27). These new BTI-based molecules showed highly planar and rigid molecular backbones and gradually decreasing LUMO levels from -2.90 eV for BTI2 to -3.55 eV for BTI5. An electron mobility in the range of 0.013 to 0.045 cm^2 V^{-1} s^{-1} was demonstrated in OFETs fabricated with these BTIn molecules.
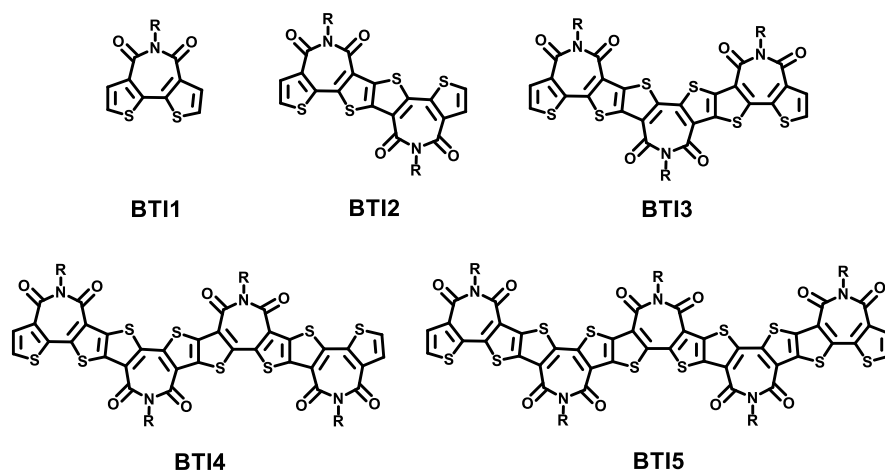
Figure I.27. Chemical structures of BTI-based ladder-type heteroarenes used as n-type semiconductors in OFETs.

I.VII.III. Ladder-type conjugated polymers

Conjugated polymers are particularly attractive because of their good solubility, excellent mechanical properties, which enables fabrication of flexible and stretchable devices by using high throughput methods, such as inkjet printing and roll-and-roll coating[234–236].

Some of the previously shown small molecules (Figure I.27) have been used as monomers to synthesize conjugated polymers. Thus, inspired by their remarkable performance, the imide-functionalized (BTI) acceptor units were incorporated into polymer semiconductors which led to excellent device performance[237,238] (Figure I.28).

P(BTim-R)

PBTI2-2FT
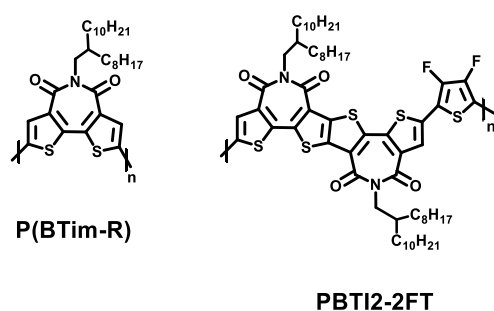
Figure I.28. Chemical structures of some BTI-based polymers used as n-type semiconductors in OFETs.

The BTI units were also incorporated in polymers (Figure I.28) since the active σ positions of the extended thiophenes lead to easily extension of the π-conjugated skeleton and/or polymerization[192,230,233,239–242]. Moreover, the β positions allow structural modifications and optimization leading to a vast library of imide-functionalized conjugated polymers. BTI unit thus, represents a versatile acceptor unit for constructing high-performance polymers with tunable frontier molecular orbitals and charge carrier mobilities. For instance, some BTI polymers (Figure I.28) showed encouraging electron mobility up to 1.13 cm^2 V^{-1} s^{-1} in OFETs[233]. These results suggest the great potential of fused BTI as building blocks for multifunctional semiconducting polymers.

I.VIII. Objectives

The relation between device performance and the chemical structure of organic semiconductors is not yet fully understood, owing to the limited knowledge of charge transport mechanisms in organic materials. Therefore, understanding charge transport in organic materials is essential in the pursuit of new materials with improved structure-property relationships.

The present thesis is focused on the study of different electron-transporting ladder-type imide-functionalized organic semiconductors (Figures I.29-I.32) with the aim of getting further insights into the understanding of charge transport mechanism in organic semiconductors.

To this end, a combined experimental/theoretical approach is used, which links spectroscopic, electrochemistry, and spectroelectrochemistry techniques with density functional theory (DFT) calculations, allowing us to obtain useful information related to the electronic structure of organic semiconductors and thus, to establish structure-properties relationships.

The ladder-type imide-functionalized organic semiconductors studied in this thesis are divided into 4 chapters.

Chapter 1 presents the study of a series of fused BTI-based heteroarenes (BTI2-BTI5 in Figure I.29), mainly focusing on understanding the reason of the previously found[231,232] monotonic decrease of electronic mobility with the extension of the conjugation backbone in these BTI compounds. To this end, we investigated the influence of the molecular length and structure of the BTI-based semiconductors on: a) the stabilization of charged states in solution and b) the stabilization of charged states in the

solid state at the dielectric/organic semiconductor interface of operational OFET devices[193].
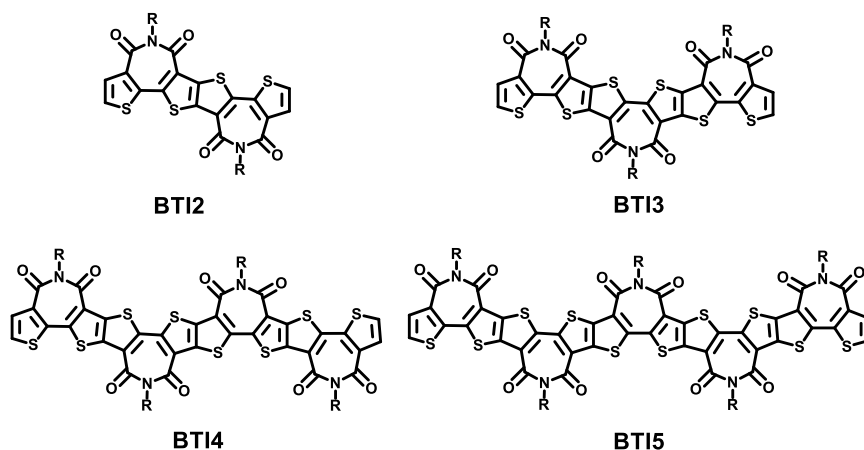
Figure I.29. Chemical structures of ladder-type heteroarenes BTI2-BTI5.

Chapter 2 presents the study of a series of two organic diradicaloids based on quinoidal oligothiophene imides[243] (BTICN and QTICN in Figure I.30) which exhibit high stability and electrical conductivity. Their aromatic counterparts (BTI and QTI in Figure I.30) are used for comparative purposes. The QTICN system, with a higher diradical character displayed a cross-conjugation assisted self-doping with the formation of a positive radical cation and a negative charged radical anion. Thus, in this chapter, we tried to provide new insights into the electron conduction mechanism of self-doped diradicaloid materials but also demonstrate the great potential of highly stable and conductive organic diradicaloids based on fused quinoidal oligothiophene imides for enabling high-performance n-type dopant-free electrically conductive materials.
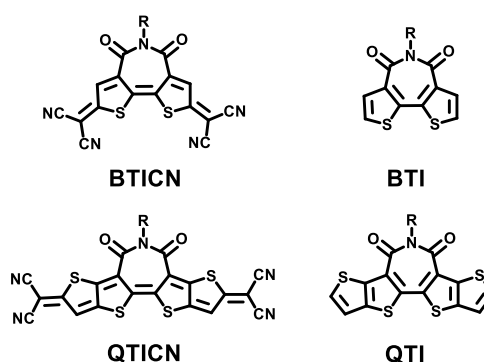
Figure I.30. Chemical structures of the quinoidal oligothiophene imides BTICN and QTICN, and their aromatic counterparts BTI and QTI.

Chapter 3 presents the study of a series of π-extended nine-ring-fused systems (naft-1-4 in Figure I.31) which were synthesized by metal-free reactions of auto-condensation and cross-condensation of pyrene and 1,8-naphthalimide moieties endowed with 1,2-diketone functionalities[244]. A combined theoretical, electrochemical, optical spectroscopy and material characterization study was carried out, which allows as to investigate the interplay of different effects such as: (i) the type of solubilizing chain, (ii) the all-acceptor versus donor-acceptor nature of the novel systems, and (iii) the molecular ordering, on the ability to stabilize multiple charges and on the OFET device response characteristics.
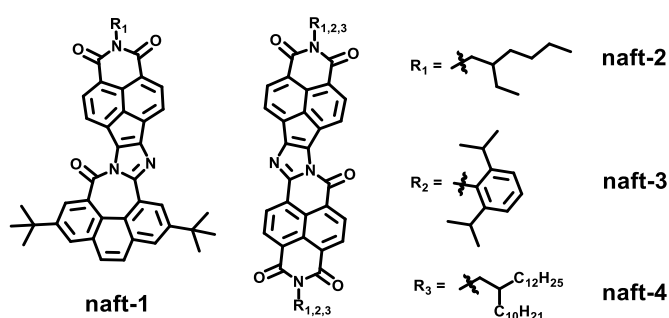
Figure I.31. Chemical structures of imide-functionalized naft-1-4 systems.

Chapter 4 presents the study of a new series of polymers based on BTI units (PBTI1-PBTI5 in Figure I.32) which exhibit high electron mobilities in OFETs[232]. As observed in the case of the monomeric units seen in Chapter 1 (BTI2-BTI5 in Figure I.29), a similar downward trend in electron mobility was also found for these series of homopolymers based on BTIn building blocks as the size of the BTI was increased. In order to study this behavior, a vibrational and theoretical study was carried out focusing both on intra- and intermolecular properties.
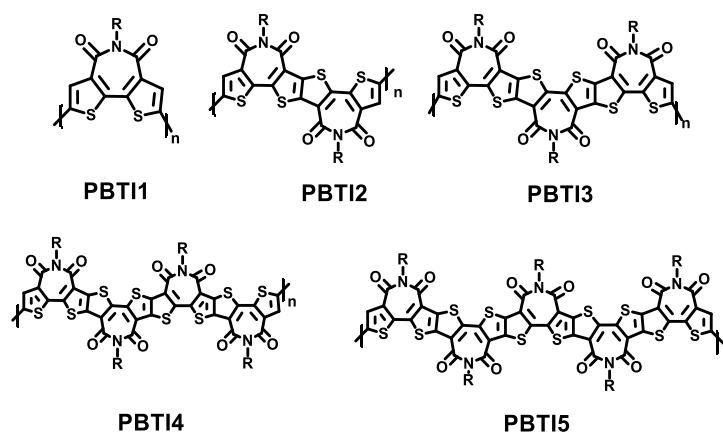
Figure I.32. Chemical structures of the semiconducting polymers PBTI1-PBTI5.

I.IX.   References

[1]   Prasanna Chandrasekhar. *Conducting Polymers, Fundamentals and Applications*; Springer US, 1999.

[2]   Deshpande. *Electron Dev & Cir-Prin & App*; McGraw Hill, 2007.

[3]   Wood, S.; Hollis, J. R.; Kim, J.-S. Raman Spectroscopy as an Advanced Structural Nanoprobe for Conjugated Molecular Semiconductors. *J. Phys. D. Appl. Phys.* **2017**, *50*, 73001.

[4]   Simon M. Sze. *Physics of Semiconductor Devices*; John Wiley and Sons: New York NY, 1981.

[5]   Martin Pope, C. E. S. *Electronic Processes in Organic Crystals and Polymers*; Oxford University Press: New York NY, 1999.

[6]   Lamport, Z. A.; Haneef, H. F.; Anand, S.; Waldrip, M.; Jurchescu, O. D. Tutorial: Organic Field-Effect Transistors: Materials, Structure and Operation. *J. Appl. Phys.* **2018**, *124*, 71101.

[7]   Forrest, S. R. The Path to Ubiquitous and Low-Cost Organic Electronic Appliances on Plastic. *Nature* **2004**, *428*, 911–918.

[8]   Eder, F.; Klauk, H.; Halik, M.; Zschieschang, U.; Schmid, G.; Dehm, C. Organic Electronics on Paper. *Appl. Phys. Lett.* **2004**, *84*, 2673–2675.

[9]   Irimia-Vladu, M.; Troshin, P. A.; Reisinger, M.; Schwabegger, G.; Ullah, M.; Schwoediauer, R.; Mumyatov, A.; Bodea, M.; Fergus, J. W.; Razumov, V. F.; Sitter, H.; Bauer, S.; Sariciftci, N. S. Environmentally Sustainable Organic Field Effect Transistors. *Org. Electron.* **2010**, *11*, 1974–1990.

[10]   Wu, X.; Ma, Y.; Zhang, G.; Chu, Y.; Du, J.; Zhang, Y.; Li, Z.; Duan, Y.; Fan, Z.; Huang, J. Thermally Stable, Biocompatible, and Flexible Organic Field-Effect Transistors and Their Application in Temperature Sensing Arrays for Artificial Skin. *Adv. Funct. Mater.* **2015**, *25*, 2138–2146.

[11]   Mühl, S.; Beyer, B. Bio-Organic Electronics—Overview and Prospects for the Future. *Electronics* . 2014.

[12]   Matsui, H.; Takeda, Y.; Tokito, S. Flexible and Printed Organic Transistors: From Materials to Integrated Circuits. *Org. Electron.* **2019**, *75*, 105432.

[13]   Lee, Y. H.; Jang, M.; Lee, M. Y.; Kweon, O. Y.; Oh, J. H. Flexible Field-Effect Transistor-Type Sensors Based on Conjugated Molecules. *Chem* **2017**, *3*, 724–763.

[14]   Strobel, N.; Seiberlich, M.; Eckstein, R.; Lemmer, U.; Hernandez-Sosa, G. Organic Photodiodes: Printing, Coating, Benchmarks, and Applications. *Flex. Print. Electron.* **2019**, *4*, 43001.

[15]   Twenty-Five Years of Conducting Polymers. *Chem. Commun.* **2003**, No. 1, 1–4.

[16]   ELEY, D. D. Phthalocyanines as Semiconductors. *Nature* **1948**, *162*, 819.

[17]   Ferraris, J.; Cowan, D. O.; Walatka, V.; Perlstein, J. H. Electron Transfer in a New Highly Conducting Donor-Acceptor Complex. *J. Am. Chem. Soc.* **1973**, *95*, 948–949.

[18]   Anderson, P. W.; Lee, P. A.; Saitoh, M. Remarks on Giant Conductivity in TTF-TCNQ. *Solid State Commun.* **1973**, *13*, 595–598.

[19]   Chiang, C. K.; Fincher, C. R.; Park, Y. W.; Heeger, A. J.; Shirakawa, H.; Louis, E. J.; Gau, S. C.; MacDiarmid, A. G. Electrical Conductivity in Doped Polyacetylene. *Phys. Rev. Lett.* **1977**, *39*, 1098–1101.

[20]   Chiang, C. K.; Druy, M. A.; Gau, S. C.; Heeger, A. J.; Louis, E. J.; MacDiarmid, A. G.; Park, Y. W.; Shirakawa, H. Synthesis of Highly Conducting Films of Derivatives of Polyacetylene, (CH)X. *J. Am. Chem. Soc.* **1978**, *100*, 1013–1015.

[21]   Catalan, G.; Scott, J. F. Physics and Applications of Bismuth Ferrite. *Adv. Mater.* **2009**, *21*, 2463–2485.

[22]   https://www.nobelprize.org/prizes/chemistry/2000/summary/.

[23]   Shirakawa, H. The Discovery of Polyacetylene Film: The Dawning of an Era of Conducting Polymers (Nobel Lecture). *Angew. Chemie Int. Ed.* **2001**, *40*, 2574–2580.

[24]   MacDiarmid, A. G. "Synthetic Metals": A Novel Role for Organic Polymers (Nobel Lecture). *Angew. Chemie Int. Ed.* **2001**, *40*, 2581–2590.

[25]   Brütting, W. Introduction to the Physics of Organic Semiconductors. *Physics of Organic Semiconductors*. May 9, 2005, pp 1–14.

[26]   Roncali, J. Molecular Engineering of the Band Gap of π-Conjugated Systems: Facing Technological Applications. *Macromol. Rapid Commun.* **2007**, *28*, 1761–1775.

[27]   Noriega, R.; Rivnay, J.; Vandewal, K.; Koch, F. P. V; Stingelin, N.; Smith, P.; Toney, M. F.; Salleo, A. A General Relationship between Disorder, Aggregation and Charge Transport in Conjugated Polymers. *Nat. Mater.* **2013**, *12*, 1038–1044.

[28]   Mei, J.; Diao, Y.; Appleton, A. L.; Fang, L.; Bao, Z. Integrated Materials Design of Organic Semiconductors for Field-Effect Transistors. *J. Am. Chem. Soc.* **2013**, *135*, 6724–6746.

[29]   Verlaak, S.; Steudel, S.; Heremans, P.; Janssen, D.; Deleuze, M. S. Nucleation of Organic Semiconductors on Inert Substrates. *Phys. Rev. B* **2003**, *68*, 195409.

[30]   Wang, C.; Liang, Z.; Liu, Y.; Wang, X.; Zhao, N.; Miao, Q.; Hu, W.; Xu, J. Single Crystal N-Channel Field Effect Transistors from Solution-Processed Silylethynylated Tetraazapentacene. *J. Mater. Chem.* **2011**, *21*, 15201–15204.

[31]   Liang, Z.; Tang, Q.; Xu, J.; Miao, Q. Soluble and Stable N-Heteropentacenes with High Field-Effect Mobility. *Adv. Mater.* **2011**, *23*, 1535–1539.

[32]   Yamada, K.; Okamoto, T.; Kudoh, K.; Wakamiya, A.; Yamaguchi, S.; Takeya, J. Single-Crystal Field-Effect Transistors of Benzoannulated Fused Oligothiophenes and Oligoselenophenes. *Appl. Phys. Lett.* **2007**, *90*, 72102.

[33]   Okamoto, T.; Kudoh, K.; Wakamiya, A.; Yamaguchi, S. General Synthesis of Thiophene and Selenophene-Based Heteroacenes. *Org. Lett.* **2005**, *7*, 5301–5304.

[34]   Takimiya, K.; Kunugi, Y.; Konda, Y.; Niihara, N.; Otsubo, T. 2,6-Diphenylbenzo[1,2-b:4,5-b‘]Dichalcogenophenes: A New Class of High-Performance Semiconductors for Organic Field-Effect Transistors. *J. Am. Chem. Soc.* **2004**, *126*, 5084–5085.

[35]   Okamoto, T.; Kudoh, K.; Wakamiya, A.; Yamaguchi, S. General Synthesis of Extended Fused Oligothiophenes Consisting of an Even Number of Thiophene Rings. *Chem. – A Eur. J.* **2007**, *13*, 548–556.

[36]   Zhang, X.; Côté, A. P.; Matzger, A. J. Synthesis and Structure of Fused α-Oligothiophenes with up to Seven Rings. *J. Am. Chem. Soc.*

2005, *127*, 10502–10503.

[37]   Xiao, K.; Liu, Y.; Qi, T.; Zhang, W.; Wang, F.; Gao, J.; Qiu, W.; Ma, Y.; Cui, G.; Chen, S.; Zhan, X.; Yu, G.; Qin, J.; Hu, W.; Zhu, D. A Highly π-Stacked Organic Semiconductor for Field-Effect Transistors Based on Linearly Condensed Pentathienoacene. *J. Am. Chem. Soc.* **2005**, *127*, 13281–13286.

[38]   Chi, X.; Li, D.; Zhang, H.; Chen, Y.; Garcia, V.; Garcia, C.; Siegrist, T. 5,6,11,12-Tetrachlorotetracene, a Tetracene Derivative with π-Stacking Structure: The Synthesis, Crystal Structure and Transistor Properties. *Org. Electron.* **2008**, *9*, 234–240.

[39]   Jones, B. A.; Ahrens, M. J.; Yoon, M.-H.; Facchetti, A.; Marks, T. J.; Wasielewski, M. R. High-Mobility Air-Stable n-Type Semiconductors with   Processing   Versatility: Dicyanoperylene-3,4:9,10-Bis(Dicarboximides). *Angew. Chemie Int. Ed.* **2004**, *43*, 6363–6366.

[40]   Sakamoto, Y.; Suzuki, T.; Kobayashi, M.; Gao, Y.; Fukai, Y.; Inoue, Y.; Sato, F.; Tokito, S. Perfluoropentacene: High-Performance P−n Junctions and Complementary Circuits with Pentacene. *J. Am. Chem. Soc.* **2004**, *126*, 8138–8140.

[41]   Usta, H.; Facchetti, A.; Marks, T. J. N-Channel Semiconductor Materials Design for Organic Complementary Circuits. *Acc. Chem. Res.* **2011**, *44*, 501–510.

[42]   Jones, B. A.; Facchetti, A.; Wasielewski, M. R.; Marks, T. J. Tuning Orbital Energetics in Arylene Diimide Semiconductors. Materials Design for Ambient Stability of n-Type Charge Transport. *J. Am. Chem. Soc.* **2007**, *129*, 15259–15278.

[43]   Newman, C. R.; Frisbie, C. D.; da Silva Filho, D. A.; Brédas, J.-L.; Ewbank, P. C.; Mann, K. R. Introduction to Organic Thin Film Transistors and Design of N-Channel Organic Semiconductors. *Chem. Mater.* **2004**, *16*, 4436–4451.

[44]   Babel, A.; Jenekhe, S. A. Alkyl Chain Length Dependence of the Field-Effect Carrier Mobility in Regioregular Poly(3-Alkylthiophene)S. *Synth. Met.* **2005**, *148*, 169–173.

[45]   Anthony, J. E. Functionalized Acenes and Heteroacenes for Organic Electronics. *Chem. Rev.* **2006**, *106*, 5028–5048.

[46]   Virkar, A. A.; Mannsfeld, S.; Bao, Z.; Stingelin, N. Organic Semiconductor Growth and Morphology Considerations for Organic Thin-

Film Transistors. *Adv. Mater.* **2010**, *22*, 3857–3875.

[47]   Mei, J.; Graham, K. R.; Stalder, R.; Tiwari, S. P.; Cheun, H.; Shim, J.; Yoshio, M.; Nuckolls, C.; Kippelen, B.; Castellano, R. K.; Reynolds, J. R. Self-Assembled Amphiphilic Diketopyrrolopyrrole-Based Oligothiophenes for Field-Effect Transistors and Solar Cells. *Chem. Mater.* **2011**, *23*, 2285–2288.

[48]   Kanimozhi, C.; Yaacobi-Gross, N.; Chou, K. W.; Amassian, A.; Anthopoulos, T. D.; Patil, S. Diketopyrrolopyrrole–Diketopyrrolopyrrole-Based Conjugated Copolymer for High-Mobility Organic Field-Effect Transistors. *J. Am. Chem. Soc.* **2012**, *134*, 16532–16535.

[49]   Miller, L. L.; Mann, K. R. π-Dimers and π-Stacks in Solution and in Conducting Polymers. *Acc. Chem. Res.* **1996**, *29*, 417–423.

[50]   Becke, A. D. A New Mixing of Hartree–Fock and Local Density-functional Theories. *J. Chem. Phys.* **1993**, *98*, 1372–1377.

[51]   Castiglioni, C.; Del Zoppo, M.; Zerbi, G. Vibrational Raman Spectroscopy of Polyconjugated Organic Oligomers and Polymers. *J. Raman Spectrosc.* **1993**, *24*, 485–494.

[52]   Yuan, Q.; Mannsfeld, S. C. B.; Tang, M. L.; Roberts, M.; Toney, M. F.; DeLongchamp, D. M.; Bao, Z. Microstructure of Oligofluorene Asymmetric Derivatives in Organic Thin Film Transistors. *Chem. Mater.* **2008**, *20*, 2763–2772.

[53]   Winfield, J. M.; Donley, C. L.; Friend, R. H.; Kim, J.-S. Probing Thin-Film Morphology of Conjugated Polymers by Raman Spectroscopy. *J. Appl. Phys.* **2010**, *107*, 24902.

[54]   Yao, Y.; Dong, H.; Hu, W. Charge Transport in Organic and Polymeric Semiconductors for Flexible and Stretchable Devices. *Adv. Mater.* **2016**, *28*, 4513–4523.

[55]   Blakesley, J. C.; Castro, F. A.; Kylberg, W.; Dibb, G. F. A.; Arantes, C.; Valaski, R.; Cremona, M.; Kim, J. S.; Kim, J.-S. Towards Reliable Charge-Mobility Benchmark Measurements for Organic Semiconductors. *Org. Electron.* **2014**, *15*, 1263–1272.

[56]   Liu, C.; Huang, K.; Park, W.-T.; Li, M.; Yang, T.; Liu, X.; Liang, L.; Minari, T.; Noh, Y.-Y. A Unified Understanding of Charge Transport in Organic Semiconductors: The Importance of Attenuated Delocalization for the Carriers. *Mater. Horizons* **2017**, *4*, 608–618.

[57]   Ma, H.; Chai, S.; Chen, D.; Huang, J.-D. Charge-Transport

Properties of 4-(1,2,2-Tri{\-}phenyl{\-}vinyl){\-}aniline Salicylaldehyde Hydrazone: Tight-Packing Induced Molecular `hardening'. *IUCrJ* **2017**, *4*, 695–699.

[58] Nan, G.; Li, Z. Crystal Structure versus Charge Transport in Organic Single Crystals of [1]Benzothieno[3,2-b][1]Benzothiophene Derivatives from a Multiscale Theoretical Study. *J. Mater. Chem. C* **2014**, *2*, 1447–1456.

[59] Marcus, R. A. Exchange Reactions and Electron Transfer Reactions Including Isotopic Exchange. Theory of Oxidation-Reduction Reactions Involving Electron Transfer. Part 4.—A Statistical-Mechanical Basis for Treating Contributions from Solvent, Ligands, and Inert Salt. *Discuss. Faraday Soc.* **1960**, *29*, 21–31.

[60] Coropceanu, V.; Cornil, J.; da Silva Filho, D. A.; Olivier, Y.; Silbey, R.; Brédas, J.-L. Charge Transport in Organic Semiconductors. *Chem. Rev.* **2007**, *107*, 926–952.

[61] Diao, Y.; Shaw, L.; Bao, Z.; Mannsfeld, S. C. B. Morphology Control Strategies for Solution-Processed Organic Semiconductor Thin Films. *Energy Environ. Sci.* **2014**, *7*, 2145–2159.

[62] Chen, W.; Nikiforov, M. P.; Darling, S. B. Morphology Characterization in Organic and Hybrid Solar Cells. *Energy Environ. Sci.* **2012**, *5*, 8045–8074.

[63] Shao, W.; Dong, H.; Jiang, L.; Hu, W. Morphology Control for High Performance Organic Thin Film Transistors. *Chem. Sci.* **2011**, *2*, 590–600.

[64] Hayashi, H.; Barker, J. E.; Cárdenas Valdivia, A.; Kishi, R.; MacMillan, S. N.; Gómez-García, C. J.; Miyauchi, H.; Nakamura, Y.; Nakano, M.; Kato, S.; Haley, M. M.; Casado, J. Monoradicals and Diradicals of Dibenzofluoreno[3,2-b]Fluorene Isomers: Mechanisms of Electronic Delocalization. *J. Am. Chem. Soc.* **2020**, *142*, 20444–20455.

[65] Streifel, B. C.; Zafra, J. L.; Espejo, G. L.; Gómez-García, C. J.; Casado, J.; Tovar, J. D. An Unusually Small Singlet–Triplet Gap in a Quinoidal 1,6-Methano[10]Annulene Resulting from Baird's 4n π-Electron Triplet Stabilization. *Angew. Chemie Int. Ed.* **2015**, *54*, 5888–5893.

[66] Casado, J.; Hernández, V.; López Navarrete, J. T. Vibrational Raman Shifts and Aromaticity: The Case of Oligothiophenes. *Chem. Rec.* **2015**, *15*, 1110–1118.

[67] Zafra, J. L.; González Cano, R. C.; Ruiz Delgado, M. C.; Sun, Z.;

Li, Y.; López Navarrete, J. T.; Wu, J.; Casado, J. Zethrene Biradicals: How pro-Aromaticity Is Expressed in the Ground Electronic State and in the Lowest Energy Singlet, Triplet, and Ionic States. *J. Chem. Phys.* **2014**, *140*, 54706.

[68]   González, S. R.; Nieto-Ortega, B.; González Cano, R. C.; Lloveras, V.; Novoa, J. J.; Mota, F.; Vidal-Gancedo, J.; Rovira, C.; Veciana, J.; del Corro, E.; Taravillo, M.; Baonza, V. G.; López Navarrete, J. T.; Casado, J. Diradicals Acting through Diamagnetic Phenylene Vinylene Bridges: Raman Spectroscopy as a Probe to Characterize Spin Delocalization. *J. Chem. Phys.* **2014**, *140*, 164903.

[69]   Ferrón, C. C.; Sheynin, Y.; Li, M.; Patra, A.; Bendikov, M.; López Navarrete, J. T.; Hernández, V.; Ruiz Delgado, M. C. Raman Spectroscopic Characterization of Polyselenophenes and Poly(3,4-Ethylenenedioxyselenophene)S. *Isr. J. Chem.* **2014**, *54*, 759–766.

[70]   Rodríguez González, S.; Ruiz Delgado, M. C.; Caballero, R.; De la Cruz, P.; Langa, F.; López Navarrete, J. T.; Casado, J. Delocalization-to-Localization Charge Transition in Diferrocenyl-Oligothienylene-Vinylene Molecular Wires as a Function of the Size by Raman Spectroscopy. *J. Am. Chem. Soc.* **2012**, *134*, 5675–5681.

[71]   Aragó, J.; Ponce Ortiz, R.; Nieto-Ortega, B.; Hernández, V.; Casado, J.; Facchetti, A.; Marks, T. J.; Viruela, P. M.; Ortí, E.; López Navarrete, J. T. Carbonyl-Functionalized Quaterthiophenes: A Study of the Vibrational Raman and Electronic Absorption/Emission Properties Guided by Theoretical Calculations. *ChemPhysChem* **2012**, *13*, 168–176.

[72]   Ponce Ortiz, R.; Casado, J.; Rodríguez González, S.; Hernández, V.; López Navarrete, J. T.; Viruela, P. M.; Ortí, E.; Takimiya, K.; Otsubo, T. Quinoidal Oligothiophenes: Towards Biradical Ground-State Species. *Chem. – A Eur. J.* **2010**, *16*, 470–484.

[73]   Casado, J.; Takimiya, K.; Otsubo, T.; Ramírez, F. J.; Quirante, J. J.; Ortiz, R. P.; González, S. R.; Oliva, M. M.; López Navarrete, J. T. Raman Spectroscopy Shows Interchain through Space Charge Delocalization in a Mixed Valence Oligothiophene Cation and in Its π-Dimeric Biradicaloid Dication. *J. Am. Chem. Soc.* **2008**, *130*, 14028–14029.

[74]   Malavé Osuna, R.; Ponce Ortiz, R.; Ruiz Delgado, M. C.; Nenajdenko, V. G.; Sumerin, V. V; Balenkova, E. S.; Hernández, V.; López Navarrete, J. T. Fourier Transform Raman and DFT Study of Three Annulated Oligothiophenes with Different Molecular Shapes. *ChemPhysChem* **2007**, *8*, 745–750.

[75]   Zhang, C.; Medina Rivero, S.; Liu, W.; Casanova, D.; Zhu, X.; Casado, J. Stable Cross-Conjugated Tetrathiophene Diradical. *Angew. Chemie Int. Ed.* **2019**, *58*, 11291–11295.

[76]   Osuna, R. M.; Ortiz, R. P.; Okamoto, T.; Suzuki, Y.; Yamaguchi, S.; Hernández, V.; López Navarrete, J. T. Thiophene- and Selenophene-Based Heteroacenes: Combined Quantum Chemical DFT and Spectroscopic Raman and UV−Vis−NIR Study. *J. Phys. Chem. B* **2007**, *111*, 7488–7496.

[77]   Ponce Ortiz, R.; Casado, J.; Hernández, V.; López Navarrete, J. T.; Viruela, P. M.; Ortí, E.; Takimiya, K.; Otsubo, T. On the Biradicaloid Nature of Long Quinoidal Oligothiophenes: Experimental Evidence Guided by Theoretical Studies. *Angew. Chemie Int. Ed.* **2007**, *46*, 9057–9061.

[78]   Ortiz, R. P.; Osuna, R. M.; Delgado, M. C. R.; Casado, J.; Hernández, V.; Navarrete, J. T. L.; Sakamoto, Y.; Suzuki, T. Perfluorination of Tetracene: Effects on the Optical Gap and Electron-Acceptor Properties. An Electrochemical, Theoretical DFT, and Raman Spectroscopic Study. In *Proc.SPIE*; 2006; Vol. 6192.

[79]   Casado, J.; Ortiz, R. P.; Ruiz Delgado, M. C.; Hernández, V.; López Navarrete, J. T.; Raimundo, J.-M.; Blanchard, P.; Allain, M.; Roncali, J. Alternated Quinoid/Aromatic Units in Terthiophenes Building Blocks for Electroactive Narrow Band Gap Polymers. Extended Spectroscopic, Solid State, Electrochemical, and Theoretical Study. *J. Phys. Chem. B* **2005**, *109*, 16616–16627.

[80]   Casado, J.; Hernández, V.; Ruiz Delgado, M. C.; Ortiz, R. P.; López Navarrete, J. T.; Facchetti, A.; Marks, T. J. Incisive Structure−Spectroscopic Correlation in Oligothiophenes Functionalized with (±) Inductive/Mesomeric Fluorine Groups: Joint Raman and DFT Study. *J. Am. Chem. Soc.* **2005**, *127*, 13364–13372.

[81]   Casado, J.; Zotti, G.; Berlin, A.; Hernández, V.; Ortiz, R. P.; Navarrete, J. T. L. Combined Theoretical and Spectroscopic Raman Study of 3,4-Ethylenedioxy and S,S-Dioxide Substituted Terthiophenes and Their Parent Polymers. *J. Mol. Struct.* **2005**, *744–747*, 551–556.

[82]   Casado, J.; Ortiz, R. P.; Ruiz Delgado, M. C.; Azumi, R.; Oakley, R. T.; Hernández, V.; López Navarrete, J. T. Multidisciplinary Physicochemical Analysis of Oligothiophenes End-Capped by Nitriles: Electrochemistry, UV−Vis−Near-IR, IR, and Raman Spectroscopies and Quantum Chemistry. *J. Phys. Chem. B* **2005**, *109*, 10115–10125.

[83]   Cuberos Guzmán, V.; Ponce Ortiz, R.; Ruiz Delgado, M. C.;

Azumi, R.; Oakley, R. T.; Casado, J.; Hernández, V.; López Navarrete, J. T. FT-Raman Spectroscopic Study, Aided by Quantum Chemical DFT Calculations, of a Series of Oligothiophenes End-Capped by Nitriles. *J. Mol. Struct.* **2005**, *744–747*, 403–409.

[84] Mayorga Burrezo, P.; Domínguez, R.; Zafra, J. L.; Pappenfus, T. M.; Cruz, P. de la; Welte, L.; Janzen, D. E.; López Navarrete, J. T.; Langa, F.; Casado, J. Oligomers of Cyclopentadithiophene-Vinylene in Aromatic and Quinoidal Versions and Redox Species with Intermediate Forms. *Chem. Sci.* **2017**, *8*, 8106–8114.

[85] Burrezo, P. M.; Zafra, J. L.; López Navarrete, J. T.; Casado, J. Quinoidal/Aromatic Transformations in π-Conjugated Oligomers: Vibrational Raman Studies on the Limits of Rupture for π-Bonds. *Angew. Chemie Int. Ed.* **2017**, *56*, 2250–2259.

[86] Qi, Q.; Burrezo, P. M.; Phan, H.; Herng, T. S.; Gopalakrishna, T. Y.; Zeng, W.; Ding, J.; Casado, J.; Wu, J. Ambient Stable Radical Cations, Diradicaloid π-Dimeric Dications, Closed-Shell Dications, and Diradical Dications of Methylthio-Capped Rylenes. *Chem. – A Eur. J.* **2017**, *23*, 7595–7606.

[87] Kawabata, K.; Osaka, I.; Sawamoto, M.; Zafra, J. L.; Mayorga Burrezo, P.; Casado, J.; Takimiya, K. Dithienyl Acenedithiophenediones as New π-Extended Quinoidal Cores: Synthesis and Properties. *Chem. – A Eur. J.* **2017**, *23*, 4579–4589.

[88] Zafra, J. L.; Qiu, L.; Yanai, N.; Mori, T.; Nakano, M.; Alvarez, M. P.; Navarrete, J. T. L.; Gómez-García, C. J.; Kertesz, M.; Takimiya, K.; Casado, J. Reversible Dimerization and Polymerization of a Janus Diradical To Produce Labile C−C Bonds and Large Chromic Effects. *Angew. Chemie Int. Ed.* **2016**, *55*, 14563–14568.

[89] Mayorga Burrezo, P.; Pelado, B.; Ponce Ortiz, R.; De la Cruz, P.; López Navarrete, J. T.; Langa, F.; Casado, J. Robust Ethylenedioxythiophene–Vinylene Oligomers from Fragile Thiophene–Vinylene Cores: Synthesis and Optical, Chemical and Electrochemical Properties of Multicharged Shapes. *Chem. – A Eur. J.* **2015**, *21*, 1713–1725.

[90] Zhou, N.; Guo, X.; Ortiz, R. P.; Harschneck, T.; Manley, E. F.; Lou, S. J.; Hartnett, P. E.; Yu, X.; Horwitz, N. E.; Burrezo, P. M.; Aldrich, T. J.; López Navarrete, J. T.; Wasielewski, M. R.; Chen, L. X.; Chang, R. P. H.; Facchetti, A.; Marks, T. J. Marked Consequences of Systematic Oligothiophene Catenation in Thieno[3,4-c]Pyrrole-4,6-Dione and Bithiopheneimide Photovoltaic Copolymers. *J. Am. Chem. Soc.* **2015**, *137*,

12565–12579.

[91]   Ferrari, A. C.; Robertson, J.; Castiglioni, C.; Tommasini, M.; Zerbi, G. Raman Spectroscopy of Polyconjugated Molecules and Materials: Confinement Effect in One and Two Dimensions. *Philos. Trans. R. Soc. London. Ser. A Math. Phys. Eng. Sci.* **2004**, *362*, 2425–2459.

[92]   Castiglioni, C.; Lopez Navarrete, J. T.; Zerbi, G.; Gussoni, M. A Simple Interpretation of the Vibrational Spectra of Undoped, Doped and Photoexcited Polyacetylene: Amplitude Mode Theory in the GF Formalism. *Solid State Commun.* **1988**, *65*, 625–630.

[93]   Lopez-Navarrete, J. T.; Tian, B.; Zerbi, G. Relation between Effective Conjugation, Vibrational Force Constants and Electronic Properties in Polyconjugated Materials. *Solid State Commun.* **1990**, *74*, 199–202.

[94]   Ruiz Delgado, M. C.; Casado, J.; Hernandez, V.; Lopez Navarrete, J. T.; Fuhrmann, G.; Bäuerle, P. Combined Raman and Computational Study of a Novel Series of Macrocyclic π-Conjugated Diacetylene-Bridged α-Linked Oligothiophenes. *J. Phys. Chem. B* **2004**, *108*, 3158–3167.

[95]   Casado, J.; Hernández, V.; Ponce Ortiz, R.; Ruiz Delgado, M. C.; López Navarrete, J. T.; Fuhrmann, G.; Bäuerle, P. Application of Raman Spectroscopy and Quantum Chemistry for Featuring the Structure of Positively Charged Species in Macrocyclic π-Conjugated Diacetylene-Bridged Oligothiophenes. *J. Raman Spectrosc.* **2004**, *35*, 592–599.

[96]   Tian, B.; Zerbi, G.; Müllen, K. Electronic and Structural Properties of Polyparaphenylenevinylene from the Vibrational Spectra. *J. Chem. Phys.* **1991**, *95*, 3198–3207.

[97]   Agosti, E.; Rivola, M.; Hernandez, V.; Del Zoppo, M.; Zerbi, G. Electronic and Dynamical Effects from the Unusual Features of the Raman Spectra of Oligo and Polythiophenes. *Synth. Met.* **1999**, *100*, 101–112.

[98]   Malavé Osuna, R.; Ruiz Delgado, M. C.; Hernández, V.; López Navarrete, J. T.; Vercelli, B.; Zotti, G.; Novoa, J. J.; Suzuki, Y.; Yamaguchi, S.; Henssler, J. T.; Matzger, A. J. Oxidation of End-Capped Pentathienoacenes and Characterization of Their Radical Cations. *Chem. – A Eur. J.* **2009**, *15*, 12346–12361.

[99]   Beard, M. C.; Turner, G. M.; Schmuttenmaer, C. A. Terahertz Spectroscopy. *J. Phys. Chem. B* **2002**, *106*, 7146–7159.

[100]   Schettino, V.; Luigi Gervasio, F.; Cardini, G.; Remigio Salvi, P. Density Functional Calculation of Structure and Vibrational Spectra of Polyenes. *J. Chem. Phys.* **1999**, *110*, 3241–3250.

[101]   Bianco, A.; Del Zoppo, M.; Zerbi, G. Experimental CC Stretching Phonon Dispersion Curves and Electron Phonon Coupling in Polyene Derivatives. *J. Chem. Phys.* **2004**, *120*, 1450–1457.

[102]   Moreno Castro, C.; Ruiz Delgado, M. C.; Hernández, V.; Hotta, S.; Casado, J.; López Navarrete, J. T. Efficiency of the π Conjugation in a Novel Family of α,A′-Bisphenyl End-Capped Oligothiophenes by Means of Raman Spectroscopy. *J. Chem. Phys.* **2002**, *116*, 10419–10427.

[103]   Casado, J.; Katz, H. E.; Hernández, V.; López Navarrete, J. T. Spectroelectrochemical Raman Study of Two End-Capped Sexithiophenes with Applications as Electroactive Molecular Materials. *J. Phys. Chem. B* **2002**, *106*, 2488–2496.

[104]   Casado, J.; Hicks, R. G.; Hernández, V.; Myles, D. J. T.; Ruiz Delgado, M. C.; López Navarrete, J. T. Infrared and Raman Features of a Series of α,ω-Bis(Arylthio)Oligothiophenes as Molecular Wires. A π-Electron Delocalization Efficiency Study. *J. Chem. Phys.* **2003**, *118*, 1912–1920.

[105]   Osuna, R. M.; Ortiz, R. P.; Ruiz Delgado, M. C.; Sakamoto, Y.; Suzuki, T.; Hernández, V.; López Navarrete, J. T. Synthesis and Characterization of Three Novel Perfluoro-Oligothiophenes Ranging in Length from the Trimer to the Pentamer. *J. Phys. Chem. B* **2005**, *109*, 20737–20745.

[106]   Yoon, M.-H.; DiBenedetto, S. A.; Facchetti, A.; Marks, T. J. Organic Thin-Film Transistors Based on Carbonyl-Functionalized Quaterthiophenes: High Mobility N-Channel Semiconductors and Ambipolar Transport. *J. Am. Chem. Soc.* **2005**, *127*, 1348–1349.

[107]   Sakamoto, A.; Furukawa, Y.; Tasumi, M. Resonance Raman and Ultraviolet to Infrared Absorption Studies of Positive Polarons and Bipolarons in Sulfuric-Acid-Treated Poly(p-Phenylenevinylene). *J. Phys. Chem.* **1994**, *98*, 4635–4640.

[108]   Hernández, V.; Casado, J.; Ramírez, F. J.; Zotti, G.; Hotta, S.; López Navarrete, J. T. Efficient π Electrons Delocalization in α,A′-dimethyl End-capped Oligothiophenes: A Vibrational Spectroscopic Study. *J. Chem. Phys.* **1996**, *104*, 9271–9282.

[109]   Yokonuma, N.; Furukawa, Y.; Tasumi, M.; Kuroda, M.; Nakayama,

J. Electronic Absorption and Raman Studies of BF4−-Doped Polythiophene Based on the Spectra of the Radical Cation and Dication of α-Sexithiophene. *Chem. Phys. Lett.* **1996**, *255*, 431–436.

[110]   Casado, J.; Otero, T. F.; Hotta, S.; Hemandez, V.; Ramírez, F. J.; Lopez Navarrete, J. T. Electrochemical Doping in a Series of α, A′-Dimethyl End-Capped Oligothienyls An FT-Raman Confirmation of a Radical Cation Generation. *Opt. Mater. (Amst).* **1998**, *9*, 82–87.

[111]   Casado, J.; Hernández, V.; Hotta, S.; López Navarrete, J. T. Vibrational Spectra of Charged Defects in a Series of α,A′-Dimethyl End-Capped Oligothiophenes Induced by Chemical Doping with Iodine. *J. Chem. Phys.* **1998**, *109*, 10419–10429.

[112]   Casado, J.; Hotta, S.; Hernández, V.; López Navarrete, J. T. Vibrational Spectroscopic Study of a Series of α,α‘-Diethyl End-Capped Oligothiophenes with Different Chain Lengths in the Neutral State. *J. Phys. Chem. A* **1999**, *103*, 816–822.

[113]   Hernández, V.; Casado, J.; Ramírez, F. J.; Zotti, G.; Hotta, S.; López Navarrete, J. T. Delocalization Length, Electronic Properties and Vibrational Spectra of Neutral α,A′ -Dimethyl End-Capped Oligothiophenes. *Synth. Met.* **1996**, *76*, 277–280.

[114]   Casado, J.; Hernández, V.; Ramírez, F. J.; Navarrete, J. T. L. A Theoretical Investigation of α,A′-Dimethyl End-Capped Oligothiophenes: Structures, Vibrational Spectra and Conjugation Defects. *Synth. Met.* **1997**, *89*, 159–160.

[115]   Hernández, V.; Casado, J.; Ramírez, F. J.; Alemany, L. J.; Hotta, S.; López Navarrete, J. T. Conformational Disorder and Mean Conjugation of Neutral α,α‘-Dimethyl End-Capped Oligothiophenes in Solution: A FT-Raman and FT-Infrared Spectroscopic Study. *J. Phys. Chem.* **1996**, *100*, 289–293.

[116]   Furukawa, Y.; Yokonuma, N.; Tasumi, M.; Kuroda, M.; Nakayama, J. Raman Studies of Doped Polythiophene and the Radical Cation and Dication of Quinquethiophene. *Mol. Cryst. Liq. Cryst. Sci. Technol. Sect. A. Mol. Cryst. Liq. Cryst.* **1994**, *256*, 113–120.

[117]   Casado, J.; Hernández, V.; Hotta, S.; Navarrete, J. T. L. FT-Raman Studies of Charged Defects Created on Methyl End-Capped Oligothiophenes by Doping with NOBF4. *Adv. Mater.* **1998**, *10*, 1458–1461.

[118]   Hernández, V.; Casado, J.; Effenberger, F.; López Navarrete, J. T.

Analysis of the Intramolecular Charge Transfer in Donor–Acceptor α,A′-Substituted Oligothiophenes from Their Vibrational Spectra. *J. Chem. Phys.* **2000**, *112*, 5105–5112.

[119]   González, M.; Segura, J. L.; Seoane, C.; Martín, N.; Garín, J.; Orduna, J.; Alcalá, R.; Villacampa, B.; Hernández, V.; López Navarrete, J. T. Tetrathiafulvalene Derivatives as NLO-Phores: Synthesis, Electrochemistry, Raman Spectroscopy, Theoretical Calculations, and NLO Properties of Novel TTF-Derived Donor-π-Acceptor Dyads. *J. Org. Chem.* **2001**, *66*, 8872–8882.

[120]   Abbotto, A.; Beverina, L.; Bradamante, S.; Facchetti, A.; Klein, C.; Pagani, G. A.; Redi-Abshiro, M.; Wortmann, R. A Distinctive Example of the Cooperative Interplay of Structure and Environment in Tuning of Intramolecular Charge Transfer in Second-Order Nonlinear Optical Chromophores. *Chem. – A Eur. J.* **2003**, *9*, 1991–2007.

[121]   Casado, J.; Pappenfus, T. M.; Miller, L. L.; Mann, K. R.; Ortí, E.; Viruela, P. M.; Pou-Amérigo, R.; Hernández, V.; López Navarrete, J. T. Nitro-Functionalized Oligothiophenes as a Novel Type of Electroactive Molecular Material: Spectroscopic, Electrochemical, and Computational Study. *J. Am. Chem. Soc.* **2003**, *125*, 2524–2534.

[122]   Casado, J.; Hernández, V.; Kim, O.-K.; Lehn, J.-M.; López Navarrete, J. T.; Delgado Ledesma, S.; Ponce Ortiz, R.; Ruiz Delgado, M. C.; Vida, Y.; Pérez-Inestrosa, E. Vibrational and Quantum-Chemical Study of Nonlinear Optical Chromophores Containing Dithienothiophene as the Electron Relay. *Chem. – A Eur. J.* **2004**, *10*, 3805–3816.

[123]   González, S. R.; Orduna, J.; Alicante, R.; Villacampa, B.; McGee, K. A.; Pina, J.; Seixas de Melo, J.; Schwaderer, K. M.; Johnson, J. C.; Blackorbay, B. A.; Hansmeier, J. J.; Bolton, V. F.; Helland, T. J.; Edlund, B. A.; Pappenfus, T. M.; López Navarrete, J. T.; Casado, J. Understanding Optoelectronic Properties of Cyano-Terminated Oligothiophenes in the Context of Intramolecular Charge Transfer. *J. Phys. Chem. B* **2011**, *115*, 10573–10585.

[124]   Ponce Ortiz, R.; Casado, J.; Hernández, V.; López Navarrete, J. T.; Ortí, E.; Viruela, P. M.; Milián, B.; Hotta, S.; Zotti, G.; Zecchin, S.; Vercelli, B. Magnetic Properties of Quinoidal Oligothiophenes: More Than Good Candidates for Ambipolar Organic Semiconductors? *Adv. Funct. Mater.* **2006**, *16*, 531–536.

[125]   González, S. R.; Ie, Y.; Aso, Y.; López Navarrete, J. T.; Casado, J. The Frontiers of Quinoidal Stability in Long Oligothiophenes: Raman Spectra of Dicationic Polaron Pairs. *J. Am. Chem. Soc.* **2011**, *133*,

16350–16353.

[126] Casado, J.; Ponce Ortiz, R.; López Navarrete, J. T. Quinoidal Oligothiophenes: New Properties behind an Unconventional Electronic Structure. *Chem. Soc. Rev.* **2012**, *41*, 5672–5686.

[127] Kim, J.-H.; Song, C. E.; Shin, N.; Kang, H.; Wood, S.; Kang, I.-N.; Kim, B. J.; Kim, B.; Kim, J.-S.; Shin, W. S.; Hwang, D.-H. High-Crystalline Medium-Band-Gap Polymers Consisting of Benzodithiophene and Benzotriazole Derivatives for Organic Photovoltaic Cells. *ACS Appl. Mater. Interfaces* **2013**, *5*, 12820–12831.

[128] Kim, J.; Baeg, K.-J.; Khim, D.; James, D. T.; Kim, J.-S.; Lim, B.; Yun, J.-M.; Jeong, H.-G.; Amegadze, P. S. K.; Noh, Y.-Y.; Kim, D.-Y. Optimal Ambipolar Charge Transport of Thienylenevinylene-Based Polymer Semiconductors by Changes in Conformation for High-Performance Organic Thin Film Transistors and Inverters. *Chem. Mater.* **2013**, *25*, 1572–1583.

[129] Fei, Z.; Boufflet, P.; Wood, S.; Wade, J.; Moriarty, J.; Gann, E.; Ratcliff, E. L.; McNeill, C. R.; Sirringhaus, H.; Kim, J.-S.; Heeney, M. Influence of Backbone Fluorination in Regioregular Poly(3-Alkyl-4-Fluoro)Thiophenes. *J. Am. Chem. Soc.* **2015**, *137*, 6866–6879.

[130] Wood, S.; Kim, J.-H.; Hwang, D.-H.; Kim, J.-S. Effects of Fluorination and Side Chain Branching on Molecular Conformation and Photovoltaic Performance of Donor–Acceptor Copolymers. *Chem. Mater.* **2015**, *27*, 4196–4204.

[131] Salzillo, T.; Della Valle, R. G.; Venuti, E.; Brillante, A.; Siegrist, T.; Masino, M.; Mezzadri, F.; Girlando, A. Two New Polymorphs of the Organic Semiconductor 9,10-Diphenylanthracene: Raman and X-Ray Analysis. *J. Phys. Chem. C* **2016**, *120*, 1831–1840.

[132] Wood, S.; Kim, J.-H.; Wade, J.; Park, J. B.; Hwang, D.-H.; Kim, J.-S. Systematic Control of Heteroatoms in Donor–Acceptor Copolymers and Its Effects on Molecular Conformation and Photovoltaic Performance. *J. Mater. Chem. C* **2016**, *4*, 7966–7978.

[133] Razzell-Hollis, J.; Limbu, S.; Kim, J.-S. Spectroscopic Investigations of Three-Phase Morphology Evolution in Polymer: Fullerene Solar Cell Blends. *J. Phys. Chem. C* **2016**, *120*, 10806–10814.

[134] Razzell-Hollis, J.; Fleischli, F.; Jahnke, A. A.; Stingelin, N.; Seferos, D. S.; Kim, J.-S. Effects of Side-Chain Length and Shape on Polytellurophene Molecular Order and Blend Morphology. *J. Phys. Chem.*

C **2017**, *121*, 2088–2098.

[135]   Brillante, A.; Bilotti, I.; Della Valle, R. G.; Venuti, E.; Girlando, A. Probing Polymorphs of Organic Semiconductors by Lattice Phonon Raman Microscopy. *CrystEngComm* **2008**, *10,* 937–946.

[136]   Razzell-Hollis, J.; Thiburce, Q.; Tsoi, W. C.; Kim, J.-S. Interfacial Chemical Composition and Molecular Order in Organic Photovoltaic Blend Thin Films Probed by Surface-Enhanced Raman Spectroscopy. *ACS Appl. Mater. Interfaces* **2016**, *8*, 31469–31481.

[137]   Xu, J.; Diao, Y.; Zhou, D.; Mao, Y.; Giri, G.; Chen, W.; Liu, N.; Mannsfeld, S. C. B.; Xue, G.; Bao, Z. Probing the Interfacial Molecular Packing in TIPS-Pentacene Organic Semiconductors by Surface Enhanced Raman Scattering. *J. Mater. Chem. C* **2014**, *2*, 2985–2991.

[138]   Di Pietro, R.; Fazzi, D.; Kehoe, T. B.; Sirringhaus, H. Spectroscopic Investigation of Oxygen- and Water-Induced Electron Trapping and Charge Transport Instabilities in n-Type Polymer Semiconductors. *J. Am. Chem. Soc.* **2012**, *134*, 14877–14889.

[139]   Angelis, F. De; Das, G.; Fabrizio, E. Di. Analysis of the Interactions between Pentacene Film and Air Molecules by Means of Raman Spectroscopy. *Chem. Phys. Lett.* **2008**, *462*, 234–237.

[140]   Tang, C. W.; VanSlyke, S. A. Organic Electroluminescent Diodes. *Appl. Phys. Lett.* **1987**, *51*, 913–915.

[141]   Burroughes, J. H.; Bradley, D. D. C.; Brown, A. R.; Marks, R. N.; Mackay, K.; Friend, R. H.; Burns, P. L.; Holmes, A. B. Light-Emitting Diodes Based on Conjugated Polymers. *Nature* **1990**, *347*, 539–541.

[142]   Friend, R. H.; Gymer, R. W.; Holmes, A. B.; Burroughes, J. H.; Marks, R. N.; Taliani, C.; Bradley, D. D. C.; Santos, D. A. Dos; Brédas, J. L.; Lögdlund, M.; Salaneck, W. R. Electroluminescence in Conjugated Polymers. *Nature* **1999**, *397*, 121–128.

[143]   Bernius, M. T.; Inbasekaran, M.; O'Brien, J.; Wu, W. Progress with Light-Emitting Polymers. *Adv. Mater.* **2000**, *12*, 1737–1750.

[144]   Nikolka, M.; Nasrallah, I.; Rose, B.; Ravva, M. K.; Broch, K.; Sadhanala, A.; Harkin, D.; Charmet, J.; Hurhangee, M.; Brown, A.; Illig, S.; Too, P.; Jongman, J.; McCulloch, I.; Bredas, J.-L.; Sirringhaus, H. High Operational and Environmental Stability of High-Mobility Conjugated Polymer Field-Effect Transistors through the Use of Molecular Additives. *Nat. Mater.* **2017**, *16*, 356–362.

[145]   Organic Semiconductors, OLEDs, and Solar Cells. *Principles of Solar Cells, LEDs and Related Devices*. October 22, 2018, pp 307–357.

[146]   Forrest, S. R. Waiting for Act 2: What Lies beyond Organic Light-Emitting Diode (OLED) Displays for Organic Electronics? *Nanophotonics* **2021**, *10*, 31–40.

[147]   Hong, G.; Gan, X.; Leonhardt, C.; Zhang, Z.; Seibert, J.; Busch, J. M.; Bräse, S. A Brief History of OLEDs—Emitter Development and Industry Milestones. *Adv. Mater.* **2021**, *33*, 2005630.

[148]   Xue, Q.; Xie, G. Thermally Activated Delayed Fluorescence beyond Through-Bond Charge Transfer for High-Performance OLEDs. *Adv. Opt. Mater.* **2021**, *n/a*, 2002204.

[149]   Xin, J.; Sun, P.; Zhu, F.; Wang, Y.; Yan, D. Doped Crystalline Thin-Film Deep-Blue Organic Light-Emitting Diodes. *J. Mater. Chem. C* **2021**, *9*, 2236–2242.

[150]   Burroughes, J. H.; Jones, C. A.; Friend, R. H. New Semiconductor Device Physics in Polymer Diodes and Transistors. *Nature* **1988**, *335*, 137–141.

[151]   Horowitz, G.; Fichou, D.; Peng, X.; Xu, Z.; Garnier, F. A Field-Effect Transistor Based on Conjugated Alpha-Sexithienyl. *Solid State Commun.* **1989**, *72*, 381–384.

[152]   Mas-Torrent, M.; Rovira, C. Novel Small Molecules for Organic Field-Effect Transistors: Towards Processability and High Performance. *Chem. Soc. Rev.* **2008**, *37*, 827–838.

[153]   Hodsden, T.; Thorley, K. J.; Basu, A.; White, A. J. P.; Wang, C.; Mitchell, W.; Glöcklhofer, F.; Anthopoulos, T. D.; Heeney, M. The Influence of Alkyl Group Regiochemistry and Backbone Fluorination on the Packing and Transistor Performance of N-Cyanoimine Functionalised Indacenodithiophenes. *Mater. Adv.* **2021**, *2*, 1706–1714.

[154]   Iguchi, K.; Mikie, T.; Saito, M.; Komeyama, K.; Seo, T.; Ie, Y.; Osaka, I. N-Type Semiconducting Polymers Based on Dicyano Naphthobisthiadiazole: High Electron Mobility with Unfavorable Backbone Twist. *Chem. Mater.* **2021**, *33*, 2218–2228.

[155]   Meng, L.; Zhang, Y.; Wan, X.; Li, C.; Zhang, X.; Wang, Y.; Ke, X.; Xiao, Z.; Ding, L.; Xia, R.; Yip, H.-L.; Cao, Y.; Chen, Y. Organic and Solution-Processed Tandem Solar Cells with 17.3% Efficiency. *Science (80-.).* **2018**, *361*, 1094 LP – 1098.

[156]   Tang, C. W. Two-layer Organic Photovoltaic Cell. *Appl. Phys. Lett.* **1986**, *48*, 183–185.

[157]   Lv, Q.; An, C.; Zhang, T.; Zhou, P.; Hou, J. Effect of Alkyl Side Chains of Twisted Conjugated Polymer Donors on Photovoltaic Performance. *Polymer (Guildf).* **2021**, *218*, 123475.

[158]   Sharma, A.; Singh, R.; Kini, G. P.; Hyeon Kim, J.; Parashar, M.; Kim, M.; Kumar, M.; Kim, J. S.; Lee, J.-J. Side-Chain Engineering of Diketopyrrolopyrrole-Based Hole-Transport Materials to Realize High-Efficiency Perovskite Solar Cells. *ACS Appl. Mater. Interfaces* **2021**, *13*, 7405–7415.

[159]   Cai, P.; Huang, X.; Zhan, T.; Chen, G.; Qiu, R.; Zhang, L.; Xue, X.; Wang, Z.; Chen, J. Cross-Linkable and Alcohol-Soluble Pyridine-Incorporated Polyfluorene Derivative as a Cathode Interface Layer for High-Efficiency and Stable Organic Solar Cells. *ACS Appl. Mater. Interfaces* **2021**, *13*, 12296–12304.

[160]   Bao, Z.; A. Rogers, J.; E. Katz, H. Printable Organic and Polymeric Semiconducting Materials and Devices. *J. Mater. Chem.* **1999**, *9*, 1895–1904.

[161]   Dimitrakopoulos, C. D.; Malenfant, P. R. L. Organic Thin Film Transistors for Large Area Electronics. *Adv. Mater.* **2002**, *14*, 99–117.

[162]   Koutsiaki, C.; Kaimakamis, T.; Zachariadis, A.; Papamichail, A.; Kamaraki, C.; Fachouri, S.; Gravalidis, C.; Laskarakis, A.; Logothetidis, S. Efficient Combination of Roll-to-Roll Compatible Techniques towards the Large Area Deposition of a Polymer Dielectric Film and the Solution-Processing of an Organic Semiconductor for the Field-Effect Transistors Fabrication on Plastic Substrate. *Org. Electron.* **2019**, *73*, 231–239.

[163]   Yan, K.; Li, J.; Pan, L.; Shi, Y. Inkjet Printing for Flexible and Wearable Electronics. *APL Mater.* **2020**, *8*, 120705.

[164]   Spanu, A.; Casula, G.; Cosseddu, P.; Lai, S.; Martines, L.; Pani, D.; Bonfiglio, A. 20 - Flexible and Wearable Monitoring Systems for Biomedical Applications in Organic Flexible Electronics: Fundamentals, Devices, and Applications. In *Woodhead Publishing Series in Electronic and Optical Materials*; Cosseddu, P., Caironi, M. B. T.-O. F. E., Eds.; Woodhead Publishing, 2021; pp 599–625.

[165]   Tsumura, A.; Koezuka, H.; Ando, T. Macromolecular Electronic Device: Field-effect Transistor with a Polythiophene Thin Film. *Appl. Phys. Lett.* **1986**, *49*, 1210–1212.

[166]   Madru, M.; Guillaud, G.; Sadoun, M. A.; Maitrot, M.; Clarisse, C.; Contellec, M. L.; André, J.-J.; Simon, J. The First Field Effect Transistor Based on an Intrinsic Molecular Semiconductor. *Chem. Phys. Lett.* **1987**, *142*, 103–105.

[167]   Schweicher, G.; Garbay, G.; Jouclas, R.; Vibert, F.; Devaux, F.; Geerts, Y. H. Molecular Semiconductors for Logic Operations: Dead-End or Bright Future? *Adv. Mater.* **2020**, *32*, 1905909.

[168]   Amin, A. Y.; Khassanov, A.; Reuter, K.; Meyer-Friedrichsen, T.; Halik, M. Low-Voltage Organic Field Effect Transistors with a 2-Tridecyl[1]Benzothieno[3,2-b][1]Benzothiophene Semiconductor Layer. *J. Am. Chem. Soc.* **2012**, *134*, 16548–16550.

[169]   Minemawari, H.; Yamada, T.; Matsui, H.; Tsutsumi, J.; Haas, S.; Chiba, R.; Kumai, R.; Hasegawa, T. Inkjet Printing of Single-Crystal Films. *Nature* **2011**, *475*, 364–367.

[170]   Li, J.; Zhao, Y.; Tan, H. S.; Guo, Y.; Di, C.-A.; Yu, G.; Liu, Y.; Lin, M.; Lim, S. H.; Zhou, Y.; Su, H.; Ong, B. S. A Stable Solution-Processed Polymer Semiconductor with Record High-Mobility for Printed Transistors. *Sci. Rep.* **2012**, *2*, 754.

[171]   Sundar, V. C.; Zaumseil, J.; Podzorov, V.; Menard, E.; Willett, R. L.; Someya, T.; Gershenson, M. E.; Rogers, J. A. Elastomeric Transistor Stamps: Reversible Probing of Charge Transport in Organic Crystals. *Science (80-.).* **2004**, *303*, 1644 LP – 1646.

[172]   Menard, E.; Podzorov, V.; Hur, S.-H.; Gaur, A.; Gershenson, M. E.; Rogers, J. A. High-Performance n- and p-Type Single-Crystal Organic Transistors with Free-Space Gate Dielectrics. *Adv. Mater.* **2004**, *16*, 2097–2101.

[173]   Jurchescu, O. D.; Popinciuc, M.; van Wees, B. J.; Palstra, T. T. M. Interface-Controlled, High-Mobility Organic Transistors. *Adv. Mater.* **2007**, *19*, 688–692.

[174]   Reese, C.; Bao, Z. High-Resolution Measurement of the Anisotropy of Charge Transport in Single Crystals. *Adv. Mater.* **2007**, *19*, 4535–4538.

[175]   Mei, Y. Chapter 4 - Organic Transistor- Device Structure, Model and Applications. In *Advanced Nanomaterials*; Kaushik, B. K. B. T.-N., Ed.; Elsevier, 2019; pp 115–129.

[176]   Roichman, Y.; Tessler, N. Structures of Polymer Field-Effect

Transistor: Experimental and Numerical Analyses. *Appl. Phys. Lett.* **2002**, *80*, 151–153.

[177] Newman, C. R.; Chesterfield, R. J.; Panzer, M. J.; Frisbie, C. D. High Mobility Top-Gated Pentacene Thin-Film Transistors. *J. Appl. Phys.* **2005**, *98*, 84506.

[178] Hagen Klauk. *Organic Electronics II: More Materials and Applications*, 1st editio.; Wiley-VCH, 2012.

[179] Allard, S.; Forster, M.; Souharce, B.; Thiem, H.; Scherf, U. Organic Semiconductors for Solution-Processable Field-Effect Transistors (OFETs). *Angew. Chemie Int. Ed.* **2008**, *47*, 4070–4098.

[180] Shehu, A.; Quiroga, S. D.; D'Angelo, P.; Albonetti, C.; Borgatti, F.; Murgia, M.; Scorzoni, A.; Stoliar, P.; Biscarini, F. Layered Distribution of Charge Carriers in Organic Thin Film Transistors. *Phys. Rev. Lett.* **2010**, *104*, 246602.

[181] Di, C.; Liu, Y.; Yu, G.; Zhu, D. Interface Engineering: An Effective Approach toward High-Performance Organic Field-Effect Transistors. *Acc. Chem. Res.* **2009**, *42*, 1573–1583.

[182] Zhang W., Y. G. Organic Semiconductors for Field-Effect Transistors. In *Organic Optoelectronic Materials. Lecture Notes in Chemistry*; Springer, Cham, 2015.

[183] Wang, C.; Dong, H.; Hu, W.; Liu, Y.; Zhu, D. Semiconducting π-Conjugated Systems in Field-Effect Transistors: A Material Odyssey of Organic Electronics. *Chem. Rev.* **2012**, *112*, 2208–2267.

[184] Braga, D.; Horowitz, G. High-Performance Organic Field-Effect Transistors. *Adv. Mater.* **2009**, *21*, 1473–1486.

[185] Weis, M.; Manaka, T.; Iwamoto, M. Origin of Electric Field Distribution in Organic Field-Effect Transistor: Experiment and Analysis. *J. Appl. Phys.* **2009**, *105*, 24505.

[186] Mishra, A.; Bäuerle, P. Small Molecule Organic Semiconductors on the Move: Promises for Future Solar Energy Technology. *Angew. Chemie Int. Ed.* **2012**, *51*, 2020–2067.

[187] Usta, H.; Facchetti, A. Polymeric and Small-Molecule Semiconductors for Organic Field-Effect Transistors. *Large Area and Flexible Electronics*. March 11, 2015, pp 1–100.

[188] Hashemi, D.; Ma, X.; Ansari, R.; Kim, J.; Kieffer, J. Design

Principles for the Energy Level Tuning in Donor/Acceptor Conjugated Polymers. *Phys. Chem. Chem. Phys.* **2019**, *21*, 789–799.

[189] Cai, Z.; Awais, M. A.; Zhang, N.; Yu, L. Exploration of Syntheses and Functions of Higher Ladder-Type π-Conjugated Heteroacenes. *Chem* **2018**, *4*, 2538–2570.

[190] Tsuda, A.; Osuka, A. Fully Conjugated Porphyrin Tapes with Electronic Absorption Bands That Reach into Infrared. *Science (80-.).* **2001**, *293*, 79 LP – 82.

[191] Prins, P.; Grozema, F. C.; Schins, J. M.; Patil, S.; Scherf, U.; Siebbeles, L. D. A. High Intrachain Hole Mobility on Molecular Wires of Ladder-Type Poly(p-Phenylenes). *Phys. Rev. Lett.* **2006**, *96*, 146601.

[192] Chen, J.; Yang, K.; Zhou, X.; Guo, X. Ladder-Type Heteroarene-Based Organic Semiconductors. *Chem. Asian J.* **2018**, *13*, 2587—2600.

[193] Harbuzaru, A.; Arrechea-Marcos, I.; Scaccabarozzi, A. D.; Wang, Y.; Guo, X.; Caironi, M.; López Navarrete, J. T.; Ruiz Delgado, M. C.; Ponce Ortiz, R. Ladder-Type Bithiophene Imide-Based Organic Semiconductors: Understanding Charge Transport Mechanisms in Organic Field Effect Transistors. *J. Mater. Chem. C* **2020**, *8*, 15759–15770.

[194] Xie, W.; McGarry, K. A.; Liu, F.; Wu, Y.; Ruden, P. P.; Douglas, C. J.; Frisbie, C. D. High-Mobility Transistors Based on Single Crystals of Isotopically Substituted Rubrene-D28. *J. Phys. Chem. C* **2013**, *117*, 11522–11529.

[195] Yada, H.; Uchida, R.; Sekine, H.; Terashige, T.; Tao, S.; Matsui, Y.; Kida, N.; Fratini, S.; Ciuchi, S.; Okada, Y.; Uemura, T.; Takeya, J.; Okamoto, H. Carrier Dynamics of Rubrene Single-Crystals Revealed by Transient Broadband Terahertz Spectroscopy. *Appl. Phys. Lett.* **2014**, *105*, 143302.

[196] Schweicher, G.; Olivier, Y.; Lemaur, V.; Geerts, Y. H. What Currently Limits Charge Carrier Mobility in Crystals of Molecular Semiconductors? *Isr. J. Chem.* **2014**, *54*, 595–620.

[197] Podzorov, V.; Menard, E.; Rogers, J. A.; Gershenson, M. E. Hall Effect in the Accumulation Layers on the Surface of Organic Semiconductors. *Phys. Rev. Lett.* **2005**, *95*, 226601.

[198] Podzorov, V.; Menard, E.; Borissov, A.; Kiryukhin, V.; Rogers, J. A.; Gershenson, M. E. Intrinsic Charge Transport on the Surface of

Organic Semiconductors. *Phys. Rev. Lett.* **2004**, *93*, 86602.

[199] Takeyama, Y.; Ono, S.; Matsumoto, Y. Organic Single Crystal Transistor Characteristics of Single-Crystal Phase Pentacene Grown by Ionic Liquid-Assisted Vacuum Deposition. *Appl. Phys. Lett.* **2012**, *101*, 83303.

[200] Anthony, J. E.; Brooks, J. S.; Eaton, D. L.; Parkin, S. R. Functionalized Pentacene: Improved Electronic Properties from Control of Solid-State Order. *J. Am. Chem. Soc.* **2001**, *123*, 9482–9483.

[201] Sheraw, C. D.; Jackson, T. N.; Eaton, D. L.; Anthony, J. E. Functionalized Pentacene Active Layer Organic Thin-Film Transistors. *Adv. Mater.* **2003**, *15*, 2009–2011.

[202] Zhang, F.; Funahashi, M.; Tamaoki, N. High-Performance Thin Film Transistors from Semiconducting Liquid Crystalline Phases by Solution Processes. *Appl. Phys. Lett.* **2007**, *91*, 63515.

[203] Mannsfeld, S. C. B.; Tee, B. C.-K.; Stoltenberg, R. M.; Chen, C. V. H.-H.; Barman, S.; Muir, B. V. O.; Sokolov, A. N.; Reese, C.; Bao, Z. Highly Sensitive Flexible Pressure Sensors with Microstructured Rubber Dielectric Layers. *Nat. Mater.* **2010**, *9*, 859–864.

[204] Niimi, K.; Shinamura, S.; Osaka, I.; Miyazaki, E.; Takimiya, K. Dianthra[2,3-b:2′,3′-f]Thieno[3,2-b]Thiophene (DATT): Synthesis, Characterization, and FET Characteristics of New π-Extended Heteroarene with Eight Fused Aromatic Rings. *J. Am. Chem. Soc.* **2011**, *133*, 8732–8739.

[205] Zade, S. S.; Bendikov, M. Heptacene and Beyond: The Longest Characterized Acenes. *Angew. Chemie Int. Ed.* **2010**, *49*, 4012–4015.

[206] Watanabe, M.; Chang, Y. J.; Liu, S.-W.; Chao, T.-H.; Goto, K.; Islam, M. M.; Yuan, C.-H.; Tao, Y.-T.; Shinmyozu, T.; Chow, T. J. The Synthesis, Crystal Structure and Charge-Transport Properties of Hexacene. *Nat. Chem.* **2012**, *4*, 574–578.

[207] Takimiya, K.; Shinamura, S.; Osaka, I.; Miyazaki, E. Thienoacene-Based Organic Semiconductors. *Adv. Mater.* **2011**, *23*, 4347–4370.

[208] Cinar, M. E.; Ozturk, T. Thienothiophenes, Dithienothiophenes, and Thienoacenes: Syntheses, Oligomers, Polymers, and Properties. *Chem. Rev.* **2015**, *115*, 3036–3140.

[209] Vegiraju, S.; Luo, X.-L.; Li, L.-H.; Afraj, S. N.; Lee, C.; Zheng, D.; Hsieh, H.-C.; Lin, C.-C.; Hong, S.-H.; Tsai, H.-C.; Lee, G.-H.; Tung, S.-H.;

Liu, C.-L.; Chen, M.-C.; Facchetti, A. Solution Processable Pseudo N-Thienoacenes via Intramolecular S···S Lock for High Performance Organic Field Effect Transistors. *Chem. Mater.* **2020**, *32*, 1422–1429.

[210]   Liu, Y.; Wang, Y.; Wu, W.; Liu, Y.; Xi, H.; Wang, L.; Qiu, W.; Lu, K.; Du, C.; Yu, G. Synthesis, Characterization, and Field-Effect Transistor Performance of Thieno[3,2-b]Thieno[2′,3′:4,5]Thieno[2,3-d]Thiophene Derivatives. *Adv. Funct. Mater.* **2009**, *19*, 772–778.

[211]   Liu, Y.; Sun, X.; Di, C.; Liu, Y.; Du, C.; Lu, K.; Ye, S.; Yu, G. Hexathienoacene: Synthesis, Characterization, and Thin-Film Transistors. *Chem. – An Asian J.* **2010**, *5*, 1550–1554.

[212]   Mazaki, Y.; Kobayashi, K. Synthesis of Tetrathieno-Acene and Pentathieno-Acene: UV-Spectral Trend in a Homologous Series of Thieno-Acenes. *Tetrahedron Lett.* **1989**, *30*, 3315–3318.

[213]   Schweicher, G.; Lemaur, V.; Niebel, C.; Ruzié, C.; Diao, Y.; Goto, O.; Lee, W.-Y.; Kim, Y.; Arlin, J.-B.; Karpinska, J.; Kennedy, A. R.; Parkin, S. R.; Olivier, Y.; Mannsfeld, S. C. B.; Cornil, J.; Geerts, Y. H.; Bao, Z. Bulky End-Capped [1]Benzothieno[3,2-b]Benzothiophenes: Reaching High-Mobility Organic Semiconductors by Fine Tuning of the Crystalline Solid-State Order. *Adv. Mater.* **2015**, *27*, 3066–3072.

[214]   Yuan, Y.; Giri, G.; Ayzner, A. L.; Zoombelt, A. P.; Mannsfeld, S. C. B.; Chen, J.; Nordlund, D.; Toney, M. F.; Huang, J.; Bao, Z. Ultra-High Mobility Transparent Organic Thin Film Transistors Grown by an off-Centre Spin-Coating Method. *Nat. Commun.* **2014**, *5*, 3005.

[215]   Takimiya, K.; Osaka, I.; Mori, T.; Nakano, M. Organic Semiconductors Based on [1]Benzothieno[3,2-b][1]Benzothiophene Substructure. *Acc. Chem. Res.* **2014**, *47*, 1493–1502.

[216]   Diao, Y.; Tee, B. C.-K.; Giri, G.; Xu, J.; Kim, D. H.; Becerril, H. A.; Stoltenberg, R. M.; Lee, T. H.; Xue, G.; Mannsfeld, S. C. B.; Bao, Z. Solution Coating of Large-Area Organic Semiconductor Thin Films with Aligned Single-Crystalline Domains. *Nat. Mater.* **2013**, *12*, 665–671.

[217]   Ebata, H.; Izawa, T.; Miyazaki, E.; Takimiya, K.; Ikeda, M.; Kuwabara, H.; Yui, T. Highly Soluble [1]Benzothieno[3,2-b]Benzothiophene (BTBT) Derivatives for High-Performance, Solution-Processed Organic Field-Effect Transistors. *J. Am. Chem. Soc.* **2007**, *129*, 15732–15733.

[218]   Yamaguchi, Y.; Kojiguchi, Y.; Kawata, S.; Mori, T.; Okamoto, K.; Tsutsui, M.; Koganezawa, T.; Katagiri, H.; Yasuda, T. Solution-

Processable Organic Semiconductors Featuring S-Shaped Dinaphthothienothiophene (S-DNTT): Effects of Alkyl Chain Length on Self-Organization and Carrier Transport Properties. *Chem. Mater.* **2020**, *32*, 5350–5360.

[219]   Kang, M. J.; Doi, I.; Mori, H.; Miyazaki, E.; Takimiya, K.; Ikeda, M.; Kuwabara, H. Alkylated Dinaphtho[2,3-b:2′,3′-f]Thieno[3,2-b]Thiophenes (Cn-DNTTs): Organic Semiconductors for High-Performance Thin-Film Transistors. *Adv. Mater.* **2011**, *23*, 1222–1225.

[220]   Lee, E.-K.; Lee, M. Y.; Choi, A.; Kim, J.-Y.; Kweon, O. Y.; Kim, J.-H.; Jung, J. Y.; Shin, T.-J.; Oh, J. H.; Park, J.-I.; Lee, S. Y. Organic Semiconductors: Phenyl Derivative of Dibenzothiopheno[6,5-b:6′,5′-f]Thieno[3,2-b]Thiophene (DPh-DBTTT): High Thermally Durable Organic Semiconductor for High-Performance Organic Field-Effect Transistors (Adv. Electron. Mater. 10/2017). *Adv. Electron. Mater.* **2017**, *3*.

[221]   Park, J.-I.; Chung, J. W.; Kim, J.-Y.; Lee, J.; Jung, J. Y.; Koo, B.; Lee, B.-L.; Lee, S. W.; Jin, Y. W.; Lee, S. Y. Dibenzothiopheno[6,5-b:6′,5′-f]Thieno[3,2-b]Thiophene (DBTTT): High-Performance Small-Molecule Organic Semiconductor for Field-Effect Transistors. *J. Am. Chem. Soc.* **2015**, *137*, 12175–12178.

[222]   Feng, J.; Jiang, W.; Wang, Z. Synthesis and Application of Rylene Imide Dyes as Organic Semiconducting Materials. *Chem. – An Asian J.* **2018**, *13*, 20–30.

[223]   He, T.; Stolte, M.; Burschka, C.; Hansen, N. H.; Musiol, T.; Kälblein, D.; Pflaum, J.; Tao, X.; Brill, J.; Würthner, F. Single-Crystal Field-Effect Transistors of New Cl2-NDI Polymorph Processed by Sublimation in Air. *Nat. Commun.* **2015**, *6*, 5954.

[224]   Molinari, A. S.; Alves, H.; Chen, Z.; Facchetti, A.; Morpurgo, A. F. High Electron Mobility in Vacuum and Ambient for PDIF-CN2 Single-Crystal Transistors. *J. Am. Chem. Soc.* **2009**, *131*, 2462–2463.

[225]   Minder, N. A.; Ono, S.; Chen, Z.; Facchetti, A.; Morpurgo, A. F. Band-Like Electron Transport in Organic Transistors and Implication of the Molecular Structure for Performance Optimization. *Adv. Mater.* **2012**, *24*, 503–508.

[226]   Minder, N. A.; Lu, S.; Fratini, S.; Ciuchi, S.; Facchetti, A.; Morpurgo, A. F. Tailoring the Molecular Structure to Suppress Extrinsic Disorder in Organic Transistors. *Adv. Mater.* **2014**, *26*, 1254–1260.

[227]   He, Z.; Shaik, S.; Bi, S.; Chen, J.; Li, D. Air-Stable Solution-

Processed n-Channel Organic Thin Film Transistors with Polymer-Enhanced Morphology. *Appl. Phys. Lett.* **2015**, *106*, 183301.

[228]   Guo, Y.; Li, Y.; Awartani, O.; Zhao, J.; Han, H.; Ade, H.; Zhao, D.; Yan, H. A Vinylene-Bridged Perylenediimide-Based Polymeric Acceptor Enabling Efficient All-Polymer Solar Cells Processed under Ambient Conditions. *Adv. Mater.* **2016**, *28*, 8483–8489.

[229]   Lv, A.; Puniredd, S. R.; Zhang, J.; Li, Z.; Zhu, H.; Jiang, W.; Dong, H.; He, Y.; Jiang, L.; Li, Y.; Pisula, W.; Meng, Q.; Hu, W.; Wang, Z. High Mobility, Air Stable, Organic Single Crystal Transistors of an n-Type Diperylene Bisimide. *Adv. Mater.* **2012**, *24*, 2626–2630.

[230]   Letizia, J. A.; Salata, M. R.; Tribout, C. M.; Facchetti, A.; Ratner, M. A.; Marks, T. J. N-Channel Polymers by Design: Optimizing the Interplay of Solubilizing Substituents, Crystal Packing, and Field-Effect Transistor Characteristics in Polymeric Bithiophene-Imide Semiconductors. *J. Am. Chem. Soc.* **2008**, *130*, 9679–9694.

[231]   Wang, Y.; Guo, H.; Ling, S.; Arrechea-Marcos, I.; Wang, Y.; López Navarrete, J. T.; Ortiz, R. P.; Guo, X. Ladder-Type Heteroarenes: Up to 15 Rings with Five Imide Groups. *Angew. Chemie Int. Ed.* **2017**, *56*, 9924–9929.

[232]   Wang, Y.; Guo, H.; Harbuzaru, A.; Uddin, M. A.; Arrechea-Marcos, I.; Ling, S.; Yu, J.; Tang, Y.; Sun, H.; López Navarrete, J. T.; Ortiz, R. P.; Woo, H. Y.; Guo, X. (Semi)Ladder-Type Bithiophene Imide-Based All-Acceptor Semiconductors: Synthesis, Structure-Property Correlations, and Unipolar n-Type Transistor Performance. *J. Am. Chem. Soc.* **2018**, *140*, 6095–6108.

[233]   Wang, Y.; Yan, Z.; Guo, H.; Uddin, M. A.; Ling, S.; Zhou, X.; Su, H.; Dai, J.; Woo, H. Y.; Guo, X. Effects of Bithiophene Imide Fusion on the Device Performance of Organic Thin-Film Transistors and All-Polymer Solar Cells. *Angew. Chemie Int. Ed.* **2017**, *56*, 15304–15308.

[234]   Kim, T.; Kim, J.-H.; Kang, T. E.; Lee, C.; Kang, H.; Shin, M.; Wang, C.; Ma, B.; Jeong, U.; Kim, T.-S.; Kim, B. J. Flexible, Highly Efficient All-Polymer Solar Cells. *Nat. Commun.* **2015**, *6*, 8547.

[235]   Diao, Y.; Zhou, Y.; Kurosawa, T.; Shaw, L.; Wang, C.; Park, S.; Guo, Y.; Reinspach, J. A.; Gu, K.; Gu, X.; Tee, B. C. K.; Pang, C.; Yan, H.; Zhao, D.; Toney, M. F.; Mannsfeld, S. C. B.; Bao, Z. Flow-Enhanced Solution Printing of All-Polymer Solar Cells. *Nat. Commun.* **2015**, *6*, 7955.

[236]   Song, S.; Kranthiraja, K.; Heo, J.; Kim, T.; Walker, B.; Jin, S.-H.;

Kim, J. Y. Efficiency Exceeding 11% in Tandem Polymer Solar Cells Employing High Open-Circuit Voltage Wide-Bandgap π-Conjugated Polymers. *Adv. Energy Mater.* **2017**, *7*, 1700782.

[237] Guo, X.; Facchetti, A.; Marks, T. J. Imide- and Amide-Functionalized Polymer Semiconductors. *Chem. Rev.* **2014**, *114*, 8943–9021.

[238] Sun, H.; Wang, L.; Wang, Y.; Guo, X. Imide-Functionalized Polymer Semiconductors. *Chem. – A Eur. J.* **2019**, *25*, 87–105.

[239] Feng, K.; Guo, H.; Wang, J.; Shi, Y.; Wu, Z.; Su, M.; Zhang, X.; Son, J. H.; Woo, H. Y.; Guo, X. Cyano-Functionalized Bithiophene Imide-Based n-Type Polymer Semiconductors: Synthesis, Structure–Property Correlations, and Thermoelectric Performance. *J. Am. Chem. Soc.* **2021**, *143*, 1539–1552.

[240] Guo, X.; Zhou, N.; Lou, S. J.; Smith, J.; Tice, D. B.; Hennek, J. W.; Ortiz, R. P.; Navarrete, J. T. L.; Li, S.; Strzalka, J.; Chen, L. X.; Chang, R. P. H.; Facchetti, A.; Marks, T. J. Polymer Solar Cells with Enhanced Fill Factors. *Nat. Photonics* **2013**, *7*, 825–833.

[241] Guo, X.; Kim, F. S.; Seger, M. J.; Jenekhe, S. A.; Watson, M. D. Naphthalene Diimide-Based Polymer Semiconductors: Synthesis, Structure–Property Correlations, and n-Channel and Ambipolar Field-Effect Transistors. *Chem. Mater.* **2012**, *24*, 1434–1442.

[242] Guo, X.; Ortiz, R. P.; Zheng, Y.; Hu, Y.; Noh, Y.-Y.; Baeg, K.-J.; Facchetti, A.; Marks, T. J. Bithiophene-Imide-Based Polymeric Semiconductors for Field-Effect Transistors: Synthesis, Structure−Property Correlations, Charge Carrier Polarity, and Device Stability. *J. Am. Chem. Soc.* **2011**, *133*, 1405–1418.

[243] Yang, K.; Zhang, X.; Harbuzaru, A.; Wang, L.; Wang, Y.; Koh, C.; Guo, H.; Shi, Y.; Chen, J.; Sun, H.; Feng, K.; Ruiz Delgado, M. C.; Woo, H. Y.; Ortiz, R. P.; Guo, X. Stable Organic Diradicals Based on Fused Quinoidal Oligothiophene Imides with High Electrical Conductivity. *J. Am. Chem. Soc.* **2020**, *142*, 4329–4340.

[244] Alonso-Navarro, M. J.; Harbuzaru, A.; Martínez-Fernández, M.; Pérez Camero, P.; López Navarrete, J. T.; Ramos, M. M.; Ponce Ortiz, R.; Segura, J. L. Synthesis and Electronic Properties of Nitrogen-Doped π-Extended Polycyclic Aromatic Dicarboximides with Multiple Redox Processes. *J. Mater. Chem. C* **2021**, *9*, 7936–7949.

II. METHODOLOGY

II.I.   Spectroscopic techniques

In this thesis, different spectroscopic techniques were used, including UV-Vis/NIR absorption spectroscopy, charge modulation spectroscopy and vibrational Raman spectroscopy. Spectroscopy is the study of the interaction of electromagnetic radiation with matter involving either absorption, emission or scattering of radiation by the system under study. This interaction, which depends on the wavelength or frequency of the radiation, can provide detailed information about the structure and chemical properties of the system[1,2].

II.I.I. Electronic absorption spectroscopy

The optical properties of the conjugated system studied in this thesis were investigated by measuring their electronic absorption spectra in solution and in the solid state, as films.

Absorption spectra in solution: For the solution preparation, different solvents were used, as a function of the series of systems under study, such as dichloromethane (CH_2Cl_2), chloroform ($CHCl_3$), 2-methiltetrahidrofuran (2Me-THF) and chlorobenzene (ClBz). CH_2Cl_2 and $CHCl_3$ solvents were mostly used for room temperature absorption spectra measurements due to the good solubility of most of the compounds studied in this thesis in those solvents. On the other hand, 2-Me-THF solvent was used for temperature dependent absorption spectra, since this solvent generates a transparent matrix in the solid state, allowing the registration of UV-Vis measurements at low temperature (80 K). On the other hand, ClBz solvent was used for the registration of UV-Vis measurements at high temperatures (380 K). The absorption spectra at variable temperature were carried out with the aid of an optical cryostat

OPTISTAT®DN from Oxford Instruments, by progressive addition of liquid nitrogen.

Absorption spectra in solid state as films: For the films preparation in Chapter 3, 4 and 6, solutions of 3 mg/ml in chloroform were prepared and deposited onto quartz substrates by spin-coating technique (1500 rpm, 30s) and then measured at ambient temperature. In Chapter 5, the films were prepared by drop-casting from chloroform solutions.

Depending on the spectral range required, the measurements of absorption spectra were carried out with different equipments:

Agilent spectrophotometer 8453 (190 - 1100 nm): multidiode spectrophotometer with spectral range from 190 nm to 1100 nm. It consists of 910 diodes, one for each nanometer, which allows very short registration times.

Cary spectrophotometer 5000 (175 - 3300 nm): spectrophotometer multidiode with spectral range from 175 nm to 3300 nm and with spectral resolution of 0.01 nm.

II.I.II. Raman spectroscopy

The Raman spectra shown in the following chapters were recorded in the solid state as bulk or/and as thin films. The equipment used for the registration of the vibrational Raman spectra was the following one:

FT-Raman spectra with 1064 nm laser excitation wavelength were recorded by using a FT-Raman accessory kit (RamII) of a Bruker Vertex 70 FT-IR interferometer and a continuous-wave Nd:YAG laser working at 1064 nm was employed for excitation. A germanium detector operating at liquid-nitrogen temperature was used and the Raman scattering radiation

was collected in a back-scattering configuration with a 4 cm^{-1} spectral resolution. 3000 Raman scans were averaged in each case to improve the signal-to-noise ratio.

The resonant Raman spectra with 785, 514, and 488 nm laser excitations were recorded both for bulk and thin film samples by using a InVia Reflex Confocal Microscope of Renishaw, which has different diffraction gratings optimized for Visible and Near IR. A CCD detector was used, and the Raman scattering radiation was collected in a back-scattering configuration with a 1 cm^{-1} spectral radiation. The operating power for these exciting laser radiations was between 0.008 and 0.04 mW. The spectra were recorded by using between 3 and 8 co-addition of 10 s each.

The resonant Raman spectra with 785, 632, and 532 nm laser excitations were recorded both for bulk and thin film samples by using the 1x1 camera of a Senterra Raman microscope of Bruker. A CCD detector operating at -50 ºC was used, and the Raman scattering radiation was collected in a back-scattering configuration with a 3-5 cm^{-1} spectral resolution. The operating power for these exciting laser radiations was between 0.2 and 10 mW. The spectra were recorded by using between 3 and 8 co-addition of 10 s each.

Variable temperature Raman spectra were recorded in the solid state as bulk material between -180 ºC and 150 ºC, by using a Linkam FTIR600 stage cooled by liquid nitrogen and with a temperature stability below 0.1 ºC.

II.II. Electrochemical techniques

II.II.I. Cyclic voltammetry

Electrochemical experiments have been conducted in dichloromethane, and/or chloroform solutions at room temperature by using 0.1 M tetra(*n*-butyl) ammonium hexafluorophosphate ((n-Bu$_4$)NPF$_6$) as supporting electrolyte. A platinum disk was used as the working electrode, and a platinum wire as the counter electrode against an Ag/AgCl pseudo-reference electrode. The ferrocene/ferrocenium (Fc/Fc$^+$) redox couple was used as the internal reference for all measurements. The scan rate was 100 mV s^{-1}.

The approximate HOMO and LUMO energies levels were determined from the first onset oxidation and the first onset reduction potentials, respectively. E$_{HOMO/LUMO}$ were calculated according to the formula E$_{HOMO/LUMO}$ (eV) = - (E$_{oxl/redl}$$^{1/2}$+ 4.80), where 4.8 eV represents the value of Fc with respect to zero vacuum level[10,11].

The CV measurements were recorded by using the following equipment:

EC EPSILON POTENTIOSTAT FROM BASi: it comes with a software that enables the most popular electrochemical techniques such as cyclic voltammetry, chronoamperometry, and chronopotentiometry.

C3 CELL STAND: an electrochemical cell which holds three electrodes, the working electrode, the counter electrode, and the reference electrode. This cell is a Faraday cage with integrated magnetic stir plate and purge lines, which are remotely controlled via the software.

II.II.II. *In situ* spectroelectrochemistry

In situ UV-Vis-NIR spectroelectrochemical experiments have been conducted in dichloromethane at room temperature by using either 0.1 M Bu_4NPF_6, Hex_4NPF_6 or Bu_4NBF_4, as the supporting electrolyte. The diluted solution was introduced in an optically transparent thin-layer electrochemical (OTTLE) cell from Specac, positioned in the sample compartment of a Varian Cary 5000 Spectrophotometer. This is a double beam spectrophotometer with a performance in the range of 175-3300 nm and a spectral resolution of 1.0 nm. It uses a PBSmart detector and three different lamps as sources of radiation. The OTTLE cell consists of three electrodes: a Pt gauze used as the working electrode (32 wires per cm), a Pt wire used as the counter electrode, and an Ag wire used as the pseudo-reference electrode. This OTTLE is connected to an EC Epsilon potentiostat which controls the BASi C3 Cell Stand accessory which provides the necessary voltage to reduce or oxidize the sample. The spectra were collected at constant potential electrolysis and the potentials were changed in intervals of 15 mV.

II.II.III. Charge modulation spectroscopy

Charge Modulation Spectroscopy (CMS) is an ideal method for characterizing charged excitons of conjugated polymers and oligomers used as active material in OFETs. This method, which is implemented at the Laboratory of Prof. Mario Caironi at the Center for Nano Science and Technology@PoliMi of the Istituto Italiano di Tecnologia (Milan, Italy), is a lock-in-based technique that records the differential change in absorption of a semiconducting layer upon modulation of the gate voltage in an operating OFET[3–5] The trapped charges cannot follow the voltage

modulation; therefore, the detected spectral features are directly associated with only mobile carriers.

The OTFTs used for the CMS measurement present a bottom contact-top gate (BCTG) architecture and their fabrication is detailed in Section II.IV.II.

For the CMS measurements, the OTFT was mounted in a cryostat which was pumped down to ca. 10^{-6} mbar ensuring vacuum conditions during the whole measurement. Figure II.1 shows a schematic picture of the home-built experiment set up for the CMS measurement.

Figure II.1. Scheme of CMS experiment set-up (simplified).

A monochromatic light, produced by passing light from a 240W tungsten lamp through a double grating monochromator, is focused onto the device. The transmitted light was then collected and focused on a photodetector connected to a transimpedance amplifier (Femto DHPCA-100). A silicon photodetector was used in the visible range for photon

energy above 1.2 eV and indium gallium arsenide (InGaAs) photodetector in the near infrared (NIR) range between 0.72 eV and 1.5 eV. The signal from the detector is measured by a digital lock-in amplifier (Stanford Research Systems SR830) and the whole experiment is controlled remotely by a Hewlett-Packard computer via a GPIB interface.

Initially a normalization scan of the required wavelength range is performed by placing a mechanical chopper in the optical path, using this as the reference to the lock-in amplifier. This gives the transmission (T) of the apparatus. Without altering any of the experimental set up the modulation scan is then measured by first biased the device into the regime to be probed by the experiment and superimposing a small a.c. voltage (V_{ac}), typically ±10V. This V_{ac}, which now serves as the reference to the lock-in amplifier, modulates the amount of charge present in the device which in turn modulates the absorption giving us a spectrum of ΔT. The voltage modulation spectrum of the device is given by ΔT/T.

This experiment allows many parameters, such as temperature, modulation frequency and d.c. voltage (V_{dc}), to be controlled, to give a detailed picture of the charge carriers present in the semiconductor. Additional information can be obtained by comparing this with OFET data, capacitance voltage, capacitance-frequency, photo induced absorption, absorption photothermal beam deflection spectra, chemical and spectroelectrochemical doping experiments[5–9].

II.III. DFT calculations

Theoretical calculations were carried out in the frame of density functional theory (DFT), using for each family of the compounds studied in this thesis, different functionals, such as B3LYP, CAM-B3LYP, ωB97XD[12] or LC-ωPBE[13–15] with the 6-31G**[16,17] basis set as implemented in the

Gaussian 09[18] and 16[19] programs. Theoretical calculations were performed either in gas phase or in solution, being this one simulated by a polarizable continuum model (PCM)[20–22] using dichloromethane as solvent. The large alkyl chains on the N-imide group of the compound studied in this thesis were replaced with methyl or isopropyl groups to reduce the computational cost. All calculations on radical anions and cations were spin unrestricted.

On the basis of the resulting ground-state optimized geometries, harmonic vibrational frequencies and Raman intensities were calculated at the same theoretical level corroborating that the optimized geometries are minima (zero imaginary frequencies).

The intramolecular reorganization energy (λ) was calculated directly from the relevant points on the potential energy surfaces by using previously reported standard procedures[23]. This energy corresponds to the sum of the isolated molecule's energy in the relaxed state ongoing from the neutral-state geometry to the charged-state geometry and vice versa (Figure II.2).

The reorganization energy is given by the following expression (Equation II.1):

$$\lambda_{reorg} = \lambda_1 + \lambda_2 \quad [Eq.\,II.\,1]$$

The terms λ_1 and λ_2 in Equation II.1 are calculated directly from the adiabatic potential energy as follows:

$$\lambda_1 = E^1(M) - E^0(M) \quad [Eq.\,II.\,2]$$

$$\lambda_2 = E^1(M^*) - E^0(M^*) \quad [Eq.\,II.\,3]$$

Thus, the reorganization energy is strongly dependent on the molecular structure of the organic semiconductor, and in order to achieve an effective charge transport, these λ values need to be small. In general, more planar, and rigid backbones give rise to lower λ values since the molecular geometries of the charged and neutral molecule are similar.

Figure II.2. Potential energy curves for neutral (M) and radical species (M*).

For the study of dimeric structures (Chapter 3), two conformations were considered: the parallel and the antiparallel dimers and the LC-wPBE functional was used, together with the empirical dispersion correction GD3BJ[24].

Gibbs energy changes associated with the formation of the dimer (ΔG_f^0) were computed based on the energies of the vibrational analysis of the neutral and radical anion monomers, as well as the π-dimer radical anion or dianion, taking into the account the thermal corrections[25].

Vertical transitions excitation energies were computed using the time dependent DFT (TD-DFT)[26] approach with the same basis set and functional than those described for the optimized geometries and for the vibrational spectra calculations. Absorption UV-Vis spectra were simulated by convolution of Gaussian functions with a full width at half maximum (FWHM) of 3000 cm^{-1}.

The calculations of E_{int}, E_{bind} and ΔG_f^0, shown in Table 1.4 in Chapter 1, were carried out as following:

(i) The interaction energy (E_{int}) is the difference between the energy of the optimized π-dimer (HF ($[BTIn]_2^{\cdot-}{}_{opt}$)) and the energy of the isolated monomers frozen at the geometry of the π-dimer ($\sum(HF)_{monomers\,sp}$). As an example, the interaction energy for the formation of a BTIn π-dimer radical anion ($[BTIn]_2^{\cdot-}$) is calculated below with *Equation II.4*:

$$E_{int}\,([BTIn]_2^{\cdot-}) = HF\,([BTIn]_2^{\cdot-}{}_{opt}) - \sum(HF)_{monomers\,sp}\;[Eq.\,II.4]$$

(ii) The binding energy (E_{bind}) is the difference between the energy of the optimized π-dimer (HF ($[BTIn]_2^{\cdot-}{}_{opt}$)) and the energy of the optimized isolated monomers ($\sum(HF)_{monomers\,opt}$). As an example, the binding energy for the formation of a BTIn π-dimer radical anion ($[BTIn]_2^{\cdot-}$) is calculated below with *Equation II.5*:

$$E_{bind}\,([BTIn]_2^{\cdot-}) = HF\,([BTIn]_2^{\cdot-}{}_{opt}) - \sum(HF)_{monomers\,opt}\;[Eq.\,II.5]$$

(iii) Finally, the free energy of formation (ΔG_f^0) is the difference between the sum of electronic and thermal free energies of the optimized π-dimer (E ($[BTIn]_2^{\cdot-}{}_{freq}$)) and the corresponding energy of the optimized isolated monomers ($\sum(E)_{monomers\,freq}$); in both cases obtained from the frequency calculation outputs. As an example, the free energy of formation for a BTIn π-dimer radical anaion ($[BTIn]_2^{\cdot-}$) at 298 K is

calculated below with *Equation II.6*:

$$\Delta G_f^0\ ([BTIn]_2^{··}) = E\ ([BTIn]_2^{··}\ freq) - \sum(E)_{monomers\ freq}\ [Eq.\ II.6]$$

All the frequency calculations are carried out on the previously optimized systems at the same theoretical level. No imaginary frequencies were found.

To simulate the singlet open-shell (OSS) structures a broken-symmetry (BS) solution with the keyword guess=mix was imposed, as well as using an unrestricted wavefunction. For the calculations of the triplet states, standard unrestricted calculations were also done.

For the diradicaloid systems of Chapter 2, the open-shell singlet diradical character (y_0) was calculated. y_0 is defined by the occupation number (n_L) of the lowest unoccupied natural orbital (LUNO)[27,28], which can adopt values between 0 and 1, where y_0=0 represents a closed-shell quinoidal state and y_0=1 represents a pure diradical state. Nevertheless, the spin-unrestricted method can suffer from spin contamination where high spin states such as triplet states are mixed in the singlet wavefunction. In such case, improved diradical character can be evaluated by employing a spin-projection correction[29] (Equation II.7), where T_i is defined as the orbital overlap and is calculated using the occupation number (n) of the natural orbitals (Equation II.8).

$$y_i = 1 - \left(\frac{2T_i}{1+T_i^2}\right)\ [Eq.\ II.7] \qquad T_i = \left(\frac{n_{HONO-i}-n_{LUNO+i}}{2}\right)\ [Eq.\ II.8]$$

For the singlet open-shell (OSS) structures, vibrational frequencies and Raman intensities were computed with the restricted approach at BS

optimized geometries, since it has been previously shown that frequencies and Raman intensity predictions of OSS structures using unrestricted approach are not reliable[30].

Computed frequencies were uniformly scaled by a factor of 0.98 for the theoretical Raman spectra in Chapter 2, and 0.96 for the eigenvectors in Chapter 4.

The DFT calculations carried out in this Thesis were obtained and processed by using the following workstation:

PICASSO: supercomputer with 4016 data processing cores, 22.4 terabytes of RAM and 5200 terabytes of storage. In addition, it contains a parallelization program which allows to share memory and processors for Gaussian calculations.

GAUSSIAN 09[18] and 16[19]: software packages used to perform DFT calculations.

In order to represent the data obtained from theoretical calculations, different programs were used:

GAUSSVIEW 5.0: advanced graphical interface designed to prepare the input files for Gaussian. This also allows to graphically examine the results of the Gaussian program.

GAUSSUM 0.8: program used to represent IR, Raman and absorption spectra from frequency and TD-DFT calculations.

CHEMDRAW ULTRA 7.0: program used to generate the chemical structures in 2D and 3D.

CHEMCRAFT[31]: graphic program used to represent theoretical data such as molecular orbitals and eigenvectors.

ORIGIN 9.1: program which allows to represent data, such as absorption and Raman spectra obtained experimentally and theoretically.

II.IV. Fabrication of OFETs

As mentioned in the introduction chapter, the OFET configurations used in this thesis were the top contact - bottom gate (TCBG) and bottom contact - top gate (BCTG), which are described in detail below.

II.IV.I. Top contact-bottom gate (TCBG) configuration

For the fabrication of top contact-bottom gate OFETs, heavily n-doped silicon wafers covered with a 300 nm thick thermally grown SiO_2 layer were employed as gate electrode and dielectric layer, respectively. These Si/SiO_2 wafers are commercially available, and their advantage is that they can be directly used as substrates achieving a high reproducibility with several organic semiconductors.

In general, most dielectric surfaces based on inorganic oxides are hydrophilic, whereas most of organic materials are mostly hydrophobic. This mismatch in surface wettability/energy is believed to hinder the formation of well-ordered organic semiconductor layers on inorganic dielectric surfaces. To overcome this mismatch, self-assembly monolayers are used to modify the dielectric surface from hydrophilic to hydrophobic character (contact angles > 90 °).

The modification of dielectric surfaces can facilitate the formation of organic semiconductor layers with enhanced crystallinity and ordering, as well as improve the growth of grains and minimize the concentration of charge carrier trap states, resulting in increased carrier mobility and device stability[32,33]. The most commonly used self-organizing materials are octadecyltrichlorosilane (OTS) and hexamethyldisilane (HMDS) as their

non-polar alkyl chains serves as a good protector to the polar insulator surface.

Prior to surface functionalization, the Si/SiO$_2$ substrates with dimensions of 2.5 x 2 cm were cleaned by immersing them twice in ethanol with sonication for 10 min each, dried by blowing N$_2$ gas, followed by UV-ozone treatment for 10 min to eliminate any organic impurities.

For the OTS treatment, the cleaned silicon substrates were immersed in a 3.0 mM humidity-exposed solution of OTS in hexane for 1 h[33]. Following OTS deposition, the substrates were subsequently cleaned by sonication in hexane, acetone, and ethanol for 10 min each and then dried by blowing N$_2$ gas to eliminate any residual ethanol.

For the HMDS treatment, the cleaned silicon substrates were exposed to HMDS vapor at room temperature in a closed air-free container under argon for one week.

The modification of the dielectric surface is followed by the deposition of the organic semiconductor. This can be deposited through vacuum evaporation or solution-processed deposition techniques.

The vacuum evaporation consists of heating the organic material up to its sublimation temperature, in an ultra-high vacuum chamber (i.e. 10^{-8}-10^{-6} Torr). This technique is usually used for small-molecules and oligomer organic semiconductors as well as for polymers with a low-degree of polymerization. For polymers with higher degree of polymerization, it is not applicable because polymers tend to decompose by cracking at high temperatures. The main advantages of the vacuum evaporation are the easy control of the thickness and purity of the deposited film, as well the ability to realize highly ordered films by monitoring the substrate temperature and the deposition rate. Therefore,

high quality, homogeneous and reproducible semiconductor films can be obtained with this technique. Nevertheless, this technique requires more sophisticated and expensive equipment, and it is no suitable for large area fabrication.

In contrast to vacuum evaporation, solution processing techniques do not need high deposition temperatures for the deposition of the organic semiconductor layer which makes them ideally suitable for realizing low-cost, large-area electronic devices on flexible substrates.

There are several solution processing methods to obtain the organic semiconductor thin film, notwithstanding, the most commonly techniques used in laboratories are drop-casting and spin-coating.

Drop-casting is a simple and low-cost deposition method for the fabrication of small-area films. This method consists in dissolving the organic semiconductor in an organic solvent and dropping this solution on a target substrate allowing the evaporation of the solvent. The potential of drop-casting as thin film deposition technique is limited due to several drawbacks such as poor reproducibility and difficulty to control the film thickness and morphology as well as the non-uniformity of the organic semiconductor thin film.

Spin-coating is one of the most common techniques for the deposition of organic semiconductor thin films in academic laboratories, because it is simple and does not require any complex equipment. This method consists in dissolving the organic semiconductor in an organic solvent, dropping this solution on a target substrate, and subsequently spinning this sample at high revolutions. The centrifugal forces dry the film instantaneously leaving the substrate covered with a uniform thin film. The thickness of the film is controlled by the concentration of the precursor in the solution, the viscosity of the solution and the working parameters of

the spin coater. However, this method is not advantageous in terms of materials since it requires concentrated solutions, and it is not suitable for large-area fabrication. Furthermore, this technique requires organic semiconductors with good solubility since highly concentrated solution (5-10 mg/ml) are needed to obtain a thin film with a suitable thickness.

The selection of the solvent is very important for the properties of the deposited thin film and, consequently, the performance of the fabricated devices. One of the most important properties of a solvent is its volatility; when a solvent evaporates slowly, it allows more time to the deposited organic semiconductor molecules to organize into more crystalline domains. The resulting increase in crystallinity is usually desirable as it typically enhances the charge carrier mobility.

The organic semiconductor layers, normally obtained by solution processing techniques, are often subjected to a thermal annealing process. This is a commonly used technique to improve the device performance in many areas of organic electronics. The annealing treatment eliminates any residual solvent remaining within the organic film as well as it improves the molecular ordering and increases the crystallinity of the organic semiconductor layers. It should be noted, however, that the thermal annealing treatment does not work properly for all organic materials.

The last step in the fabrication of OFETs with top contact-bottom gate configuration is the deposition of the source and drain electrodes. For laboratory purposes, gold is the most used metal as electrode because is stable and inert, although platinum and aluminum are also commonly used. Source and drain electrodes are obtained by thermal evaporation of gold in high vacuum and through shadow masks. The channel width (W)

oscillates between 100 and 5000 μm and the channel length between 10 and 100 μm.

The selection of metals of appropriate work function is of utmost importance for the operation of organic semiconductor devices. A good match of the work function with either the electron affinity (EA) of the organic semiconductor for electron injection, or its ionization potential (IP) for hole injection is imperative. In a rather simplified notion, to obtain an effective charge injection into the organic semiconductor, the work function of the metal electrodes must be higher that the IP for hole injection or lower than EA for electron injection. In this case, the metal-semiconductor is considered as an ohmic contact. However, in many cases, the work function of the metal electrodes does not meet this requirement which consequently introduces a potential difference which must be surmounted for charge injection to take place. This potential difference is known as injection barrier.

For n-channel transistors, the work function of the metal electrodes should be low enough to promote easy electron injection in the LUMO level of the organic semiconductor. For this kind of transport, gold electrodes are less appropriate since they give rise to high injection barrier for electrons at the contacts due to their high work function. Therefore, low work function metals, such as calcium, magnesium or aluminum are preferred for n-channel transistor, however these metals are not environmentally stable.

For p-channel transistors, the work function of the metal electrodes should be high enough to promote easy electron withdrawing from the HOMO level of the organic semiconductor.

II.IV.II. Bottom contact-top gate (BCTG) configuration

For the fabrication of bottom contact-top gate configuration OFETs, thoroughly cleaned 1737F borosilicate glass was used as substrate on top of which interdigitated Au source and drain electrodes (30 nm thick) with a channel length L = 40 μm and a channel width W = 2 cm, were defined by a lift-off photolithographic process with a 3 nm thick Cr adhesion layer. Chromium and gold layers were thermally deposited on the substrate in high vacuum, through shadow masks. Then, the glass substrates with the source and drain electrodes were subsequently cleaned by sonication in acetone and isopropanol followed by UV-ozone and oxygen plasma treatment. To reduce the contact resistance, a thin layer of cesium fluoride (CsF) was spin-coated from 2-methoxyethanol solution (2 mg mL^{-1}) onto the gold electrodes to facilitate electron injection[34]. A chloroform solution of BTI2-BTI4 (3 mg mL^{-1}) was then deposited by spin-coating at 1000 rpm for 60 seconds, yielding an approx. 40-60 nm thick film, followed by a thermal annealing on a hot plate at 80 ºC for 20 min in a nitrogen atmosphere. Afterwards, a 400 nm CYTOP (CTL-809M:CT-SOLV180 = 2:1 (v:v), Asahi Glass Co., Ltd.) dielectric layer was spin-coated on top at 4000 rpm for 60 s, followed by a thermal annealing on a hot plate at 100 ºC for 30 min, in a nitrogen atmosphere. Finally, a 7 nm thick Al, followed by 4 nm Au electrode, was thermally evaporated as the gate contact to complete the device fabrication. The transistor fabrication and characterization were carried out in a nitrogen-filled glovebox.

The equipment used for the fabrication of OFET devices has been the following:

UVO CLEANER 342-220: ozone surface cleaning equipment.

LAURELL TECHNOLOGIES WS-650MZ-23NPP: *spin-coater* used to deposit the thin films. The speed, acceleration and working time can be varied depending on the semiconductor, the solvent and the concentration of the solution used in the fabrication. In most of the materials studied in this Ph.D. Thesis, the speed used was 1500 r.p.m. and the time 30 s.

OERLIKON UNIVEX 250 EVAPORATOR: This evaporator has a rotary and a turbomolecular pump that allows us to reach pressure values of 10^{-6} mbar in two or three hours. It also has a temperature controller, which allows the substrates to be preheated or held at a given temperature during sublimation. It allows the sublimation of organic compounds for the deposit of the semiconductor layer and metals for the manufacture of electrodes, controlling the deposit speed and the thickness of the layers by means of a quartz microbalance.

II.V. Electrical characterization of OFETs

The OFET devices were characterized under vacuum and ambient conditions in different probe stations:

TRINOS VACUUM PROBE STATION: This customized probe station was made by the Spanish company Trinos Vacuum which allows us to characterize the transistors in vacuum conditions. It reaches a pressure of 10^{-6} mbar.

PROBE STATION EVERBEING INT'L COMPANY: this probe station allows the characterization of the transistors under ambient conditions.

These probe stations were used for the characterization of the semiconductor in combination with a 4200-SCS Keithley potentiostat.

The electrical characterization provides the output and transfer curves which define the transport properties of the organic semiconductors, as seen in Chapter I.

II.VI. References

[1]   Harris, D.C. and Bertolucci, M.D. *Symmetry and Spectroscopy. An Introduction to Vibrational and Electronic Spectroscopy.*; Docer Publications, Ed.; 1989.

[2]   Hollas, J.M. *Modern Spectroscopy*; ed. J.W. Sons., Ed.; 1992.

[3]   Sirringhaus, H.; Brown, P. J.; Friend, R. H.; Nielsen, M. M.; Bechgaard, K.; Langeveld-Voss, B. M. W.; Spiering, A. J. H.; Janssen, R. A. J.; Meijer, E. W.; Herwig, P.; de Leeuw, D. M. Two-Dimensional Charge Transport in Self-Organized, High-Mobility Conjugated Polymers. *Nature* **1999**, *401*, 685–688.

[4]   Brown, P. J.; Sirringhaus, H.; Harrison, M.; Shkunov, M.; Friend, R. H. Optical Spectroscopy of Field-Induced Charge in Self-Organized High Mobility Poly(3-Hexylthiophene). *Phys. Rev. B* **2001**, *63*, 125204.

[5]   Caironi, M.; Bird, M.; Fazzi, D.; Chen, Z.; Di Pietro, R.; Newman, C.; Facchetti, A.; Sirringhaus, H. Very Low Degree of Energetic Disorder as the Origin of High Mobility in an N-Channel Polymer Semiconductor. *Adv. Funct. Mater.* **2011**, *21*, 3371–3381.

[6]   Harrison, M. G.; Friend, R. H.; Garnier, F.; Yassar, A. The Charged Excitations in Thin Films of α-Sexithiophene within Semi-Transparent Field-Effect Devices: Investigation by Optical Spectroscopy of Field-Induced Charge and by Photoimpedance Spectroscopy. *Synth. Met.* **1994**, *67*, 215–221.

[7]   Kijima, M.; Mukai, S.; Ohmura, K.; Shirakawa, H.; Kyotani, M. Synthesis of Conjugated Polymer with Carbynoid Structure by Dehydrochlorination of Chlorinated Polyacetylene Film. *Synth. Met.* **1999**, *101*, 59–60.

[8]   Luzio, A.; Criante, L.; D'Innocenzo, V.; Caironi, M. Control of Charge Transport in a Semiconducting Copolymer by Solvent-Induced Long-Range Order. *Sci. Rep.* **2013**, *3*, 3425.

[9]   Fazzi, D.; Caironi, M. Multi-Length-Scale Relationships between the Polymer Molecular Structure and Charge Transport: The Case of Poly-Naphthalene Diimide Bithiophene. *Phys. Chem. Chem. Phys.* **2015**, *17*, 8573–8590.

[10]   Cardona, C. M.; Li, W.; Kaifer, A. E.; Stockdale, D.; Bazan, G. C. Electrochemical Considerations for Determining Absolute Frontier Orbital Energy Levels of Conjugated Polymers for Solar Cell Applications. *Adv.*

Mater. **2011**, *23*, 2367–2371.

[11]   Bredas, J.-L. Mind the Gap! *Mater. Horizons* **2014**, *1*, 17–19.

[12]   Chai, J.-D.; Head-Gordon, M. Long-Range Corrected Hybrid Density Functionals with Damped Atom–Atom Dispersion Corrections. *Phys. Chem. Chem. Phys.* **2008**, *10*, 6615–6620.

[13]   Vydrov, O. A.; Scuseria, G. E. Assessment of a Long-Range Corrected Hybrid Functional. *J. Chem. Phys.* **2006**, *125*, 234109.

[14]   Vydrov, O. A.; Heyd, J.; Krukau, A. V; Scuseria, G. E. Importance of Short-Range versus Long-Range Hartree-Fock Exchange for the Performance of Hybrid Density Functionals. *J. Chem. Phys.* **2006**, *125*, 74106.

[15]   Vydrov, O. A.; Scuseria, G. E.; Perdew, J. P. Tests of Functionals for Systems with Fractional Electron Number. *J. Chem. Phys.* **2007**, *126*, 154109.

[16]   Hehre, W. J.; Ditchfield, R.; Pople, J. A. Self—Consistent Molecular Orbital Methods. XII. Further Extensions of Gaussian—Type Basis Sets for Use in Molecular Orbital Studies of Organic Molecules. *J. Chem. Phys.* **1972**, *56*, 2257–2261.

[17]   Hariharan, P. C.; Pople, J. A. The Influence of Polarization Functions on Molecular Orbital Hydrogenation Energies. *Theor. Chim. Acta* **1973**, *28*, 213–222.

[18]   M. J. Frisch, G. W. Trucks, H. B. Schlegel, G. E. Scuseria, M. A. Robb, J. R. Cheeseman, G. Scalmani, V. Barone, G. A. Petersson, H. Nakatsuji, X. Li, M. Caricato, A. Marenich, J. Bloino, B. G. Janesko, R. Gomperts, B. Mennucci, H. P. Hratchian, J. V. Ort, and D. J. F. Gaussian 09, Revision C.01. Gaussian, Inc., Wallingford CT 2009.

[19]   M. J. Frisch, G. W. Trucks, H. B. Schlegel, G. E. Scuseria, M. A. Robb, J. R. Cheeseman, G. Scalmani, V. Barone, G. A. Petersson, H. Nakatsuji, X. Li, M. Caricato, A. V. Marenich, J. Bloino, B. G. Janesko, R. Gomperts, B. Mennucci, H. P. Hratchian, J. V., and D. J. F. Gaussian 16, Revision A.03,. Gaussian, Inc., Wallingford CT 2016.

[20]   Tomasi, J.; Mennucci, B.; Cammi, R. Quantum Mechanical Continuum Solvation Models. *Chem. Rev.* **2005**, *105*, 2999–3094.

[21]   Improta, R.; Barone, V.; Scalmani, G.; Frisch, M. J. A State-Specific Polarizable Continuum Model Time Dependent Density Functional Theory Method for Excited State Calculations in Solution. *J.*

Chem. Phys. **2006**, *125*, 54103.

[22]   Improta, R.; Scalmani, G.; Frisch, M. J.; Barone, V. Toward Effective and Reliable Fluorescence Energies in Solution by a New State Specific Polarizable Continuum Model Time Dependent Density Functional Theory Approach. *J. Chem. Phys.* **2007**, *127*, 74504.

[23]   Casado, J.; Pappenfus, T. M.; Mann, K. R.; Ortí, E.; Viruela, P. M.; Milián, B.; Hernández, V.; López Navarrete, J. T. Spectroscopic and Theoretical Study of the Molecular and Electronic Structures of a Terthiophene-Based Quinodimethane. *ChemPhysChem* **2004**, *5*, 529–539.

[24]   Grimme, S.; Ehrlich, S.; Goerigk, L. Effect of the Damping Function in Dispersion Corrected Density Functional Theory. *J. Comput. Chem.* **2011**, *32*, 1456–1465.

[25]   Harbuzaru, A.; Arrechea-Marcos, I.; Scaccabarozzi, A. D.; Wang, Y.; Guo, X.; Caironi, M.; López Navarrete, J. T.; Ruiz Delgado, M. C.; Ponce Ortiz, R. Ladder-Type Bithiophene Imide-Based Organic Semiconductors: Understanding Charge Transport Mechanisms in Organic Field Effect Transistors. *J. Mater. Chem. C* **2020**, *8*, 15759–15770.

[26]   Runge, E.; Gross, E. K. U. Density-Functional Theory for Time-Dependent Systems. *Phys. Rev. Lett.* **1984**, *52*, 997–1000.

[27]   Kishi, R.; Murata, Y.; Saito, M.; Morita, K.; Abe, M.; Nakano, M. Theoretical Study on Diradical Characters and Nonlinear Optical Properties of 1,3-Diradical Compounds. *J. Phys. Chem. A* **2014**, *118*, 10837–10848.

[28]   Kishi, R.; Ochi, S.; Izumi, S.; Makino, A.; Nagami, T.; Fujiyoshi, J.; Matsushita, N.; Saito, M.; Nakano, M. Diradical Character Tuning for the Third-Order Nonlinear Optical Properties of Quinoidal Oligothiophenes by Introducing Thiophene-S,S-Dioxide Rings. *Chem. – A Eur. J.* **2016**, *22*, 1493–1500.

[29]   Nakano, M.; Minami, T.; Fukui, H.; Yoneda, K.; Shigeta, Y.; Kishi, R.; Champagne, B.; Botek, E. Approximate Spin Projected Spin-Unrestricted Density Functional Theory Method: Application to Diradical Character Dependences of Second Hyperpolarizabilities. *AIP Conf. Proc.* **2015**, *1642*, 30–34.

[30]   Fazzi, D.; Canesi, E. V; Negri, F.; Bertarelli, C.; Castiglioni, C. Biradicaloid Character of Thiophene-Based Heterophenoquinones: The

Role of Electron–Phonon Coupling. *ChemPhysChem* **2010**, *11*, 3685–3695.

[31]   https://www.chemcraftprog.com.

[32]   DiBenedetto, S. A.; Facchetti, A.; Ratner, M. A.; Marks, T. J. Molecular Self-Assembled Monolayers and Multilayers for Organic and Unconventional Inorganic Thin-Film Transistor Applications. *Adv. Mater.* **2009**, *21*, 1407–1433.

[33]   Yoon, M.-H.; Kim, C.; Facchetti, A.; Marks, T. J. Gate Dielectric Chemical Structure−Organic Field-Effect Transistor Performance Correlations for Electron, Hole, and Ambipolar Organic Semiconductors. *J. Am. Chem. Soc.* **2006**, *128*, 12851–12869.

[34]   Baeg, K.-J.; Kim, J.; Khim, D.; Caironi, M.; Kim, D.-Y.; You, I.-K.; Quinn, J. R.; Facchetti, A.; Noh, Y.-Y. Charge Injection Engineering of Ambipolar Field-Effect Transistors for High-Performance Organic Complementary Circuits. *ACS Appl. Mater. Interfaces* **2011**, *3*, 3205–3214.

III. RESULTS

Contents:

Chapter 1. Ladder-type organic semiconductors based on bithienoimide units

Contents:

UNIVERSIDAD
DE MÁLAGA

1.1. Introduction

In this chapter, we study a series of fused BTI-based heteroarenes (BTI2-5 in Figure 1.1), mainly focusing on understanding the reason of the previously found monotonic decrease of electronic mobility with the extension of the conjugation backbone from two to five fused BTI units[1]. One of the reasons for this unexpected electron mobility decrease could be related to the reduced molecular mobility in the solid-state as the repeated unit is extended, leading to poorer self-assembly and lower degree of film crystallinity.

However, in order to get further insights into the charge transport mechanism of these small molecules, we investigated the influence of the molecular length and structure of the BTI-based semiconductors on: i) the stabilization of charged states in solution and ii) the stabilization of charged states in the solid state at the dielectric/organic semiconductor interface of operational OFET devices.

We also studied the π-dimerization processes of BTI2-BTI5 radical anions in both solution and solid-state. This will allow us to investigate how intra- and interchain interactions between charged extended π-systems are affected by the length of the BTI unit and hence elucidate their role on the thin film charge transport properties.

In the last years, there has been a growing interest in the study of π-dimerization reactions of ions which have been found that strongly influence charge transport mechanisms. Therefore, these kinds of reactions are well-suited as models to study intermolecular spatial charge delocalization in conjugated materials[2–5].

Up to now, π-dimerization reactions of radical cations have been well investigated[5–17]; nevertheless, studies related to the intermolecular dimerization of radical anions are still limited[18–20].
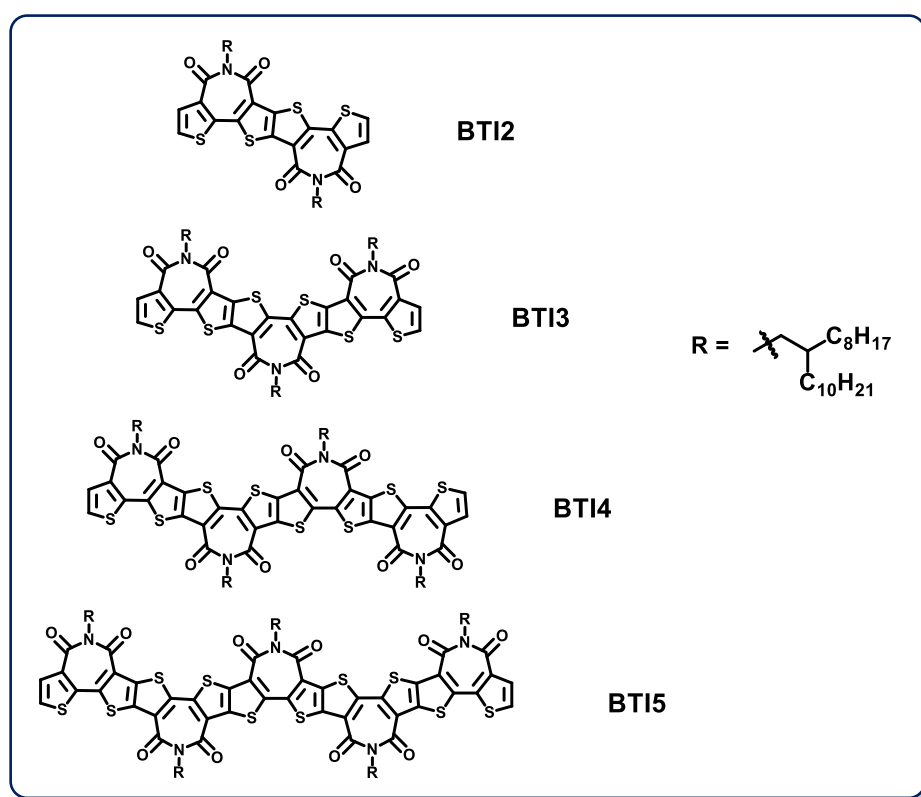
Figure 1.1. Chemical structures of the BTI-based heteroarenes BTI2-BTI5.

In this chapter, a combined experimental/theoretical approach is used, which links UV-Vis absorption, *in situ* spectroelectrochemistry (UV-Vis/NIR) and charge modulation spectroscopy (CMS) with DFT and TD-DFT calculations. In addition, the electrical properties of these fused systems in OFETs have been examined using solution-deposited films which were then characterized by 2D-GIWAXS and AFM techniques.

1.2. Experimental and theoretical study of neutral species

1.2.1. DFT-optimized molecular geometries

The geometries of BTI2-BTI5, optimized at the B3LYP/6-31G** level, are shown in Figure 1.2.
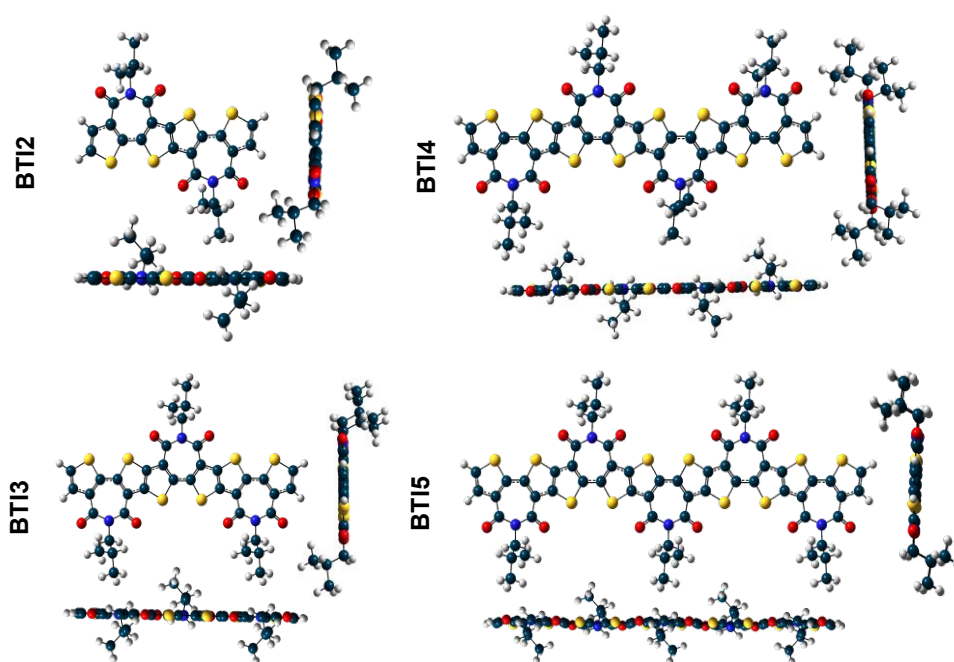
Figure 1.2. Frontal and lateral views of DFT-optimized geometries of BTI2-BTI5 systems at B3LYP/6-31G** level. The long alkyl chains have been replaced by isopropyl groups to simplify calculations and reduce the computational cost and resources.

The optimized minimum energy geometries present highly planar backbones for BTI2-BTI5, with dihedral angles of less than 1º, even for the largest monomer (BTI5). The planar backbones are beneficial for

materials packing and film ordering, and thus for intermolecular interactions which favors the charge-carrier mobility[21–23].

Figure 1.3 shows the molecular frontier orbital profiles of BTI2-BTI5 systems.
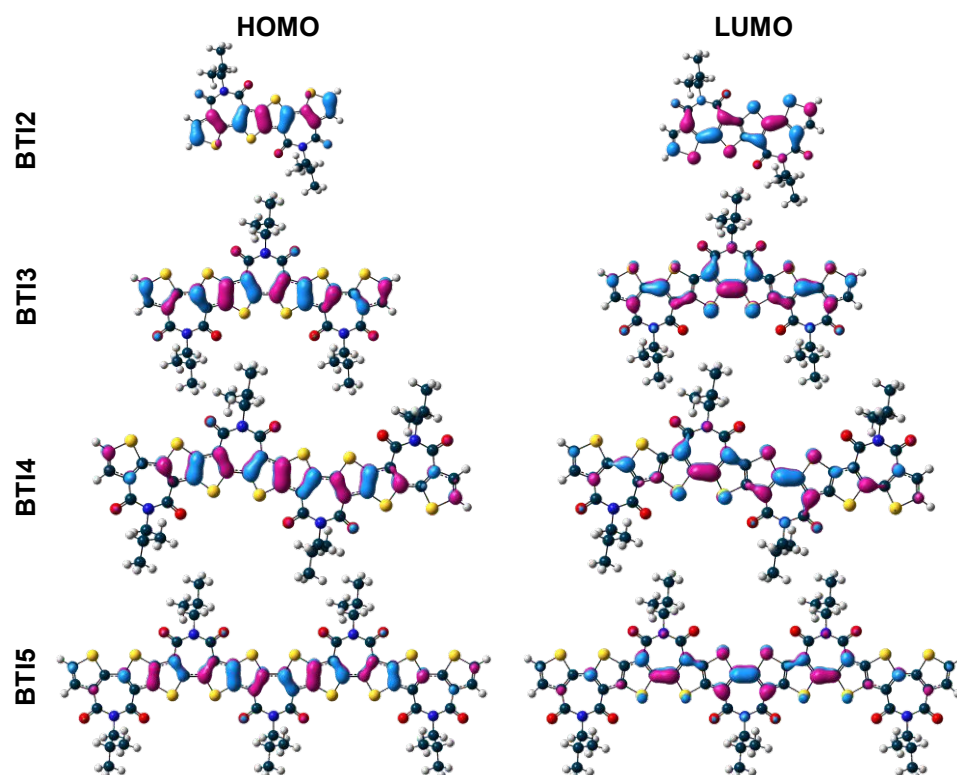
Figure 1.3. DFT-calculated frontier molecular orbital topologies of BTI2-BTI5 systems at B3LYP/6-31G** level.

In the shortest system (BTI2) both HOMO and LUMO are highly delocalized over the whole conjugated skeleton, however a noticeable electron density confinement in the central part of the conjugated skeleton is found for BTI4 and BTI5 monomers, thus rendering similar extension.
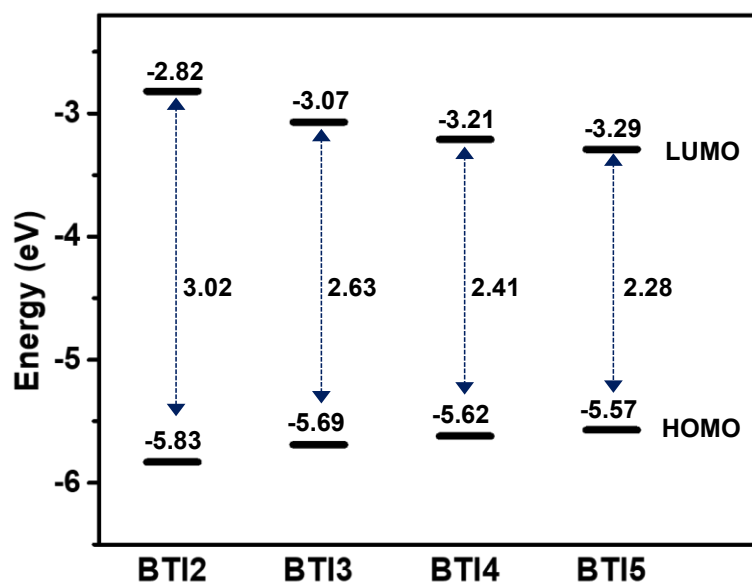
Figure 1.4. Frontier molecular orbital energies and energy gap values predicted for BTI2-BTI5 at B3LYP/6-31G** level.

As can be seen in Figure 1.4 and Table 1.1, the theoretically predicted HOMO-LUMO gaps decrease from 3.02 to 2.28 eV upon going from BTI2 to BTI5, which is more pronounced from BTI2 to BTI3 (with an energy difference of ~ 0.40 eV) than from BTI3 to BTI5 (with an energy difference of ~ 0.10 eV), showing a similar trend to that found experimentally (see Table 1.1).

Table 1.1. Experimentally and theoretically calculated HOMO and LUMO energy levels, and E_{gap} for BTI2-BTI5 monomers at the B3LYP/6-31G** level.

Molecules	Experimental data				Theoretical data			
	E_{LUMO} (eV)[a]	E_{HOMO} (eV)[b]	E_g^{EC} (eV)[c]	E_g^{opt} (eV)[d]	E_{LUMO} (eV)	E_{HOMO} (eV)	E_g (eV)	ΔE_g (eV)
BTI2	-2.90	-5.38	2.48	2.48	-2.82	-5.83	3.02	0.39
BTI3	-3.15	-5.34	2.19	2.19	-3.07	-5.69	2.63	0.22
BTI4	-3.26	-5.26	2.00	2.00	-3.21	-5.62	2.41	0.13
BTI5	-3.55	-5.48	1.93	1.93	-3.29	-5.57	2.28	

[a,b,c]Electrochemically determined vs Fc/Fc⁺: E_{LUMO} = - (E_{red}^{onset} + 4.80). [b]E_{HOMO} = E_{LUMO} – E_g^{opt}. [c]E_g^{EC}=E_{LUMO}-E_{HOMO}; [d]Optical band gap estimated from the absorption edge of as-cast thin films.

1.2.2. Optical properties and TD-DFT vertical transition energies

The optical properties of BTI2-BTI5 molecules were investigated by measuring their UV-Vis absorption spectra both in solution at different temperatures and as thin films (Figure 1.5), which highlight the easiness of these fused molecules to form aggregates in solution. The aggregation processes play a very important role in the charge transport mechanism and therefore, understanding how these highly planar molecules pack up and how this affects the stabilization of charged states in organic thin layers and the charge transfer processes, could help us to shed light on charge transport mechanisms in electronic devices.
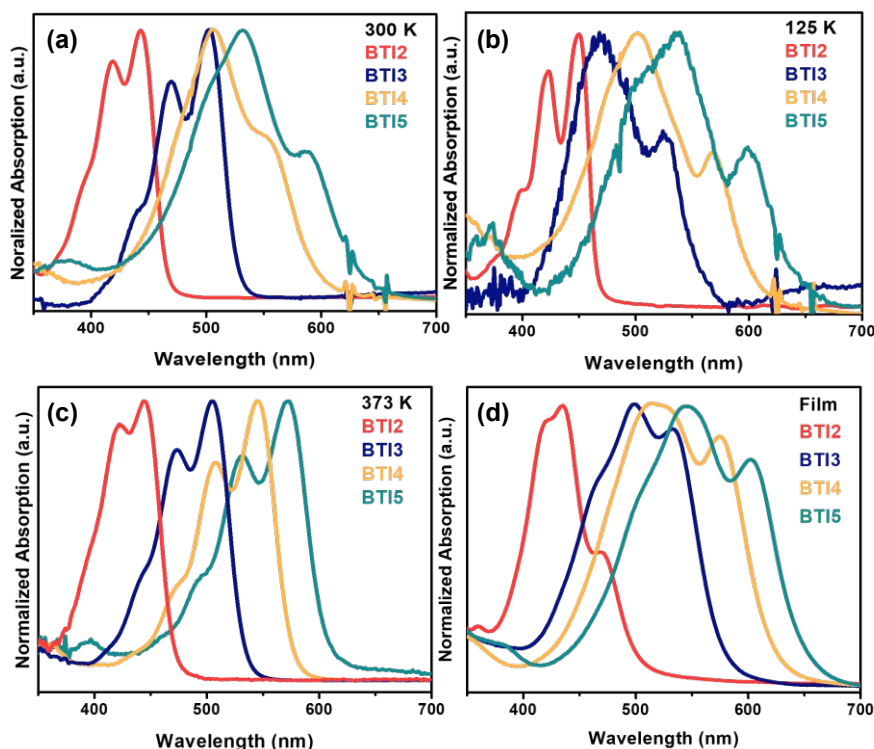
Figure 1.5. UV-Vis absorption spectra of BTI2-BTI5 systems in (a) 2-methyl tetrahydrofuran (2-MeTHF) solution at room and (b) low temperature, (c) chlorobenzene (ClBz) at 373 K, (d) as thin films.

At room temperature (Figure 1.5(a)), the optical absorption spectra of BTI2-BTI5 systems in solution show, in all cases, a two structured peak profile with different relative intensities depending on the chain length. As the chain length increases, the maximum absorption peak (λ_{max}) is bathochromically shifted from 445 nm for BTI2 to 532 nm for BTI5, in line with the extension of the π-conjugated core. This tendency is also observed in the spectra recorded at low and high temperatures (Figures 1.5(b) and (c), respectively) as well as for those recorded as thin films (Figures 1.5(d)).

By comparing the optical absorption spectrum of BTI3 at room temperature (Figure 1.5(a)) with that at low temperature (Figure 1.5(b)), we can observe a reversal intensity pattern for the two structured peaks. This pattern is in fact similar to those obtained for BTI4 and BTI5 at either room or low temperatures (Figure 1.5(a-b)), indicating the tendency of BTI3 to form aggregates at low temperature, although it appears to be in a non-aggregated form at 300 K. Thus, in the case of BTI4 and BTI5, the similitude of the intensity pattern of the two structured peaks in the absorption spectra at room and low temperatures (Figure 1.5(a) and (b), respectively), indicates the tendency of these systems to form aggregates in diluted solutions already at room temperature. On the other hand, in the case of BTI2 absorption spectrum at low temperatures (Figure 1.5(b)), this presents a similar spectral profile to that obtained at room temperature (Figure 1.5(a)), which indicates that BTI2 does not easily tend to form aggregates in low-concentration solutions.

At high temperatures (Figure 1.5(c)), a similar spectral profile is observed for the four compounds, with the low energy peak being the most intense in all the systems. Interestingly, the absorption profiles of BTI4 and BTI5 show a reverse intensity pattern, in comparison to those obtained at room temperature (Figure 1.5(a)), indicating the disappearance of aggregates at high temperatures.

In the film state (Figure 1.5(d)), all the compounds show red-shifted absorption peaks in comparison with their solution, showing also broadened absorption bands, and a reverse pattern in the shorter systems, suggesting more extensive aggregation.

These experimental results are supported by TD-DFT theoretical calculations at the B3LYP/6-31G** level (Figure 1.6). The experimental and theoretical data are summarized in Table 1.2.
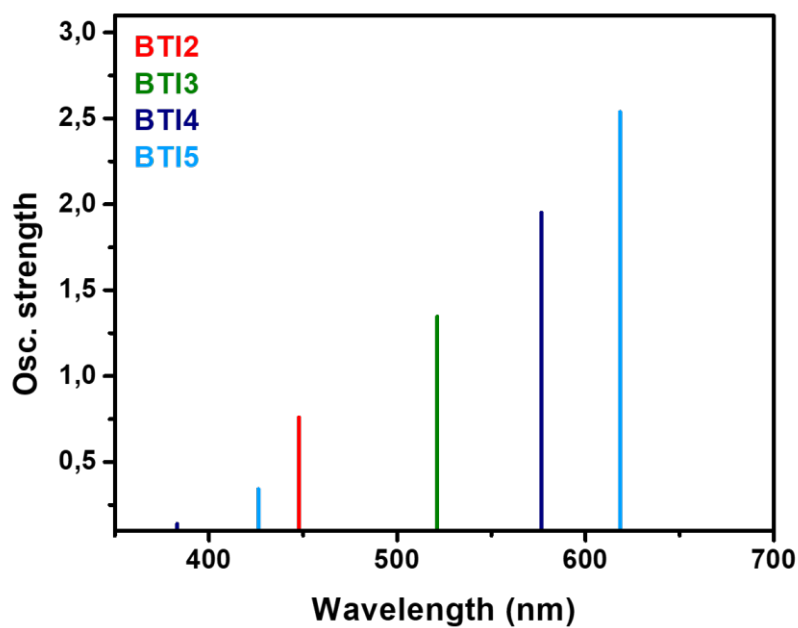
Figure 1.6. TD-DFT calculated vertical transition energies for BTI2-BTI5 as neutral species at the B3LYP/6-31G** level.

As can be seen in Figure 1.6 and Table 1.2, TD-DFT calculated vertical transition energies for neutral BTI2-BTI5 are in good agreement with the experimental data (Figure 1.5(a)), predicting the existence of one intense transition that is redshifted ongoing from BTI2 to BTI5. This transition implies the promotion of one electron from the HOMO to the LUMO orbitals (see OMs topologies in Figure 1.3).

Table 1.2. Photophysical properties of BTI2-BTI5 systems as neutral species and TD-DFT calculations at B3LYP/6-31G** level.

Experimental data			
Molecules	λ_{abs}^{max} **2-MeTHF at 300K (nm)**	λ_{abs}^{max} **2-MeTHF at 125 K (nm)**	λ_{abs}^{max} **ClBz at 373 K(nm)**	λ_{abs}^{max} **film (nm)[b]**
BTI2	419 (sh[a]), 443	423 (sh), 450	422 (sh), 444	435, 469 (sh)
BTI3	469 (sh), 502	468, 525 (sh)	474 (sh), 505	499, 533 (sh)
BTI4	506, 551 (sh)	502, 569 (sh)	508 (sh), 545	516, 575 (sh)
BTI5	535, 587 (sh)	537, 599 (sh)	532 (sh), 572	545, 602 (sh)
Theoretical data			
Molecules	λ **(nm)**	**f**	**Description**
BTI2	448	0.76	HOMO → LUMO (99%)
BTI3	522	1.35	HOMO → LUMO (99%)
BTI4	576	1.95	HOMO → LUMO (99%)
BTI5	618	2.54	HOMO → LUMO (98%)
[a]sh = shoulder, [b]From as-cast films.			

In order to better understand the molecular aggregation of BTI2-BTI5 systems, temperature dependent electronic absorption spectra were recorded in 2-MeTHF (Figure 1.7(a-d)).
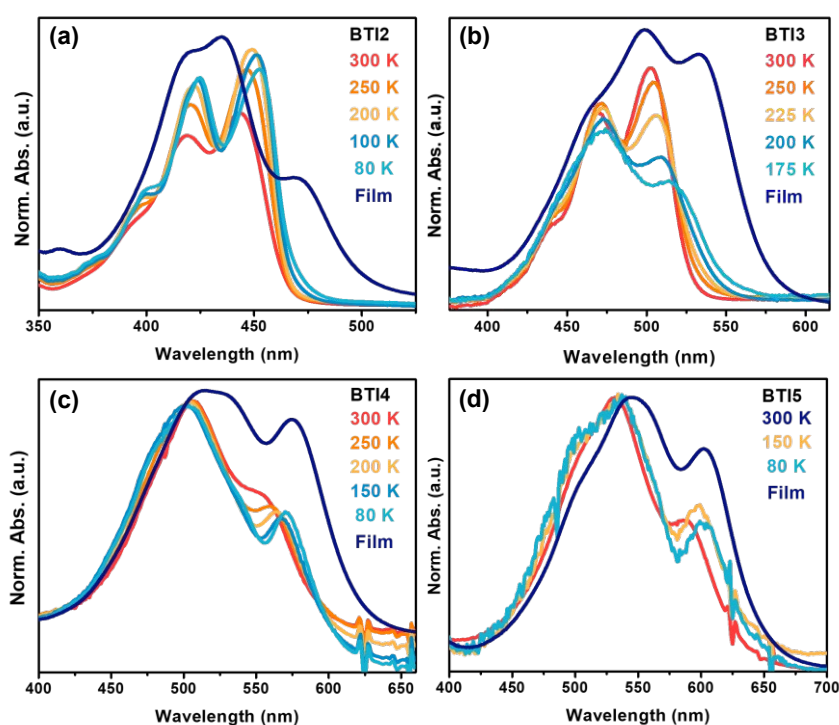
Figure 1.7. UV-Vis spectra of (a) BTI2, (b) BTI3, (c) BTI4, (d) BTI5 systems in 2-MeTHF during heating and cooling down processes.

Significant changes were observed in the case of BTI3 semiconductor as the temperature decreases (Figure 1.7(b)); a relative intensities swap of the absorption bands was found, as well as a slight, red-shifted broadening of the band upon cooling down, highlighting the high tendency of BTI3 to form aggregates at low temperature, as it was observed in the film absorption spectrum.

On the contrary, the UV-Vis spectrum of BTI2 (Figure 1.7(a)) only shows a slightly red-shifted broadening band with the temperature, remaining basically unaltered throughout the whole temperature range analyzed, which means that BTI2 does not easily form aggregates in diluted solutions.

The absorption spectrum for the longest systems (BTI4 and BTI5, Figures 1.7(c) and (d), respectively), also show a noticeable broadening of the absorption band and the appearance of a low-energy shoulder as the temperature decreases, similar to that registered in the thin film spectra, thus being in agreement with the formation of aggregates. In this case the spectrum at low temperature is quite similar to that at room temperature, indicating that aggregates are easily formed for these compounds even at low concentrations and moderate temperatures.

1.3. Experimental and theoretical study of charged species in solution

1.3.1. DFT-optimized molecular geometries of dimeric species

In this section we performed DFT calculations on monomeric and π-dimeric systems (Figure 1.8), to further elucidate the stability, nature, and molecular structure of the charged species in solution. In this case, LC-ωPBE functional together with the D3 Grimme's dispersion correction was used since it has been seen that it predicts more accurate geometrical structures for π-dimeric systems[20]. The solution environment in all cases is described by a polarizable continuum model (PCM) using dichloromethane (CH_2Cl_2) as solvent. The optimized geometries of BTI2-BTI4 radical anion monomers and π-dimers, both anions and dianions, are shown in Figure 1.8.
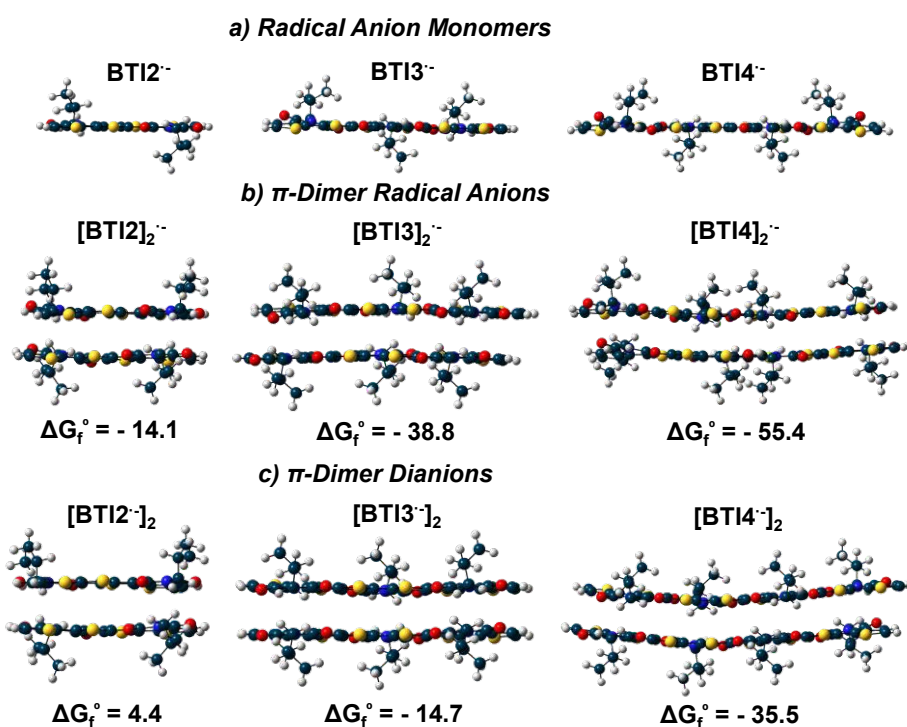
Figure 1.8. DFT-optimized molecular structures of BTI2-BTI4 monomers as (a) radical anion monomers, (b) π-dimer radical anions and (c) π-dimer dianions at LC-ωPBE-GD3BJ/6-31G** - PCM(CH$_2$Cl$_2$) level. The π-dimers shown here present a *syn*-configuration. ΔG_f^o values are given in kcal/mol.

Two configurations were considered for the spatial disposition of the two monomers in the π-dimer formation: 1) the parallel π-stacking, which represent the N atoms in distinct monomers in a *syn*-configuration and 2) the antiparallel π-stacking with the respective N atoms in an *anti*-configuration. Both, parallel and antiparallel configurations were found to be stable against dissociation (see Table 1.3), with the parallel conformer slightly more stable than the antiparallel one (ΔG_f^o) especially in the case of the largest monomers. Therefore, the nearly isoenergetic *anti* and *syn* configurations may co-exist in solution.

118

The impact of the orientations of the branched side chains relative to the ring plane on the dimer stability was also tested, being the configuration with the branched side chains out of the plane more stable for each conformer.

Table 1.3. Interaction energy (E_{int}), binding energy (E_{bind}) and the free energy of Gibbs ($\Delta G_f°$) at 298 K of π-dimer radical anions ([BTI]$_2$$^{·-}$) and π-dimer dianions ([BTI$^{·-}$]$_2$) in *syn* and *anti* configurations calculated at the LC-ωPBE-GD3BJ/6-31G** - PCM(CH$_2$Cl$_2$) level.

Configurations	E_{int}[a] (kcal/mol)	E_{bind}[a] (kcal/mol)	ΔG_f^0 (kcal/mol)
π-dimer radical anion			
Syn-[BTI2]$_2$$^{·-}$	**-40.4**	**-36.4**	**-14.1**
Anti-[BTI2]$_2$$^{·-}$	-40.4	-36.3	-13.5
Syn-[BTI3]$_2$$^{·-}$	**-75.7**	**-64.5**	**-38.8**
Anti-[BTI3]$_2$$^{·-}$	71.4	-63.6	-38.7
Syn-[BTI4]$_2$$^{·-}$	**-88.1**	**-86.4**	**-55.4**
Anti-[BTI4]$_2$$^{·-}$	-	-	-
π-dimer dianion			
Syn-[BTI2$^{·-}$]$_2$	**-30.9**	**-19.3**	**4.4**
Anti-[BTI2$^{·-}$]$_2$	-33.2	-21.0	4.9
Syn-[BTI3$^{·-}$]$_2$	**-53.3**	**-42.6**	**-14.7**
Anti-[BTI3$^{·-}$]$_2$	-54.5	-42.4	-15.6
Syn-[BTI4$^{·-}$]$_2$	**-84.1**	**-70.6**	**-35.5**
Anti-[BTI4$^{·-}$]$_2$	-	-	-
E_{int}, E_{bind} and ΔG_f^0 were calculated as: E_{int} = HF$_{π-dimer\ opt}$ - $\sum$(HF)$_{monomers\ sp}$; E_{bind} = HF$_{π-dimer\ opt}$ - $\sum$(HF)$_{monomers\ opt.}$; ΔG_f^0 = E$_{π-dimer\ freq}$ - $\sum$(E)$_{monomers\ freq.}$			

As can be seen in Table 1.3, both binding and interaction energies of the corresponding π-dimers are very similar which is due to the planarity of the BTI molecules. However, the Gibbs free energy (ΔG_f^0) is about 20 kcal/mol lower than the binding and interaction energies due to the entropic factor. These values are found to be more negative upon elongation of the building block units, indicating the greater tendency towards π-dimer formation for the longest systems.

Although both types of π-dimers are stable against dissociation for BTI3-BTI5, the π-dimer dianions show lower ΔG_f° energy values than the corresponding π-dimer radical anions, being even unstable in the case of BTI2, with a positive ΔG_f° of 4.4 kcal/mol.

1.3.2. Spectroelectrochemistry and TD-DFT vertical transition energies

In order to analyze the charged species and their aggregation in solution, the evolution of the UV-Vis/NIR spectra was recorded by progressive electrochemical reduction of low concentration solutions of BTI2-BTI5 in dichloromethane solutions at room temperature, in presence of high excess of (n-Bu)$_4$NPF$_6$ supporting electrolyte (Figure 1.9).
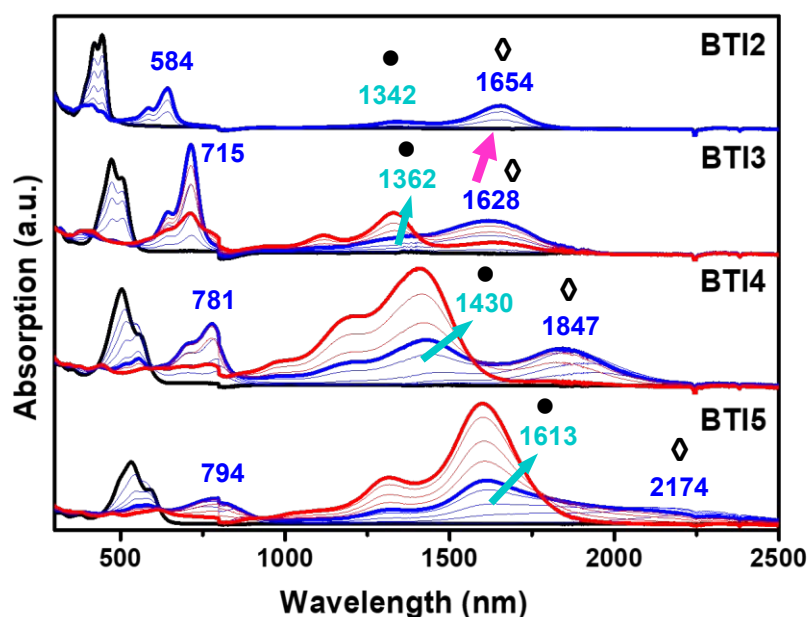
Figure 1.9. UV-Vis/NIR absorption spectra changes of BTI2-BTI5 recorded upon electrochemical reduction in dichloromethane at room temperature, in presence of (n-Bu)$_4$NPF$_6$ supporting electrolyte within an OTTLE cell. The black curves represent the neutral species, the blue curves represents both isolated anions (◊) and π-dimeric radical anion bands (●) which coexist in solution, and the red curves represent the π-dimer dianions species.

Upon progressive electrochemical reduction, the UV-Vis absorption spectra of all parental neutral species (black curves)

progressively vanished in time giving rise to two sharp peaks (blue curves) at higher wavelengths, with clear isosbestic points (Figure 1.9). The absorption bands of the BTI2-BTI5 molecules as radical anions exhibit a progressive redshift with the increase of the building block unit lengths, as expected since the π-conjugation length increases ongoing from BTI2 to BTI5. However, an unexpected behavior of the high energy band (1654 nm) for the shortest building block (BTI2) is observed, which consists in a 26 nm redshift compared with the next building block unit (BTI3), whose band appears at lower wavelengths (1628 nm). In addition, is also noteworthy, that ongoing from BTI2 to BTI3 (Figure 1.9) a modest displacement of the π-dimer radical anion absorptions (1342 *vs.* 1362 nm) is observed, in comparison with the displacement observed for longer molecules (BTI3-BTI5), which could be explained by the similar charge delocalization in both systems, as can be seen later

Upon further increasing the reduction potential, a new spectral profile (red curve, Figure 1.9) is recorded for BTI3-BTI5 molecules. These red curves exhibit a strong absorption band appearing at 1300-1900 nm, except for the smallest monomer (BTI2) of this series of compounds, which is explained later.

To analyze in more detail the different species formed during the first step of the electrochemical reduction, a comparative analysis of the impact of the chain length on the spectroelectrochemical behavior is now described (Figure 1.9). Thus, by comparing the BTI2-BTI5 radical anion species spectra (blue curve), it can be observed that the band at higher wavelength (~ 1100-2500 nm, ●◊) exhibit a higher energy shoulder (~ 1100-2000 nm, ●), which increases in intensity upon increasing the chain length. Considering that the tendency to form aggregates increases with the building block unit, these shoulder bands (●) are assigned to a π-dimer radical anion. Thus, the isolated radical anions coexist with the π-

dimer radical anions in the blue spectra. Consequently, the red curve represents the π-dimer dianion, which is also more favored for the longest systems with the most intense band recorded for BTI5. On the contrary, in the case of BTI2 systems, although the presence of π-dimer radical anions is recorded (●), the increase of the applied potential does not lead to the introduction of an extra electron in the dimeric form. As can be seen in Figure 3.9, the red bands are blue-shifted regarding those of the π-dimer radical anions (●), probably due to the inherent destabilization by increased electrostatic repulsion in the double charged π-dimer (see the explanation later).

In order to interpret these experimental results, TD-DFT theoretical calculations were carried out at the ωB97XD/6-31G**//LC-ωPBE/6-31G** - PCM(CH$_2$Cl$_2$) level (Figure 1.10). ωB97XD functional was used in this case since it provides sligltly more accurate results for these experimental results. The experimental and theoretical data are summarized in Table 1.4.
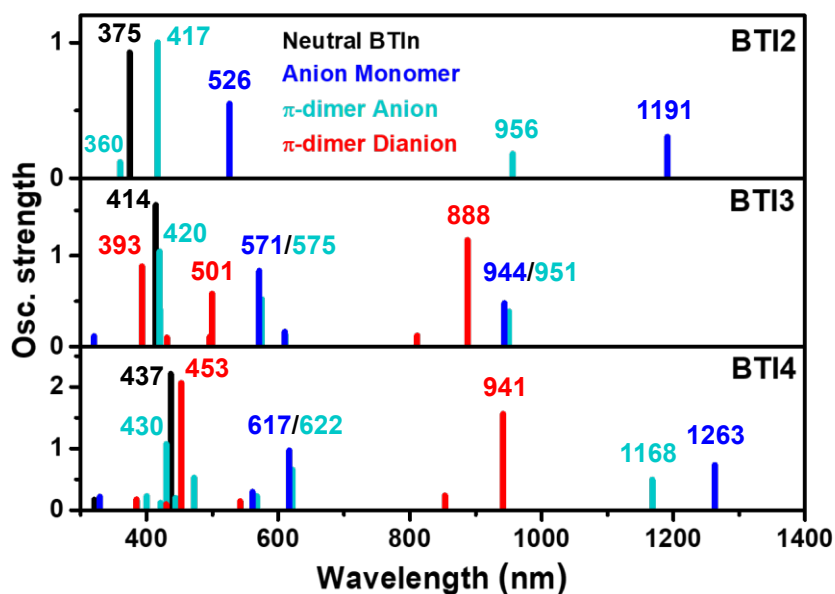
Figure 1.10. TD-DFT calculated vertical transition energies for BTI2-BIT4 as neutral (black bars), isolated radical anion (blue bars), π-dimer radical anion (cyan bars) and π-dimer dianion (red bars) species at ωB97XD/6-31G**//LC-ωPBE/6-31G** - PCM(CH$_2$Cl$_2$) level.

As can be seen in Figure 1.10 and Table 1.4, TD-DFT calculated vertical transition energies for BTI2-BTI4, both in neutral and reduced states as isolated radical anion, π-dimer radical anion and π-dimer dianion species, are in good agreement with the experimental data (Figure 1.9). The calculations predict the existence of two red-shifted transitions with high oscillator strengths for both π-dimer radical anions (cyan bars) and dianions (red bars) and also for the isolated radical anions (blue bars), compared to the neutral band (black bars).

Table 1.4. UV-Vis/NIR absorption data of BTI2-BTI4 as neutral, isolated radical anion, π-dimer radical anion and π-dimer dianion species and TD-DFT calculations at ωB97XD/6-31G**//LC-ωPBE/6-31G** - PCM(CH_2Cl_2) level.

	Experimental data (nm)			
	Neutral	**Radical anion**	**π-dimer radical anion**[a]	**π-dimer dianion**[a]
BTI2	421 (sh), 445	582 (sh), 645, 1654	412, 584, 1342	-
BTI3	473 (sh), 506	645 (sh), 715, 1628	376, 643, 1362	409, 715, 1118 (sh), 1331
BTI4	503, 560 (sh)	704 (sh), 781, 1847	558, 1197, 1430	442, 779, 1197 (sh), 1411
BTI5	532, 591 (sh)	794, 2174	566, 1611	614, 1602
	Theoretical data (nm)			
BTI2	375 (0.93)	526 (0.55), 1191 (0.31)	360 (0.06), 417 (1.00), 956 (0.18)	-
BTI3	414 (1.56)	571 (0.84), 944 (0.48)	420 (1.05), 575 (0.52), 951 (0.39)	393 (0.88), 501 (0.59), 888 (1.17)
BTI4	437 (2.21)	617 (0.97), 1263 (0.73)	430 (1.07), 622 (0.66), 1168 (0.50)	453 (2.06), 941 (1.56)
BTI5	451 (2.89)	637 (1.32), 1246 (1.01)	-	-
[a]The π-dimer radical anion and the π-dimer dianion species are referred to the *syn* configurations. The values in parenthesis are the oscillator strengths.				

Focusing on the electronic transitions of the BTI2 and BTI3 isolated radical anion species (blue bars in Figure 1.10), two intense electronic transitions were computed for BTI2 radical anion (BTI2·⁻) at 526/1191 nm and for the BTI3 radical anion (BTI3·⁻) at 571/944 nm, which nicely correspond to the experimental absorption bands measured at 645/1654 nm for BTI2 and 715/1628 nm for BTI3 (blue bands in Figure 1.9). Therefore, theoretical calculations successfully predict the blue-shift of the experimental absorption band from 1654 nm in BTI2 to 1628 nm in BTI3 isolated radical anions (blue bands marked with ◊ in Figure 1.9); this can be understood considering the similar charge delocalization over the conjugated skeleton for BTI2 and BTI3 monomers (Figure 1.11), where in

both cases is extended over ~ 5 rings despite the longer conjugated skeleton in BTI3.
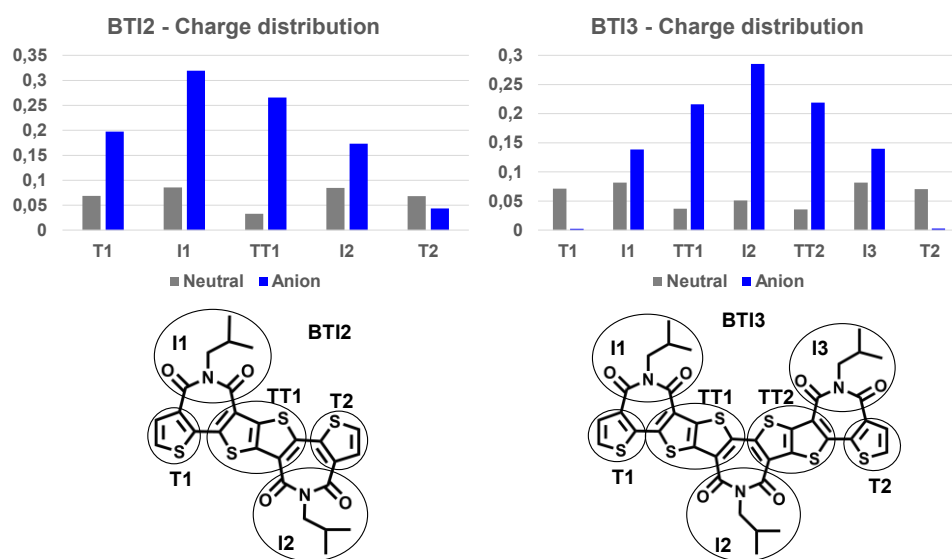
Figure 1.11. Selected Mulliken atomic charges on the molecular domains for the neutral and radical anion species of BTI2 and BTI3 isolated monomers calculated at LC-ωPBE-GD3BJ/6-31G** level.

On the other hand, focusing on the electronic transitions of the BTI2 and BTI3 π-dimer radical anions species (cyan bars in Figure 1.10), three bands are theoretically predicted at 360, 417 and 956 nm for the former ($[BTI2]_2^{\cdot-}$) and at 420, 575 and 951 nm for the latter one ($[BTI3]_2^{\cdot-}$). These predicted transitions are in good agreement with the experimental formation of the π-dimer radical anion (412, 584, 1342 nm for $[BTI2]_2^{\cdot-}$ and 376, 643, 1362 nm for $[BTI3]_2^{\cdot-}$, blue bands in Figure 1.9). Therefore, theoretical calculations successfully predict the modest displacement of the π-dimer radical anion absorption (1342 *vs.* 1362 nm) on going from BTI2 to BTI3 (Figure 1.9) in comparison with the displacement observed for longer molecules (BTI3-BTI5); this can be understood considering the

similar charge delocalization extension in both π-dimer radical anions. In the BTI2 π-dimer radical anions ([BTI2]$_2^{\cdot-}$), the injected charge is delocalized over ~8 rings, considering the two molecules of the π-dimer, while in the BTI3 π-dimer radical anion species ([BTI3]$_2^{\cdot-}$), the charge is delocalized over ~7 rings (Figure 1.12).
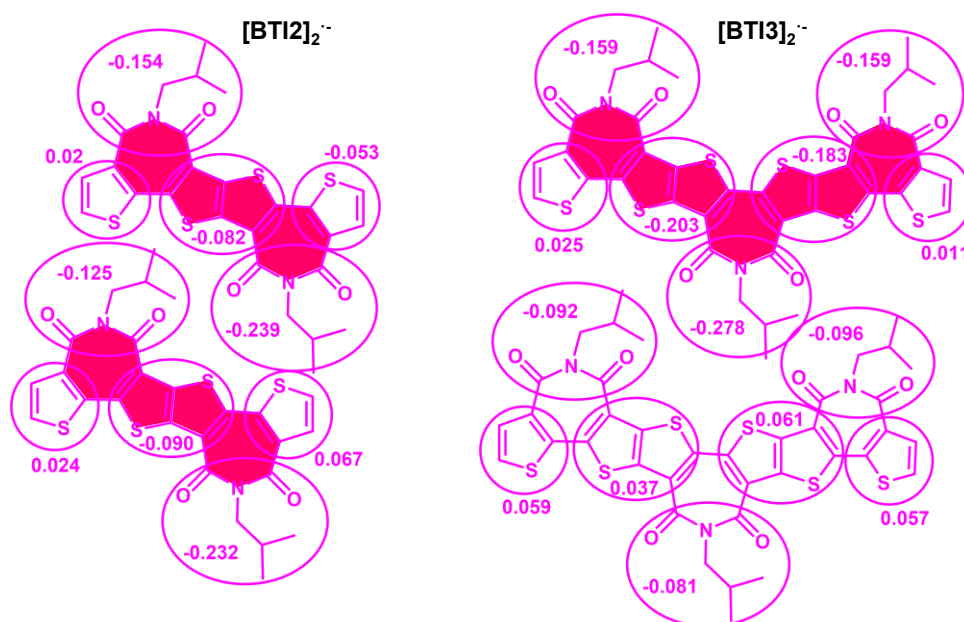
Figure 1.12. Selected Mülliken atomic charges on the molecular domains of BTI2-BTI3 π-dimer radical anions calculated at LC-ωPBE-GD3BJ/6-31G** level. The charge delocalization extension in the π-dimers is highlighted in pink.

The three main intense bands of these BTI radical anion π-dimers, ongoing from lower to higher wavenumbers are associated with the HOMO-SOMO, SOMO-LUMO and HOMO-LUMO transitions, respectively (see molecular orbitals in Figure 1.13). The redshift of the bands corresponding to the π-dimer radical anion compared to the neutral species, are presumably due to the effective through-space electronic interaction within the dimer.
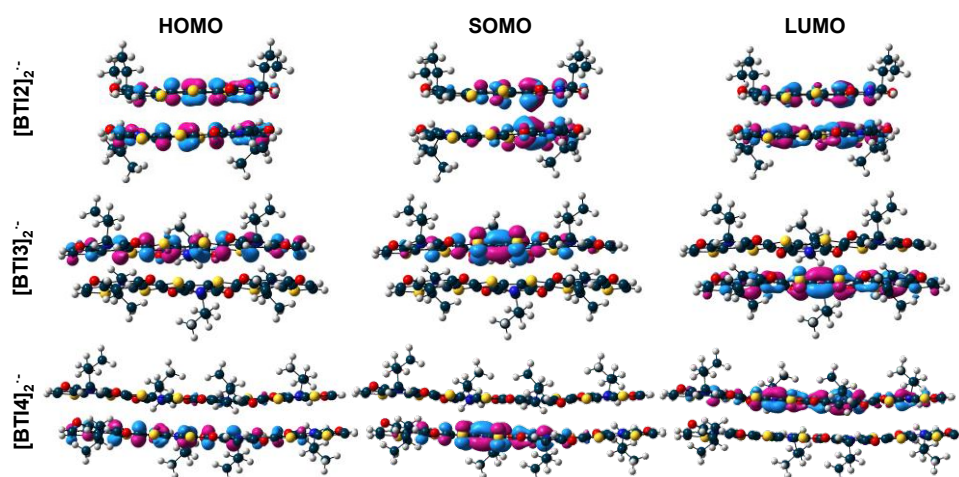
Figure 1.13. DFT-calculated frontier molecular orbital topologies (HOMO, SOMO and LUMO) of BTI2-BTI4 π-dimer radical anions at LC-ωPBE-GD3BJ/6-31G** - PCM(CH_2Cl_2) level. Isovalue: 0.035.

As can be seen in Figure 1.13, in the shortest system (BTI2) the molecular orbitals are highly delocalized over both monomers in the π-dimer radical anion species, however, a noticeable electron density confinement in one of the monomers is found for the larger systems (BTI3-BTI5). This fact supports the difficulty of injecting another electron in BTI2 π-dimer radical anion, because of charge repulsion, while π-dimer radical anions built up with BTI3-BTI5 molecules are able to accommodate one extra charge. Therefore, based on the previous experimental and theoretical results, we can confirm the instability of the dianion π-dimer in the case of BTI2. Note that π-dimer radical anions built up with BTI3-BTI5 molecules are able to accommodate one extra charge that is delocalized on one single molecule in the π-dimer radical dianions (see Figure 1.14(b)). However, the injection of another electron in BTI2 π-dimer radical anion would not be feasible due to charge repulsion since the two molecules bear approximately half of the injected charge.
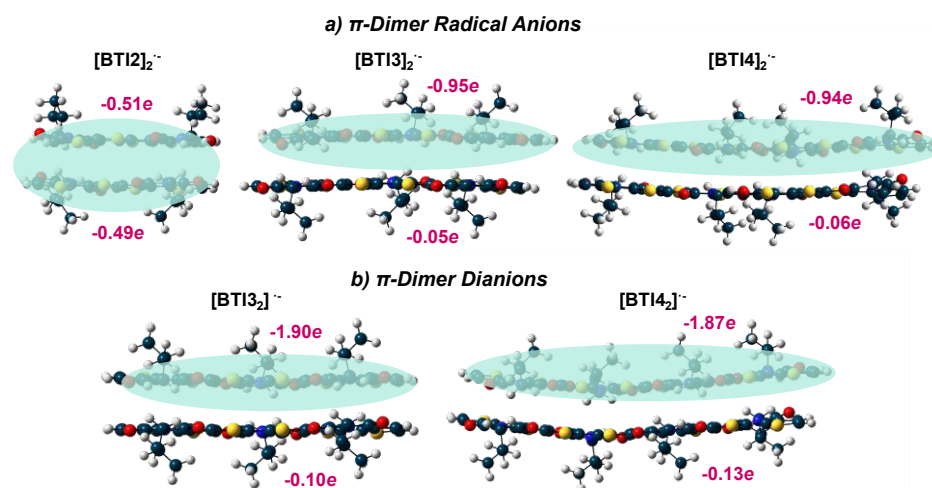
Figure 1.14. DFT-calculated charge delocalization in BTI2-BTI4 π-dimers, both radical anions (a) and dianions (b) at the LC-ωPBE-GD3BJ/6-31G** - PCM(CH$_2$Cl$_2$) level.

1.3.3. Effect of concentration and counterion size on the spectroelectrochemical reductions

In order to further study the nature of the different charged species, the spectroelectrochemical reduction processes were recorded as a function of the nature of counterions and the concentration of BTI2-BTI5 solutions.

The impact of the size of counterions on the π-dimer species formation has been analyzed by inspecting the absorption spectral changes recorded upon electrochemical reduction of BTI2-BTI5 in the presence of (*n*-Bu)$_4$NPF$_6$ or (*n*-Hex)$_4$NPF$_6$ supporting electrolytes (Figure 1.15(a) and (b)).
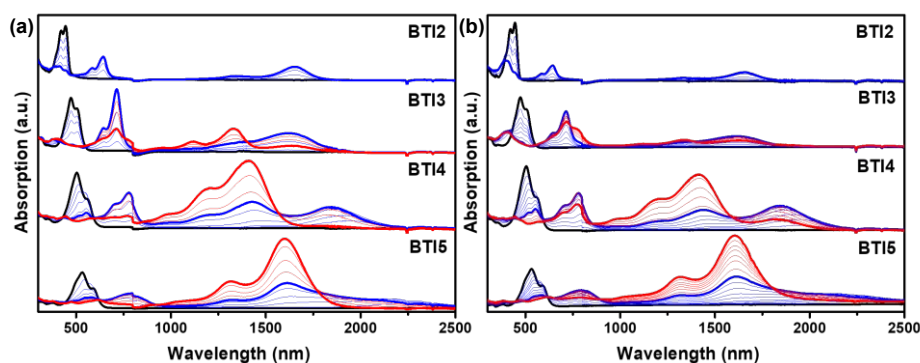
Figure 1.15. UV-Vis/NIR absorption spectra changes of BTI2-BTI5 upon electrochemical reduction in CH_2Cl_2 solution at room temperature, in presence of (a) (n-Bu)$_4$NPF$_6$ and (b) (n-Hex)$_4$NPF$_6$ supporting electrolytes within an OTTLE cell.

As can be seen in Figure 1.15, similar spectral profiles were obtained regardless the size of the counterions; however, the extension of the counterions alkyl chains from butyl (Bu$_4^+$, Figure 1.15(a)) to hexyl (Hex$_4^+$, Figure 1.15(b)) chains slightly destabilizes the formation of π-dimeric species, which could be probably due to steric hindrance effects. This is particularly evident in the formation of BTI3 π-dimer dianions (red curves), which are clearly favored in the presence of the less bulky alkyl chain (*n*-Bu)$_4$NPF$_6$ supporting electrolyte (Figure 1.15(a)).

The impact of the BTI concentration on the formation of the π-dimers was also studied. In this case and in order to simplify the results, only the BTI3 spectral profile is shown in Figure 1.16.
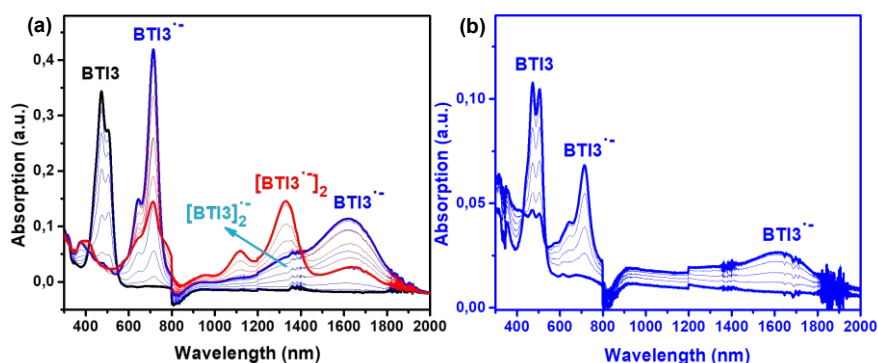
Figure 1.16. UV-Vis/NIR absorption spectra changes of BTI3 recorded upon electrochemical reduction in CH_2Cl_2 solution with concentrations of (a) 3×10^{-7} M and (b) 8×10^{-8} M at room temperature, in presence of $(n\text{-Bu})_4NPF_6$ supporting electrolyte within an OTTLE cell.

Thus, as can be seen in Figure 1.16, the spectral profile of the first reduced species (blue curves) of BTI3 in CH_2Cl_2 is similar at high and very low concentrations; however, the shoulder located at around 1300 nm, which was ascribed to π-dimer radical anion ($[BTI3]_2^{\cdot\cdot}$), basically disappears due to the low molecular concentration (Figure 1.16(b)).

Further increase of the applied potential does not modify the spectral profile at low concentration of BTI3 (Figure 1.16(b)), however at high concentration of BTI3 a new band appears at around 1300 nm (red curve, Figure 1.16(a)), which was ascribed to the formation of π-dimer dianions ($[BTI3^{\cdot\cdot}]_2$). These results support the π-dimeric nature of both the red spectra and the shoulder peak at around 1300 nm of the blue spectra, as previously indicated by theoretical calculations.

1.4. Experimental study of charged species in solid state

In the previous sections it has been demonstrated the predominance of aggregates both in neutral and charged states in these BTI2-BTI5 semiconductors even in diluted solutions, due to their rigid and planar structures. Molecular aggregation is key in thin film devices since charge carriers need to be stabilized and transported through the device active channel[24,25]. Therefore, in this section we focus on the study of charged species in the solid state.

1.4.1. Organic Field Effect Transistors

To better understand how charge is transported in solid state films based on these promising ladder-type BTI2-BTI5 molecules, OFETs with a BCTG configuration were first fabricated and characterized. As previously reported in our group[1], a remarkable decrease in field effect mobility is recorded as the BTI unit gets longer, with more than one order of magnitude drop for BTI5 with respect to the shortest members of the series (see data in Table 1.5). This has been ascribed to different facts: (i) the degree of crystallinity was reported to decrease as the length of the BTI unit increased, with BTI2 showing the highest degree of order. Indeed, X-ray diffraction (XRD) measurements show that BTI2 exhibits the most pronounced lamellar scattering, while larger grain size is found in AFM topographies[26] (see Section 1.5). Nevertheless, other effects may also be considered, such as: (ii) the injected charge density is confined in the three internal fused BTI units in BTI3-BTI5, so that longer fused BTI systems than BTI3 are, in principle, not necessary in terms of conjugation and charge stabilization; (iii) processability issues are found in the longest members of the series due to the strong aggregation even at low concentration solutions, which is ultimately related to a poor film formation and thus to a lower degree of order[1,26].

Table 1.5. BCTG OFET performance of BTI2-BTI5. Average field-effect mobility values from at least 5 devices are shown.

Semiconductor	$\mu_{e,sat}$ (cm^2 V^{-1} s^{-1})[a]	V$_{TH}$ (V)	I$_{ON}$/I$_{OFF}$
BTI2	0.074	2	10^4
BTI3	0.017	4	10^4
BTI4	0.014	9	10^4
BTI5	0.0019	15	10^3
The mobilities were calculated with the average slop within V$_{GS}$ = 70–80 V.			

1.4.2. Charge modulation spectroscopy

Despite the indications mentioned above, the remarkable increase in the field-effect mobility observed for the shortest member of the series, BTI2, may not be solely understood under these terms. Thus, in order to shed light on the charge transport mechanism of BTI2-BTI5 fused systems, charge modulation spectroscopic (CMS) measurements of semi-transparent OFETs have been performed.

As mentioned above, BCTG configuration OFETs were used in this case, and for their fabrication, Cr and Au layers were used as contact electrodes, on top of which a thin layer of cesium fluoride (CsF) was deposited from solution to reduce contact resistance and to facilitate electron injection[27]. Afterwards, the BTI2-BTI4 semiconductors were deposited, followed by the CYTOP dielectric layer, both of them from solution by spin-coating, and were subsequently thermally annealed. Finally, Al and Au where thermally evaporated as gate electrodes to complete the device fabrication. The transistor fabrication and characterization were carried out in a nitrogen-filled glovebox.

CMS is a powerful technique which allows us to study the molecular nature of the charge carriers present in the OFET accumulated

channel[28,29,38–45,30–37]. In this experiment, the charge density in the thin semiconducting film, at the interface with the dielectric, is modulated by changing the applied gate bias in a semitransparent OFET, and then measuring the variation in light transmission normalized to the total transmission (ΔT/T). The ΔT signal is associated to the formation of new intragap states, owing to the modulation of mobile charges, while immobilized charges cannot be observed in the CMS spectrum since they cannot be modulated.

The CMS spectra of BTI2-BTI4 OFETs in full accumulation mode, measured at various applied gate voltages (V_G) ranging from 20 to 60 V and with a modulating voltage (V_{ac}) of ±20 V, are shown in Figure 1.17.
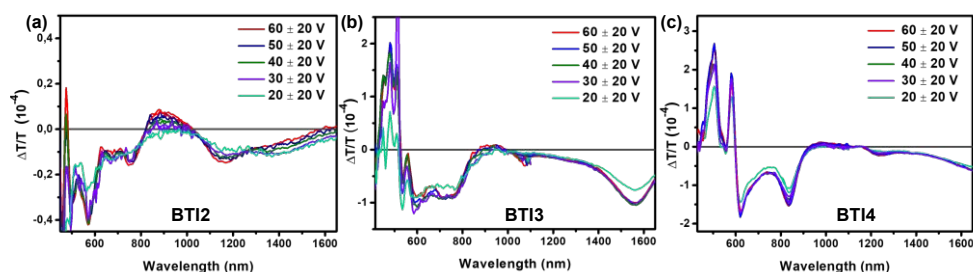
Figure 1.17. Evolution of the CMS spectra of semitransparent working OFETs with BTI2, BTI3 and BTI4 semiconductors as the active material (T=300 K).

In these spectra, the ΔT/T negative region is associated with sub band gap states induced by localized, polaronic charges present in the accumulation layer, while the positive signal is related to the bleaching of the neutral absorption. Bleaching of BTI2 (Figure 1.17(a)) could not be measured since the neutral absorbance of this molecule peaks below 450 nm, a range where the CMS experimental set-up is not sensitive enough.

Some similarities are present in all CMS spectra (Figure 1.17): (i) the bleaching of neutral states (ΔT/T > 0) exhibits highly pronounced

vibronic structures, better resolved than their UV-Vis absorption counterparts (Figure 1.5(d)). This is commonly observed since charge carriers are located in the most ordered regions of the films. (ii) The charge absorption regions ($\Delta T/T < 0$) exhibit two distinct contributions. One at low wavelengths, immediately next to the bleaching and another at higher wavelengths. (iii) A high similitude between the sub gap features attributed to charged species obtained by spectroelectrochemical and CMS experiments (Figures 1.18-1.20) is observed. Yet, CMS spectra show no fingerprint of dianion π-dimer formation, probably related to the lower charge carrier density achieved in the channel of an accumulated transistor when compared to that of spectroelectrochemistry, upon strong reduction. The charge absorption signals fit well the peaks of radical anions, although some changes in peak position are present, probably because of differences in polarization between the solid state and solution.

The spectra of the reduced species in solution were then employed as a reference to interpret the CMS spectra. The comparison between CMS and spectroelectrochemistry data for BTI2 is shown in Figure 1.18.
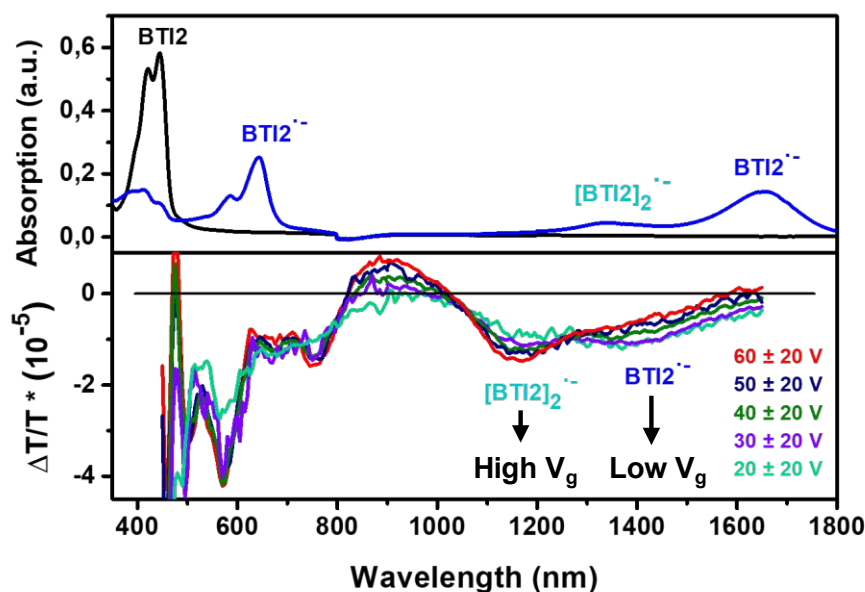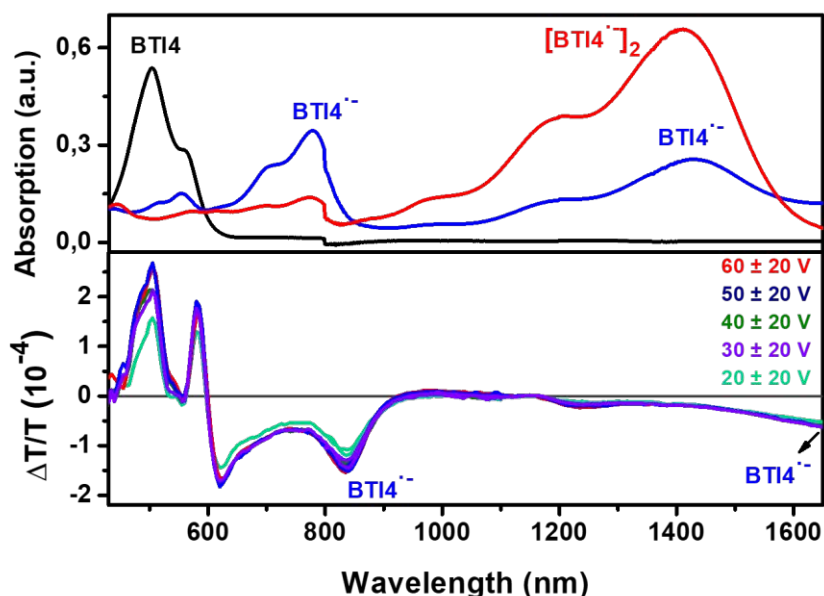
Figure 1.18. Comparison between UV-Vis/NIR absorption spectra changes of BTI2 in dichloromethane solution at room temperature, containing (n-Bu)$_4$NPF$_6$ and measured in an OTTLE cell (Top) and evolution of the CMS spectra of semitransparent BTI2-based OFETs at T=300 K (Bottom).

In particular, the spectroelectrochemistry reference of BTI2 (Figure 1.18) shows the presence of two features at high wavelengths (1000-1900 nm), being the shoulder at lower wavelengths related to π-dimer radical anion (1342 nm) and the peak at higher wavelengths related to the isolated anion (1654 nm). In BTI2 CMS spectra, at low gate voltage, the spectral profile also shows two contributions peaking at ~ 1400 nm and ~ 1200 nm, with a similar relative intensity. Thus, these peaks are interpreted as the isolated anion and the π-dimer radical anion, respectively. Upon increasing the gate voltage, the shoulder at 1400 nm decreases and vanishes, while the peak at 1200 nm becomes more pronounced. Thus, CMS spectra suggest a stronger contribution coming from the π-dimer radical anion than from the isolated anion at increasing

charge density. In particular, in full accumulation, charge carriers in BTI2 systems are likely stabilized within two consecutive molecules, as predicted by DFT calculations (Figure 1.14). In this case, the hopping process within the active channel may be seen as charge transfer between neighboring π-dimers, which improves BTI2 field-effect mobility.

In BTI3, the scenario is different, and transitions associated to the isolated anion become dominant (Figure 1.19).
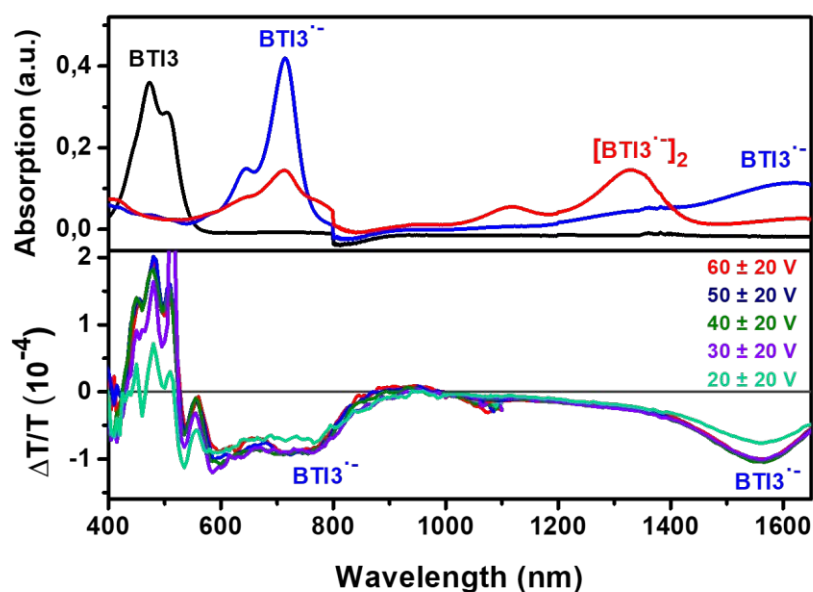
Figure 1.19. Comparison between UV-Vis/NIR absorption spectra changes at room temperature of BTI3 in dichloromethane solution at room temperature, containing (*n*-Bu)$_4$NPF$_6$and measured in an OTTLE cell (Top) and evolution of the CMS spectra of semitransparent OFETs with BTI3 semiconductors as the active material at T=300 K (Bottom).

The BTI3 CMS spectra exhibit a strong signal at ~ 1600 nm that matches well the isolated anion peak (1628 nm) observed in spectroelectrochemistry, while at lower wavelengths (1000 – 1300 nm)

only a broad feature is present, indicating probably a lower contribution of the π-dimer radical anion. V_G dependent spectra show only minor changes as voltage increases, in particular the peak at ~ 600 nm – associated to isolated radical anion in solution – reduces in intensity. Therefore, despite a dominant signal coming from the isolated anion, an increase of voltage seems to reduce the confinement of charge carriers on a single molecule. It can be noted that the CMS experimental set-up is not sensitive enough above 1600 - 1700 nm, therefore the reduction of intensity above those wavelengths is an artefact associated to the limitations of the measurement.

The case of BTI4 (Figure 1.20), is similar to that obtained for BTI3, thus above 1500 nm the intensity rises and reaches a maximum at 1700 nm. This is again an artefact due to the limited resolution at those wavelengths, hence it could only be detected the onset of a strong charge absorption signal, which is probably related to the isolated anion peak.

Figure 1.20. Comparison between UV-Vis/NIR spectra changes of BTI4 in dichloromethane solution at room temperature, containing $(n\text{-Bu})_4NPF_6$ and measured in an OTTLE cell (Top) and evolution of the CMS spectra of semitransparent OFETs with BTI4 semiconductors as the active material at T=300 K (Bottom).

At lower wavelengths, between 1000 – 1500 nm, only a broad and low intensity signal is detected. The charge absorption spectra next to the bleaching show sharp vibronic at ~ 600 nm and 850 nm, in a spectral range where the isolated anion was shown to exhibit two peaks. These sharp vibronic transitions, together with the higher wavelength spectra suggest that the charge carriers are mainly localized on a single molecule.

In conclusion, as the BTI length is increased, CMS suggests that charge carriers within the film tend to be localized on isolated molecules, while BTI2 shows spectra suggesting charge relaxation within two molecules, in a π-dimer configuration. This is promoted by the more

efficient crystal packing of BTI2 semiconductor and the fact that charge stabilization is improved in the BTI2 π-dimer radical anion due to delocalization over the two interacting molecules.

In addition, the theoretical calculations are in good agreement with these CMS experimental data, evidencing that in the BTI2 π-dimer radical anion system the charge is delocalized over the two monomers, in opposite to the BTI3-BTI5 π-dimers, for which the charge is delocalized over a single molecule.

1.5. Morphological characterization of thin films

1.5.1. 2D-GIWAXS and AFM measurements

In order to better understand the mobility trend in this series of small molecules, we studied the molecular packing as well as the morphologies of BTI2-BTI5 thin films prepared under the same conditions used for the optimal OTFT fabrication. To this end, two-dimensional grazing incidence wide angle X-ray scattering (2D-GIWAXS) and atomic force microscopy (AFM) measurements were carried out (Figure 1.21 and 1.22, respectively).
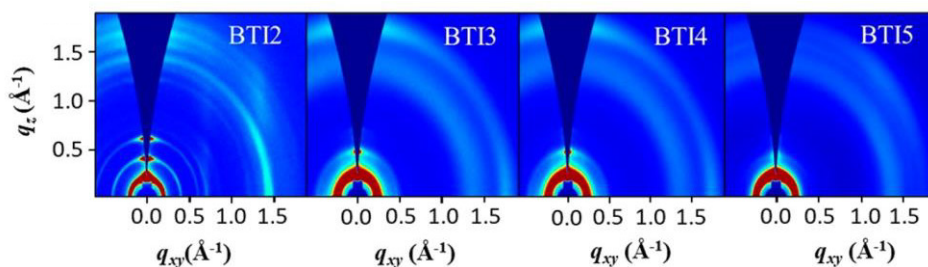
Figure 1.21. 2D-GIWAXS images of BTI2-BTI5 films prepared under the optimal device fabrication conditions.

BTI2 shows the most pronounced lamellar scattering up to (300) in the out-of-plane (OOP) direction, together with a distinctive (010) π-π stacking peak in the in-plane (IP) direction suggesting a predominant edge-on orientation with the highest crystallinity among the series. The lamellar d-spacing was determined to be 31.4 Å, by integration of the in-plane peak (q_z or q_{xy} (100) ≈ 0.2 Å^{-1}), and the π-π stacking distance was measured to be 4.3 Å, which was determined by integration of the normally out-of-plane peak (q_{xy} (010) ≈ 1.47 Å^{-1}).

With the extension of the fused BTI rings (BTI3-BTI5), closer lamellar d-spacing of 26-27 Å were obtained, but the higher order (200) and (300) scattering peaks become weaker, which indicates reduced film crystallinities.

The AFM measurements (Figure 1.22) reveal that the BTI3-BTI5 films are quite smooth, with root-mean-square roughness (RMS) below 1 nm, indicative of weak film crystallinity. However, BTI2 films shows the largest grain size and much higher RMS of ~ 4.5 nm, resulting from its highest crystallinity in the BTIn series, which is in good agreement with its highest mobility.
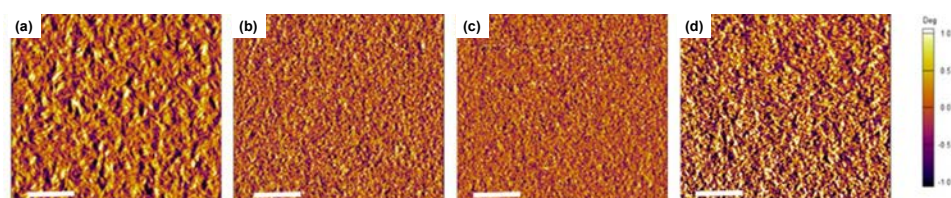
Figure 1.21. AFM phase images of the thin films of (a-d) BTI2-BTI5, respectively, prepared under the optimal device fabrication conditions. Scale bar: 1μm.

1.6. References

[1]   Wang, Y.; Guo, H.; Ling, S.; Arrechea-Marcos, I.; Wang, Y.; López Navarrete, J. T.; Ortiz, R. P.; Guo, X. Ladder-Type Heteroarenes: Up to 15 Rings with Five Imide Groups. *Angew. Chemie Int. Ed.* **2017**, *56*, 9924–9929.

[2]   Zheng, T.; Cai, Z.; Ho-Wu, R.; Yau, S. H.; Shaparov, V.; Goodson, T.; Yu, L. Synthesis of Ladder-Type Thienoacenes and Their Electronic and Optical Properties. *J. Am. Chem. Soc.* **2016**, *138*, 868–875.

[3]   Jones, B. A.; Facchetti, A.; Wasielewski, M. R.; Marks, T. J. Tuning Orbital Energetics in Arylene Diimide Semiconductors. Materials Design for Ambient Stability of n-Type Charge Transport. *J. Am. Chem. Soc.* **2007**, *129*, 15259–15278.

[4]   Payne, M. M.; Parkin, S. R.; Anthony, J. E.; Kuo, C.-C.; Jackson, T. N. Organic Field-Effect Transistors from Solution-Deposited Functionalized Acenes with Mobilities as High as 1 Cm2/V·s. *J. Am. Chem. Soc.* **2005**, *127*, 4986–4987.

[5]   Nishinaga, T.; Komatsu, K. Persistent π Radical Cations: Self-Association and Its Steric Control in the Condensed Phase. *Org. Biomol. Chem.* **2005**, *3*, 561–569.

[6]   Rapta, P.; Schulte, N.; Schlüter, A. D.; Dunsch, L. In Situ Spectroelectrochemical Studies on Ladder-Type Oligomers in Solution and the Solid State. *Chem. – A Eur. J.* **2006**, *12*, 3103–3113.

[7]   Rizalman, N. S.; Ferrón, C. C.; Niu, W.; Wallace, A. L.; He, M.; Balster, R.; Lampkin, J.; Hernández, V.; López Navarrete, J. T.; Ruiz Delgado, M. C.; Hartl, F. Radical Cations of End-Capped Tetrathienoacenes and Their π-Dimerization Controlled by the Nature of α-Substituents and Counterion Concentration. *RSC Adv.* **2013**, *3*, 25644–25647.

[8]   Khodorkovsky, V.; Shapiro, L.; Krief, P.; Shames, A.; Mabon, G.; Gorgues, A.; Giffard, M. Do π-Dimers of Tetrathiafulvalene Cation Radicals Really Exist at Room Temperature? *Chem. Commun.* **2001**, No. 24, 2736–2737.

[9]   Hill, M. G.; Mann, K. R.; Miller, L. L.; Penneau, J. F. Oligothiophene Cation Radical Dimers. An Alternative to Bipolarons in Oxidized Polythiophene. *J. Am. Chem. Soc.* **1992**, *114*, 2728–2730.

[10]   Graf, D. D.; Duan, R. G.; Campbell, J. P.; Miller, L. L.; Mann, K. R.

From Monomers to π-Stacks. A Comprehensive Study of the Structure and Properties of Monomeric, π-Dimerized, and π-Stacked Forms of the Cation Radical of 3',4'-Dibutyl-2,5''-Diphenyl-2,2':5',2''-Terthiophene. *J. Am. Chem. Soc.* **1997**, *119*, 5888–5899.

[11]   Mayorga Burrezo, P.; Pelado, B.; Ponce Ortiz, R.; De la Cruz, P.; López Navarrete, J. T.; Langa, F.; Casado, J. Robust Ethylenedioxythiophene–Vinylene Oligomers from Fragile Thiophene–Vinylene Cores: Synthesis and Optical, Chemical and Electrochemical Properties of Multicharged Shapes. *Chem. – A Eur. J.* **2015**, *21*, 1713–1725.

[12]   Zhang, F.; Götz, G.; Mena-Osteritz, E.; Weil, M.; Sarkar, B.; Kaim, W.; Bäuerle, P. Molecular and Electronic Structure of Cyclo[10]Thiophene in Various Oxidation States: Polaron Pair vs. Bipolaron. *Chem. Sci.* **2011**, *2*, 781–784.

[13]   Baeuerle, P.; Segelbacher, U.; Maier, A.; Mehring, M. Electronic Structure of Mono- and Dimeric Cation Radicals in End-Capped Oligothiophenes. *J. Am. Chem. Soc.* **1993**, *115*, 10217–10223.

[14]   Hill, M. G.; Penneau, J. F.; Zinger, B.; Mann, K. R.; Miller, L. L. Oligothiophene Cation Radicals. .Pi.-Dimers as Alternatives to Bipolarons in Oxidized Polythiophenes. *Chem. Mater.* **1992**, *4*, 1106–1113.

[15]   Ferrón, C. C.; Delgado, M. C. R.; Hernández, V.; Navarrete, J. T. L.; Vercelli, B.; Zotti, G.; Cortada, M. C.; Novoa, J. J.; Niu, W.; He, M.; Hartl, F. Substituent and Counterion Effects on the Formation of π-Dimer Dications of End-Capped Heptathienoacenes. *Chem. Commun.* **2011**, *47*, 12622–12624.

[16]   Haubner, K.; Tarábek, J.; Ziegs, F.; Lukeš, V.; Jaehne, E.; Dunsch, L. Charged States of α,ω-Dicyano β,B′-Dibutylquaterthiophene as Studied by in Situ ESR UV−Vis NIR Spectroelectrochemistry. *J. Phys. Chem. A* **2010**, *114*, 11545–11551.

[17]   Ferrón, C. C.; Capdevila-Cortada, M.; Balster, R.; Hartl, F.; Niu, W.; He, M.; Novoa, J. J.; López Navarrete, J. T.; Hernández, V.; Ruiz Delgado, M. C. Multistep π Dimerization of Tetrakis(n-Decyl)Heptathienoacene Radical Cations: A Combined Experimental and Theoretical Study. *Chem. – A Eur. J.* **2014**, *20*, 10351–10359.

[18]   Dunsch, L.; Rapta, P.; Schulte, N.; Schlüter, A. D. Structural Dependence of Redox-Induced Dimerization as Studied by In Situ ESR/UV/Vis-NIR Spectroelectrochemistry: The Fluoranthenopyracylene Oligomers. *Angew. Chemie Int. Ed.* **2002**, *41*, 2082–2086.

[19]   Wu, Y.; Frasconi, M.; Gardner, D. M.; McGonigal, P. R.; Schneebeli, S. T.; Wasielewski, M. R.; Stoddart, J. F. Electron Delocalization in a Rigid Cofacial Naphthalene-1,8:4,5-Bis(Dicarboximide) Dimer. *Angew. Chemie Int. Ed.* **2014**, *53*, 9476–9481.

[20]   Mani, T.; Grills, D. C. Probing Intermolecular Electron Delocalization in Dimer Radical Anions by Vibrational Spectroscopy. *J. Phys. Chem. B* **2017**, *121*, 7327–7335.

[21]   Brédas, J. L.; Calbert, J. P.; da Silva Filho, D. A.; Cornil, J. Organic Semiconductors: A Theoretical Characterization of the Basic Parameters Governing Charge Transport. *Proc. Natl. Acad. Sci.* **2002**, *99*, 5804 LP – 5809.

[22]   Zhang, C.; Zang, Y.; Gann, E.; McNeill, C. R.; Zhu, X.; Di, C.; Zhu, D. Two-Dimensional π-Expanded Quinoidal Terthiophenes Terminated with Dicyanomethylenes as n-Type Semiconductors for High-Performance Organic Thin-Film Transistors. *J. Am. Chem. Soc.* **2014**, *136*, 16176–16184.

[23]   Yamamoto, K.; Ie, Y.; Nitani, M.; Tohnai, N.; Kakiuchi, F.; Zhang, K.; Pisula, W.; Asadi, K.; Blom, P. W. M.; Aso, Y. Oligothiophene Quinoids Containing a Benzo[c]Thiophene Unit for the Stabilization of the Quinoidal Electronic Structure. *J. Mater. Chem. C* **2018**, *6*, 7493–7500.

[24]   Arrechea-Marcos, I.; de Echegaray, P.; Mancheño, M. J.; Ruiz Delgado, M. C.; Ramos, M. M.; Quintana, J. A.; Villalvilla, J. M.; Díaz-García, M. A.; López Navarrete, J. T.; Ponce Ortiz, R.; Segura, J. L. Molecular Aggregation of Naphthalimide Organic Semiconductors Assisted by Amphiphilic and Lipophilic Interactions: A Joint Theoretical and Experimental Study. *Phys. Chem. Chem. Phys.* **2017**, *19*, 6206–6215.

[25]   Cornil, J.; Beljonne, D.; Calbert, J.-P.; Brédas, J.-L. Interchain Interactions in Organic π-Conjugated Materials: Impact on Electronic Structure, Optical Response, and Charge Transport. *Adv. Mater.* **2001**, *13*, 1053–1067.

[26]   Wang, Y.; Guo, H.; Harbuzaru, A.; Uddin, M. A.; Arrechea-Marcos, I.; Ling, S.; Yu, J.; Tang, Y.; Sun, H.; López Navarrete, J. T.; Ortiz, R. P.; Woo, H. Y.; Guo, X. (Semi)Ladder-Type Bithiophene Imide-Based All-Acceptor Semiconductors: Synthesis, Structure-Property Correlations, and Unipolar n-Type Transistor Performance. *J. Am. Chem. Soc.* **2018**, *140*, 6095–6108.

[27]   Baeg, K.-J.; Kim, J.; Khim, D.; Caironi, M.; Kim, D.-Y.; You, I.-K.; Quinn, J. R.; Facchetti, A.; Noh, Y.-Y. Charge Injection Engineering of Ambipolar   Field-Effect   Transistors   for   High-Performance   Organic

Complementary Circuits. *ACS Appl. Mater. Interfaces* **2011**, *3*, 3205–3214.

[28]   Sung, M. J.; Luzio, A.; Park, W.-T.; Kim, R.; Gann, E.; Maddalena, F.; Pace, G.; Xu, Y.; Natali, D.; de Falco, C.; Dang, L.; McNeill, C. R.; Caironi, M.; Noh, Y.-Y.; Kim, Y.-H. High-Mobility Naphthalene Diimide and Selenophene-Vinylene-Selenophene-Based Conjugated Polymer: N-Channel Organic Field-Effect Transistors and Structure–Property Relationship. *Adv. Funct. Mater.* **2016**, *26*, 4984–4997.

[29]   Brown, P. J.; Sirringhaus, H.; Friend, R. H. Electro-Optical Characterisation of Field Effect Devices With Regioregular Poly-Hexylthiophene Active Layers. *Synth. Met.* **1999**, *101*, 557–560.

[30]   Chen, Z.; Bird, M.; Lemaur, V.; Radtke, G.; Cornil, J.; Heeney, M.; McCulloch, I.; Sirringhaus, H. Origin of the Different Transport Properties of Electron and Hole Polarons in an Ambipolar Polyselenophene-Based Conjugated Polymer. *Phys. Rev. B* **2011**, *84*, 115211.

[31]   Beljonne, D.; Cornil, J.; Sirringhaus, H.; Brown, P. J.; Shkunov, M.; Friend, R. H.; Brédas, J.-L. Optical Signature of Delocalized Polarons in Conjugated Polymers. *Adv. Funct. Mater.* **2001**, *11*, 229–234.

[32]   Deng, Y. Y.; Sirringhaus, H. Optical Absorptions of Polyfluorene Transistors. *Phys. Rev. B* **2005**, *72*, 45207.

[33]   Itoh, E.; Terashima, K.; Nagai, H.; Miyairi, K. Evaluation of Poly(3-Hexylthiophene)/Polymeric Insulator Interface by Charge Modulation Spectroscopy Technique. *Thin Solid Films* **2009**, *518*, 810–813.

[34]   Ziemelis, K. E.; Hussain, A. T.; Bradley, D. D. C.; Friend, R. H.; Rühe, J.; Wegner, G. Optical Spectroscopy of Field-Induced Charge in Poly(3-Hexyl Thienylene) Metal-Insulator-Semiconductor Structures: Evidence for Polarons. *Phys. Rev. Lett.* **1991**, *66*, 2231–2234.

[35]   Sirringhaus, H. Device Physics of Solution-Processed Organic Field-Effect Transistors. *Adv. Mater.* **2005**, *17*, 2411–2425.

[36]   Khatib, O.; Mueller, A. S.; Stinson, H. T.; Yuen, J. D.; Heeger, A. J.; Basov, D. N. Electron and Hole Polaron Accumulation in Low-Bandgap Ambipolar Donor-Acceptor Polymer Transistors Imaged by Infrared Microscopy. *Phys. Rev. B* **2014**, *90*, 235307.

[37]   Harrison, M. G.; Friend, R. H.; Garnier, F.; Yassar, A. A Study of the Charged Excitations in Thin Films of α-Sexithiophene by Voltage-Modulation Spectroscopy and Photoimpedance Measurements. *Mol. Cryst. Liq. Cryst. Sci. Technol. Sect. A. Mol. Cryst. Liq. Cryst.* **1994**, *252*,

165–174.

[38]   Sirringhaus, H.; Brown, P. J.; Friend, R. H.; Nielsen, M. M.; Bechgaard, K.; Langeveld-Voss, B. M. W.; Spiering, A. J. H.; Janssen, R. A. J.; Meijer, E. W.; Herwig, P.; de Leeuw, D. M. Two-Dimensional Charge Transport in Self-Organized, High-Mobility Conjugated Polymers. *Nature* **1999**, *401*, 685–688.

[39]   Sakanoue, T.; Sirringhaus, H. Band-like Temperature Dependence of Mobility in a Solution-Processed Organic Semiconductor. *Nat. Mater.* **2010**, *9*, 736–740.

[40]   Zhao, N.; Noh, Y.-Y.; Chang, J.-F.; Heeney, M.; McCulloch, I.; Sirringhaus, H. Polaron Localization at Interfaces in High-Mobility Microcrystalline Conjugated Polymers. *Adv. Mater.* **2009**, *21*, 3759–3763.

[41]   Caironi, M.; Bird, M.; Fazzi, D.; Chen, Z.; Di Pietro, R.; Newman, C.; Facchetti, A.; Sirringhaus, H. Very Low Degree of Energetic Disorder as the Origin of High Mobility in an N-Channel Polymer Semiconductor. *Adv. Funct. Mater.* **2011**, *21*, 3371–3381.

[42]   Brown, P. J.; Sirringhaus, H.; Harrison, M.; Shkunov, M.; Friend, R. H. Optical Spectroscopy of Field-Induced Charge in Self-Organized High Mobility Poly(3-Hexylthiophene). *Phys. Rev. B* **2001**, *63*, 125204.

[43]   Fazzi, D.; Caironi, M. Multi-Length-Scale Relationships between the Polymer Molecular Structure and Charge Transport: The Case of Poly-Naphthalene Diimide Bithiophene. *Phys. Chem. Chem. Phys.* **2015**, *17*, 8573–8590.

[44]   Luzio, A.; Criante, L.; D'Innocenzo, V.; Caironi, M. Control of Charge Transport in a Semiconducting Copolymer by Solvent-Induced Long-Range Order. *Sci. Rep.* **2013**, *3*, 3425.

[45]   Harrison, M. G.; Friend, R. H.; Garnier, F.; Yassar, A. The Charged Excitations in Thin Films of α-Sexithiophene within Semi-Transparent Field-Effect Devices: Investigation by Optical Spectroscopy of Field-Induced Charge and by Photoimpedance Spectroscopy. *Synth. Met.* **1994**, *67*, 215–221.

Chapter 2. Fused quinoidal oligothienoimides with high electrical conductivity

Contents:

2.1. Introduction

Organic diradicaloids based on quinoidal oligothiophenes derivatives (QOTs) are promising semiconductor components in organic electronics such as n-channel organic field effect transistors (OFETs)[1–9] and organic thermoelectrics (OTEs)[10].

Quinoidal oligothiophenes with relatively small HOMO-LUMO gaps lead to extremely high chemical reactivities, since the electrons can be easily promoted from the HOMO to the LUMO energy levels[11]. As a consequence, the quinoidal systems are provided with diradical character which increases as the energy gap decreases[12,13]. Thus, the electronic structure in the ground state can be represented by a resonance between the singlet closed-shell (CS) quinoidal structure and the open-shell singlet (OSS) diradical in thermal equilibrium with a low-energy triplet state (OST), as shown in the example given in Scheme 2.1, which provide these quinoidal systems of unique optoelectronic and magnetic properties[12,14–17].

Closed Shell Singlet (CS)   **Open Shell Singlet (OSS)**   **Open Shell Triplet (OST)**
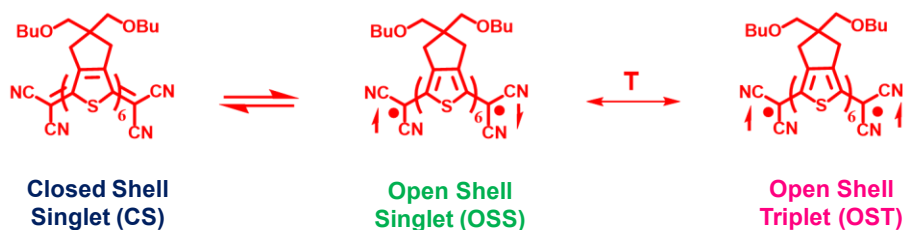
Scheme 2.1. Quinoidal closed-shell (CS) and biradical (OSS) resonant structures proposed for the singlet ground state of quinoidal systems (Qn) in equilibrium with the triplet (OST) species[12].

Despite their intrinsic poor stability, which needs to be properly addressed, the presence of unpaired electrons in open-shell diradical

molecules enable them the capability of delivering high electrical conductivity without chemical doping[10]. Thus, the conductive materials based on undoped diradicaloids (or so-called self-doped semiconductors) can eliminate the drawbacks of the traditional chemical doping approach, such as low doping efficiency, heavily reliance on the processing conditions, and deteriorated material or device stabilities, which provide a promising alternative path to achieve more advanced organic conducting materials[18].

In organic diradicaloids the presence of two unpaired electrons in the open-shell diradical form may induce a more efficient intrachain-like transport with doubled intermolecular spin-spin interactions[19]. The intermolecular electron transfer between the open-shell (diradical canonical form) and the closed-shell (quinoidal form) structures could give rise to a self-doped characteristic with the generation of free charge carriers which leads to high electrical conductivity without doping[20].

In this chapter and inspired by previous excellent performances of quinoidal systems, two organic diradicaloids based on fused quinoidal bithiophene imide systems (BTICN and QTICN) and their aromatic counterparts (BTI and QTI) will be studied (Figure 2.1).

These quinoidal systems with increasing chain length from 3 to 5 fused rings *per* building block, end-caped with strongly electron-withdrawing dicyanomethylene groups, hold great promise in the pursuit of dopant-free materials for n-type electronic devices with high electron transport capability and superior ambient stability.
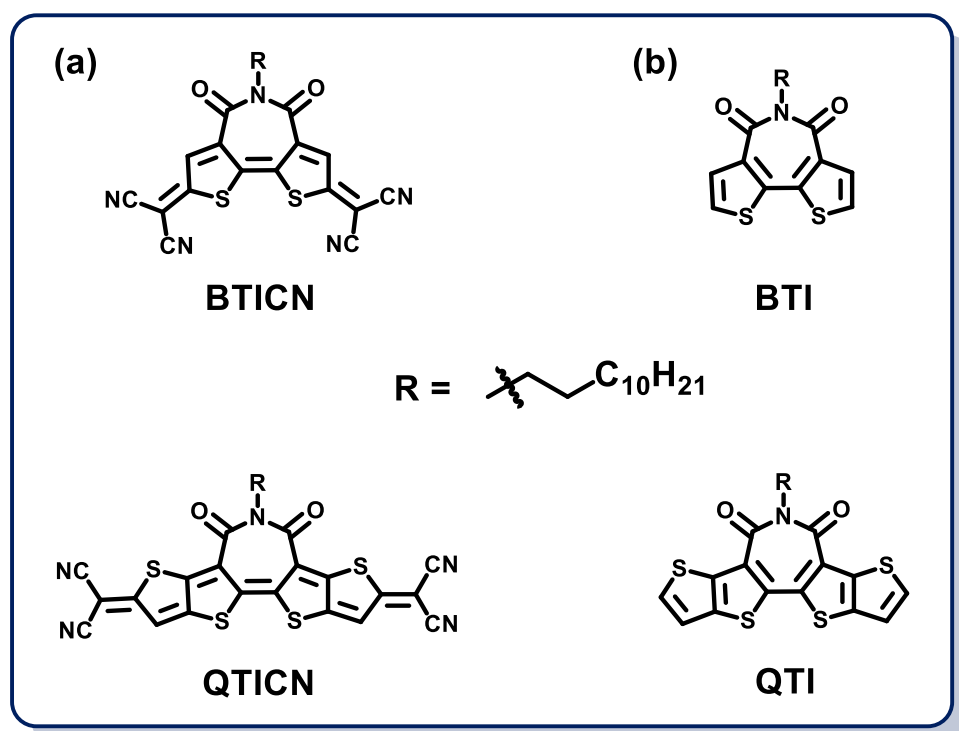
Figure 2.1. Chemical structures of (a) quinoidal systems BTICN and QTICN and (b) aromatic counterparts BTI and QTI.

In this chapter, a combined experimental/theoretical approach is used, which links UV-Vis absorption, cyclic voltammetry (CV), *in situ* spectroelectrochemistry, resonant and non-resonant Raman Spectroscopy with DFT and TD-DFT calculations. In addition, the electrical properties of these fused systems in OFETs have been examined using vapor-deposited films, which were then characterized by XPS and 2D-GIWAXS techniques.

2.2. Experimental and theoretical study of neutral species

2.2.1. DFT-optimized molecular geometries

The optimized geometries of BTICN and QTICN, optimized at the B3LYP/6-31G** level, are shown in Figure 2.2.
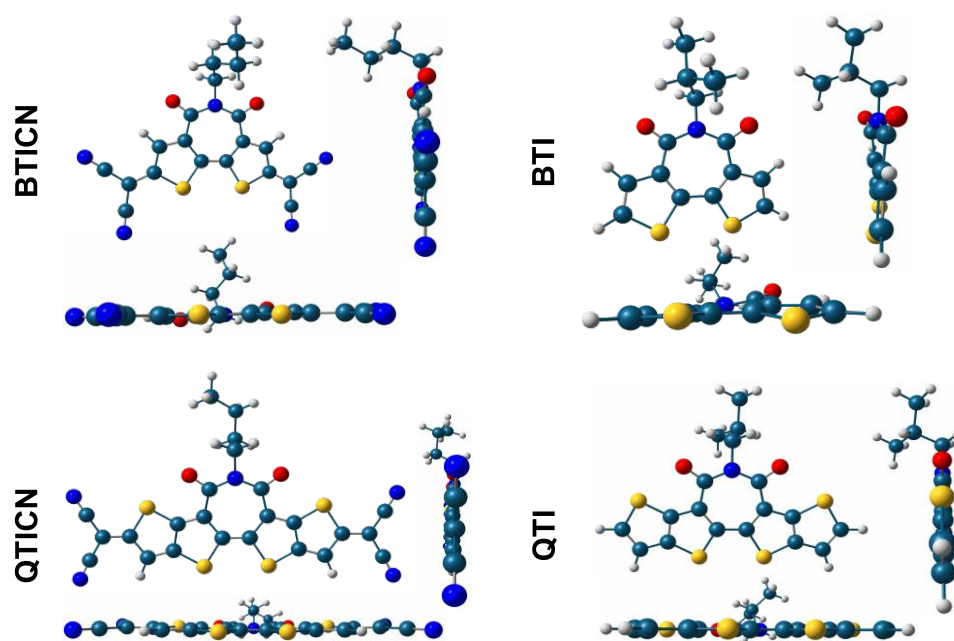
Figure 2.2. Frontal and lateral views of DFT-optimized of BTICN and QTICN systems and their aromatic counterparts BTI and QTI at B3LYP/6-31G** level. The long alkyl chains have been replaced by butyl or isopropyl groups to simplify calculations and reduce the computational costs and resources.

The optimized minimum energy geometries, shown in Figure 2.2, present totally planar skeletons for BTICN and QTICN, that is also the case for the aromatic counterparts. The fact that these π-conjugated

systems are rigid (there is no freedom of rotation) allows efficient stacking between molecules.

Figure 2.3 shows the frontier molecular orbital profiles of BTICN and QTICN, together with their aromatic counterparts, BTI and QTI.
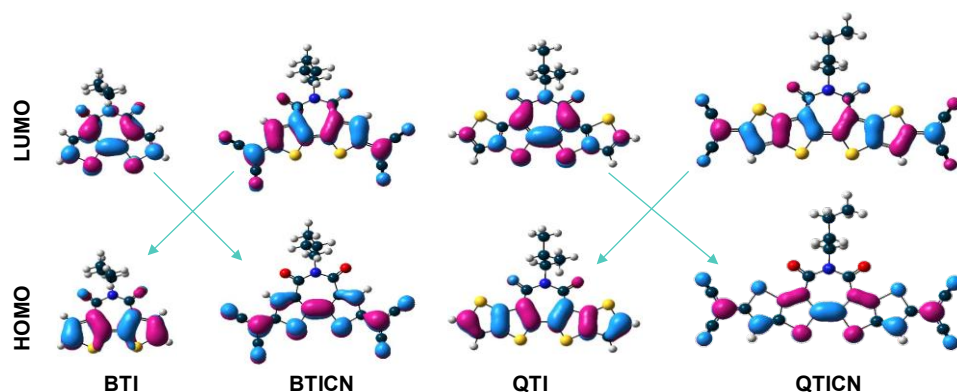
Figure 2.3. DFT-calculated frontier molecular orbital topologies of BTICN and QTICN and their aromatic counterparts BTI and QTI at B3LYP/6-31G** level.

In both quinoidal and aromatic systems, the HOMO and LUMO orbitals are of π-nature and spread over the whole conjugated path with large contributions on the dicyanomethylene groups in the quinoidal systems. These topologies are reversed with respect to those computed for their aromatic counterparts as a result of the quinoid structures of BTICN and QTICN.

2.2.2. Optical properties and TD-DFT vertical transition energies

The optical properties of the fused quinoidal BTICN and QTICN, as well as their aromatic counterparts were investigated by measuring their UV-Vis/NIR absorption spectra in both solution (Figure 2.4) and film state (Figure 2.5).
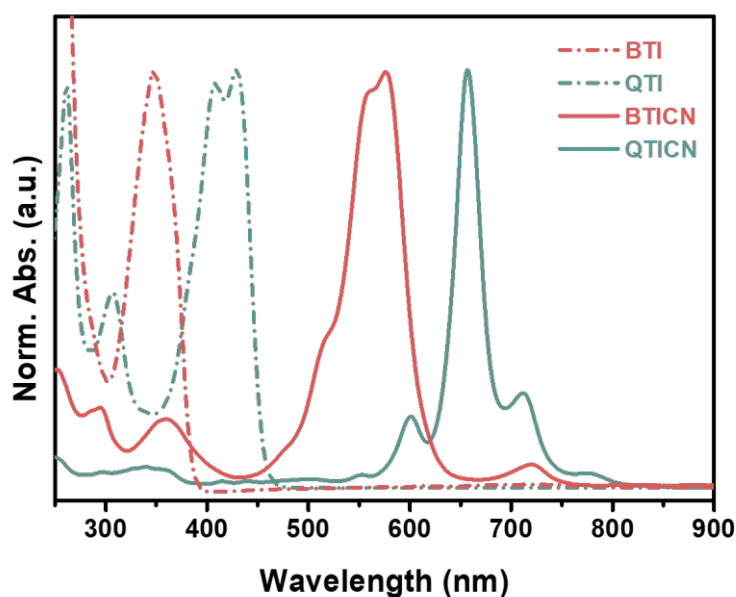
Figure 2.4. UV-Vis/NIR absorption spectra of quinoidal systems BTICN and QTICN and their aromatic counterparts BTI and QTI recorded in dichloromethane solutions at 298 K.

Both quinoidal systems show red-shifted absorptions in comparison to their aromatic counterparts, which is in line with the small HOMO-LUMO energy gap of these quinoidal systems. In both aromatic and quinoidal systems, the maximum absorption peak (λ_{max}) is bathochromically shifted as the chain length increases, from 234 (BTI) to

400 nm (QTI), and from 587 (BTICN) to 668 nm (QTICN), which is in line with the expected larger π-conjugation extension in the systems with higher number of thiophene rings, QTI and QTICN.

These experimental results are supported by TD-DFT theoretical calculations at the ωB97XD/6-31G** level by considering the closed-shell quinoidal optimized structures (Figure 2.5). Both experimental and theoretical data are summarized in Table 2.1. ωB97XD was used in this case, since predicts more accurate vertical transition energies.
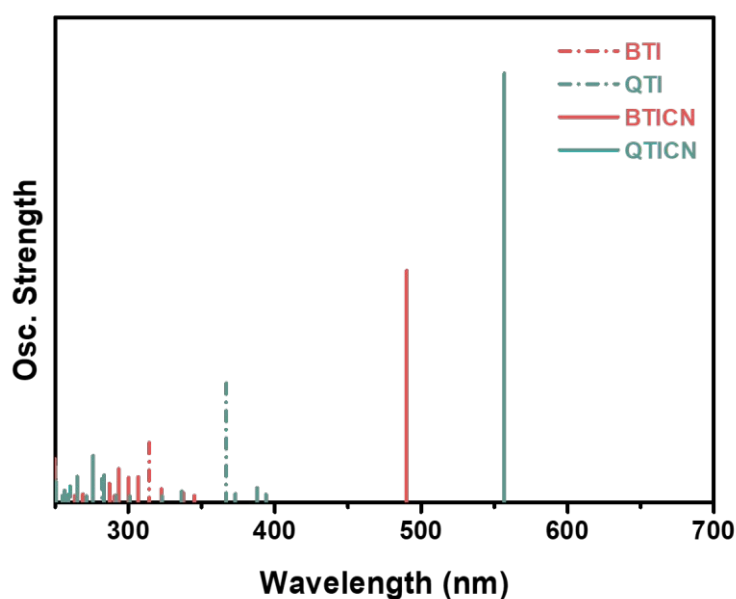
Figure 2.5. TD-DFT calculated vertical transition energies for the closed-shell BTICN and QTICN systems and the aromatic counterparts BTI and QTI, at the ωB97XD/6-31G** level.

As can be seen in Figure 2.5 and Table 2.1, TD-DFT calculated vertical transition energies for neutral BTI, QTI, BTICN and QTICN are in good agreement with the experimental data, predicting the existence of

one intense transition that is redshifted on going from BTI and QTI to BTICN and QTICN, as found experimentally. This transition implies the promotion of one electron from the HOMO to the LUMO orbitals (see OMs topologies in Figure 2.3).

Table 2.1. Photophysical properties of the fused oligothiophene imides and TD-DFT calculations at ωB97XD/6-31G** level.

Experimental data				
	λ_{abs}^{max} CH$_2$Cl$_2$ (nm)[a]	λ_{abs}^{max} film (nm)[b]	λ_{onset} film (nm)[b]	E_g^{opt} (eV)[c]
BTICN	587	616	697	1.78
QTICN	668	747	940	1.32
BTI	347	-	-	-
QTI	430	-	-	-
Theoretical data				
	λ (nm)	f	Description	
BTICN	490	1.08	HOMO → LUMO (98%)	
QTICN	557	2.03	HOMO → LUMO (98%)	
BTI	311	0.26	HOMO → LUMO (96%)	
QTI	367	0.54	HOMO → LUMO (95%)	
[a]From diluted solutions at room temperature. [b]From as-cast films. [c]Optical band gap estimated from the absorption edge of the as-cast thin films and calculated based on the equation: $E_g^{opt}=1240/\lambda_{onset\ of\ film}$.				

The behavior of the BTICN and QTICN systems in the solid state was also studied by UV-Vis spectroscopy and shown below, together with the absorption spectra obtained in solution (previously shown in Figure 2.4), for a comparative purpose (Figure 2.6).
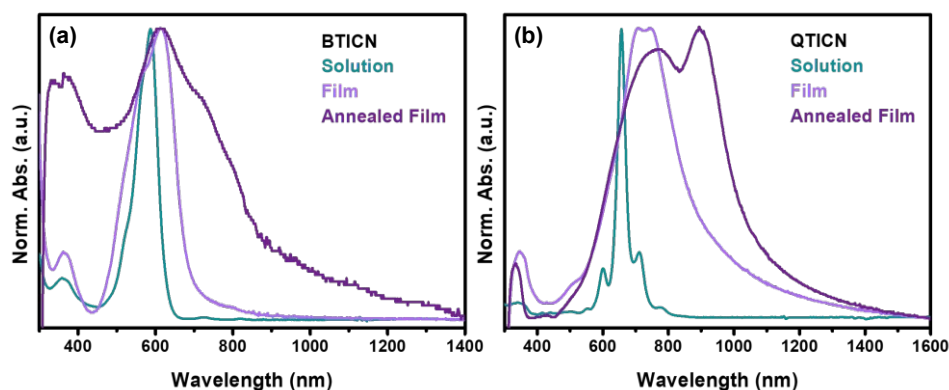
Figure 2.6. UV-vis absorption spectra of quinoidal systems (a) BTICN and (b) QTICN in dichloromethane solutions at 298 K, and as thin films, before and after the annealing treatment.

Compared to the solution spectra, red-shifted maximum absorptions (λ_{max}) were observed for the quinoidal systems, BTICN and QTICN as thin films; particularly, QTICN shows an absorption edge near 1000 nm. The larger, red-shifted absorption maximum of QTICN as thin film (>220 nm, Figure 2.6(b)) compared to BTICN thin film indicates a more effective π-conjugation in QTICN. In addition, the presence of a well-structured shoulder in QTICN annealed thin film is attributed to intermolecular electronic interactions of π-π stacked backbones, which are beneficial for achieving more efficient charge transport in thin-film devices.[15,21,22]

The optical HOMO-LUMO energy gaps (E_g^{opt} in Table 2.1) of these compounds were estimated from the onsets of the absorption spectra and were found to be 1.78 and 1.32 eV for BTICN and QTICN, respectively.

2.2.3. Evaluation of the diradical character

In this section, the structure-diradical character relationship of the fused quinoidal thiophene imide is evaluated in the framework of the DFT method. As a theoretical model, we used the terthiophene imide framework (TTICN in Scheme 2.2) in order to have a symmetrically study of the increase of the diradical character upon increasing the conjugated skeleton length (Scheme 2.2). The theoretical results are summarized in Figure 2.7.

As mentioned in Section 2.1, it is well known that quinoidal systems with small HOMO-LUMO gaps are characterized by resonance between the closed-shell (CS) quinoidal structure and the open-shell (OSS) pseudo-aromatic diradical form in their electronic ground state (Scheme 2.2). The relative weight of these two forms would determine the diradical contribution to the electronic ground state. A thermal equilibrium between the open-shell singlet and a low-lying triplet state (OST) must be considered in order to explain the magnetic properties of these quinoidal systems (see Section 2.4).
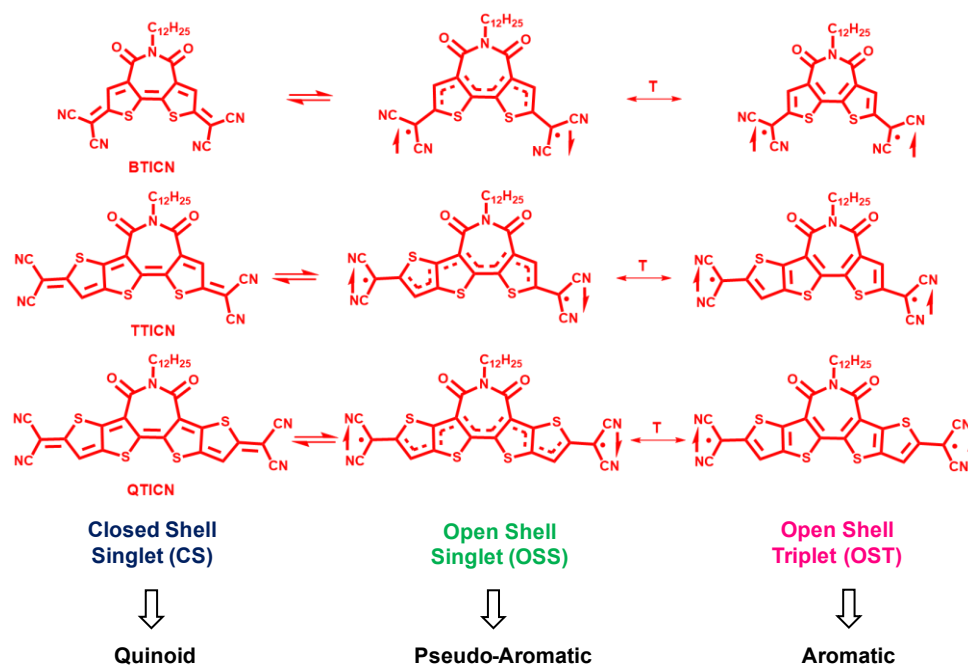
Scheme 2.2. Quinoidal closed-shell (CS) and diradical open-shell (OSS) resonant structures proposed for the singlet ground state of BTICN, TTICN and QTICN in equilibrium with their triplet (OST) species.

Therefore, the parameters to analyze in this section will be i) the energy differences between the resonant structures in the ground state (Figure 2.7(a)), ii) the singlet-triplet energy gap (ΔE_{ST}, Figure 2.7(c)), iii) the HOMO-LUMO gap (Figure 2.7(b)) and iv) the diradical character (y_0) (Figure 2.7(d)).
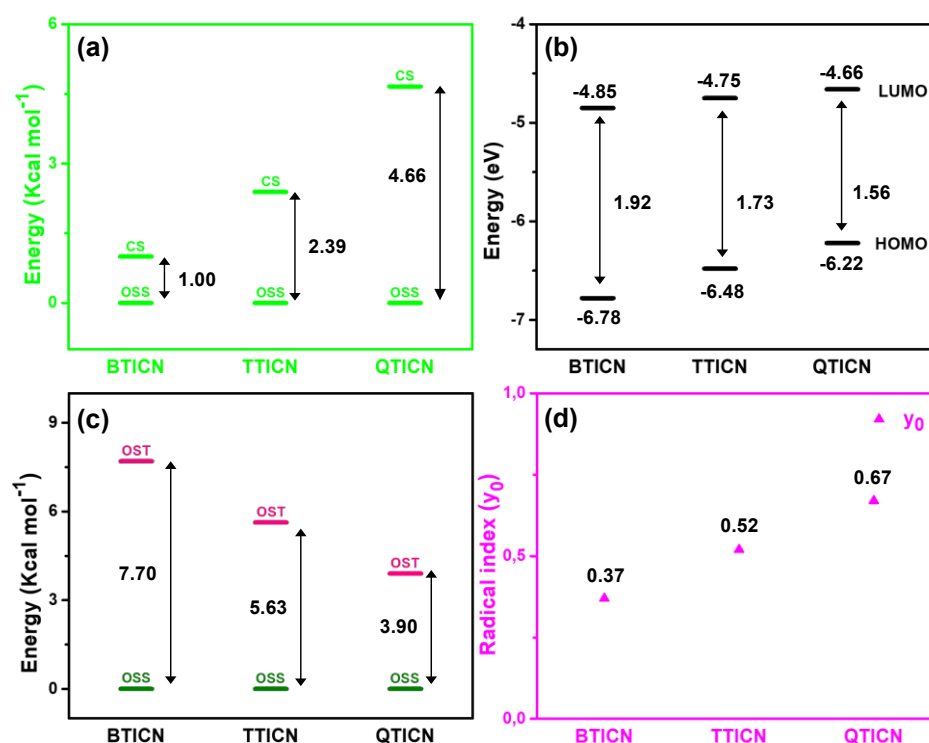
Figure 2.7. Theoretical calculations at the ωB97XD/6-31G** level of a) energy differences between the singlet open shell (OSS) and the quinoidal closed-shell (CS) resonance structures b) HOMO-LUMO gap (B3LYP/6-31G**), c) energy differences between the triplet (OST) and open-shell singlet (OSS) states, d) diradical character values (y_0) for BTICN, TTICN and QTICN.

As shown in Figure 2.7(a), the theoretical calculations predict that, in all these fused quinoidal systems the open-shell singlet state (UωB97XD broken-symmetry) is more stable than the closed-shell singlet state (ωB97XD) in 1, ~2 or ~4 Kcal/mol for BTICN, TTICN and QTICN, respectively. This progressive stabilization of the open-shell diradical form is explained by the decrease of the HOMO-LUMO[11,23] energy gap with the chain lengthening (Figure 2.7(b)). It is well known that the smaller the HOMO-LUMO gap, the easier the promotion of one electron from the

HOMO to the LUMO energy level[11]. The theoretical band gap decreases ongoing from BTICN to QTICN, showing the same trend found experimentally (see Table 2.4).

On the other hand, and as seen in most Kekulé diradicals[24,25], the open-shell singlet state is also more stable than the triplet state (Figure 2.7(c)); therefore, the ground electronic state of these quinoidal systems is characterized by an open-shell singlet geometry[25] (Scheme 2.2). The calculated singlet-triplet energy gap ΔE_{ST} values are decreasing from 7.70 to 5.8 and to 3.90 kcal/mol on going from BTICN to TTICN and QTICN, which is understood considering the decreasing HOMO-LUMO gap values in the same direction.

The fact that the open-shell singlet state is stabilized over the triplet state does not follow the Hund's rules[26,27] which tell us that high spin states (triplet over singlet states) are always preferred. However, in SOMO orbitals with disjoint nature[28–30] (Figure 2.8), the unpaired electrons can be confined to different sets of atoms (with parallel or antiparallel configurations) to minimize the Coulombic energy coming from electrons with opposite spin (Pauli-allowed[31]). This can be explained by the dynamic spin polarization (DSP) mechanism[32,33] which selectively stabilizes the singlet over the triplet state and give rise to singlet diradicals[12,24,25,30,34–36].

SOMO-α   **SOMO-β**
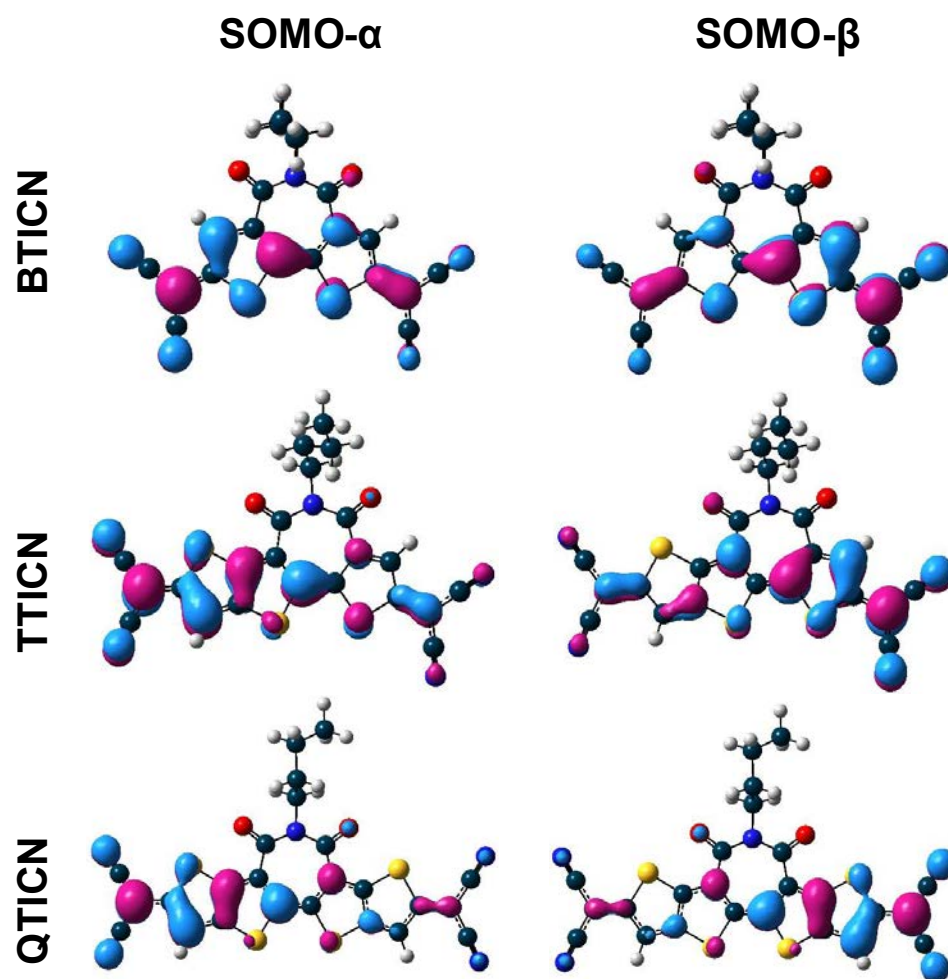
BTICN

TTICN

QTICN

Figure 2.8. DFT-calculated singly occupied molecular orbital (SOMO) topologies of BTICN, TTICN and QTICN at ωB97XD/6-31G** level.

As can be seen in Figure 2.8, the SOMO orbitals in the largest quinoidal system (QTICN) show a typical disjoint feature, with the spin density evenly distributed along the whole π-conjugated framework, however in BTICN quinoidal system, the disjoint character is less pronounced, which might be due to its smaller conjugated backbone size. A quinoidal molecule can be classified as a singlet disjoint diradical when

the electron density is separated on two halves of the molecule with almost no overlap between them (weak radical-radical coupling). Therefore, the unpaired electrons reside on different parts of the molecule, one part is more quinoidal and the other one, more aromatic[12,24,37]. As the SOMO-α and SOMO-β orbital segregation is getting larger, the diradical character increases, which explains the larger diradical character in QTICN (Figure 2.7(d)).

The quinoidal systems with open-shell singlet electronic ground state, are provided with diradical character which increases as the HOMO-LUMO energy gap decreases. This parameter can be theoretically described by the occupation number of the spin-unrestricted lowest unoccupied natural orbital (LUNO[11,36]) and can adopt values between 0 and 1, where y_0=0 represents a closed-shell quinoidal state and y_0=1 represents a pure diradical state. These data are summarized in Figure 2.7(d) and Table 2.2, showing that the elongation of the π-conjugated quinoidal backbone with additional thiophene units leads to a larger diradical character (y_0) up to 0.67 for QTICN.

Nevertheless, the spin-unrestricted method can suffer from spin contamination where high spin states such as triplet states are mixed in the singlet wavefunction. In such case, improved diradical character can be evaluated by employing a spin-projection correction[38] (Equation II.7), where T_i is defined as the orbital overlap and is calculated using the occupation number (n) of the UωB97XD natural orbitals (Equation II.8). The results are summarized in Table 2.2. The diradical character calculated using the spin projected correction (y_i) gives smaller values when compared to y_0, but a similar trend is found with y_i values upon elongation of the π-conjugated core.

Table 2.2. DFT-calculated singlet diradical character values (y_0, y_i) for BTICN, TTICN and QTICN systems at UωB97XD/6-31G** level of theory.

Molecules	Open-shell singlet state (S_0) - UωB97XD/6-31G**	
	Singlet diradical character	
	y_0 (n_{LUNO})	y_i
BTICN	0.37	0.10
TTICN	0.52	0.22
QTICN	0.67	0.40

The spin density distributions for the singlet diradicals of BTICN, TTICN and QTICN (Figure 2.9) were also calculated and show that the spins are uniformly delocalized through the whole π-conjugated backbone with the density on the carbon atoms linked to the CN groups larger in QTICN when compared to BTICN (0.46 vs 0.39, respectively). This is explained by the increased diradical character predicted for QTICN when compared to BTICN (0.67 *vs* 0.37, respectively, Figure 2.7(d)).
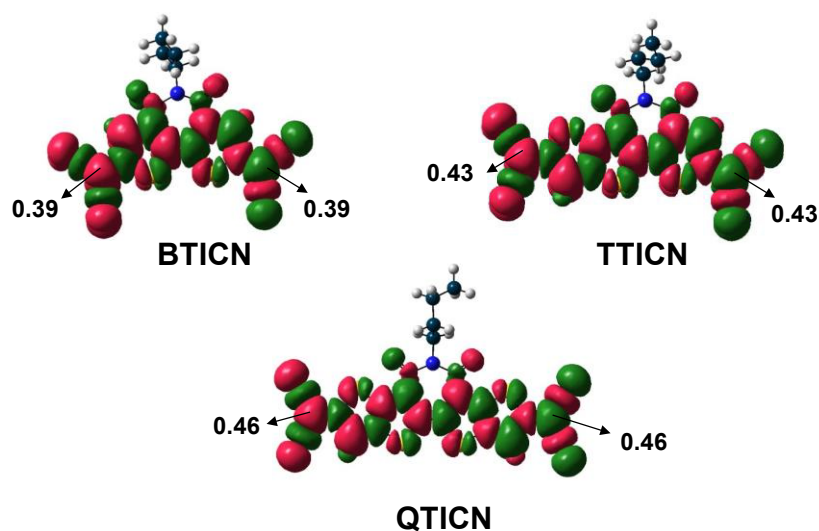

Figure 2.9. DFT-calculated spin density distribution of BTICN, TTICN and QTICN at ωB97XD/6-31G** level. The values shown represent the largest density in the carbon atoms linked to the CN groups.

2.2.4. Diradical stability: half-life time values

Figure 2.10 shows the monitorization of the UV-Vis/NIR absorption spectra of the quinoidal oligothiophene imide solutions (10^{-5} M in CH_2Cl_2) with exposition to ambient air and light.
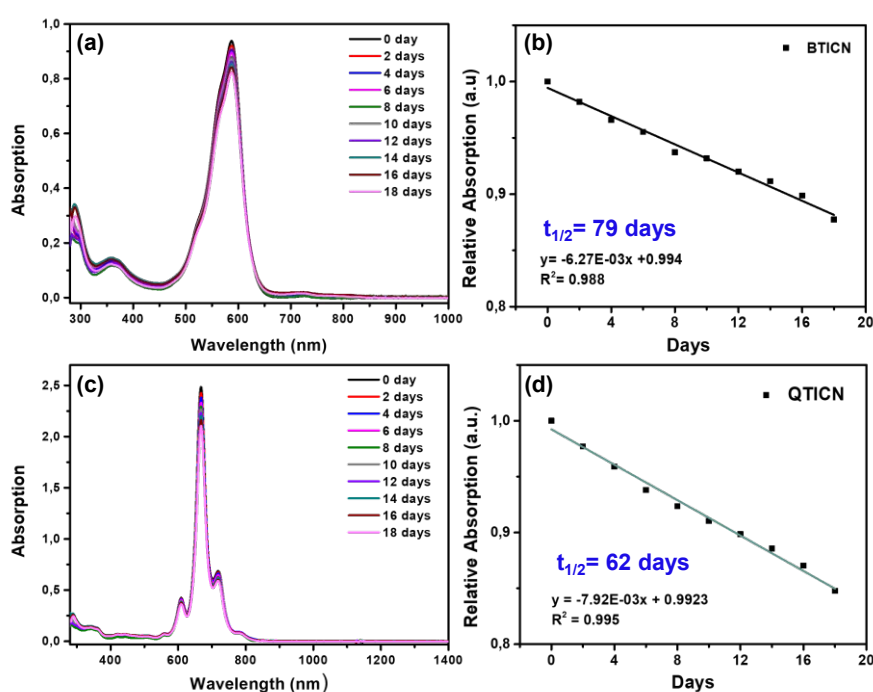
Figure 2.10. Absorption spectra of a) BTICN and c) QTICN in CH_2Cl_2 recorded during 18 days when exposed to ambient air and light. b) and d) Linear regression of the maximum absorption wavelength and extrapolation to % change = 0.50 giving a half-life of 79 days for BTICN and 62 days for QTICN.

The half-lives of the two diradicals molecules were estimated to be 79 and 62 days for BTICN (Figure 2.10(a-b)) and QTICN (Figure 2.10(c-d)), respectively. The much-improved stability of BTICN and QTICN under ambient conditions clearly implies the great advantage of using fused-ring quinoidal frameworks in constructing highly stable diradicaloid-based

materials, especially when considering their similar LUMO energy levels and comparable diradical characters.

2.3. Experimental and theoretical study of charged species in solution

2.3.1. Cyclic voltammetry

Figure 2.11 shows the CV spectra registered for BTICN and QTICN in dichloromethane solution at room temperature using 0.1 M (*n*-Bu)$_4$NPF$_6$ as supporting electrolyte at a scan rate of 100 mVs^{-1}. Potentials were recorded *versus* Fc/Fc$^+$. The electrochemical and the theoretical results are summarized in Table 2.4.
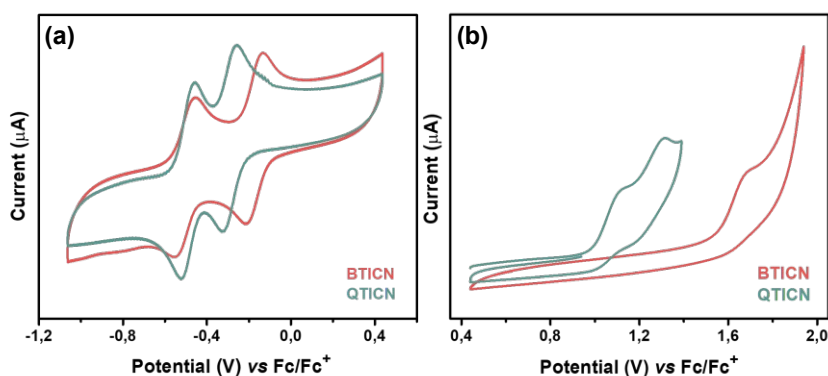
Figure 2.11. Cyclic voltammograms of BTICN and QTICN registered in CH$_2$Cl$_2$ solutions in presence of 0.1 M of (*n*-Bu)$_4$NPF$_4$ supporting electrolyte, in order to characterize the electrochemical a) reduction and b) oxidation processes.

Figure 2.11(a) shows two reversible reduction waves for both BTICN and QTICN quinoidal systems at low potentials of -0.1/-0.44 and -0.22/0.42 V, respectively. These two cathodic processes correspond to

the consecutive formation of the radical anion and dianion, respectively. The low reduction potentials suggest that the reduced species can be readily obtained through stepwise reduction processes, revealing the strong electron-accepting characteristics of these quinoidal oligothiophene imides. Based on the first reduction peaks, the LUMO energy levels of BTICN and QTICN were calculated to be -4.69 and -4.58 eV, which are very deep values and, therefore, should facilitate electron injection and promote n-type transport as well as ambient stability in these fused quinoidal oligothiophenes imides.

Figure 2.11(b) shows a non-reversible and a quasi-reversible oxidation wave for BTICN and QTICN, respectively. Based on the oxidation peaks the HOMO energy levels were extracted to be -6.34 and -5.78 eV, which lead to electrochemical bandgaps of 1.64 and 1.20 eV for BTICN and QTICN, respectively, in good agreement with their optical band gaps.

By comparing the molecular orbital energy values of the shortest and the largest quinoidal systems, BTICN shows both lower-lying HOMO and LUMO energy levels than QTICN as also revealed by DFT-calculations (see Figure 2.7(b) and Table 2.4). This is attributed to the less electron-rich characteristics of the thiophene-based framework in BTICN.

Table 2.4. Electrochemical redox properties of BTICN and QTICN systems, extracted from the data shown in Figure 2.11.

Molecules	Experimental data[a]					
	$E_{ox}^{1/2}$ (eV)	$E_{redI}^{1/2}$ (eV)	$E_{redII}^{1/2}$ (eV)	E_{LUMO} (eV)[a]	E_{HOMO} (eV)[b]	E_g^{EC} (eV)[c]
BTICN	1.54	-0.10	-0.44	-4.70	-6.34	1.64
QTICN	0.98	-0.22	-0.42	-4.58	-5.78	1.20
[a]Electrochemically determined vs Fc/Fc$^+$. [a]E_{LUMO} = - ($E_{redI}^{1/2}$ + 4.80), [b]E_{HOMO} = -($E_{ox}^{1/2}$ + 4.80), [c]E_g^{EC}=E_{LUMO}-E_{HOMO}						

2.3.2. Intramolecular reorganization energy calculations

The intramolecular reorganization energy (λ) is one of the parameters controlling charge-transport, and essentially reflects the geometrical changes needed to accommodate a positive ($λ_h$) or a negative ($λ_e$) charge. Thus, the reorganization energy is strongly dependent on the molecular structure of the organic semiconductor, both in the neutral and charged states, and in order to achieve an effective charge transport, these λ values need to be small. In general, more planar and rigid backbones give rise to lower λ values since the molecular geometry undergoes less changes on going from the charged to the neutral state[39]. The internal reorganization energies values for the quinoidal systems, calculated at the ωB97XD/6-31G** level, are collected in Table 2.5.

Table 2.5. DFT-calculated intramolecular reorganization energies for holes ($λ_h$) and electrons ($λ_e$) at ωB97XD/6-31G** level.

| Molecules	λ (meV)	
	Electron transport ($λ_e$)	Hole transport ($λ_h$)
BTICN	290	130
TTICN	280	120
QTICN	260	110

The λ values, shown in Table 2.5, decrease upon increasing the building block unit length. Ongoing from BTICN to QTICN, the λ_e shows a progressive reduction, which is reasonable, considering that charge delocalization is easier in systems with a larger number of alternated C-C/C=C bonds.

2.3.3. Spectroelectrochemistry and TD-DFT vertical transition energies

Figures 2.12 and 2.13 show the evolution of the UV-Vis/NIR spectra obtained by i) reductive titration analysis using tetrabutylammonium borohydride ((n-Bu)$_4$NBH$_4$) as reducing agent and ii) progressive spectroelectrochemical reduction of BTICN and QTICN in dichloromethane solutions at room temperature, in presence of high excess of (n-Bu)$_4$NPF$_6$ supporting electrolyte.

Both chemical (Figure 2.12) and electrochemical (Figure 2.13) reduction of the neutral BTICN and QTICN leads to the progressively disappearance of the original absorption bands (574 nm for BTICN and 657 nm for QTICN) followed by the growth of new features at higher wavelengths which corresponds to the radical anion absorption peaks (719 nm and 1271 nm for BTICN; 836 and 1333 nm for QTICN) through the formation of clear isosbestic points. Further chemical and electrochemical reductions lead to the progressively disappearance of the radical anion bands while a new distinct absorption peak grows at a shorter wavelength near 600 nm, which corresponds to the typical absorption evolvement from radical anion to the dianion species.
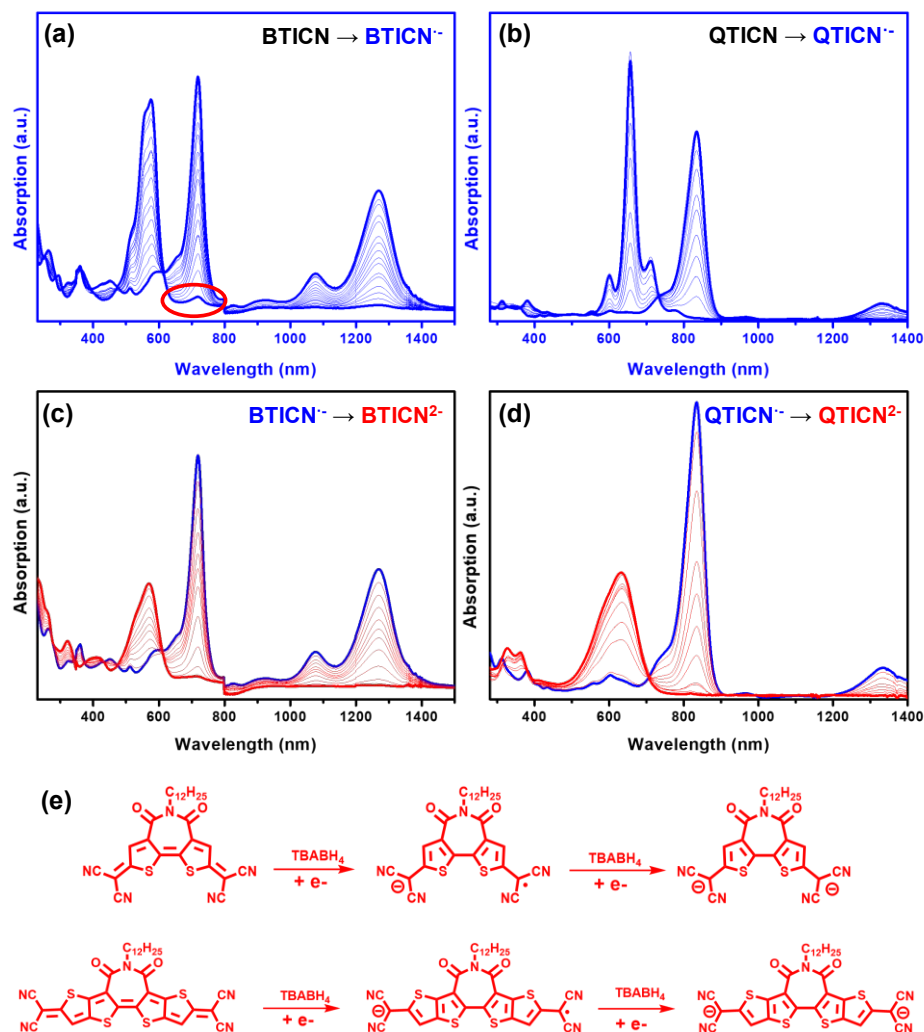
Figure 2.12. UV-Vis/NIR absorption spectra changes of BTICN and QTICN recorded upon reductive titration with ((n-Bu)$_4$NBH$_4$) as reducing agent in degassed anhydrous CH$_2$Cl$_2$ solution at room temperature, in presence of (n-Bu)$_4$NPF$_6$ supporting electrolyte. a) and b) represent the progressive reduction from the neutral to the anion species of BTICN and QTICN respectively and c) and d) represent the progressive reduction from the anion to the dianion species of BTICN and QTICN, respectively, (e) Scheme of the reductive titration of BTICN and QTICN using ((n-Bu)$_4$NBH$_4$).
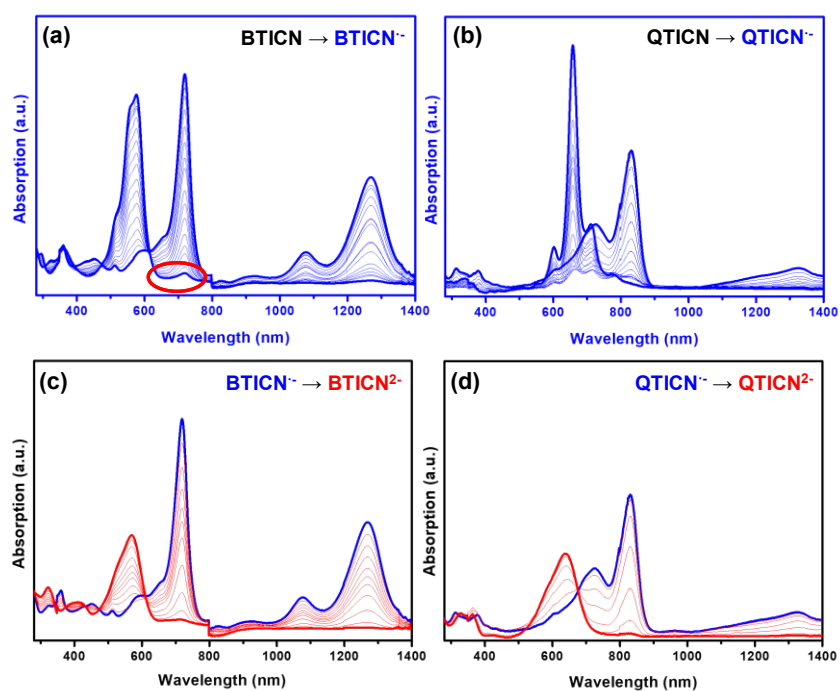
Figure 2.13. UV-Vis/NIR spectra changes of BTICN and QTICN recorded upon electrochemical reduction in CH_2Cl_2 solution at room temperature, in presence of (n-Bu)$_4$NPF$_6$ supporting electrolyte. a) and b) represent the progressive reduction from the neutral to the anion species of BTICN and QTICN respectively and c) and d) represent the progressive reduction from the anion to the dianion species of BTICN and QTICN, respectively.

Note however, that a strikingly absorption (circled in red) bump was observed at 720 nm for the BTICN solution (Figure 2.12 and 2.13) before any (*n*-Bu)$_4$NBH$_4$) was introduced or any potential was applied, which can be attributed to the radical anion. This indicates that a doping process occurs during the solution preparation of BTICN, since this is carried out in air. Such absorption bump was not observed in the case of QTICN solution, suggesting that the stability of the largest quinoidal

system in ambiental conditions is better than that of the shortest one. This is likely due to the reduced electron deficiency of QTICN molecules.

These experimental results are supported by TD-DFT theoretical calculations at the ωB97XD/6-31G** level (Figure 2.14). TD-DFT calculations been performed for BTICN and QTICN, both in neutral and in reduced states, and the obtained data support the sequential reduction of BTICN and QTICN from neutral to radical anion and from radical anion to dianion species, with stepwise addition of 1 and 2 equivalents of (*n*-Bu)$_4$NBH$_4$, respectively, or by applying progressively negative potentials. Both experimental and theoretical data are summarized in Table 2.6.
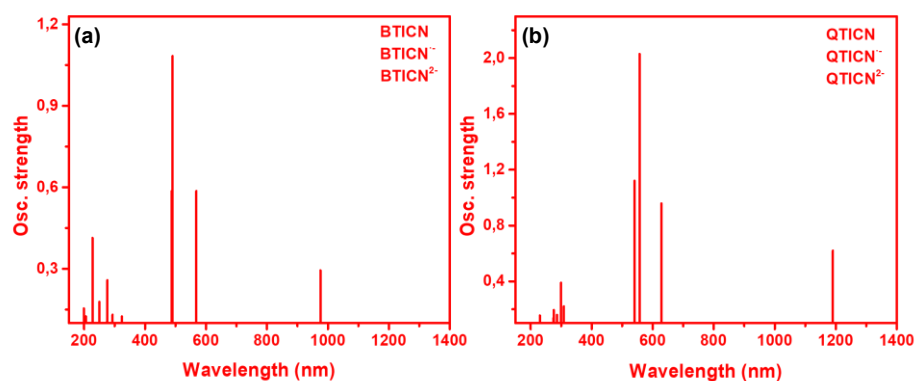
Figure 2.14. TD-DFT calculated vertical transition energies for (a) BTICN and (b) QTICN as neutral, radical anion and dianion species at the ωB97XD/6-31G** level.

Table 2.6. UV-Vis/NIR absorption data of BTICN and QTICN in their neutral, anion and dianion states and TD-DFT calculations at ωB97XD/6-31G** level.

Experimental data (nm)		
BTICN	**BTICN$^{.-}$**	**BTICN^{2-}**
574	719, 1271	566
QTICN	**QTICN$^{.-}$**	**QTICN^{2-}**
657	836, 1333	632
Theoretical data (nm)		
BTICN	**BTICN$^{.-}$**	**BTICN^{2-}**
490 (1.08)	324 (0.12), 568 (0.59), 976 (0.29)	276 (0.26), 488 (0.6)
QTICN	**QTICN$^{.-}$**	**QTICN^{2-}**
557 (2.03)	309 (0.22), 629 (0.96),1191 (0.62)	230 (0.39), 540 (1.12)
The values in parenthesis are the oscillator strengths.		

Figure 2.15 shows the distribution of the atomic charges calculated using Mülliken population analysis at the (R/U)ωB97XD/6-31G** level for BTICN and QTICN as neutral, anion and dianion species. The analysis of the charge distribution indicates that the additional electrons acquired during the two reduction processes are practically distributed over the whole molecule. However, the amount of negative charge accepted by the dicyanomethylene groups during the first and second reduction steps is slightly higher in BTICN (–0.24/–0.29 *e*) than QTICN (–0.21/–0.26 *e*). On the contrary, the amount of negative charge received by the thieno groups is moderately higher in QTICN (–0.46/–0.39 *e*) than in BTICN (–0.33/–0.27 *e*), which is attributed to the less electron-rich character of the thiophene-based framework in BTICN.
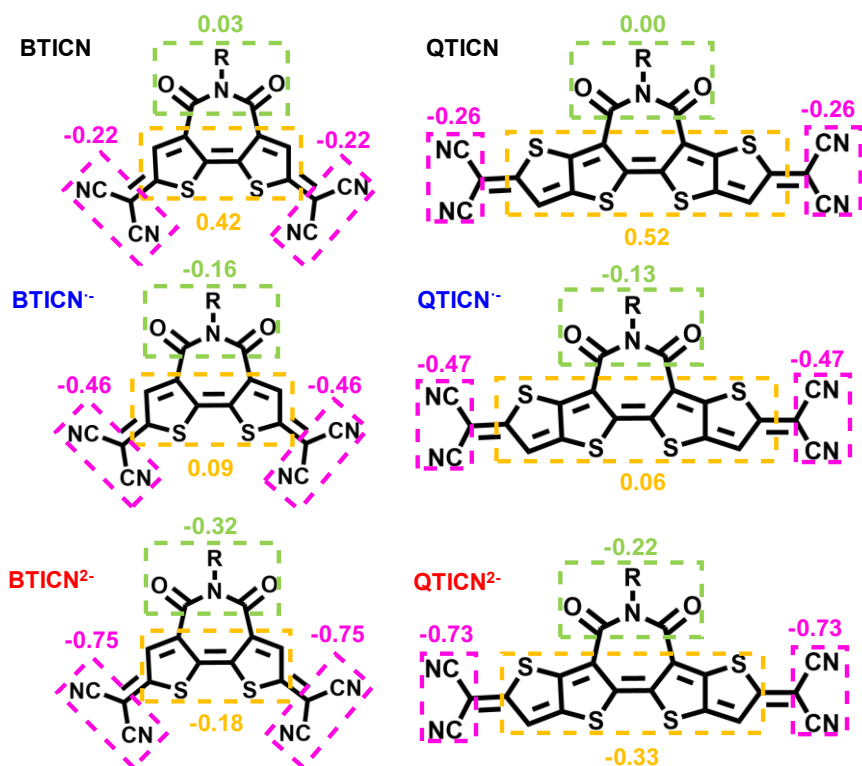
Figure 2.15. Distribution of Mülliken atomic charges (*e*) over various molecular domains of BTICN and QTICN as neutral, anion and dianion species, as derived from the Mülliken population analysis at the ωB97XD/6-31G** level of theory.

2.4. Electron spin resonance spectroscopy

The electron spin resonance spectroscopy (ESR) is a useful tool to study molecules with unpaired electrons. Therefore, this technique provides information related to the electronic and molecular structure of paramagnetic centers. Figure 2.16 shows the ESR spectra of the fused quinoidal imides under study, in the film state at room temperature.
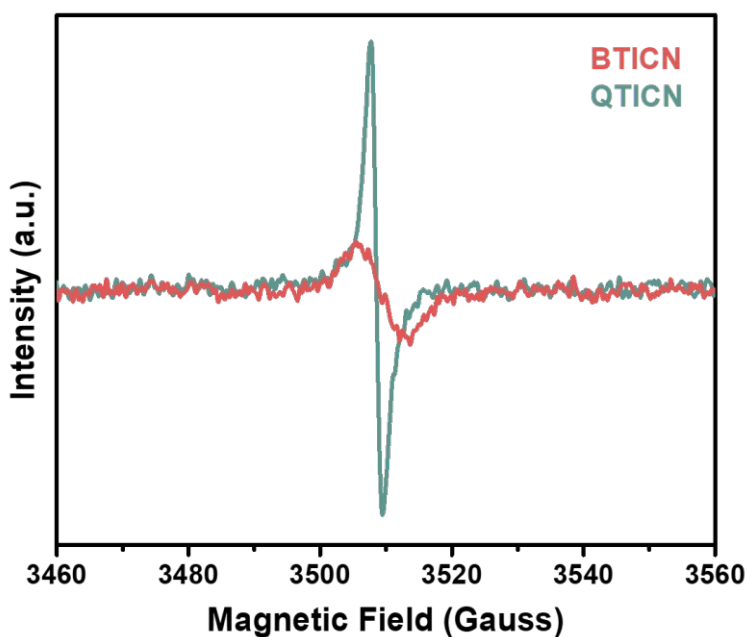
Figure 2.16. ESR spectra of BTICN and QTICN thin films.

The electron spin resonance (ESR) signal for both BTICN and QTICN, implies the existence of a thermal equilibrium between a diradical open-shell singlet state (S_0) and a magnetically active triplet state (T_1), which is energetically populated at room temperature through rapid S_0-T_1 intersystem crossing.

The ESR spectra for both BTICN and QTICN are well correlated with the DFT calculations at the ωB97XD/6-31G** level. The ESR response peak obtained for QTICN as thin film (thickness ~ 80 nm) exhibits much stronger intensity than BTICN as thin film, which displays only weak response considering its large ΔE ($S_0 \rightarrow T_1$) barrier of 7.70 Kcal/mol (See Figure 2.7(b)).

2.5. Raman spectroscopy

2.5.1. Non-resonant Raman spectroscopy

Figure 2.17 shows the FT-Raman (λ_{exc}= 1064 nm) spectra of BTICN and QTICN as bulk materials, together with their aromatic counterparts BTI and QTI. FT-Raman experiments were registered to get further information at the molecular level for closed-shell and open-shell species[24].

In order to identify the Raman bands in the FT-Raman spectra registered for the quinoidal systems, vibrational frequencies and Raman intensities were computed with the restricted approach, considering the open-shell structures (Figure 2.19). Different functionals (CAM-B3LYP and ωB97XD) were used to optimize the geometries, however, for the theoretical Raman spectra, CAM-B3LYP functional was chosen since this one was found to be slightly better in reproducing the experimental spectra when compared to ωB97XD.

The most intense Raman bands of the quinoidal systems (Figure 2.17) are downshifted in comparison to those of the aromatic counterparts, which confirm the quinoidization of these conjugated backbones, implying highly delocalized electrons along the π-conjugated backbone[17].
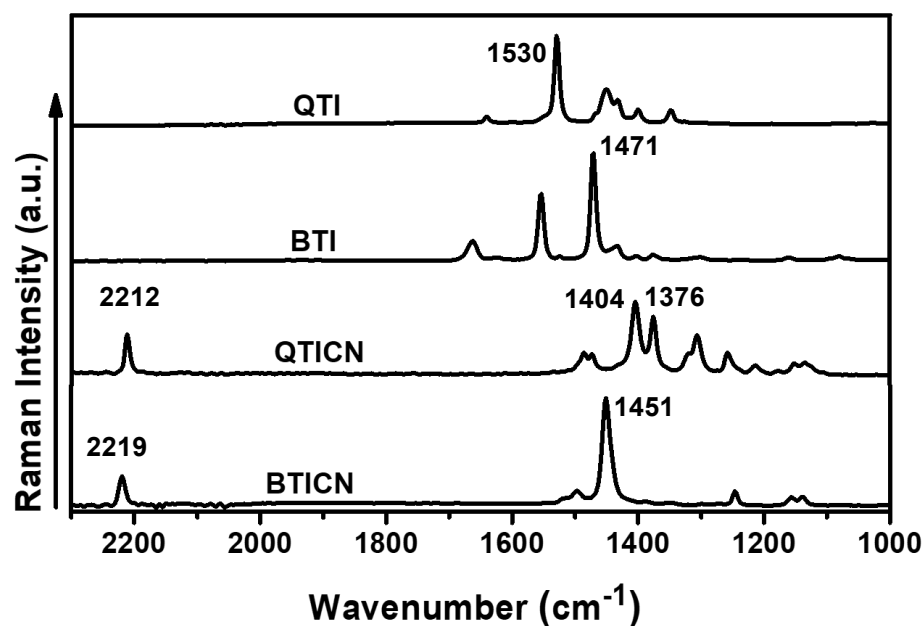
Figure 2.17. FT-Raman spectra (λ_{exc} = 1064 nm) of aromatic BTI and QTI and quinoidal BTICN and QTICN as powder samples at room temperature.

On the other hand, the comparison of the FT-Raman spectra of the quinoidal systems shows a displacement towards lower frequencies of the stronger Raman band, ongoing from the shortest quinoidal system (BTICN) to the largest one (QTICN), which indicates a progressive increase in the π-conjugation extension with chain lengthening. This is in line with the data obtained from the absorption spectra, with QTICN showing the largest π-conjugation extension.

The shortest quinoidal system, BTICN, shows a rather simple spectral profile dominated by one intense Raman band at 1451 cm^{-1}, which is assigned to a collective C=C/C-C vibration delocalized over the whole conjugated skeleton (see eigenvectors in Figure 2.18).

1456 (1451) cm⁻¹

BTICN

1451 (1404) cm⁻¹

1425 (1376) cm⁻¹
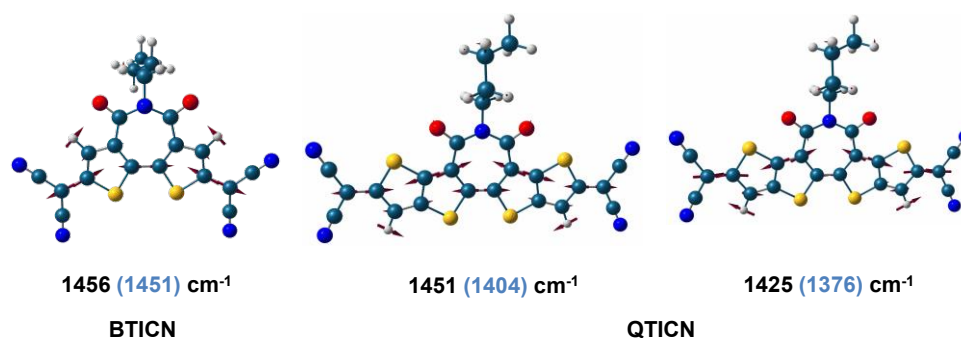
QTICN

Figure 2.18. Eigenvectors (CAM-B3LYP/6-31G**) of the vibrational Raman normal modes corresponding to the most intense Raman bands for BTICN and QTICN as closed-shell structures. The experimental frequency values are given in parenthesis.

On the other hand, the largest quinoidal system (QTICN) shows a much more complex spectral profile where the collective C=C/C-C vibration is splitted into two bands located at 1404 cm⁻¹ and 1376 cm⁻¹. This spectrum will be discussed in detail later in this chapter in order to better understand the molecular structure of the largest quinoidal system.
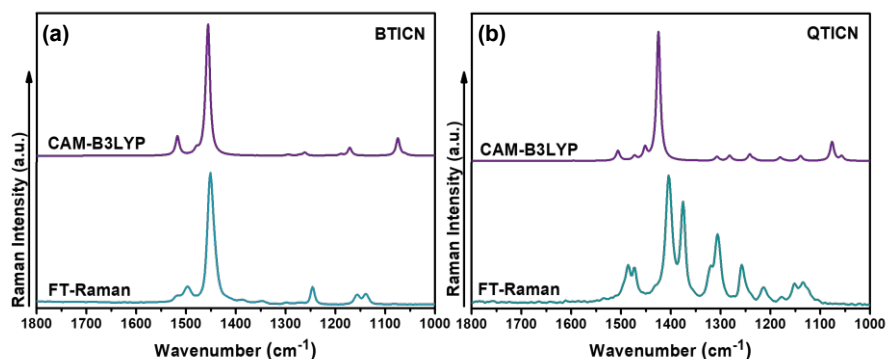
Figure 2.19. Down: FT-Raman spectra (λ_{exc} = 1064 nm) of (a) BTICN and (b) QTICN as powder samples at room temperature. **Top:** Theoretically predicted CAM-B3LYP/6-31G** Raman spectra for (a) BTICN and (b) QTICN quinoidal closed-shell systems using the optimized open-shell structures.

Theoretical Raman spectrum of BTICN is in good agreement with the experimental data (Figure 2.19(b)), which confirms the quite low diradical character for this one. Nevertheless, the predicted pattern for QTICN as closed-shell structure is not coincident with the experimental Raman spectrum, which may indicate a diradical nature for QTICN, as shown in Scheme 2.3.

Now, the Raman spectrum of the largest quinoidal system, QTICN, is analyzed in depth, in order to better understand the molecular structure and to elucidate its diradical nature. Figure 2.20 shows the Raman spectrum of the largest quinoidal system QTICN and its aromatic counterpart QTI.

As seen above, QTICN shows a much more complicated spectral profile than BTICN. The two most intense Raman bands at 1404 and 1376 cm^{-1}, which correspond to the collective C=C/C-C vibration, indicates a pseudoaromatic-pseudoquinoidal character, based on previous published studies[24].
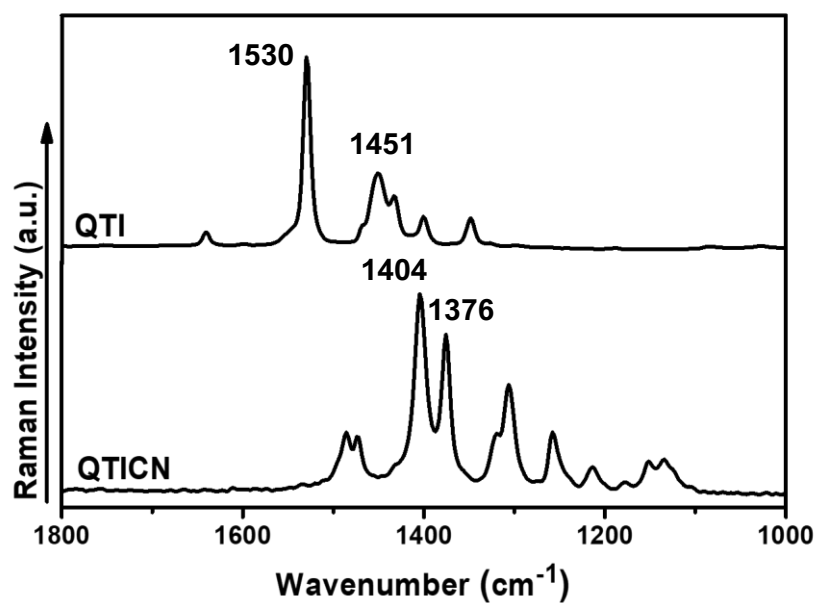
Figure 2.20. FT-Raman spectra (λ_{exc} = 1064 nm) of quinoidal system (QTICN) and its aromatic counterpart (QTI), as powder samples.
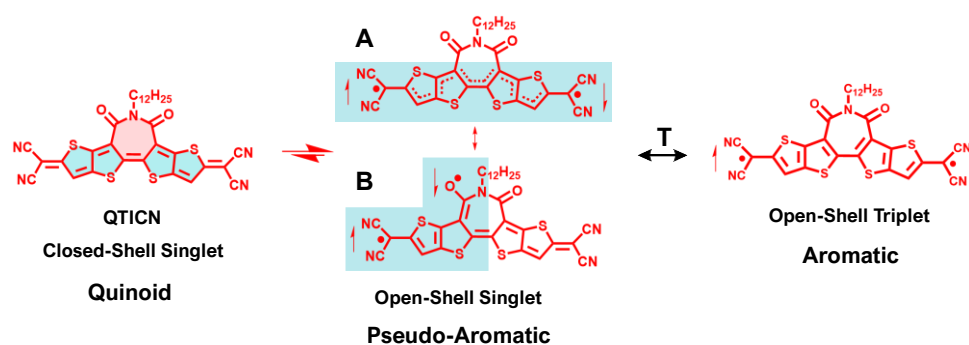
Scheme 2.3. Closed-shell and open-shell singlet canonical forms A (linear conjugation) and B (cross-conjugation) proposed for QTICN in thermal equilibrium with a low-lying triplet state.

Considering the resonance form A in Scheme 2.3, where the diradical stabilization is obtained through aromatization of the linear

conjugated path, one might expect the delocalized C=C/C-C vibration at similar wavenumbers to those recorded for the aromatic counterpart, QTICN, at 1530 cm^{-1} (Figure 2.20). However, in QTICN these Raman vibrations appeared at lower wavenumbers, which indicate a diradical stabilization mainly along the cross-conjugated path (the resonance form B in Scheme 2.3).

The optimized geometries of the quinoidal and aromatic structures were analyzed, in order to better understand the conjugation pattern in BTICN and QTICN. The comparison of C=C/C-C bond lengths for closed-shell S_0 and the open-shell S_0 and T_1 states structures at ωB97XD/6-31G** functional are depicted in Figures 2.22 and 2.23 for BTICN and QTICN, respectively.

The inversion of the shortest and longest bonds in BTICN (Figure 2.21) and QTICN (Figure 2.22) compared to the aromatic counterparts BTI and QTI, respectively, confirms the quinoidal structure of BTICN and QTICN.

The C=C/C-C bond length alternation is more pronounced in the central conjugated fused rings for both quinoidal systems. On another hand, this bond length alternation is reduced in the case of open-shell triplet forms, which present a more aromatic structure. The open-shell singlet forms show an intermediate C=C/C-C bond length between the quinoidal closed-shell and the triplet state structure. These tendencies agree well with the experimental Raman spectra (Figure 2.20).
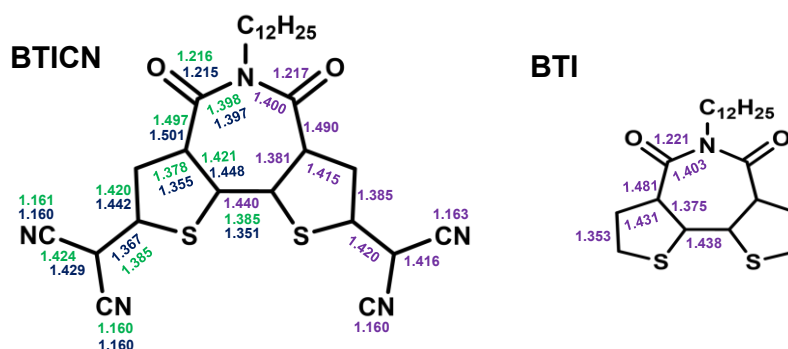
Figure 2.21. ωB97XD/6-31G** optimized bond lengths (in Å) for BTICN and its aromatic counterpart BTI. Values in blue refer to the closed-shell ωB97XD geometry of the singlet ground state, S_0. Values in green refer to the open-shell UωB97XD (BS) geometry of the singlet state, S_0. Values in purple refer to the open-shell UωB97XD geometry of the triplet state, T_1. Schematic structures shown in Scheme 2.2 are drawn for OSS and OST by considering bond distances below 1.390 A as double bonds and those above 1.410 A as single bonds.
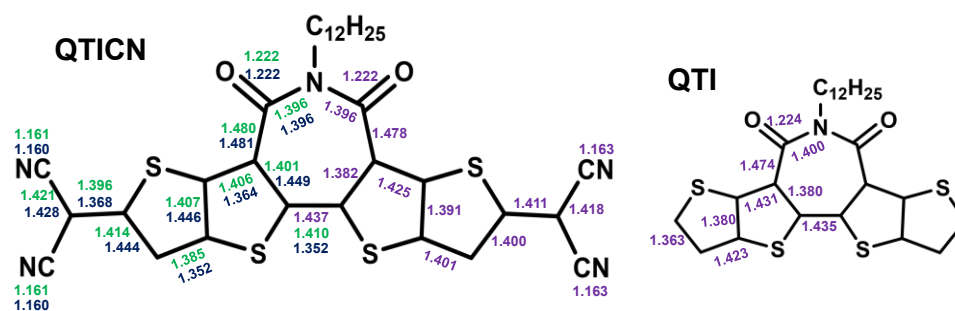
Figure 2.22. ωB97XD/6-31G** optimized bond lengths (in Å) for QTICN and its aromatic counterpart QTI. Values in blue refer to the closed-shell ωB97XD geometry of the singlet ground state, S_0. Values in green refer to the open-shell UωB97XD (BS) geometry of the singlet state, S_0. Values in purple refer to the open-shell UωB97XD geometry of the triplet state, T_1. Schematic structures shown in Schemes 2.2 and 2.3 are drawn for OSS and OST by considering bond distances below 1.390 A as double bonds and those above 1.410 A as single bonds.

2.5.2. Resonant Raman spectroscopy

In order to get further insights into the electronic configuration of the different species in these fused quinoidal systems, BTICN and QTICN, resonant Raman spectroscopy in comparison to the off-resonance Raman spectra were recorded. The laser wavelength used in this case is close to an electronic transition and consequently leads to the selectively enhancement of the Raman signal by several orders of magnitude (Figure 2.23). This allows us to identify different species presented in the samples in very low concentrations[40–43].

By analyzing the UV-Vis/NIR and the predicted TD-DFT spectra (Figure 2.23), the excitation laser wavelength, which allows to register the Raman spectra in resonance with the different species can be selected. In the TD-DFT spectra, the transitions of the triplet species appear at lower wavelengths (Figure 2.23(a) and (c)), and those corresponding to the closed-shell species appears at higher wavelengths. The transitions corresponding to the singlet open-shell structures appear at wavelengths between those corresponding to the triplet and close-shell structures. Thus, by using a 473 nm excitation laser, resonant conditions should be achieved for the triplet and the singlet diradical species of BTICN and QTICN while at 532 nm, resonant conditions should be achieved for the singlet diradical and the quinoid closed-shell species. Finally, by using the 1064 nm excitation laser wavelength, non-resonance conditions are achieved. Therefore, by recording the Raman spectra using a wide range of laser excitation wavelengths, it is possible to gather information from both resonant and non-resonant conditions in order to have a more detailed comparative (Figure 2.24).
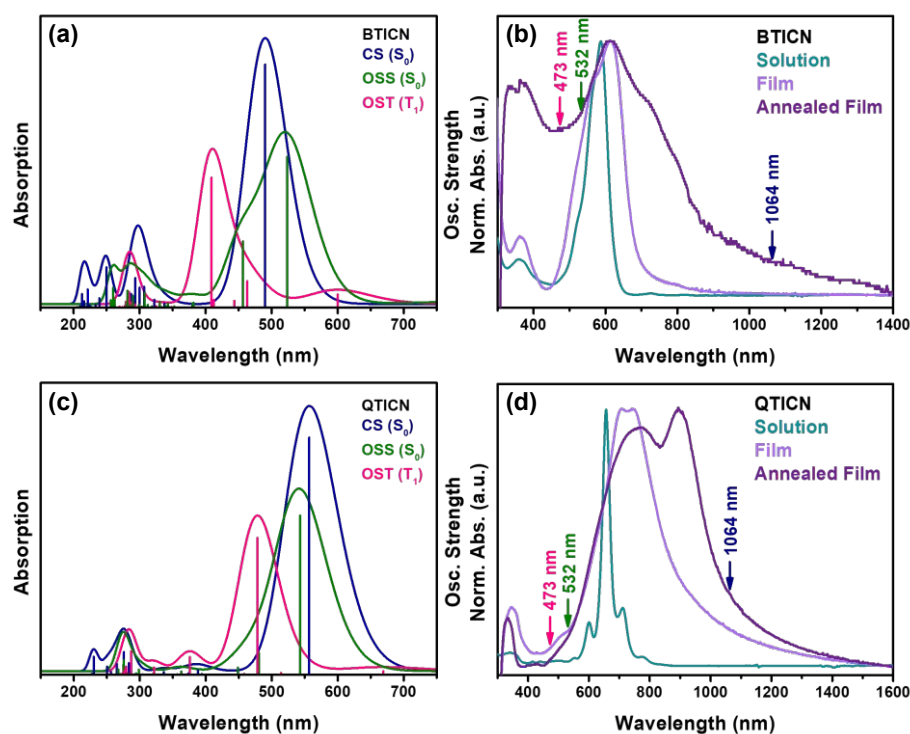
Figure 2.23. (a) and (c) TD-DFT calculated vertical transition energies at ωB97XD/6-31G** level for the CS, OSS and OST resonant structures, and (b) and (d) experimental UV-Vis/NIR spectra of BTICN and QTICN, respectively, indicating resonance conditions with the different excitation laser wavelengths.

The Raman spectra profile of BTICN (Figure 2.24(a)) recorded at 473 nm is basically superimposable to those recorded at 532 and 1064 nm, with the presence of one intense Raman band at 1451 cm^{-1}. This indicates that the shortest system shows predominantly closed-shell quinoidal character. In order to get further insights into the different species in BTICN, temperature dependent resonant Raman spectra were recorded (Figure 2.24(b)) and no spectral changes were observed as temperature increases from 25 ºC to 200 ºC and therefore no triplet state population should be expected. This fact can be explained by the large

singlet-triplet gap (ΔE_{ST} = 7.70 kcal/mol) calculated in Section 2.2.3. A different situation may be expected in the case of QTICN since the singlet-triplet gap (ΔE_{ST} = 3.90 kcal/mol) is smaller than that of BTICN.
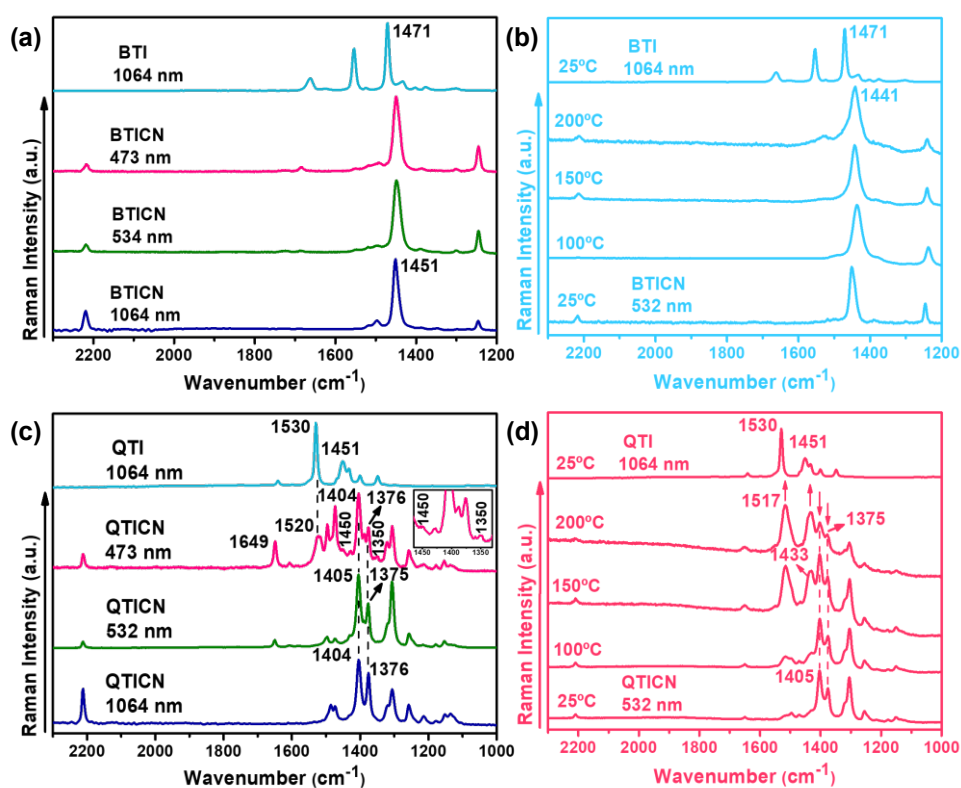
Figure 2.24. Resonance Raman spectra of the (a) BTICN and (c) QTICN as solid powder under resonance conditions (λ_{exc} = 532 and 473 nm) and non-resonant conditions (λ_{exc} = 1064 nm). Temperature dependent resonance Raman spectra of the (b) BTICN and (d) QTICN, as solid powder, under λ_{exc} = 514 nm. The Raman spectra excitation of aromatic counterparts, BTI and QTI, recorded at λ_{exc} = 1064 nm are also shown for a comparative purpose.

On the other hand, the Raman spectra of QTICN registered at 532 and 1064 nm laser excitation are basically coincident. However, the Raman spectra recorded at 473 nm is quite different and shows an

emerging band at 1520 cm^{-1}, which is close to the band at 1530 cm^{-1} in the Raman spectrum of QTI, recorded at 1064 nm laser excitation. This new band implies the existence of an aromatic structure in QTICN system which is in agreement with resonant conditions for both triplet state and singlet diradical form (see Scheme 2.2). The latest one is confirmed by the presence of the Raman bands located at 1404 and 1376 cm^{-1}.

Furthermore, the resonant conditions allow the intensification of the vibration corresponding to the carbonyl group (v(C=O) in QTICN, which appears at 1649 cm^{-1} (Figure 2.24(c)). In addition, two new Raman bands emerged at around 1450 and 1350 cm^{-1} (see inset Figure 2.24(c)) which can be related respectively to the symmetric and antisymmetric v(C-O) stretching, appearing as consequence of the singlet diradical stabilization through the cross-conjugated path (see canonical form B in Scheme 2.3).

The coexistence of triplet species and the diradical singlet forms were also confirmed by recording temperature dependent Raman spectra (Figure 2.24) using the 532 nm laser excitation. As expected, due to a low ΔE_{ST} of 3.90 kcal/mol, a gradual population of the triplet state is recorded for QTICN, which is shown by the increase of a Raman band at 1517 cm^{-1} at the expense of the Raman bands related to the singlet diradical, at 1405 and 1375 cm^{-1}. The Raman band emerging at higher temperatures (1517 cm^{-1}), appears at similar frequencies to the most intense Raman band of QTI (1530 cm^{-1}), which indicates the quasi-aromatic structure of the QTICN triplet.

2.6. Electrical characterization

2.6.1. Organic Field Effect Transistors

In order to evaluate the charge transport properties of the two fused quinoidal thiophene imides, OFETs with a BCTG configuration were fabricated. To this end, Cr and Au layers were used as contact electrodes, which were previously defined by photolithography onto borosilicate glass. Afterwards, the two oligothiophene imides semiconductors were deposited, followed by the CYTOP dielectric layer, both of them from solution by spin-coating, and were subsequently thermally annealed. Finally, Al was thermally evaporated as gate electrode to complete the device fabrication. The transistor fabrication and characterization were carried out in a nitrogen-filled glovebox.

As seen in Figure 2.25, BTICN and QTICN exhibit pronounced n-type OFET characteristics, however p-type transport characteristics were not noticed which indicates that these quinoidal molecules can be easily reduced but not oxidized, agreeing well with their HOMO and LUMO energy levels. However, the devices of both quinoidal imide compounds displayed indiscernible on and off states with large off-current (I_{OFF}) up to 10^{-4} A at zero gate bias ($V_G = 0$). Large drain current when no gate bias is applied implies the existence of substantial charge carriers in the conduction channel which is likely attributed to a self-doping process of these two materials.
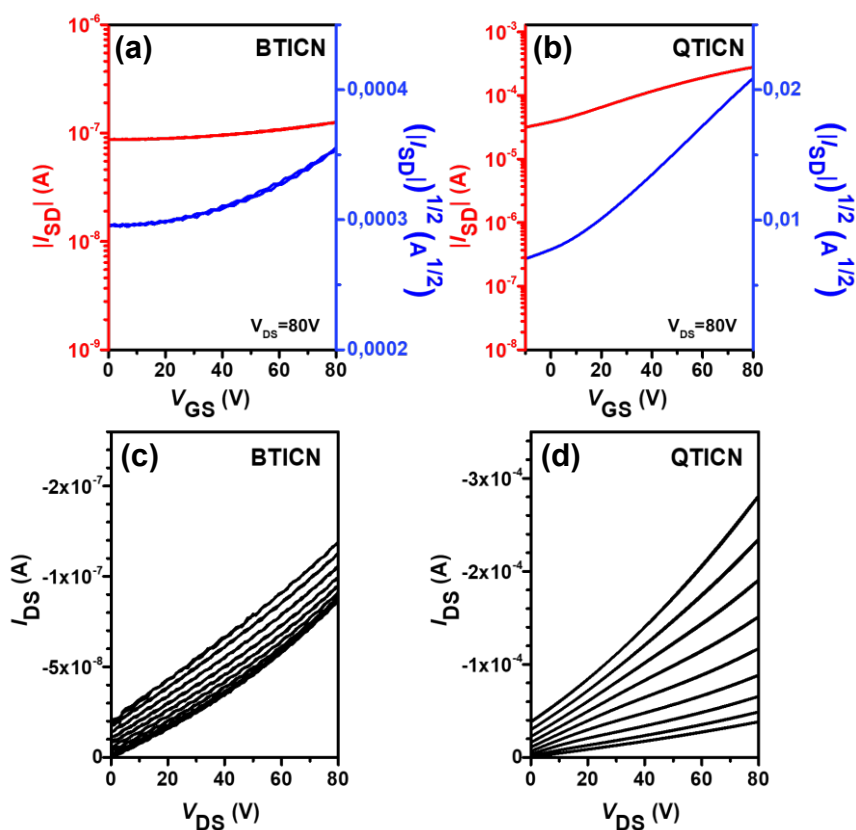
Figure 2.25. (a, b) Transfer and (c, d) output characteristics of OFET devices based on (a, c) BTICN and (b, d) QTICN. The gate voltage range in the output plots is 0 - 80 V with 10 V intervals. The channel length and width are 50 µm and 5 mm, respectively, for all devices.

In the chemical and electrochemical reduction analysis (Figures 2.12 and 2.13), it could be observed that BTICN is partially doped by the presence of the peak at 700 nm, before any potential was applied, or reductive agent added. However, QTICN is demonstrated to be free of any external doping. Therefore, a self-doping mechanism should be responsible for the electrical conductivity observed for QTICN-based OFET devices. Specifically, the drain current at $V_G = 0$ increased from 10^{-7}

A for BTICN to 10^{-5} A for QTICN by ca. 2 orders of magnitude upon the expansion of the quinoidal core, indicating the presence of much higher background charge carrier density as the result of strengthened self-doping efficiency of QTICN films.

2.6.2. Electrical conductivity

The electrical conductivity of these two fused-ring quinoidal oligothiophene imides as thin films treated by thermal annealing, was evaluated by using a four-point probe method (Figure 2.26).
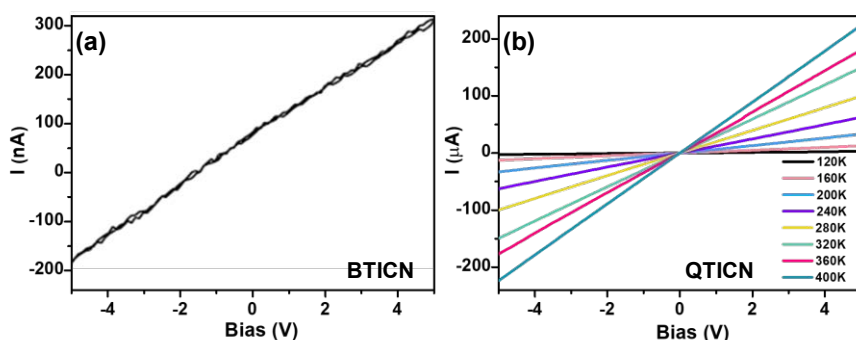
Figure 2.26. Current versus voltage (I-V) characteristics of planar diodes based on (a) BTICN and (b) QTICN as a function of temperature.

While a relatively low conductivity of 9.4 x 10^{-6} S cm^{-1} (Figure 2.26(a)) was measured for the BTICN film, the QTICN exhibited a remarkable electrical conductivity reaching 0.34 S cm^{-1} (Figure 2.26(b)). This much higher electrical conductivity should be ascribed to the higher self-doping efficiency enabled by its larger diradical characteristics as well as the more ordered packing as evidenced by the 2D-GIWAXS measurements (see next section, Figure 2.32).

2.7. Characterization of thin films

2.7.1. X-ray photoelectron spectroscopy in the film state

To further probe the mechanism of self-doping and charge conduction, the organic diradicaloid films were investigated by X-ray photoelectron spectroscopy (XPS) measurements. Figure 2.27 shows the high-resolution N(1s) and O(1s) XPS spectra of BTICN and QTICN as thin film after thermal annealing.
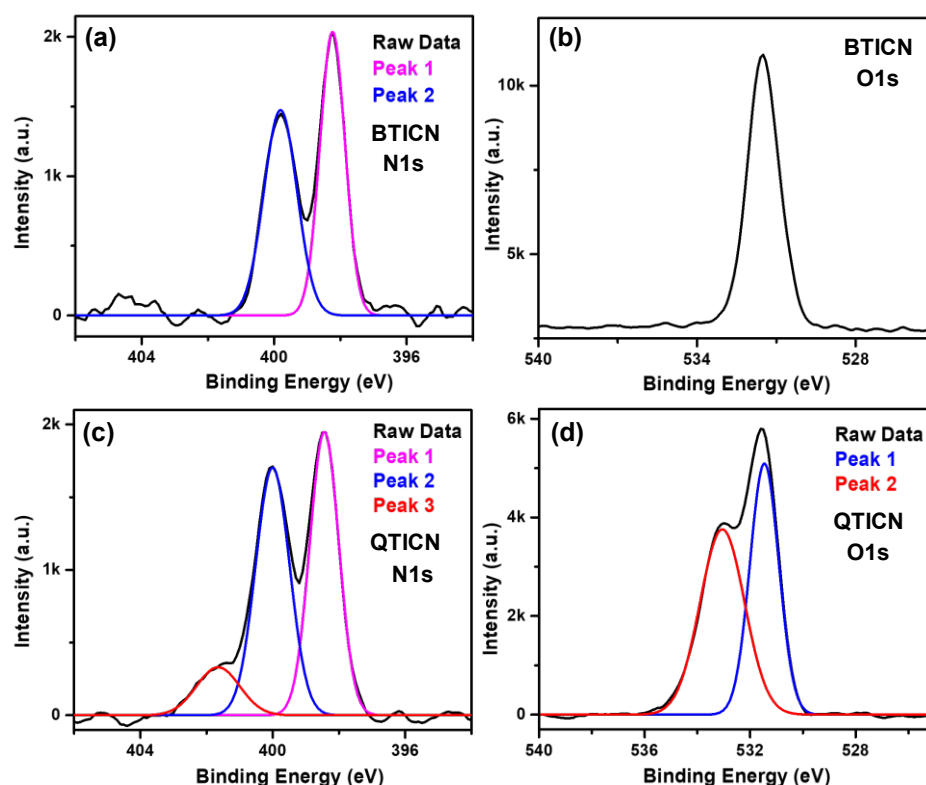
Figure 2.27. The N(1s) and O(1s) XPS spectra of (a,b) BTICN and (c,d) QTICN as annealed thin films, respectively.

The high-resolution N(1s) XPS spectrum of BTICN annealed thin film (Figure 2.27(a)) shows as expected, two peaks, one centered at 400

eV, which corresponds to the nitrogen atoms of imide (CO-NR-CO) group and another one centered at 398 eV, corresponding to cyano (CN) group, respectively. On the other hand, the high-resolution O(1s) XPS spectrum of BTICN annealed thin film (Figure 2.28(b)) shows only one peak at 532 eV, which corresponds to the oxygen atom in the carbonyl group.

In the case of QTICN, instead, the high-resolution N(1s) XPS spectrum (Figure 2.27(c)) of the annealed thin film shows three peaks, the two peaks at 398.4 and 400.1 eV, corresponding to the nitrogen atoms of imide (CO-NR-CO) and cyano (CN) groups, respectively, and a new peak centered at 401.7 eV. This new peak is assigned to a nitrogen atom with positive charge (N⁺), which should correspond to the self-doped species (Scheme 2.4)[10,20].

Interestingly, the high-resolution O(1s) spectrum of QTICN annealed thin film (Figure 2.27(d)) shows also a new peak, centered at 530.8 eV, in addition to the peak at 531.1 eV. The peak at higher binding energy corresponds to the oxygen atom in the carbonyl group, however the peak at low binding energy should be ascribed to the negatively charged oxygen atom (O⁻) in the self-doped species (Scheme 2.4).

Therefore, the absence of these two extra peaks in the N(1s) and O(1s) XPS spectra of BTICN (Figure 2.27(a-b)), indicates the absence of strong self-doping characteristics in the corresponding annealed thin film. These results agree well with the limited conductivity observed for the BTICN film, which might be ascribed to the lower diradical character induced by the shorter conjugation length of the BTICN molecule respect to QTICN.

On the basis of the XPS results, the positive charge for the self-doped species of QTICN is proposed here to be confined on the nitrogen atom in the cyano group and not on the nitrogen atom at the imide group

(CO-NR-CO) because of the conjugation-break nature of this one. On the other hand, the negative charge is confined on the oxygen atom in the carbonyl group. Therefore, the formation of a radical cation with a positively charged nitrogen atom (on the N=C=C group in Scheme 2.4) accompanied by a radical anion with a negatively charged oxygen atom (on the carbonyl group in Scheme 2.4) serving as the counter-charged species is expected.
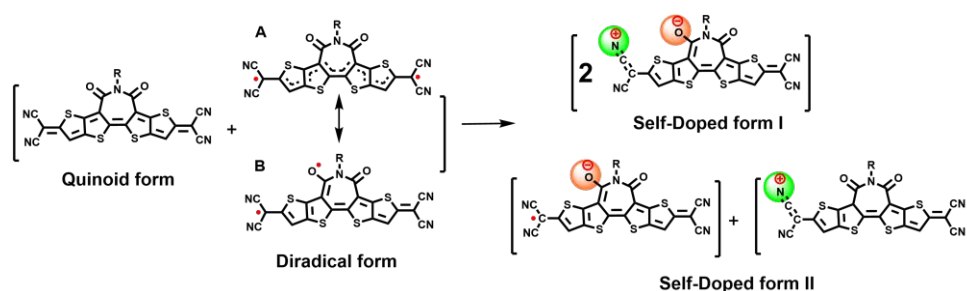
Scheme 2.4. The proposed two possible self-doping mechanism of QTICN through the formation of an intramolecular charge-transferred zwitterionic form (self-doped form I) and an intermolecular charge transfer species (self-doped form II).

In Scheme 2.4 two proposed self-doped forms are shown. The self-doped form I is represented by the intramolecular charge-transferred zwitterion form (I) where the positively charged N atom and the negatively charged O atom are located on the same molecule. The self-doped form II is represented by two separated species with an intermolecular charge transfer which leads to a radical cation with a positive charge N atom and a radical anion with a negative charge O atom. Therefore, the population of radical species in the self-doped form I should be lower than that in the self-doped form II, which will be confirmed by ESR measurements (Figure 2.28(b)).

In order to support the results shown above we measured the electron spin resonance spectra of BTICN and QTICN thin films before and after thermal annealing (Figure 2.28).
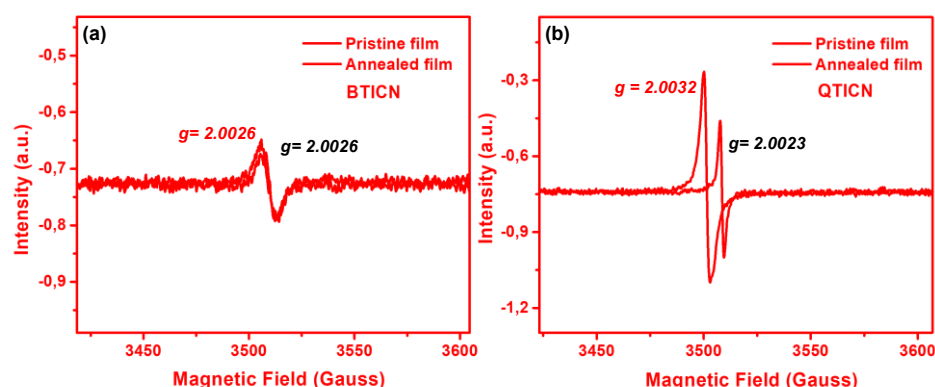
Figure 2.28. ESR spectra of (a) BTICN and (b) QTICN thin films before and after thermal annealing.

By comparing the ESR spectra of BTICN films before and after thermal treatment (Figure 2.28(a)), no significant changes were observed which confirm the low diradical character of the shortest quinoidal system.

However, by comparing the ESR spectra of QTICN films before and after thermal treatment (Figure 2.28(b)), a significant increase in the ESR signal was observed in the QTICN thin film after thermal treatment, accompanied by a shift of the g-value which indicate the formation of more diradical species. This fact suggests that the formation of intramolecular charge-separated zwitterions is unlikely because this self-doped form with low amount of radical species should lead to a lower ESR signal.

Therefore, the charged species including N^+-containing radical cations and O^--containing radical anions, generated via an intermolecular

electron transfer process between two neighboring molecules, should be responsible for the high electrical conductivity of the QTICN film.

2.7.2. Resonant Raman spectroscopy in the film state

The thin film Raman spectra were also recorded in order to find further evidence on the self-doping mechanism. Thus, the QTICN and BTICN, thin film, both annealed and unannealed (Figures 2.29 and 2.30), were measured by using the 473 and 532 nm laser wavelengths, being in these conditions, in resonance with the different species present in the thin films.
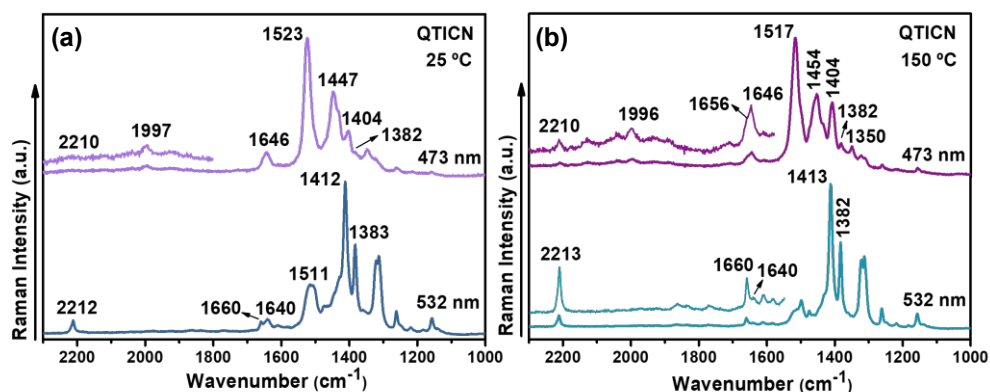
Figure 2.29. Resonance Raman (473 and 532 nm laser excitations) spectra recorded for QTICN thin films (a) before and (b) after thermal annealing at 150ºC.

Similar to what was previously observed in bulk samples (Figure 2.24(c)), the existence of triplet species is clear in the spectrum recorded at 473 nm for QTICN (Figure 2.29(a)), where the most intense Raman band appears at 1523 cm^{-1}, a similar wavenumber to that recorded for the aromatic counterpart QTI (1530 cm^{-1} in Figure 2.20). This Raman band,

corresponding to C=C/C-C vibrations, is also observed in the spectra recorded at 532 nm laser wavelength as an incipient band (1511 cm^{-1}), however in the spectra recorded at 473 nm, this Raman band is the most intense one.

In addition, the Raman bands ascribed to diradical singlet species are also present at around 1400 and 1380 cm^{-1} (Figure 2.29(a)), which correspond to C-C stretching modes delocalized over the conjugated skeleton, as well as the Raman bands at 1350 and 1454 cm^{-1}, which are related to C-O stretching modes, indicating the lengthening of one of the carbonyl bonds due to the radical stabilization (see self-doped form II in Scheme 2.4). The (C=O) vibration is also registered at ca. 1650 cm^{-1}, which is slightly shifted to lower frequencies than that recorded for other carbonyl groups, probably due to the cross-conjugation effect (see Scheme 2.4)[44].

As can be seen in Figure 2.29, the Raman spectra of the samples before and after annealing are quite similar, however, after the thermal treatment of the films (Figure 2.29(b)), the Raman band corresponding to the radical species (singlet and triplet) are more intensified than before the thermal annealing (Figure 2.29(a)).

In the proposed self-doped species shown in Scheme 2.4, a N=C=C- group and a practically single C-O bond are present in the positively and negatively doped molecules, respectively. Raman spectroscopy also provides evidence on the presence of those self-doped species.

In the Raman spectra (Figure 2.29), the v(C≡N) vibration appears at around 2210-2214 cm^{-1} in all spectra. However, in the case of the 473 nm excitation wavelength in both annealed and unannealed films, a very weak Raman band at 1996 cm^{-1} is observed which is ascribed to the

N=C=C- symmetrical vibration. The symmetrical vibration of this group has been previously reported[45,46] at ca. 2000 cm^{-1}. In addition, and by comparative with the bulk spectra registered at 473 nm, the increase in intensity of the 1350 and 1454 cm^{-1} Raman bands, relative to the presence of C-O single bonds, is another clear indicator of the self-doping process in QTICN annealed thin films.

In the case of BTICN films, surprisingly, a quite different spectral profile was observed in the Raman spectrum at 473 nm for the annealed film (Figure 2.30(b)), in contrast with the results obtained for BTICN unannealed thin films (Figure 2.30(a)) and for BTICN as bulk material (Figure 2.24(a)) under different excitation wavelengths.
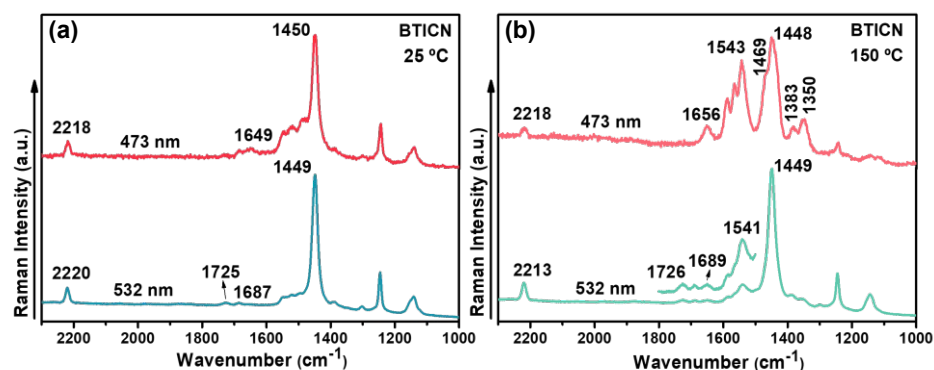
Figure 2.30. Resonance Raman (473 and 532 nm laser excitations) spectra recorded for BTICN thin films (a) before and (b) after thermal annealing at 150ºC.

In particular, in the Raman spectrum of BTICN annealed thin film registered at 473 nm laser wavelength, the most intense band located at 1448 cm^{-1} is broadened with a high energy shoulder at 1469 cm^{-1}, and is almost coincident with the most intense band recorded for the aromatic counterpart BTI (1471 cm^{-1}), shown in Figure 2.24(a). In addition, a surprising enhancement of three bands at around 1588-1543 cm^{-1} is also

registered. These changes can be related to the intensification of the Raman bands as a consequence of the resonant condition, considering the striking difference of the UV-Vis spectra (see Figure 2.31 and the explanation below), in the 300-500 nm region, between BTICN thin films before and after annealing thermal treatment.

In the case of BTICN (Figure 2.30(b)), it should also be noted that a displacement of the v(C=O) vibration from 1726 and 1689 in the 532 nm spectrum to 1656 cm^{-1} in the 473 nm spectrum is recorded together with the appearance of a Raman vibration at around 1350 cm^{-1}, indicative of a lessening of the C=O bond. All these data indicate the possible stabilization of a diradical form in the BTICN annealed thin films. However, the absence of the v(N=C=C) vibration at ca. 2000 cm^{-1} is a proof of the absence of self-doped species in BTICN.

As mentioned above, the enhancement of the three bands at around 1588-1543 cm^{-1} in Figure 2.30(b) is a consequence of the striking difference of the UV-Vis spectra in the 300-500 nm region, between BTICN thin films before and after annealing thermal treatment (Figure 2.31(a)). In order to give an explanation of this surprising enhancement, a theoretical-experimental comparative was carried out (Figure 2.31(b-d)).
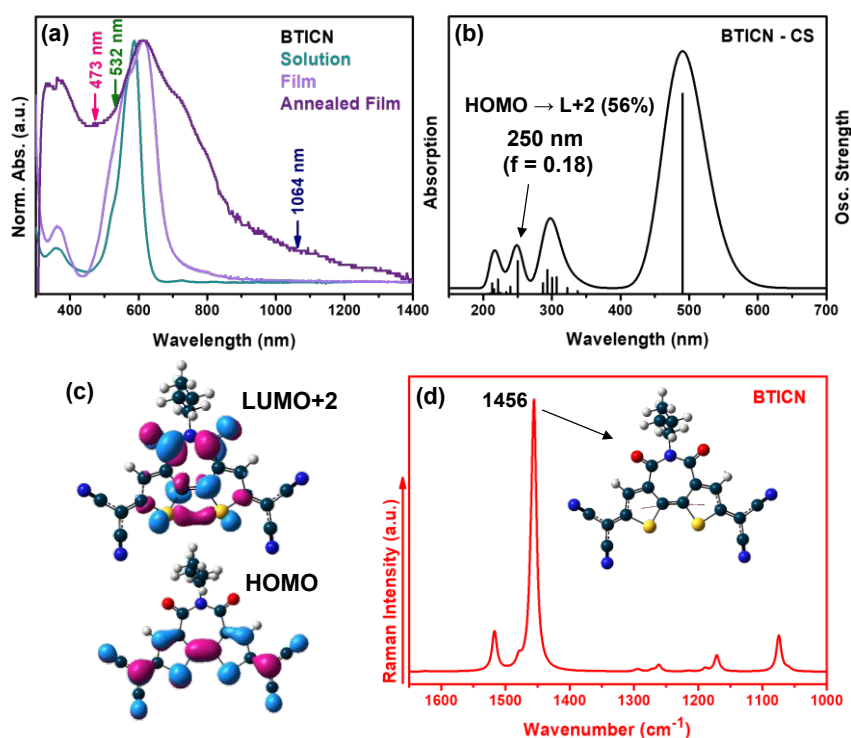
Figure 2.31. (a) Comparison between UV-Vis spectra of BTICN in solution and as thin films before and after thermal annealing. (b) TD-DFT simulated absorption spectra at ωB97XD/6-31G** level showing the transitions with higher oscillator strengths for the closed-shell calculations of BTICN. (c) Topologies of the molecular orbitals involved in the electronic transition with higher oscillator strength in the most energetic region of BTICN spectra. (d) Theoretical Raman spectrum and the vibrational eigenvector of BTICN, calculated at the at CAM-B3LYP/6-31G** level, associated to the greatly intensified Raman normal mode upon 473 nm laser excitation.

Thus, in the simulated absorption spectrum of BTICN (Figure 2.31(b)), the most intense predicted transitions in the region between 200 and 400 nm mostly involve a one electron excitation, which corresponds to the transition of the electron from HOMO to LUMO+2 orbitals. The topologies of these molecular orbitals (Figure 2.31(c)) indicates that these

excitations are primary located on the central C=C bond of the BTI unit. On another hand, by analyzing the theoretical Raman spectra of the BTICN molecule (Figure 2.31(d)) we can conclude that the experimentally bands intensified upon 473 nm laser excitation are those involving a symmetric vibration also mostly centered in that central C=C bond. Thus, the great intensification found in the 473 nm Raman spectra of BTICN annealed films (Figure 2.30(b)) can be ascribed to Resonance Raman effects.

2.7.3. 2D-GIWAXS measurements

In order to study the molecular packing of BTICN and QTICN films, the thin films have been investigated by using 2D-GIWAXS measurements. Figure 2.32 displays the 2D-GIWAXS patterns for BTICN (a and b) and QTICN thin films (c and d) before and after thermal annealing, respectively. The BTICN and QTICN films were prepared on Si substrates using identical conditions as for the electrical conductivity measurements.

As shown in Figure 2.32(a-b), a relatively amorphous feature was observed for BTICN thin films, however, the QTICN film (Figure 2.32(c-d)) exhibited a strong edge-on lamellar packing motif up to (400) diffraction peak with a d-spacing of 29.8 Å (q_z or q_{xy} (100) ≈ 0.21 Å^{-1}). Therefore, the more ordered molecular packing in QTICN thin film, together with its larger diradical character, lead to the higher self-doping, and therefore, to the much higher electrical conductivity observed in the previous sections.
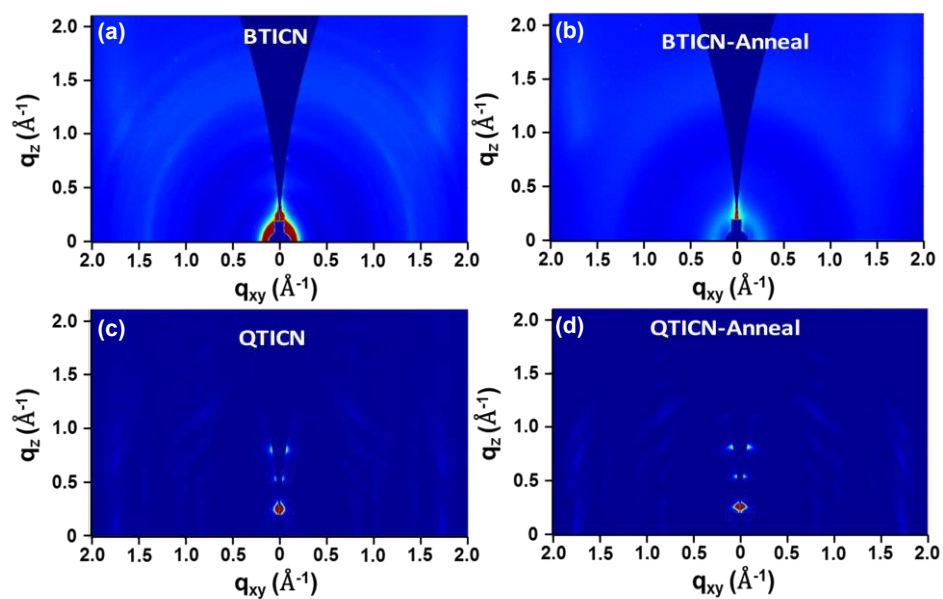
Figure 2.32. 2D-GIWAXS images of (a-b) BTICN and QTICN (c-d) before and after thermal annealing, respectively.

2.8. References

[1]   Qiao, Y.; Guo, Y.; Yu, C.; Zhang, F.; Xu, W.; Liu, Y.; Zhu, D. Diketopyrrolopyrrole-Containing Quinoidal Small Molecules for High-Performance, Air-Stable, and Solution-Processable n-Channel Organic Field-Effect Transistors. *J. Am. Chem. Soc.* **2012**, *134*, 4084–4087.

[2]   Li, J.; Qiao, X.; Xiong, Y.; Hong, W.; Gao, X.; Li, H. A Solution-Processable Dicyano-Substituted Quinoidal Oligothiophene for Air-Stable Ambipolar Organic Field-Effect Transistors. *J. Mater. Chem. C* **2013**, *1*, 5128–5132.

[3]   Wang, C.; Zang, Y.; Qin, Y.; Zhang, Q.; Sun, Y.; Di, C.; Xu, W.; Zhu, D. Thieno[3,2-b]Thiophene-Diketopyrrolopyrrole-Based Quinoidal Small Molecules: Synthesis, Characterization, Redox Behavior, and n-Channel Organic Field-Effect Transistors. *Chem. – A Eur. J.* **2014**, *20*, 13755–13761.

[4]   Zeng, Z.; Shi, X.; Chi, C.; López Navarrete, J. T.; Casado, J.; Wu, J. Pro-Aromatic and Anti-Aromatic π-Conjugated Molecules: An Irresistible Wish to Be Diradicals. *Chem. Soc. Rev.* **2015**, *44*, 6578–6596.

[5]   Zhang, C.; Zang, Y.; Zhang, F.; Diao, Y.; McNeill, C. R.; Di, C.; Zhu, X.; Zhu, D. Pursuing High-Mobility n-Type Organic Semiconductors by Combination of "Molecule-Framework" and "Side-Chain" Engineering. *Adv. Mater.* **2016**, *28*, 8456–8462.

[6]   Casado, J.; Ponce Ortiz, R.; López Navarrete, J. T. Quinoidal Oligothiophenes: New Properties behind an Unconventional Electronic Structure. *Chem. Soc. Rev.* **2012**, *41*, 5672–5686.

[7]   Casado, J.; Miller, L. L.; Mann, K. R.; Pappenfus, T. M.; Higuchi, H.; Ortí, E.; Milián, B.; Pou-Amérigo, R.; Hernández, V.; López Navarrete, J. T. Quinonoid Oligothiophenes as Electron-Donor and Electron-Acceptor Materials. A Spectroelectrochemical and Theoretical Study. *J. Am. Chem. Soc.* **2002**, *124*, 12380–12388.

[8]   Chesterfield, R. J.; Newman, C. R.; Pappenfus, T. M.; Ewbank, P. C.; Haukaas, M. H.; Mann, K. R.; Miller, L. L.; Frisbie, C. D. High Electron Mobility and Ambipolar Transport in Organic Thin-Film Transistors Based on a π-Stacking Quinoidal Terthiophene. *Adv. Mater.* **2003**, *15*, 1278–1282.

[9]   Pappenfus, T. M.; Chesterfield, R. J.; Frisbie, C. D.; Mann, K. R.; Casado, J.; Raff, J. D.; Miller, L. L. A π-Stacking Terthiophene-Based

Quinodimethane Is an n-Channel Conductor in a Thin Film Transistor. *J. Am. Chem. Soc.* **2002**, *124*, 4184–4185.

[10] Yuan, D.; Guo, Y.; Zeng, Y.; Fan, Q.; Wang, J.; Yi, Y.; Zhu, X. Air-Stable n-Type Thermoelectric Materials Enabled by Organic Diradicaloids. *Angew. Chemie Int. Ed.* **2019**, *58*, 4958–4962.

[11] Kubo, T.; Sakamoto, M.; Nakasuji, K. Biradicaloid Character of Phenalenyl-Based Aromatic Compounds with a Small HOMO–LUMO Gap. *Polyhedron* **2005**, *24*, 2522–2527.

[12] Ponce Ortiz, R.; Casado, J.; Hernández, V.; López Navarrete, J. T.; Viruela, P. M.; Ortí, E.; Takimiya, K.; Otsubo, T. On the Biradicaloid Nature of Long Quinoidal Oligothiophenes: Experimental Evidence Guided by Theoretical Studies. *Angew. Chemie Int. Ed.* **2007**, *46*, 9057–9061.

[13] Ponce Ortiz, R.; Casado, J.; Rodríguez González, S.; Hernández, V.; López Navarrete, J. T.; Viruela, P. M.; Ortí, E.; Takimiya, K.; Otsubo, T. Quinoidal Oligothiophenes: Towards Biradical Ground-State Species. *Chem. – A Eur. J.* **2010**, *16*, 470–484.

[14] Ray, S.; Sharma, S.; Salzner, U.; Patil, S. Synthesis and Characterization of Quinoidal Diketopyrrolopyrrole Derivatives with Exceptionally High Electron Affinities. *J. Phys. Chem. C* **2017**, *121*, 16088–16097.

[15] Zhang, C.; Zang, Y.; Gann, E.; McNeill, C. R.; Zhu, X.; Di, C.; Zhu, D. Two-Dimensional π-Expanded Quinoidal Terthiophenes Terminated with Dicyanomethylenes as n-Type Semiconductors for High-Performance Organic Thin-Film Transistors. *J. Am. Chem. Soc.* **2014**, *136*, 16176–16184.

[16] Dressler, J. J.; Teraoka, M.; Espejo, G. L.; Kishi, R.; Takamuku, S.; Gómez-García, C. J.; Zakharov, L. N.; Nakano, M.; Casado, J.; Haley, M. M. Thiophene and Its Sulfur Inhibit Indenoindenodibenzothiophene Diradicals from Low-Energy Lying Thermal Triplets. *Nat. Chem.* **2018**, *10*, 1134–1140.

[17] Huang, Y.; Egap, E. Open-Shell Organic Semiconductors: An Emerging Class of Materials with Novel Properties. *Polym. J.* **2018**, *50*, 603–614.

[18] Russ, B.; Robb, M. J.; Popere, B. C.; Perry, E. E.; Mai, C.-K.; Fronk, S. L.; Patel, S. N.; Mates, T. E.; Bazan, G. C.; Urban, J. J.; Chabinyc, M. L.; Hawker, C. J.; Segalman, R. A. Tethered Tertiary Amines as Solid-State n-Type Dopants for Solution-Processable Organic

Semiconductors. *Chem. Sci.* **2016**, *7*, 1914–1919.

[19]   Shimizu, A.; Uruichi, M.; Yakushi, K.; Matsuzaki, H.; Okamoto, H.; Nakano, M.; Hirao, Y.; Matsumoto, K.; Kurata, H.; Kubo, T. Resonance Balance Shift in Stacks of Delocalized Singlet Biradicals. *Angew. Chemie Int. Ed.* **2009**, *48*, 5482–5486.

[20]   Zhang, Y.; Zheng, Y.; Zhou, H.; Miao, M.-S.; Wudl, F.; Nguyen, T.-Q. Temperature Tunable Self-Doping in Stable Diradicaloid Thin-Film Devices. *Adv. Mater.* **2015**, *27*, 7412–7419.

[21]   Brédas, J. L.; Calbert, J. P.; da Silva Filho, D. A.; Cornil, J. Organic Semiconductors: A Theoretical Characterization of the Basic Parameters Governing Charge Transport. *Proc. Natl. Acad. Sci.* **2002**, *99*, 5804 LP – 5809.

[22]   Yamamoto, K.; Ie, Y.; Nitani, M.; Tohnai, N.; Kakiuchi, F.; Zhang, K.; Pisula, W.; Asadi, K.; Blom, P. W. M.; Aso, Y. Oligothiophene Quinoids Containing a Benzo[c]Thiophene Unit for the Stabilization of the Quinoidal Electronic Structure. *J. Mater. Chem. C* **2018**, *6*, 7493–7500.

[23]   Zeng, W.; Phan, H.; Herng, T. S.; Gopalakrishna, T. Y.; Aratani, N.; Zeng, Z.; Yamada, H.; Ding, J.; Wu, J. Rylene Ribbons with Unusual Diradical Character. *Chem* **2017**, *2*, 81–92.

[24]   Zeng, Z.; Sung, Y. M.; Bao, N.; Tan, D.; Lee, R.; Zafra, J. L.; Lee, B. S.; Ishida, M.; Ding, J.; López Navarrete, J. T.; Li, Y.; Zeng, W.; Kim, D.; Huang, K.-W.; Webster, R. D.; Casado, J.; Wu, J. Stable Tetrabenzo-Chichibabin's Hydrocarbons: Tunable Ground State and Unusual Transition between Their Closed-Shell and Open-Shell Resonance Forms. *J. Am. Chem. Soc.* **2012**, *134*, 14513–14525.

[25]   Zafra, J. L.; González Cano, R. C.; Ruiz Delgado, M. C.; Sun, Z.; Li, Y.; López Navarrete, J. T.; Wu, J.; Casado, J. Zethrene Biradicals: How pro-Aromaticity Is Expressed in the Ground Electronic State and in the Lowest Energy Singlet, Triplet, and Ionic States. *J. Chem. Phys.* **2014**, *140*, 54706.

[26]   WARNER, J. W.; BERRY, R. S. Hund's Rule. *Nature* **1985**, *313*, 160.

[27]   Levine, I. N. *Quantum Quemistry*, 4th ed.; Prentice-Hall, 1991.

[28]   Borden, W. T. Can a Square or Effectively Square Singlet Be the Ground State of Cyclobutadiene. *J. Am. Chem. Soc.* **1975**, *97*, 5968–5970.

[29] Berson, J. A. A New Class of Non-Kekulé Molecules with Tunable Singlet−Triplet Energy Spacings. *Acc. Chem. Res.* **1997**, *30*, 238–244.

[30] Borden, W. T.; Davidson, E. R. Effects of Electron Repulsion in Conjugated Hydrocarbon Diradicals. *J. Am. Chem. Soc.* **1977**, *99*, 4587–4594.

[31] Classification of the Pauli-Allowed States in Atoms and Molecules. *The Pauli Exclusion Principle*. December 7, 2016, pp 64–105.

[32] Karafiloglou, P. The Double (or Dynamic) Spin Polarization in π Diradicals. *J. Chem. Educ.* **1989**, *66*, 816.

[33] Salem, L.; Rowland, C. The Electronic Properties of Diradicals. *Angew. Chemie Int. Ed. English* **1972**, *11*, 92–111.

[34] Filatov, M.; Shaik, S. Tetramethyleneethane (TME) Diradical: Experiment and Density Functional Theory Reach an Agreement. *J. Phys. Chem. A* **1999**, *103*, 8885–8889.

[35] Borden, W. T.; Iwamura, H.; Berson, J. A. Violations of Hund's Rule in Non-Kekule Hydrocarbons: Theoretical Prediction and Experimental Verification. *Acc. Chem. Res.* **1994**, *27*, 109–116.

[36] Y. Gopalakrishna, T.; Zeng, W.; Lu, X.; Wu, J. From Open-Shell Singlet Diradicaloids to Polyradicaloids. *Chem. Commun.* **2018**, *54*, 2186–2199.

[37] Shi, X.; Burrezo, P. M.; Lee, S.; Zhang, W.; Zheng, B.; Dai, G.; Chang, J.; López Navarrete, J. T.; Huang, K.-W.; Kim, D.; Casado, J.; Chi, C. Antiaromatic Bisindeno-[n]Thienoacenes with Small Singlet Biradical Characters: Syntheses, Structures and Chain Length Dependent Physical Properties. *Chem. Sci.* **2014**, *5*, 4490–4503.

[38] Fukui, H.; Nakano, M.; Shigeta, Y.; Champagne, B. Origin of the Enhancement of the Second Hyperpolarizabilities in Open-Shell Singlet Transition-Metal Systems with Metal–Metal Multiple Bonds. *J. Phys. Chem. Lett.* **2011**, *2*, 2063–2066.

[39] Di Donato, E.; Fornari, R. P.; Di Motta, S.; Li, Y.; Wang, Z.; Negri, F. N-Type Charge Transport and Mobility of Fluorinated Perylene Bisimide Semiconductors. *J. Phys. Chem. B* **2010**, *114*, 5327–5334.

[40] Monezi, N. M.; Ando, R. A. Resonance Raman and UV–VIS Spectroscopic Investigation of the Reaction of Tetracyanoethylene and N-Methyldiphenylamine. *J. Raman Spectrosc.* **2017**, *48*, 758–764.

[41]   Reish, M. E.; Nam, S.; Lee, W.; Woo, H. Y.; Gordon, K. C. A Spectroscopic and DFT Study of the Electronic Properties of Carbazole-Based D–A Type Copolymers. *J. Phys. Chem. C* **2012**, *116*, 21255–21266.

[42]   Efremov, E. V; Ariese, F.; Gooijer, C. Achievements in Resonance Raman Spectroscopy: Review of a Technique with a Distinct Analytical Chemistry Potential. *Anal. Chim. Acta* **2008**, *606*, 119–134.

[43]   Johnson, B. B.; Peticolas, W. L. The Resonant Raman Effect. *Annu. Rev. Phys. Chem.* **1976**, *27*, 465–521.

[44]   Yuan, D.; Medina Rivero, S.; Mayorga Burrezo, P.; Ren, L.; Sandoval-Salinas, M. E.; Grabowski, S. J.; Casanova, D.; Zhu, X.; Casado, J. Thieno[3,4-c]Pyrrole-4,6-Dione Oligothiophenes Have Two Crossed Paths for Electron Delocalization. *Chem. – A Eur. J.* **2018**, *24*, 13523–13534.

[45]   Huang, J. Y.; Huang, H. G.; Ning, Y. S.; Liu, Q. P.; Alshahateet, S. F.; Sun, Y. M.; Xu, G. Q. Coexistence of Ketenimine Species and Tetra-σ Adduct at Acetyl Cyanide/Si(100)-2×1. *Chem. Phys. Lett.* **2005**, *411*, 75–80.

[46]   Wolf, R.; Stadtmüller, S.; Wong, M. W.; Wentrup, C.; Barbieux-Flammang, M.; Flammang, R. Novel Heterocumulenes: Bisiminopropadienes and Linear Ketenimines. *Chem. – A Eur. J.* **1996**, *2*, 1318–1329.

Chapter 3. Nitrogen-doped π-extended polycyclic aromatic dicarboximides

Contents:

3.1. Introduction

Polycyclic aromatic dicarboximides (PADI)[1–4] and their heteroatom-doped analogues[5] are emerging classes of semiconducting materials derived from the well-known family of polycyclic hydrocarbons (PAH)[6–9]. These materials have been successfully applied in organic (opto)electronics[10][11,12] and more recently, as electrodes in energy storage devices due to their remarkable redox behavior[13,14].

Among various PADIs molecules, π-conjugated compounds containing imide groups[15,16], such as naphthalene and perylene diimides (NDI and PDI, Figure I.15)[17–19] are the most intensively studied n-type semiconductors. This is due to several factors such as i) the presence of imide groups with strong electron-withdrawing character, which lowers the LUMO energy levels of the semiconductor, and facilitate electron injection and charge stabilization through the π-conjugated systems[20,21]; ii) conjugated skeletons that can be chemically modified, offering the possibility of tuning the redox potentials and promoting the generation of reversible polyanionic species, for their use as electrode materials in batteries[22,23]; and iii) their processability that can be easily modulated by the appropriate selection of alkyl chains substituents at the nitrogen atom of the imide groups. Thus, long alkyl chains provide good film forming ability through enhanced solubility, even in large planar π-extended systems with many fused rings, while intermolecular interactions can be promoted by the absence of lateral substituents, for applications as electrodes. However, most π-extended PADI systems are obtained via metal-based cross coupling or C-H arylation reactions[3,24], being the synthesis of π-extended polycyclic aromatic dicarboximide by metal-free reactions relatively unexplored.

Therefore, inspired by the excellent properties of these organic semiconductors and by the relative scarcity of metal-free reactions for their synthesis, a novel family of π-extended nitrogen-doped polycyclic aromatic mono and dicarboximide[25] (naft-1-4 in Figure 3.1) was synthesized at Segura group at UCM, by metal-free reactions of auto-condensation and cross-condensation of pyrene[26] and 1,8-naphthalimide[27−29] moieties endowed with 1,2-diketone functionalities[30].
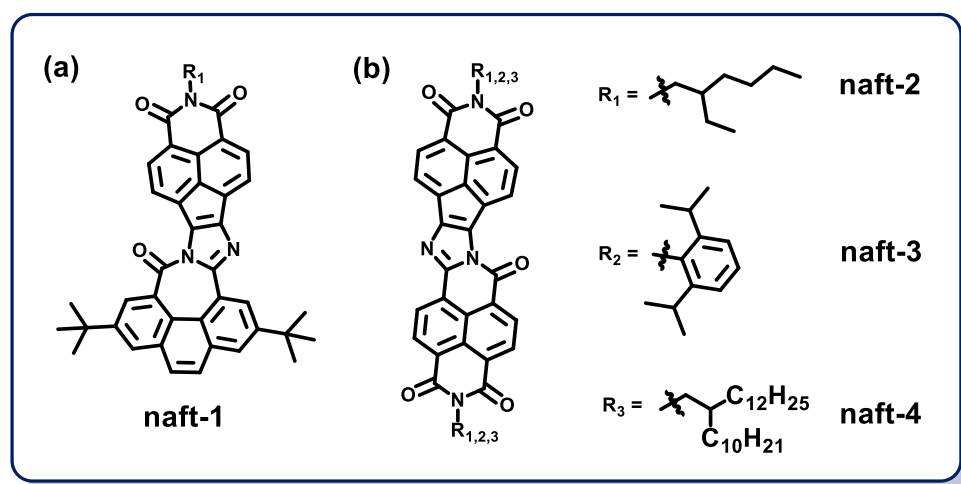
Figure 3.1. Chemical structures of (a) naft-1, cross or T-shape system formed by a naphthalimide group and a pyrene group and (b) naft-2-4, linear system formed by two naphthalimide groups which differ on the N-substituents of the imide groups.

The naft-1 system (Figure 3.1(a)) is based on pyrene and 1,8-naphthalimide moieties with a T-shape, which is expected to exhibit ambipolar behavior. On the other hand, naft-2-4 compounds (Figure 3.1(b)) are based only on naphthalimide units with a linear form and are designed to present electron-transporting properties. These three latest systems differ in the solubilizing chains incorporated at the nitrogen atom

of the imide groups, which can lead to different supramolecular aggregations, solubility and film-forming abilities[31].

In this chapter, a combined experimental/theoretical approach is used in order to characterize these new systems (naft-1-4 in Figure 3.1), which links UV-Vis absorption, cyclic voltammetry (CV), *in situ* spectroelectrochemistry (UV-Vis/NIR) with DFT and TD-DFT calculations. In addition, the electrical properties of these fused systems in OFETs have been examined using vapor-deposited films which were then characterized by XRD and AFM techniques.

3.2. Experimental and theoretical study of neutral species

3.2.1. DFT-calculated molecular geometries

The geometries of naft-1-4, optimized at the PBE0/6-31G** level, are shown in Figure 3.2. The PBE0 functional was chosen because it is well-known that provides a good assignment of intermolecular charge transfer (ICT) states[32]. The solution environment is described by the polarizable continuum model (PCM) using dichloromethane (CH_2Cl_2) as solvent.
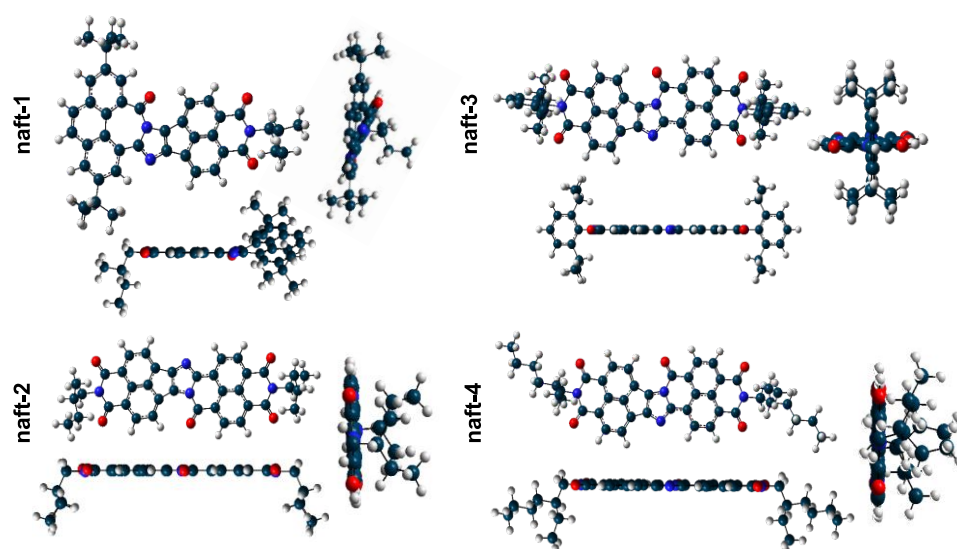
Figure 3.2. Frontal and lateral views of DFT-optimized geometries of naft-1-4 monomers at PBE0/6-31G** - PCM(CH$_2$Cl$_2$) level. The long alkyl chains have been replaced by shorter chain groups to simplify calculations and reduce the computational cost and resources.

The optimized minimum energy geometries, shown in Figure 3.2, present highly planar backbones for naft-2-4, while in naft-1, the pyrene unit forms a 16º dihedral angle with the naphthalimide unit. The fact that these π-conjugated systems are rigid (there is no freedom of rotation) allows efficient stacking between molecules.

Figure 3.3 shows the molecular frontier orbital profiles of naft-1-4 systems.
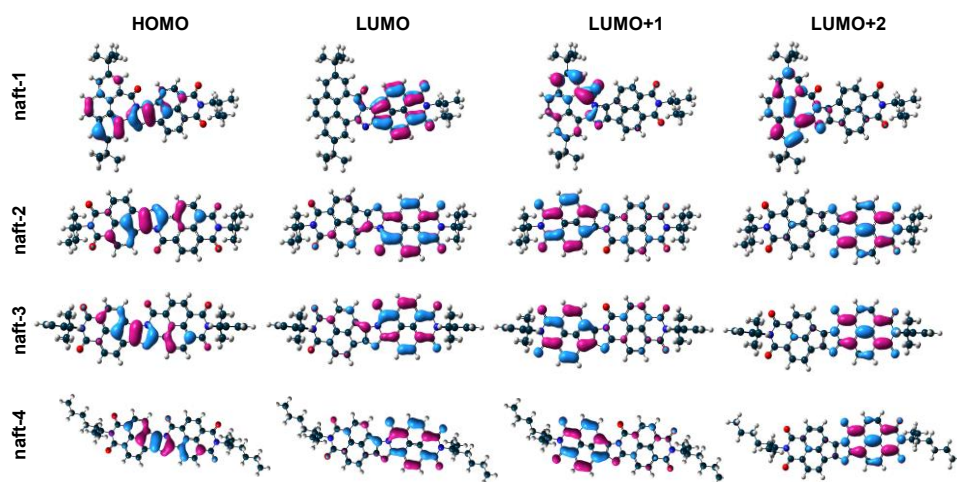
Figure 3.3. DFT-calculated molecular orbital topologies of naft-1-4 at PBE0/6-31G** - PCM(CH$_2$Cl$_2$) level.

In naft-1 system, based on pyrene and naphthalimide units with a T-shape, the HOMO orbital is localized over the pyrene group and the central part of the molecule, while the LUMO orbital is totally localized over the naphthalimide unit. On the other hand, in naft-2-4, based only on naphthalimide units with a linear form, the HOMO orbital is mainly localized over the imidazole ring, while the LUMO orbital is totally localized over the naphthalimide moiety. It is also noteworthy that the substituents at the nitrogen atom of the imide group do not influence the distribution of the electron density in the molecular orbitals.

As can be seen in the frontier molecular orbital energy diagram (Figure 3.4), both HOMO and LUMO orbitals stabilize when passing from naft-1 to naft-2-4, which is due to the greater electron-deficient character of the naphthalimide group compared to pyrene group. The theoretically

predicted HOMO-LUMO gaps decrease from 2.89 to 2.72 eV when comparing the naft-1 with naft-2-4 (see Figure 3.4).
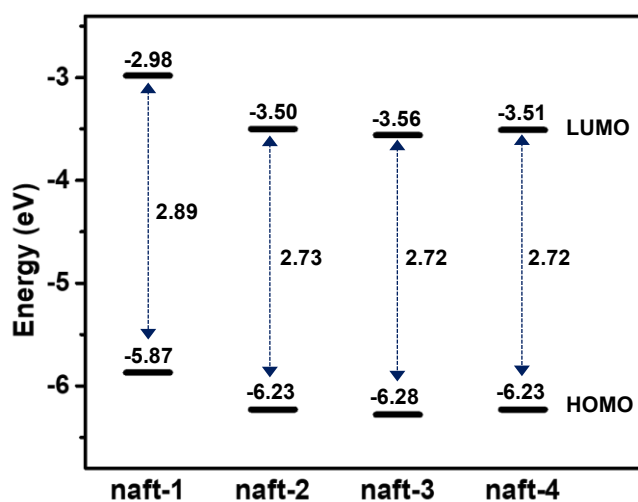
Figure 3.4. Frontier molecular orbital energies and energy gap values predicted for naft-1-4 at PBE0/6-31G** - PCM(CH_2Cl_2) level.

3.2.2. Optical properties and TD-DFT vertical transition energies

The optical properties of naft-1-4 molecules were investigated by measuring their UV-Vis absorption spectra in both solution at room temperature (Figure 3.5) and film state (Figure 3.7).
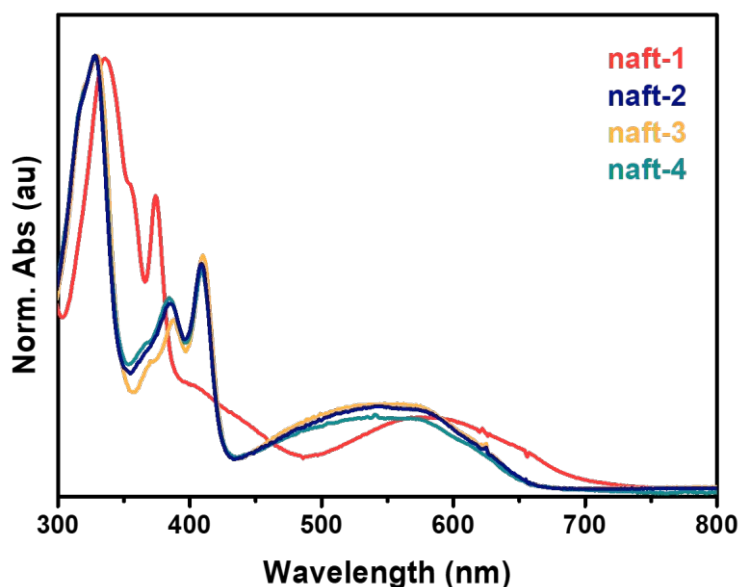
Figure 3.5. UV-Vis absorption spectra of naft-1-4 systems in dichloromethane solutions at 298 K.

The optical absorption spectra of naft-1-4 in dichloromethane solutions at room temperature (Figure 3.5 and Table 3.1) show a high-energy band (300-420 nm) and a lower-energy band (420-750 nm). From our previous experience in similar systems, we can anticipate that, the absorption bands at higher energies could be ascribed to the π-π* transition and the broad absorption bands at lower energies could be ascribed to an intramolecular charge transfer transition (ICT)[33].

The linear systems (naft-2-4), consisting of two fused naphthalimide groups, present nearly identical spectral profiles in solution despite their different substituents at the imide groups (Figure 3.5). All three systems have a maximum absorption band at 329 nm followed by vibronic structured absorptions around 400 nm and then, the higher-energy band at 551 nm. The nitrogen atoms in the imide groups are not involved in the π-conjugation of the system, therefore, variations in the alkyl or aryl chains do not affect the absorption spectra significantly.

On the other hand, naft-1 presents a different absorption profile, due to the variation of its conjugated skeleton with respect to naft-2-4, consisting of the fusion of a naphthalimide group and a pyrene group in a T-shape. In this case, the maximum absorption at 335 nm and the ICT band at 587 nm, are slightly shifted towards higher wavelengths compared to those of naft-2-4.

It is worth mentioning that the ICT character may be expected for naft-1 compound considering its structure which consists of a naphthalimide (electron-acceptor character) and a pyrene (electron-donor character) moiety in a T form, where the charge transfer occurs from the donor to the acceptor unit. However, the presence of the ICT bands in naft-2-4 is unforeseen, as they are composed of two naphthalimide acceptor units in a linear form.

These experimental results are supported by TD-DFT theoretical calculations at the PBE0/6-31G**-PCM(CH_2Cl_2) level (Figure 3.6). The experimental and theoretical data are summarized in Table 3.1.
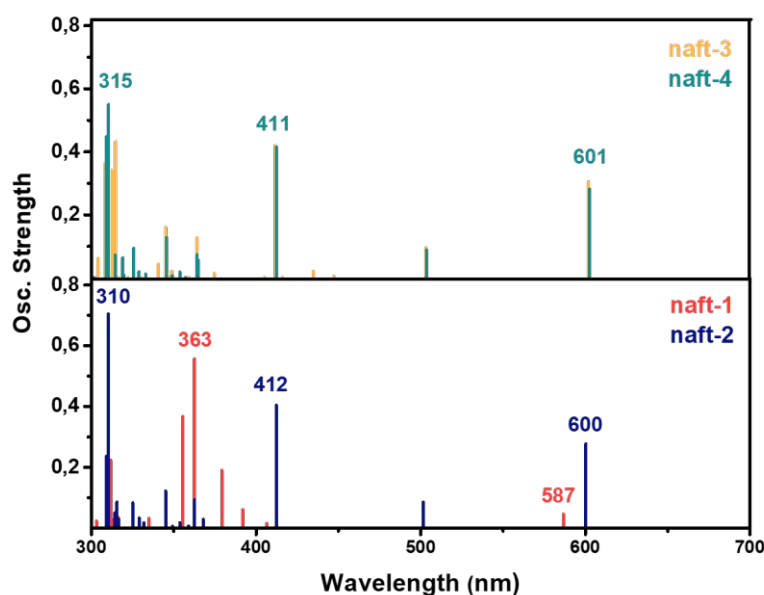
Figure 3.6. TD-DFT calculated vertical transition energies for neutral naft-1-4 at the PBE0/6-31G** - PCM(CH_2Cl_2) level.

These TD-DFT calculations are in good agreement with the experimental data, predicting the existence of one intense electronic transition at around 300 nm and a second one at around 600 nm similar to the experimental electronic absorptions at around 300 and 550 nm, respectively. In addition, the theoretical calculations confirm the ICT excitation at around 600 nm, which is described as a one-electron HOMO-LUMO excitation, consisting of the displacement of the electron density from HOMO, mainly localized over the imidazole ring in naft-2-4 or pyrene group in naft-1, to the LUMO, which is totally localized over the naphthalimide moiety in all cases (see OMs topologies in Figure 3.3). The high energy transition, at around 300 nm, implies the promotion of one electron from the HOMO to the LUMO+2 orbitals.

Table 3.1. Photophysical properties of the naft-1-4 systems and TD-DFT calculations at PBE0/6-31G** - PCM(CH_2Cl_2) level.

Experimental data						
Molecules	λ_{abs}^{max} $CHCl_3$ at 300K (nm)	λ_{abs}^{ITC} $CHCl_3$ at 300 K (nm)	λ_{abs}^{onset} $CHCl_3$ at 300 K (nm)	E_g^{opt} (eV)[a]	λ_{abs}^{max} film (nm)	λ_{abs}^{ITC} film (nm)
naft-1	335	587	716	1.73	336	558
naft-2	328	551	655	1.89	325	599
naft-3	329	551	651	1.90	327	551
naft-4	328	551	670	1.85	320	551
Theoretical data						
Molecules	λ_{max} (nm)	f	Description	λ_{ITC} (nm)	f	Description
naft-1	363	0.56	H-3→LUMO (82%)	587	0.05	HOMO→LUMO (94%)
naft-2	310	0.70	H-2→L+1 (20%) HOMO→L+2 (52%)	600	0.28	HOMO→LUMO (95%)
naft-3	315	0.43	H-12→LUMO (31%) HOMO→L+2 (37%)	601	0.31	HOMO→LUMO (95%)
naft-4	310	0.55	H-2→L+1 (34%) HOMO→L+2 (36%)	602	0.28	HOMO→LUMO (95%)
[a]Optical band gap estimated from the absorption edge of the as-cast thin films and calculated based on the equation: $E_g^{opt}=1240/\lambda_{onset\ of\ film}$.						

The behavior of the naft-1-4 systems in the solid state was also studied by UV-Vis spectroscopy and shown below, together with the absorption spectra obtained in solution, for a comparative purpose (Figure 3.7).
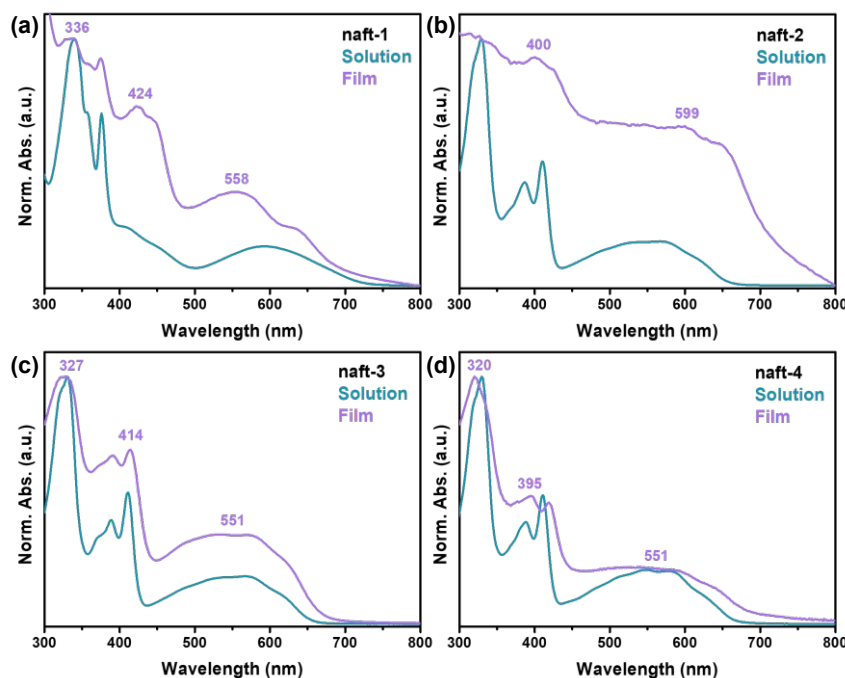
Figure 3.7. UV-Vis absorption spectra of naft-1-4 systems in chloroform solutions at 300 K and as-cast thin films.

Compared to the solution spectra, red-shifted maximum absorptions were observed for the naft-2 and naft-4 systems as thin films (Figure 3.7(b) and (d), respectively), which implies stronger molecular interactions in these derivatives in the solid state[34]. In the case of naft-3 (Figure 3.7(c)), the absorption spectral profile of this system as thin film is very similar to that obtained in solution. This was to be expected considering the bulky steric hindrance of the 3,5-diisopropylphenyl

substituents at the imide group in this system, which implies unfavored π-π interactions in the solid state.

Finally, the absorption spectrum of naft-1 as thin film (Figure 3.7(a)) shows slightly blue-shifted bands in comparison to its absorption spectrum in solution which suggests also strong molecular interactions in the solid state.

3.3. Experimental and theoretical study of charged species in solution

3.3.1. Cyclic voltammetry

Figure 3.8 shows the CV spectra registered for naft-1-4 in dichloromethane and chloroform solutions at room temperature using 0.1M (n-Bu)$_4$NPF$_6$ as supporting electrolyte at a scan rate of 100 mVs^{-1}. Potentials were recorded *versus* Fc/Fc$^+$. The electrochemical together with the theoretical data are summarized in Table 3.2.
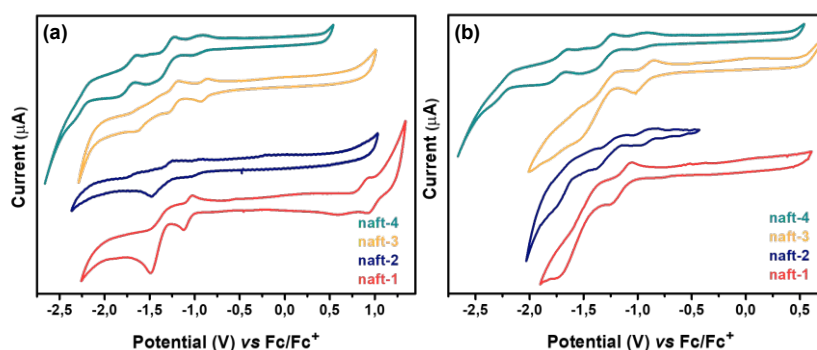
Figure 3.8. Cyclic voltammograms of naft-1-4 in (a) CH$_2$Cl$_2$ and (b) CHCl$_3$ solutions in presence of 0.1 M of (n-Bu)$_4$NPF$_4$ supporting electrolyte.

The CV registered in CH_2Cl_2 solution (Figure 3.8(a)) for naft-1 shows one reversible oxidation wave and two reversible reduction waves at 0.92 V, -1.08 and -1.37 V, respectively, while for naft-2-4 systems only reversible reduction waves were recorded at ~ -0.9, -1.25, -1.50 and -1.7 V, with only small differences in the reduction wave values due to the different substituents at the imide nitrogen, as previously described in literature[35,36]. The anodic process corresponds to the formation of the radical cation and the cathodic processes correspond to the consecutive formation of reduced species, starting from the radical anion and up to tetranion species.

It is worth pointing out that the CV spectra of naft-2-4 systems show up to four reversible reduction waves, while the naft-1 system shows only two reduction processes (Table 3.2). This behavior is consistent with the presence of only one naphthalimide unit in naft-1 versus two naphthalimide moieties in naft-2-4. In addition, the appearance of the oxidation wave in naft-1 is due to the presence of pyrene moiety in this compound. It is interesting to note that the first reduction potential of naft-1 with only one naphthalimide unit is approximately 100 mV more negative than that of naft-2-4 with two naphthalimide units (Table 3.2).

The redox properties of naft-1-4 compounds were also studied in chloroform solutions (Figure 3.8(b)) at the same experimental conditions previously described for dichloromethane solvent. The aim of this experiment is to improve the solubility of naft-2 and also to study the effect of the solvent on the charge stabilization of these compounds. These measurements were also carried out for naft-1, naft-3 and naft-4 for a comparative purpose.

Table 3.2. Electrochemical redox properties of naft-1-4 systems, extracted from the data shown in Figure 3.8 and theoretically calculated HOMO and LUMO energy levels, and E_{gap} for naft-1-4 at PBE0/6-31G**-PCM(CH$_2$Cl$_2$) level.

Molecules	Experimental redox properties in CH$_2$Cl$_2$[a]				
	$E^{1/2}_{ox}$	$E^{1/2}_{redI}$	$E^{1/2}_{redII}$	$E^{1/2}_{redIII}$	$E^{1/2}_{redIV}$
naft-1	0.92	-1.08	-1.37	-	-
naft-2	-	-0.98	-1.28	-1.45	-1.69
naft-3	-	-0.89	-1.23	-1.49	-1.65
naft-4	-	-0.98	-1.30	-1.52	-1.72
Molecules	Experimental redox properties in CHCl$_3$[a]				
	$E^{1/2}_{ox}$	$E^{1/2}_{redI}$	$E^{1/2}_{redII}$	$E^{1/2}_{redIII}$	$E^{1/2}_{redIV}$
naft-1	-	-1.15	-1.51	-	-
naft-2	-	-0.94	-1.29	-1.51	-1.72
naft-3	-	-0.92	-1.30	-1.59	-1.73
naft-4	-	-0.95	-1.31	-1.49	
Molecules	Experimental data[a]			Theoretical data	
	E_{LUMO} (eV)[b]	E_{HOMO} (eV)	E_g^{EC} (eV)[e]	E_{LUMO} (eV)	E_{HOMO} (eV)
naft-1	-3.72	-5.72[c]	2.00	-2.98	-5.87
naft-2	-4.12	-5.71[d]	1.89	-3.50	-6.23
naft-3	-4.21	-5.81[d]	1.90	-3.56	-6.28
naft-4	-3.82	-5.67[d]	1.89	-3.51	-6.23

[a]Electrochemically determined vs Fc/Fc+. [b]$E_{LUMO} = - (E_{redI}^{1/2} + 4.8$ eV) and [c]$E_{HOMO} = - (E_{ox}^{1/2} + 4.8$ eV). [d]Estimated from $E_{HOMO} = E_g^{opt} - E_{LUMO}$; [e]$E_g^{EC} = E_{HOMO} - E_{LUMO}$;

As can be seen in Table 3.2, the redox properties of naft-1-4 systems measured in chloroform are shifted in comparison with the values obtained in dichloromethane. This phenomenon is related to different stabilization charge behavior due to the different dielectric constants of the solvents (9 for dichloromethane vs 4.8 for chloroform) as confirmed by theoretical calculations, which indicate that the charged species in chloroform are less stable than in dichloromethane (see Table 3.3).

Table 3.2 also shows the comparison between the predicted and experimental frontier molecular orbital energies, and although the absolute

values are not always fully consistent, DFT calculations are able to predict the general trend in orbital energy levels and bandgaps.

Table 3.3. Relative energies difference (in Kcal/mol) between the optimized geometries calculated at PBE0/6-31G**- PCM with dichloromethane (CH_2Cl_2) and PCM with chloroform ($CHCl_3$) for naft-1-2 in their neutral, radical cation, radical anion, dianion, trianion and tetranion states.

Theoretical data						
Solvent	**naft-1**	**naft-1$^{.+}$**	**naft-1$^{.-}$**	**naft-1^{2-}**	**naft-1^{3-}**	**naft-1^{4-}**
CH_2Cl_2	0	0	0	0	-	-
$CHCl_3$	1.3	3.9	5.3	15.5	-	-
Solvent	**naft-2**	**naft-2$^{.+}$**	**naft-2$^{.-}$**	**naft-2^{2-}**	**naft-2^{3-}**	**naft-2^{4-}**
CH_2Cl_2	0	-	0	0	0	0
$CHCl_3$	1.4	-	4.1	12.3	26.2	45.5

3.3.2. Intramolecular reorganization energy calculations

The intramolecular reorganization energies values for naft-1-4, calculated using the PBE0/6-31G**, are collected in Table 3.4.

Table 3.4. DFT-calculated intramolecular reorganization energies for holes (λ_h) and electrons (λ_e) at PBE0 level.

Molecules	λ (meV)	
	Electron transport (λ_e)	**Hole transport (λ_h)**
naft-1	280	290
naft-2	210	300
naft-3	220	300
naft-4	220	300

The λ values, shown in Table 3.4, indicate similar reorganization energies for both hole and electron transport in naft-1; however, in the case of naft-2-4 systems, the intramolecular reorganization energies for electron transport are notably lower that those predicted for hole transport. This can be related to the easiness to accommodate negative charges over the two naphthalimide units.

3.3.3. Spectroelectrochemistry and TD-DFT vertical transition energies

Figures 3.9, 3.10 and 3.11 show the evolution of the UV-Vis/NIR spectra obtained by progressive spectroelectrochemical reduction of low concentration of naft-1-4 in dichloromethane and chloroform at room temperature, in presence of high excess of (n-Bu)$_4$NBF$_4$ supporting electrolyte.
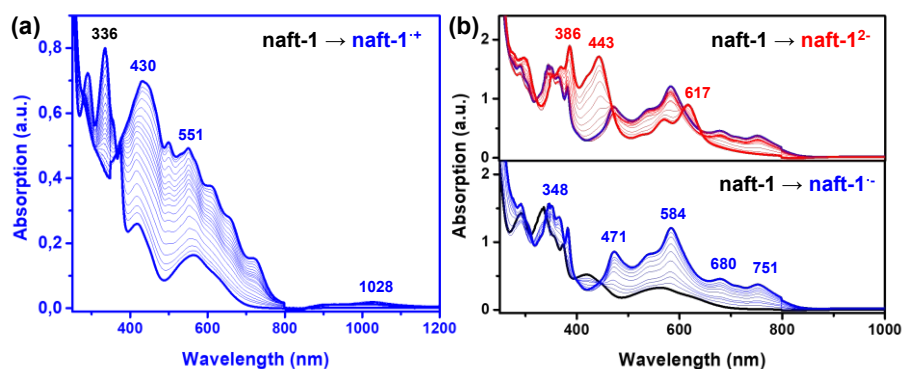
Figure 3.9. UV-Vis/NIR absorption spectra of naft-1 recorded (a) upon electrochemical oxidation (1.37 V), and (b) during the first step of electrochemical reduction (-0.79 V, blue curve) and the second step of the electrochemical reduction (-1.38 V, red curve) in CH$_2$Cl$_2$ solution at room temperature, in presence of (n-Bu)$_4$NBF$_4$ supporting electrolyte within an OTTLE cell.

As expected, in the case of naft-1, both electrochemical reduction and oxidation processes were recorded (Figure 3.9) due to its amphoteric redox behavior. Upon progressive electrochemical oxidation (Figure 3.9(a)), the UV-Vis absorption spectra of naft-1 neutral species (black curves) progressively vanishes giving rise to the formation of two absorption band (blue curves) with the main peaks at 430 and 1028 nm.

Upon progressive electrochemical reduction (Figure 3.9(b)), the UV-Vis absorption spectra of naft-1 neutral species (black curves) progressively vanishes giving rise to the formation of the radical anion (-800 mV) with main absorption peaks at 348 and 584 nm (blue curve). Further reduction at ~ -1000 mV gives to new bands with peaks at 386, 443 and 617 nm, which nicely correspond to the formation of the dianion (red curve). Thus, the potential necessary to generate the dianion is approximately 250 mV higher than that for the obtention of the anion species (Table 3.5), fitting perfectly with the potential difference between the second and first reduction processes in cyclic voltammetry experiments (Table 3.2).

Table 3.5. Electrochemical potentials used in the *in-situ* UV-Vis/NIR spectroelectrochemical studies in dichloromethane and chloroform, for the generation of oxidized and reduced species.

Molecules	Dichloromethane				
	$E^{1/2}_{oxI}$	$E^{1/2}_{redI}$	$E^{1/2}_{redII}$	$E^{1/2}_{redIII}$	$E^{1/2}_{redIV}$
naft-1	1.37	-0.79	-1.38	-	-
naft-2	-	-0.55	-	-0.97	-1.16
naft-3	-	-0.49	-	-0.71	-1.05
naft-4	-	-0.47	-	-0.99	-1.16
	Chloroform				
naft-1	1.60	-1.06	-1.46	-	-
naft-2	-	-0.76	-	-1.16	-1.44
naft-3	-	-0.62	-	-1.11	-1.35
naft-4	-	-0.67	-	-1.09	-1.38

For the case of naft-2-4 systems formed by the fusion of two naphthalimide units (Figures 3.10 and 3.11), we divided these systems in two groups for an easier understanding of their spectroelectrochemical properties. The first group comprises the systems in which the substituents at the imide group are branched alkyl chains (the case of naft-2 and naft-4, Figure 3.10), and on the other hand the molecule in which the substituent at the imide group is a bulkier group, namely 3,5-diisopropylphenyl substituent (the case of naft-3, Figure 3.11).

In the first group, the electrochemical reductions of naft-2 and naft-4 (Figure 3.10) follow the same reduction absorption pattern, although they present different alkyl substituents at the imide group. The gradual application of negative potentials (-550 and -470 mV, respectively, Figure 3.10) leads to the progressively disappearance of the neutral absorption bands (black curve), followed by the growth of new features at 354, 497, 800 and 1586 nm (blue curve), which correspond to the radical anion absorption peaks through the formation of clear isosbestic points. Further

electrochemical reduction of naft-2 and naft-4 (-970 and -990 mV, respectively) leads to the progressively disappearance of the radial anion bands followed by the growth of new features at 382, 606 and 1783 nm (cyan curve) which correspond to the absorption evolvement from radical anion to the trianion species, confirmed later by TD-DFT calculations (see Figure 3.13). The increase of the reduction potential to about -1200 mV leads in both cases to the progressively disappearance of the trianion bands followed by the growth of new features at 389, 467 and 604 nm (pink curve), which correspond to the absorption evolvement from the trianion to the tetranion species, which are also confirmed by TD-DFT calculations (Figure 3.13).
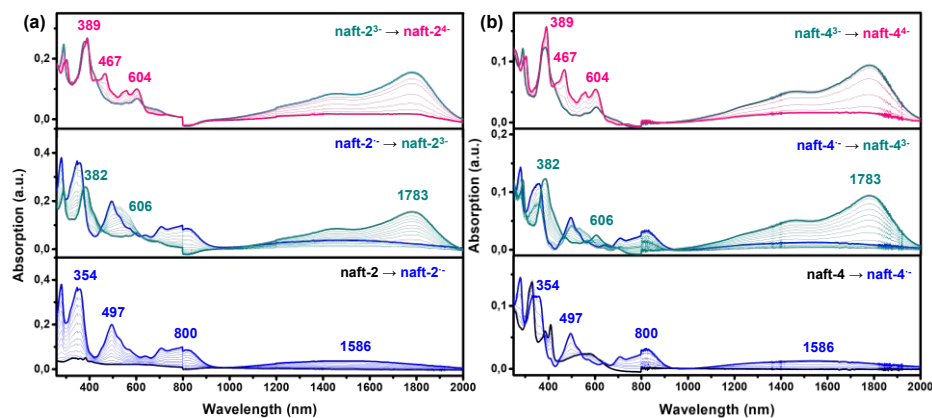
Figure 3.10. UV-Vis/NIR absorption spectra of (a) naft-2, and (b) naft-4 recorded during the first step of electrochemical reduction (~ -0.50 V, blue curve), the second step of the electrochemical reduction (~ -1.00 V, cyan curve) and the third step of electrochemical reduction (~ -1.20 V, pink curve) in CH₂Cl₂ solution at room temperature, in presence of (*n*-Bu)₄NBF₄ supporting electrolyte within an OTTLE cell.

The electrochemical reduction of naft-3 (Figure 3.11) follows the same reduction absorption pattern as naft-2 and naft-4, even if naft-3 have

a bulkier substituent at the imide group. However, for this system, the reduction potentials are lower than in the case of naft-2 and naft-4 (see Table 3.5).
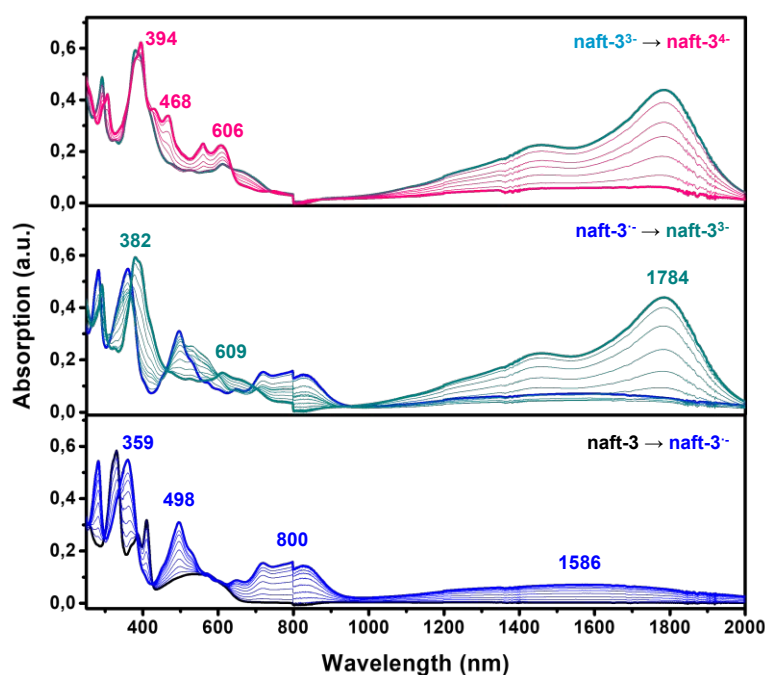
Figure 3.11. UV-Vis/NIR absorption spectra of naft-3 recorded during the first step of electrochemical reduction (-0.49 V, blue curve), the second step of the electrochemical reduction (-0.71 V, cyan curve) and the third step of electrochemical reduction (-1.05 V, pink curve) in CH_2Cl_2 solution at room temperature, in presence of $(n\text{-Bu})_4NBF_4$ supporting electrolyte within an OTTLE cell.

Note that the differences between the applied reduction potentials in the spectroelectrochemical experiments follow a similar trend to those of the electrochemical potentials in the cyclic voltammetry experiment, necessary to generate the radical anion, trianion and tetranion species, thus, further supporting the formation of these species also by

spectroelectrochemical measurements (see Table 3.2 and Table 3.5). The simultaneous two-electron injection in the second reduction process can be understood considering the LUMO and LUMO+1 orbital topologies (see Figure 3.3); while the two electrons inserted in the LUMO must be accommodated in half the molecular length, a third electron is easily delocalized in the other half of the molecule, thus mitigating charge repulsion.

These experimental results are supported by TD-DFT theoretical calculations at PBE0/6-31G** - PCM(CH_2Cl_2) level (Figures 3.12 and 3.13). TD-DFT calculations have been performed for naft-1-4, both in neutral and in oxidized or reduced states up to tetranion species. The theoretical data together with the experimental results are summarized in Table 3.6.

TD-DFT calculated vertical transitions energies for naft-1 as neutral and radical cation are shown in Figure 3.12(a), and those of naft-1 as neutral, radical anion and dianion species are shown in Figure 3.12(b).
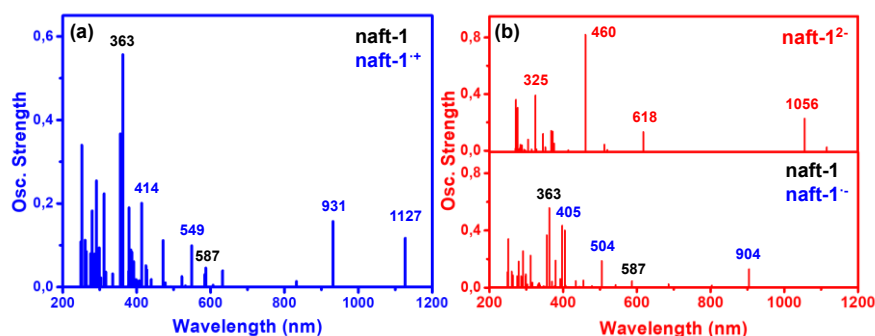
Figure 3.12. TD-DFT calculated vertical transition energies for naft-1 as (a) neutral and the radical cation and (b) neutral, radical anion and dianion species at the PBE0/6-31G** - PCM(CH_2Cl_2) level.

Note that Figure 3.12(a) shows numerous electronic transitions corresponding to the cation that appear between ~380-700 nm and two main electronic transitions between 900 and 1200 nm, explaining the experimental bands at 430 and 551 nm as well as the low and broad experimental absorption centered at 1029 nm, respectively, in Figure 3.9(a). On the other hand, Figure 3.12(b) shows the electronic transitions of the radical anion and dianion red-shifted compared to the neutral species, thus, TD-DFT calculations provide a reliable assignment of the UV-Vis/NIR absorption spectra of the naft-1 oxidized and reduced species.

TD-DFT calculations of naft-2-4 systems (Figure 3.13), indicate that for these systems, the first isolated reduced specie is indeed a radical anion (blue bars); however, a gradual increment of the potential leads directly to a triple negatively charged species (cyan bars), followed by the tetranion formation (pink bars).
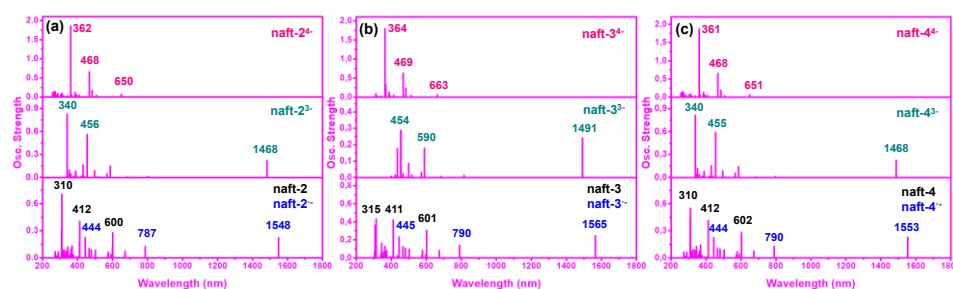
Figure 3.13. TD-DFT calculated vertical transition energies for naft-2-4 as neutral, radical anion, trianion and tetranion species at the PBE0/6-31G** - PCM(CH$_2$Cl$_2$) level.

Table 3.6. UV-Vis/NIR absorption data of naft-1-4 as neutral, anion, dianion, trianion and tetranion species and TD-DFT calculations at PBE0/6-31G**-PCM(CH_2Cl_2) level.

Experimental data (nm)				
naft-1	**naft-1·+**	**naft-1·-**		**naft-1²⁻**
336, 376, 587	430, 1028	348, 584		387, 443, 617
naft-2	**naft-2·+**	**naft-2·-**	**naft-2³⁻**	**naft-2⁴⁻**
328, 411, 551	-	354, 497, 800, 1586	382, 606, 1783	389, 467, 604
naft-3	**naft-3·+**	**naft-3·-**	**naft-3³⁻**	**naft-3⁴⁻**
329, 411, 551	-	359, 498, 800, 1586	382, 606, 1784	394, 606
naft-4	**naft-4·+**	**naft-4·-**	**naft-4³⁻**	**naft-4⁴⁻**
328, 410, 551	-	354, 497, 800, 1586	382, 531, 1783	389, 467, 604
Theoretical data (nm)				
naft-1	**naft-1·+**	**naft-1·-**	**naft-1³⁻**	**naft-1⁴⁻**
363 (f), 587	414, 549, 931, 1127	405, 504, 904	-	-
naft-2	**naft-2·+**	**naft-1·-**	**naft-2³⁻**	**naft-2⁴⁻**
310, 412, 600	-	444, 787, 1548	340, 456, 1468	362, 468, 650
naft-3	**naft-3·+**	**naft-3·-**	**naft-3³⁻**	**naft-3⁴⁻**
315, 411, 601	-	445, 790, 1565	454, 590, 1491	364, 469, 663
naft-4	**naft-4·+**	**naft-4·-**	**naft-4³⁻**	**naft-4⁴⁻**
361, 468, 651	-	444, 790, 1553	340, 455, 1468	361, 468, 651
The values in parenthesis are the oscillator strengths.				

The spectroelectrochemical experiment for naft-1-4 were also performed in chloroform solutions in the presence of high excess of (*n*-Bu)₄NBF₄ as supporting electrolyte (Figure 3.14 and 3.15). In this case, a similar reduction absorption pattern was obtained, however the reduced species are less stabilized in chloroform than in dichloromethane (Table 3.6). This stabilization was predicted theoretically (see Table 3.3).
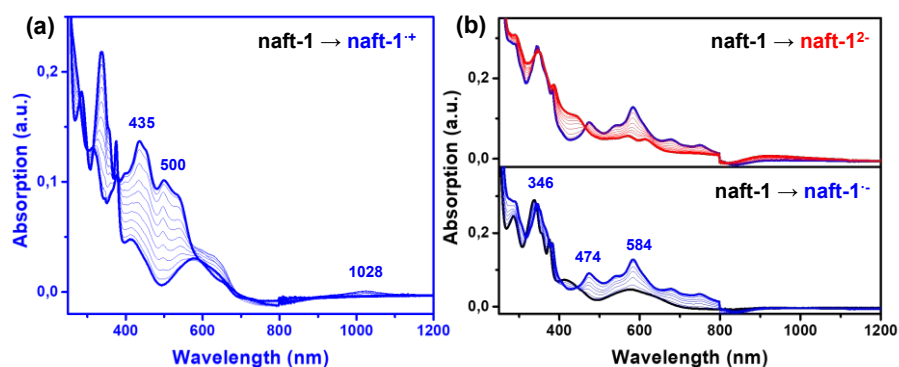
Figure 3.14. UV-Vis/NIR absorption spectra of naft-1 recorded (a) upon electrochemical oxidation (1.60 V), and (b) during the first step of electrochemical reduction (-1.06 V, blue curve) and the second step of the electrochemical reduction (-1.46 V, red curve) in CHCl$_3$ solution at room temperature in presence of (n-Bu)$_4$NBF$_4$ supporting electrolyte within an OTTLE cell.
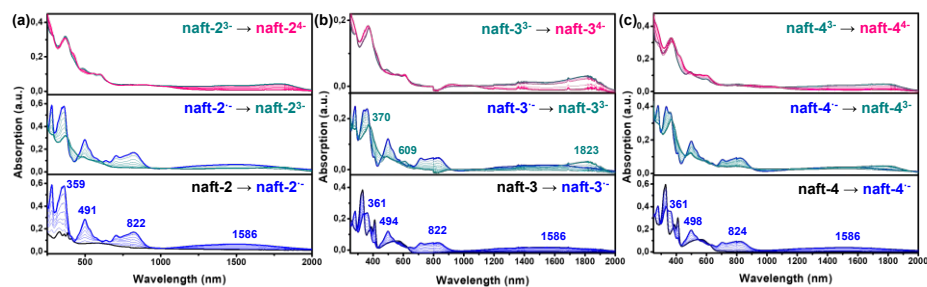
Figure 3.15. UV-Vis/NIR absorption spectra of (a) naft-2, (b) naft-3 and (c) naft-4 recorded during the first step of electrochemical reduction (~ -0.70 V, blue curve), the second step of the electrochemical reduction (~ -1.10 V, cyan curve) and the third step of electrochemical reduction (~ -1.30 V, pink curve) in CHCl$_3$ solution at room temperature in presence of (n-Bu)$_4$NBF$_4$ supporting electrolyte within an OTTLE cell.

3.4. Electrical characterization

3.4.1. Organic Field Effect Transistors

In order to evaluate the charge transport properties of naft-1-4 semiconductors, OFETs with a TCBG configuration were fabricated. To this end Si/SiO$_2$ substrates were used, previously functionalized with octadecyltrichlorosilane (OTS) SAM, on top of which the naft-1-4 semiconducors were thermally evaporated. During the thermal evaporation of the semiconductors, the substrate temperature was set at 25 and 90 ºC. Finally, Au was thermally evaporated as contact electrodes to complete the device fabrication. The transistor characterization was carried out under vacuum conditions. The representative transistor curves of the OFETs fabricated under the optimal conditions are illustrated in Figure 3.16 and 3.17, and their performance parameters are summarized in Table 3.7.

Table 3.7 TCBG OFET performance parameters of the naft-1-4 semiconductors fabricated under the optimal conditions. The semiconductor layers were vapor deposited films and the parameters were measured in vacuum. Average field-effect mobility values from at least 5 devices are shown.

Electron transporting properties				
Semiconductor	Deposition conditions	$\mu_{e,sat}$ $(cm^2 V^{-1} s^{-1})^a$	V_{TH} (V)	I_{ON}/I_{OFF}
naft-1	OTS, 25 ºC	-	-	-
naft-1	OTS, 90 ºC	$7x10^{-4}$	14	10^3
naft-2	OTS, 25 ºC	-	-	-
naft-2	OTS, 90 ºC	$2x10^{-4}$	44	10^1
naft-4	OTS, 25 ºC	$6x10^{-3}$	-18	10^4
naft-4	OTS, 90 ºC	$5x10^{-3}$	22	10^4
Hole transporting properties				
naft-1	OTS, 25 ºC	-	-	-
naft-1	OTS, 90 ºC	$6x10^{-5}$	-46	$7x10^4$
[a]The mobilities were calculated with the average slop within V_{GS} = 70–80 V.				

As seen in Table 3.7 and Figure 3.16, naft-1 exhibits both n-type and p-type OFET characteristics, in good agreement with its amphoteric redox behavior. However, for naft-2 and naft-4 only electron mobilities were recorded. On the other hand, no electrical activity was observed for naft-3 semiconductor.
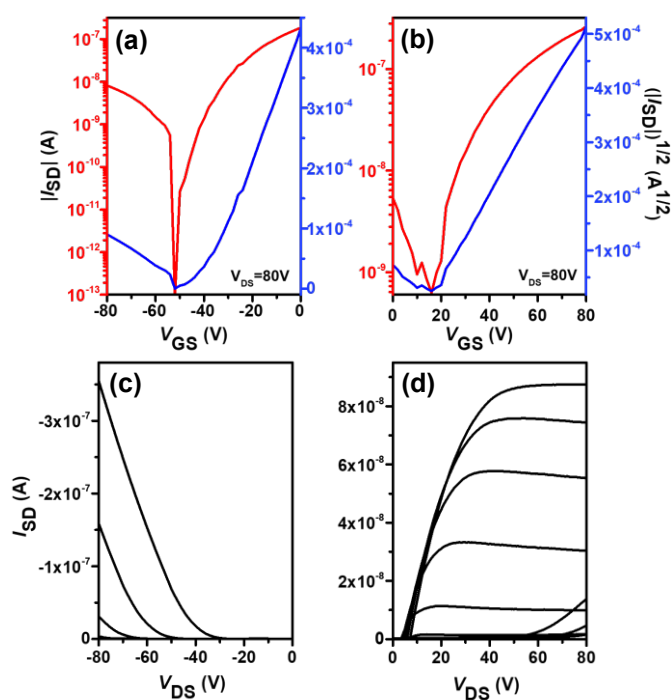
Figure 3.16. OFET transfer (V_{DS} = -80V and 80V, respectively) and output (V_{GS} ranges from 0 to -80 V and from 0 to 80 V, respectively, in steps of 10 V) characteristics of naft-1 semiconductor deposited at 90 ºC: (a-c) as hole transporting and (b-d) as electron transporting materials.

As seen in Table 3.8, naft-1 thin films deposited at 90 ºC exhibit electron and hole mobilities of ~ 7 x 10^{-4} $cm^2 V^{-1} s^{-1}$ and ~ 6 x 10^{-5} $cm^2 V^{-1} s^{-1}$, respectively. The electron field-effect mobility is though one order of magnitude lower than those obtained for naft-4 (Figure 3.17 (b-c) and (e-f)), the best performing material within the series. This can be understood considering the lower ability of naft-1 to stabilize an extra electron and also the naft-1 skeletal distortion of ~16 º (Figure 3.2), compared to naft-4.
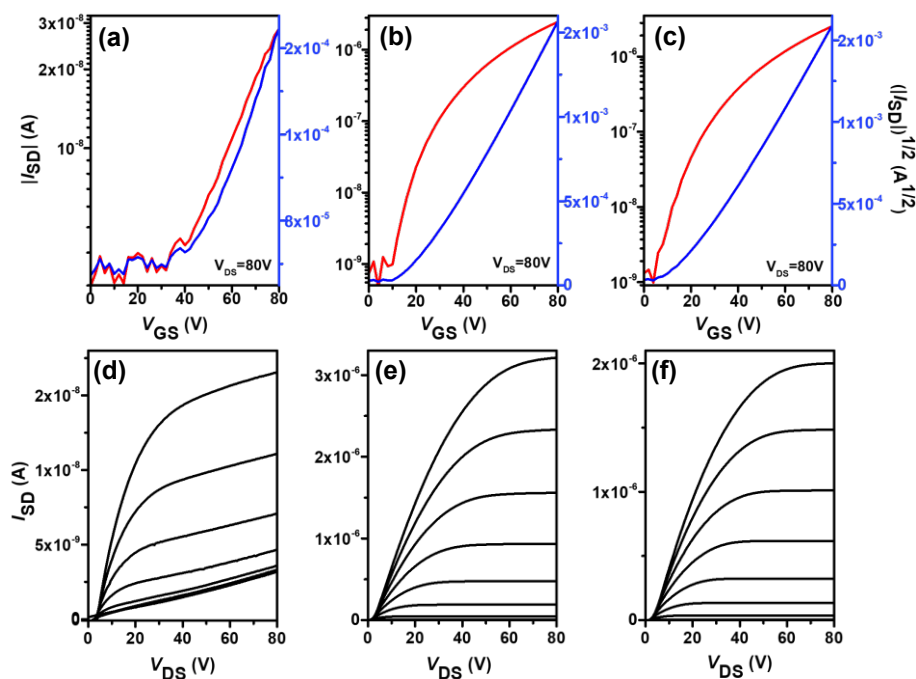
Figure 3.17. (a-c) Transfer and (d-f) output characteristics of OFET devices of (a,d) naft-2 and (b,e) naft-4 semiconductors deposited on the substrate at 90 °C and (c,f) naft-4 semiconductor deposited on the substrate at 25 °C. The gate voltage range in the output plots is 0-80 V with 10 V intervals.

On the other hand, the presence of different substituents at the imide nitrogen in naft-2-4 seems to be crucial to tune the electron transport, since molecular aggregation and crystal packing is greatly affected by the lateral substituents. Thus, devices fabricated by using naft-3, with bulky 3,5-diisopropylphenyl lateral groups, were not active. In contrast, naft-4 exhibits the highest electron mobility (Figure 3.17 (b) and (e)), with a maximum value of 6 x 10^{-3} cm^2 V^{-1} s^{-1} for films deposited at 90 °C. A similar electron mobility was obtained when the film of naft-4 was grown at room temperature (Figure 3.17 (c) and (f)).

The OFET performance of naft-2 (Figure 3.17 (a) and (d)), with shorter alkyl chains at the imide nitrogen, decreases by approximately 10-fold in comparison to naft-4 films when deposited at 90ºC, and no electrical activity was observed for naft-2 OFETs when films were grown at room temperature. Note that the alkyl substituents at the imide nitrogen atoms are longer in naft-4, and thus intermolecular hydrophobic interactions between the long alkyl chains, also known as fastener effect, may be the reason behind the higher electrical performance, due to enhanced intermolecular overlap of the semiconductor layer[37–40].

3.5.   Morphological characterization of thin films

3.5.1. XRD and AFM measurements

The charge transport through the channel in OFETs occurs at the semiconductor-dielectric interface. Therefore, the organic semiconductor films must exhibit large grains, and low boundary and trap density at the interface to favor effective charge carrier transport[41]. In addition, the semiconductor molecules must preferentially be oriented in the way where π-π interactions go in the charge transport direction. A direct characterization of the semiconductor-dielectric interface is not an easy task, however characterizing the semiconductor layers could help to correlate the microstructure of these layers with the charge transport in the active region.

Thus, thin film morphologies of naft-1-4 vacuum deposited on Si/SiO$_2$ were characterized by X-ray diffraction (XRD) and atomic force microscopy (AFM) (Figure 3.18 and 3.19, respectively).

XRD profiles of naft-2 and naft-4, grown at 25 and 90 °C (Figure 3.18), show one sharp peak, indicating certain molecular ordering at the interface. However, films grown at 90 °C show higher crystallinity than films grown at 25 °C. In the case of naft-4 semiconductor, the longer substituents render more ordered films, in agreement with stronger intermolecular hydrophobic interactions promoted by the alkyl substituents.
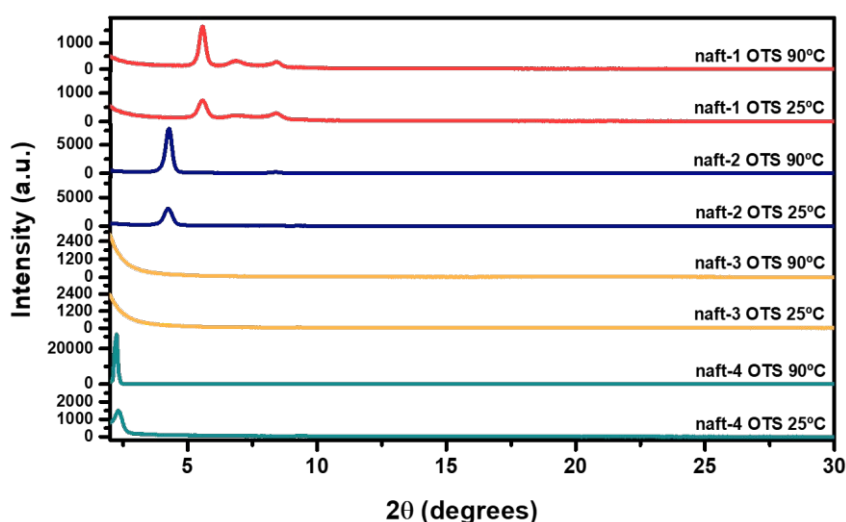
Figure 3.18. Ɵ-2Ɵ X-ray diffraction scans of vapor-deposited naft-1-4 thin films grown on OTS-treated Si/SiO$_2$ substrates at different substrate temperatures.

On the contrary, the morphology of naft-3 is very different from that of naft-2 and naft-4 films. XRD data show a completely amorphous film for this semiconductor (Figure 3.18), due to the incorporation of bulky substituents at the N of the imide group. These diisopropylphenyl groups are orthogonal to the π-conjugated core (see Figure 3.5), thus preventing proper molecular organization at the semiconducting layer, which is translated to poorly performing devices.

The XRD pattern of naft-1 also shows certain molecular ordering, with the recording of several diffraction peaks that gain intensity after a thermal annealing.

naft-2-4 thin films deposited at 25 and 90ºC were also characterized by AFM and the images are shown in Figure 3.19. The AFM image of naft-1 film shows the formation of needle-like crystallites in accordance with the ordered structures. AFM images nicely follow the trend found by XRD and in the electrical characterization of the studied semiconductors. In fact, quite amorphous morphologies are found for naft-3 films, having bulky and non-planar substituents.
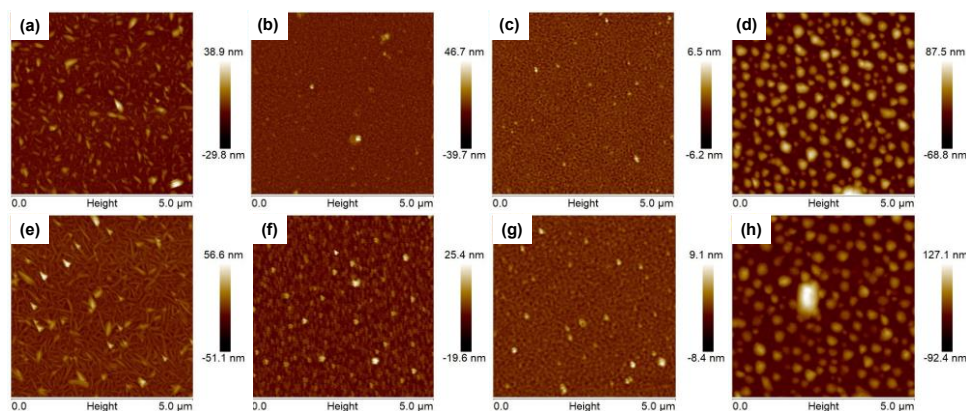
Figure 3.19. AFM phase images of thin films of (a,e) naft-1, (b,f) naft-2 (c,g) naft-3 and (d,h) naft-4 before and after thermal annealing, respectively, grown by vapor deposition on OTS-treated Si/SiO$_2$ substrates. (e-f) show the conditions yielding optimum OFET performance. Image size 5 x 5 mm.

On the other hand, round features are found for naft-2 and naft-4 thin films deposited at 90 ºC, the latter showing bigger crystalline domains due to more efficient hydrophobic intermolecular interactions between longer alkyl chains. Note that the same features are found for naft-4 films

deposited at 25 ºC, however the AFM image of naft-2 film grown at 25 ºC shows quite amorphous morphology, which is translated to poorly performing devices.

3.6. References

[1]   Seifert, S.; Schmidt, D.; Shoyama, K.; Würthner, F. Base-Selective Five- versus Six-Membered Ring Annulation in Palladium-Catalyzed C–C Coupling Cascade Reactions: New Access to Electron-Poor Polycyclic Aromatic Dicarboximides. *Angew. Chemie Int. Ed.* **2017**, *56*, 7595–7600.

[2]   Seifert, S.; Schmidt, D.; Würthner, F. A Cross-Coupling-Annulation Cascade from Peri-Dibromonaphthalimide to Pseudo-Rylene Bisimides. *Org. Chem. Front.* **2016**, *3*, 1435–1442.

[3]   Shoyama, K.; Mahl, M.; Seifert, S.; Würthner, F. A General Synthetic Route to Polycyclic Aromatic Dicarboximides by Palladium-Catalyzed Annulation Reaction. *J. Org. Chem.* **2018**, *83*, 5339–5346.

[4]   Zhylitskaya, H.; Cybińska, J.; Chmielewski, P.; Lis, T.; Stępień, M. Bandgap Engineering in π-Extended Pyrroles. A Modular Approach to Electron-Deficient Chromophores with Multi-Redox Activity. *J. Am. Chem. Soc.* **2016**, *138*, 11390–11398.

[5]   Liang, N.; Meng, D.; Wang, Z. Giant Rylene Imide-Based Electron Acceptors for Organic Photovoltaics. *Acc. Chem. Res.* **2021**, *54*, 961–975.

[6]   Pigulski, B.; Ximenis, M.; Shoyama, K.; Würthner, F. Synthesis of Polycyclic Aromatic Hydrocarbons by Palladium-Catalysed [3 + 3] Annulation. *Org. Chem. Front.* **2020**, *7*, 2925–2930.

[7]   Đorđević, L.; Milano, D.; Demitri, N.; Bonifazi, D. O-Annulation to Polycyclic Aromatic Hydrocarbons: A Tale of Optoelectronic Properties from Five- to Seven-Membered Rings. *Org. Lett.* **2020**, *22*, 4283–4288.

[8]   Wu, W.; Liu, Y.; Zhu, D. π-Conjugated Molecules with Fused Rings for Organic Field-Effect Transistors: Design, Synthesis and Applications. *Chem. Soc. Rev.* **2010**, *39*, 1489–1502.

[9]   Shi, Q.; Shi, X.; Feng, C.; Wu, Y.; Zheng, N.; Liu, J.; Wu, X.; Chen, H.; Peng, A.; Li, J.; Jiang, L.; Fu, H.; Xie, Z.; Marder, S. R.; Blakey, S. B.; Huang, H. Synthetic Routes for Heteroatom-Containing Alkylated/Arylated Polycyclic Aromatic Hydrocarbons. *Angew. Chemie Int. Ed.* **2021**, *60*, 2924–2928.

[10]   Liu, S.; Li, C.; Xu, Y.; Li, Z.; Huang, H.; Fu, N.; Shao, J.; Zhao, B.; Huang, H.; Huang, W. Optoelectronic Properties and Aggregation Effects on the Performance of Planar versus Contorted Pyrene-Cored Perylenediimide Dimers for Organic Solar Cells. *Dye. Pigment.* **2020**, *173*, 107976.

[11]   Liu, W.; Shaikh, D. B.; Rao, P. S.; Bhosale, R. S.; Said, A. A.; Mak, A. M.; Wang, Z.; Zhao, M.; Gao, W.; Chen, B.; Lam, Y. M.; Fan, W.; Bhosale, S. V; Bhosale, S. V; Zhang, Q. Molecular Aggregation of Naphthalene Diimide(NDI) Derivatives in Electron Transport Layers of Inverted Perovskite Solar Cells and Their Influence on the Device Performance. *Chem. – An Asian J.* **2020**, *15*, 112–121.

[12]   Kumari, N.; Naqvi, S.; Ahuja, M.; Bhardwaj, K.; Kumar, R. Facile Synthesis of Naphthalene Diimide (NDI) Derivatives: Aggregation-Induced Emission, Photophysical and Transport Properties. *J. Mater. Sci. Mater. Electron.* **2020**, *31*, 4310–4322.

[13]   Murata, T.; Koide, T.; Nobukuni, H.; Tsuji, R.; and Morita, Y. 2D Coordination Network of Trioxotriangulene with Multiple Redox Abilities and Its Rechargeable Battery Performance. *Int. J. Mol. Sci.* **2020**, *21*, 4723–4736.

[14]   Schon, T. B.; McAllister, B. T.; Li, P.-F.; Seferos, D. S. The Rise of Organic Electrode Materials for Energy Storage. *Chem. Soc. Rev.* **2016**, *45*, 6345–6404.

[15]   Liu, G.; Xiao, C.; Negri, F.; Li, Y.; Wang, Z. Dodecatwistarene Imides with Zigzag-Twisted Conformation for Organic Electronics. *Angew. Chemie Int. Ed.* **2020**, *59*, 2008–2012.

[16]   Wang, R.; Shi, K.; Cai, K.; Guo, Y.; Yang, X.; Wang, J.-Y.; Pei, J.; Zhao, D. Syntheses of Polycyclic Aromatic Diimides via Intramolecular Cyclization of Maleic Acid Derivatives. *New J. Chem.* **2016**, *40*, 113–121.

[17]   Sun, H.; Wang, L.; Wang, Y.; Guo, X. Imide-Functionalized Polymer Semiconductors. *Chem. – A Eur. J.* **2019**, *25*, 87–105.

[18]   Jones, B. A.; Facchetti, A.; Wasielewski, M. R.; Marks, T. J. Tuning Orbital Energetics in Arylene Diimide Semiconductors. Materials Design for Ambient Stability of n-Type Charge Transport. *J. Am. Chem. Soc.* **2007**, *129*, 15259–15278.

[19]   Ledwon, P.; Ovsiannikova, D.; Jarosz, T.; Gogoc, S.; Nitschke, P.; Domagala, W. Insight into the Properties and Redox States of N-Dopable Conjugated Polymers Based on Naphtalene Diimide Units. *Electrochim. Acta* **2019**, *307*, 525–535.

[20]   Di Donato, E.; Fornari, R. P.; Di Motta, S.; Li, Y.; Wang, Z.; Negri, F. N-Type Charge Transport and Mobility of Fluorinated Perylene Bisimide Semiconductors. *J. Phys. Chem. B* **2010**, *114*, 5327–5334.

[21]   Ortiz, R. P.; Herrera, H.; Blanco, R.; Huang, H.; Facchetti, A.; Marks, T. J.; Zheng, Y.; Segura, J. L. Organic N-Channel Field-Effect Transistors Based on Arylenediimide-Thiophene Derivatives. *J. Am. Chem. Soc.* **2010**, *132*, 8440–8452.

[22]   Merz, J.; Steffen, A.; Nitsch, J.; Fink, J.; Schürger, C. B.; Friedrich, A.; Krummenacher, I.; Braunschweig, H.; Moos, M.; Mims, D.; Lambert, C.; Marder, T. B. Synthesis, Photophysical and Electronic Properties of Tetra-Donor- or Acceptor-Substituted Ortho-Perylenes Displaying Four Reversible Oxidations or Reductions. *Chem. Sci.* **2019**, *10*, 7516–7534.

[23]   Shi, Y.; Tang, H.; Jiang, S.; Kayser, L. V; Li, M.; Liu, F.; Ji, F.; Lipomi, D. J.; Ong, S. P.; Chen, Z. Understanding the Electrochemical Properties of Naphthalene Diimide: Implication for Stable and High-Rate Lithium-Ion Battery Electrodes. *Chem. Mater.* **2018**, *30*, 3508–3517.

[24]   Ackermann, L.; Vicente, R.; Kapdi, A. R. Transition-Metal-Catalyzed Direct Arylation of (Hetero)Arenes by C□H Bond Cleavage. *Angew. Chemie Int. Ed.* **2009**, *48*, 9792–9826.

[25]   Alonso-Navarro, M. J.; Harbuzaru, A.; Martínez-Fernández, M.; Pérez Camero, P.; López Navarrete, J. T.; Ramos, M. M.; Ponce Ortiz, R.; Segura, J. L. Synthesis and Electronic Properties of Nitrogen-Doped π-Extended Polycyclic Aromatic Dicarboximides with Multiple Redox Processes. *J. Mater. Chem. C* **2021**, *9*, 7936–7949.

[26]   Hu, J.; Zhang, D.; Harris, F. W. Ruthenium(III) Chloride Catalyzed Oxidation of Pyrene and 2,7-Disubstitued Pyrenes: An Efficient, One-Step Synthesis of Pyrene-4,5-Diones and Pyrene-4,5,9,10-Tetraones. *J. Org. Chem.* **2005**, *70*, 707–708.

[27]   Li, H.; Kim, F. S.; Ren, G.; Hollenbeck, E. C.; Subramaniyan, S.; Jenekhe, S. A. Tetraazabenzodifluoranthene Diimides: Building Blocks for Solution-Processable n-Type Organic Semiconductors. *Angew. Chemie Int. Ed.* **2013**, *52*, 5513–5517.

[28]   Herrera, H.; de Echegaray, P.; Urdanpilleta, M.; Mancheño, M. J.; Mena-Osteritz, E.; Bäuerle, P.; Segura, J. L. Linear and Star-Shaped Naphthalimide-Fused Pyrazinacenes. *Chem. Commun.* **2013**, *49*, 713–715.

[29]   de Echegaray, P.; Mancheño, M. J.; Arrechea-Marcos, I.; Juárez, R.; López-Espejo, G.; López Navarrete, J. T.; Ramos, M. M.; Seoane, C.; Ortiz, R. P.; Segura, J. L. Synthesis of Perylene Imide Diones as Platforms for the Development of Pyrazine Based Organic Semiconductors. *J. Org. Chem.* **2016**, *81*, 11256–11267.

[30]   Richards, G. J.; Cador, A.; Yamada, S.; Middleton, A.; Webre, W. A.; Labuta, J.; Karr, P. A.; Ariga, K.; D'Souza, F.; Kahlal, S.; Halet, J.-F.; Hill, J. P. Amphiprotism-Coupled Near-Infrared Emission in Extended Pyrazinacenes Containing Seven Linearly Fused Pyrazine Units. *J. Am. Chem. Soc.* **2019**, *141*, 19570–19574.

[31]   Ferrón, C. C.; Delgado, M. C. R.; Hernández, V.; Navarrete, J. T. L.; Vercelli, B.; Zotti, G.; Cortada, M. C.; Novoa, J. J.; Niu, W.; He, M.; Hartl, F. Substituent and Counterion Effects on the Formation of π-Dimer Dications of End-Capped Heptathienoacenes. *Chem. Commun.* **2011**, *47*, 12622–12624.

[32]   Adamo, C.; Barone, V. Toward Reliable Density Functional Methods without Adjustable Parameters: The PBE0 Model. *J. Chem. Phys.* **1999**, *110*, 6158–6170.

[33]   de la Peña, A.; Arrechea-Marcos, I.; Mancheño, M. J.; Ruiz Delgado, M. C.; López Navarrete, J. T.; Segura, J. L.; Ponce Ortiz, R. Tuning of the Electronic Levels of Oligothiophene–Naphthalimide Assemblies by Chemical Modification. *Chem. – A Eur. J.* **2016**, *22*, 13643–13652.

[34]   Drolet, N.; Morin, J.-F.; Leclerc, N.; Wakim, S.; Tao, Y.; Leclerc, M. 2,7-Carbazolenevinylene-Based Oligomer Thin-Film Transistors: High Mobility Through Structural Ordering. *Adv. Funct. Mater.* **2005**, *15*, 1671–1682.

[35]   Gawrys, P.; Marszalek, T.; Bartnik, E.; Kucinska, M.; Ulanski, J.; Zagorska, M. Novel, Low-Cost, Highly Soluble n-Type Semiconductors: Tetraazaanthracene Tetraesters. *Org. Lett.* **2011**, *13*, 6090–6093.

[36]   Zhu, M.; Zhang, J.; Yu, G.; Chen, H.; Huang, J.; Liu, Y. Dialkyl-14H-Benzo[4,5]Isoquino[2,3-a]Perimidin-14-One-3,4,10,11-Tetracarboxylic Diimides: A New Family of n-Type Organic Semiconductors. *Chem. – An Asian J.* **2012**, *7*, 2208–2212.

[37]   Yamaguchi, Y.; Kojiguchi, Y.; Kawata, S.; Mori, T.; Okamoto, K.; Tsutsui, M.; Koganezawa, T.; Katagiri, H.; Yasuda, T. Solution-Processable Organic Semiconductors Featuring S-Shaped Dinaphthothienothiophene (S-DNTT): Effects of Alkyl Chain Length on Self-Organization and Carrier Transport Properties. *Chem. Mater.* **2020**, *32*, 5350–5360.

[38]   Welford, A.; Maniam, S.; Gann, E.; Jiao, X.; Thomsen, L.; Langford, S. J.; McNeill, C. R. Influence of Alkyl Side-Chain Type and Length on the Thin Film Microstructure and OFET Performance of

Naphthalene Diimide-Based Organic Semiconductors. *Org. Electron.* **2019**, *75*, 105378.

[39]   Izawa, T.; Miyazaki, E.; Takimiya, K. Molecular Ordering of High-Performance Soluble Molecular Semiconductors and Re-Evaluation of Their Field-Effect Transistor Characteristics. *Adv. Mater.* **2008**, *20*, 3388–3392.

[40]   Inokuchi, H.; Saito, G.; Wu, P.; Seki, K.; Tang, T. B.; Mori, T.; Imaeda, K.; Enoki, T.; Higuchi, Y.; Inaka, K.; Yasuoka, N. A Novel Type of Organic Semiconductors. Molecular Fastener. *Chem. Lett.* **1986**, *15*, 1263–1266.

[41]   Di, C.; Liu, Y.; Yu, G.; Zhu, D. Interface Engineering: An Effective Approach toward High-Performance Organic Field-Effect Transistors. *Acc. Chem. Res.* **2009**, *42*, 1573–1583.

Chapter 4. (Semi)ladder-type all-acceptor polymers based on bithienoimide units

Contents:

4.1. Introduction

The bithienoimide (BTI) molecules[1–7] presented in the Chapter 1 are one of the most promising building blocks for constructing high-performance acceptor-acceptor (A-A)-type polymers[6–20], whose development is still a great challenge.

A-A-type polymers are highly desired for more ideal transistor performance characteristics, since they could lead to semiconductors with deep LUMOs, which facilitate electron injection, and low-lying HOMOs, necessary to suppress hole accumulation, in order to achieve unipolar n-type semiconductors. Nevertheless, the development of polymers based on electron-deficient acceptor (A-A) units is limited by factors such as: i) the limited choice of the acceptor units[21], which make challenging the design and synthesis of new polymer semiconductors, leading to a limited library of materials; and ii) the high backbone torsion normally caused by strong electron-withdrawing groups; for instance, carbonyl and cyano groups can enable n-type performance, but since they are typically bulky, may generate a significant steric hindrance leading to twisted polymer chains[13,22,23]. The backbone torsions are detrimental not only to the intrachain delocalization of charge carriers, but also to the interchain transport as a result of poor molecular packing and low film crystallinity, which subsequently lead to low electron mobility[14].

Ladder-type conjugated molecules based on bithienoimide (BTI) units are an effective structure to explore materials for high electron mobility, since they combine features such as rigidity, planar backbone and thus, enhanced π-π stacking, with the electron-deficiency of the BTI units[1,2,5–7,16,24]. The incorporation of this building block into polymers afforded a series of semiconductors with remarkable performance in

OFETs[2] (mobilities up to 0.2 cm^{2}V^{-1}s^{-1}) and OSCs[6,25] (fill factor of 76-80%).
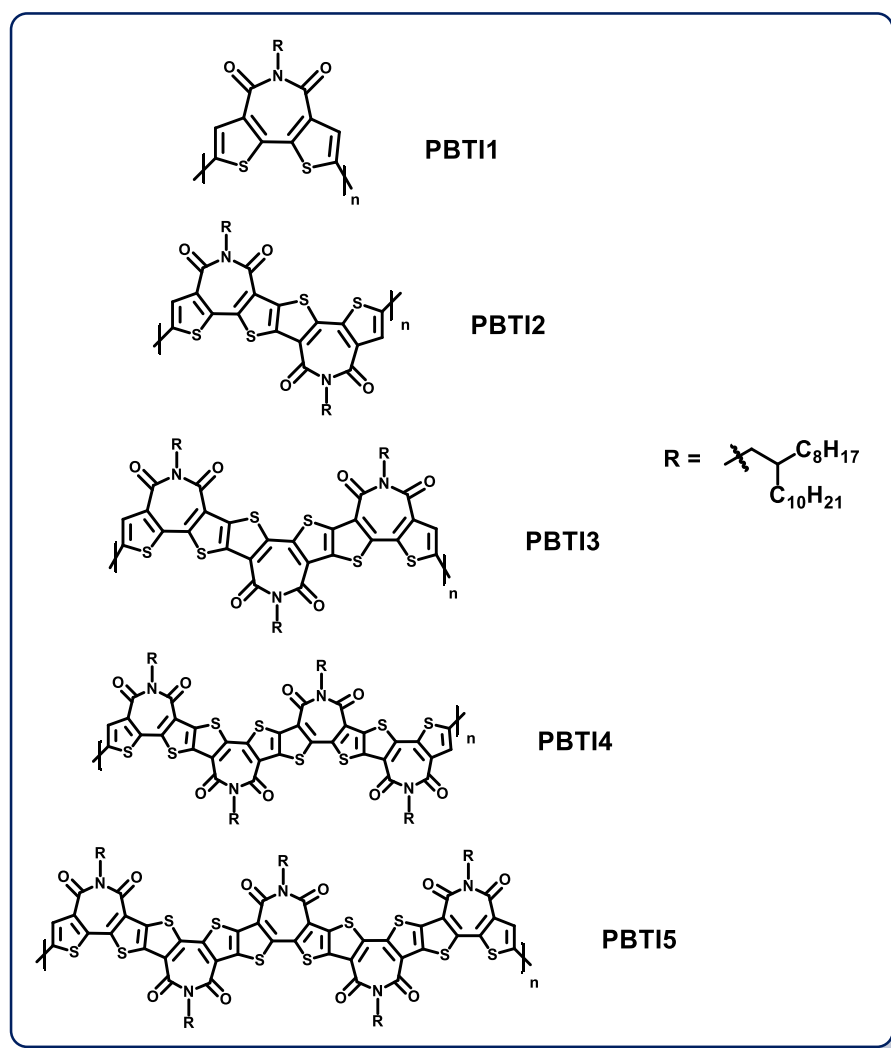
Figure 4.1. Chemical structures of the semiconducting polymers PBTI1-PBTI5.

Therefore, inspired by the excellent performance of BTI-based polymers[1,2,6,25], we studied, in this chapter, a new series of (semi)ladder-

type homopolymers based on BTI units, with increasing chain length from 3 to 15 fused rings *per* building block, respectively (PBTI1-PBTI5 polymers in Figure 4.1).

To this end, a combined experimental/theoretical approach is used in order to characterize these homopolymers (PBTI1-PBTI5), which links UV-Vis absorption, non-resonant and resonant Raman Spectroscopy with DFT and TD-DFT calculations. Raman spectroscopy is used in this chapter with the scope of studying the supramolecular properties of PBTI2-PBTI5 thin films, as previously described by Kim *et al.*[26–33]. In addition, the electrical properties of these fused systems in OFETs have been examined using solution-deposited films which were then characterized by 2D-GIWAXS and AFM techniques.

4.2. Experimental and theoretical study of neutral species

4.2.1. DFT-calculated molecular geometries

The geometries of PBTI1-PBTI5 dimeric models (two repetitive building blocks), optimized at the B3LYP/6-31G** level, are shown in Figure 4.2.

The optimized minimum energy geometries, have quite planar skeletons with dihedral angles, between the two building blocks, lower than 1º, for all the series and having the linkage between the repeating units in a trans configuration.
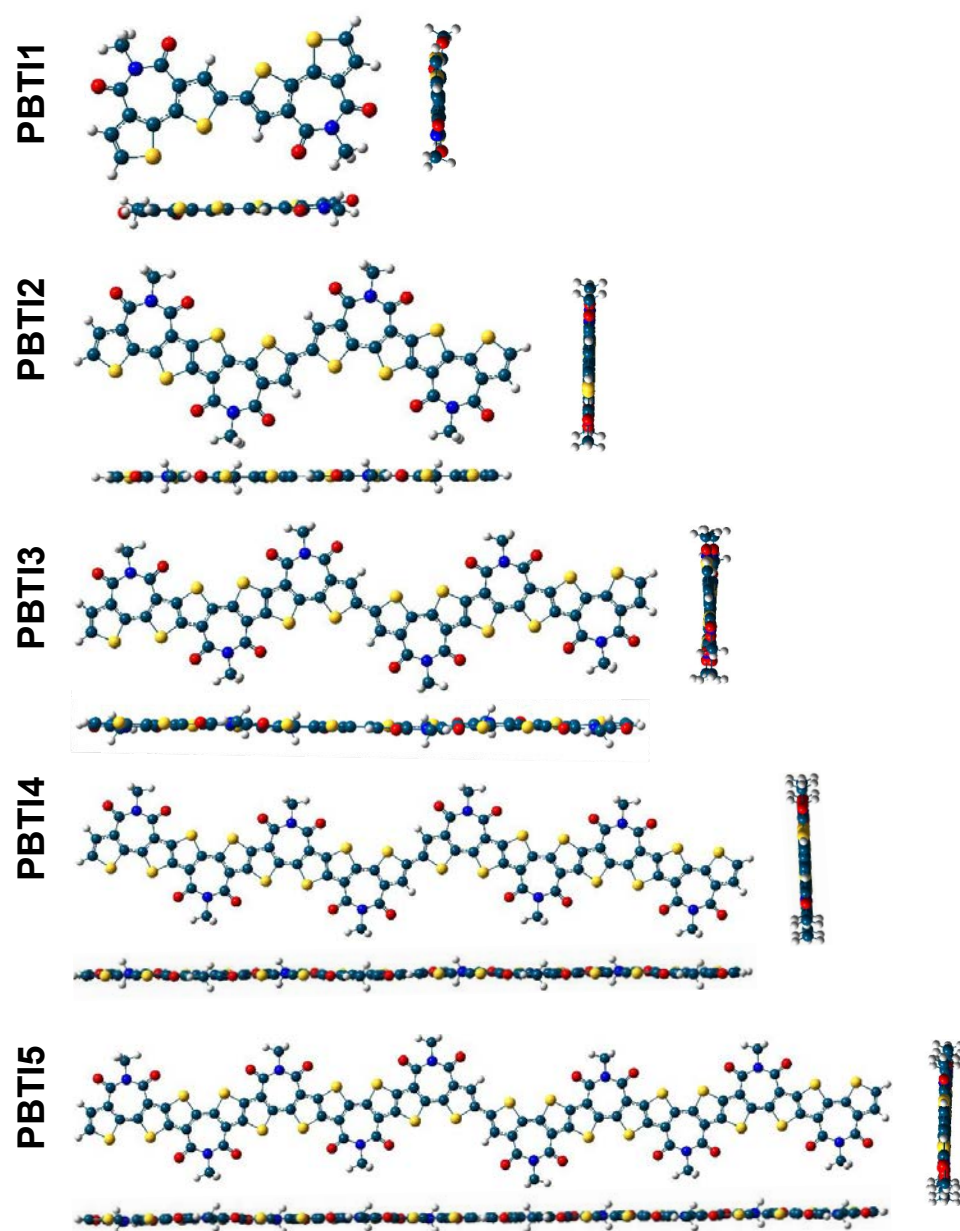
Figure 4.2. Frontal and lateral views of DFT-optimized geometries of PBTI1-PBTI5 dimeric models at B3LYP/6-31G** level. The long alkyl chains have been replaced by methyl groups to simplify calculations and reduce the computational costs and resources.

Figure 4.3 shows the molecular frontier orbital profiles of PBTI1-PBTI5 dimeric models.
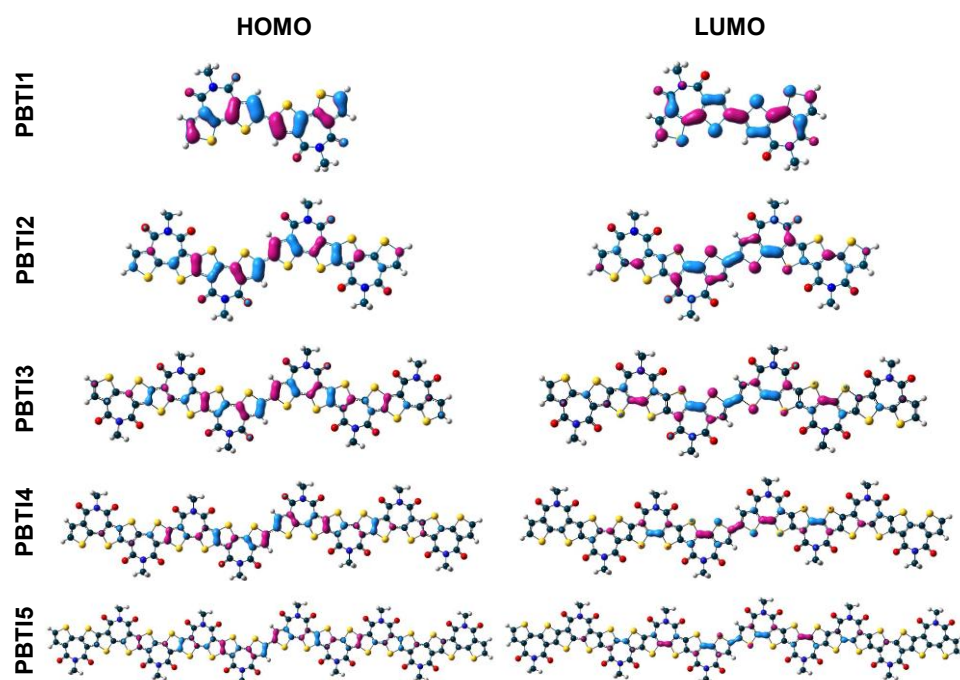
Figure 4.3. DFT-calculated frontier molecular orbital topologies of PBTI1-PBTI5 theoretical models at B3LYP/6-31G** level.

In the shortest system (PBTI1) both HOMO and LUMO are highly delocalized over the whole conjugated skeleton, however a noticeable density confinement in the central part of the conjugated skeleton is found for PBTI2-PBTI5 dimeric models.
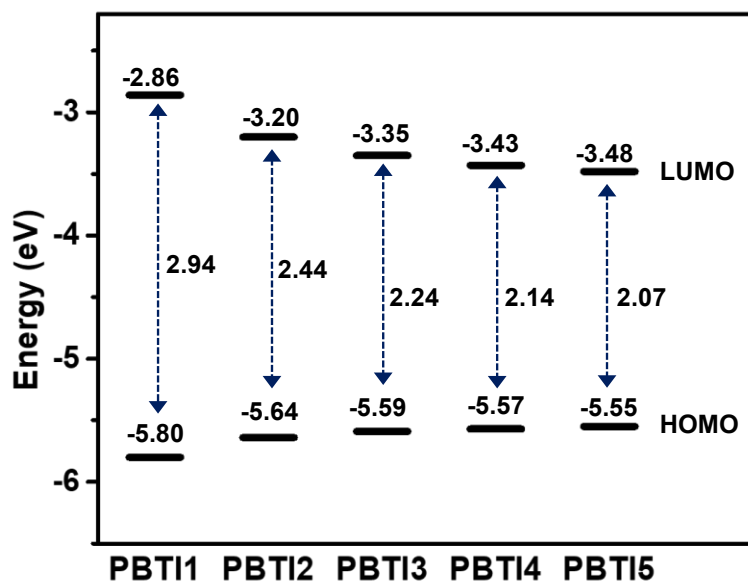
Figure 4.4. DFT-calculated frontier molecular orbital energies and energy gap values for PBTI1-PBTI5 theoretical models at B3LYP/6-31G** level.

As can be seen in Figure 4.4 and Table 4.1, the theoretically predicted HOMO-LUMO gaps decrease from 2.94 to 2.07 eV upon going from PBTI1 to PBTI5, being the decrease more pronounced from PBTI1 to PBTI2 (0.50 eV) than from PBTI2 to PBTI5, showing a similar trend to that found experimentally (see Table 4.1).

Table 4.1. Experimentally and theoretically calculated HOMO and LUMO energy levels, and E_{gap} for PBTI1-PBTI5 homopolymers at the B3LYP/6-31G** level.

	Experimental data			Theoretical data			
	E_{LUMO} (eV)[a]	E_{HOMO} (eV)[b]	E_g^{opt} (eV)	E_{LUMO} (eV)	E_{HOMO} (eV)	E_g (eV)	ΔE_g (eV)
PBTI1	-3.48	-5.46	1.98	-2.86	-5.80	2.94	0.50
PBTI2	-3.53	-5.39	1.86	-3.20	-5.64	2.44	0.20
PBTI3	-3.59	-5.41	1.82	-3.35	-5.59	2.24	0.10
PBTI4	-3.67	-5.47	1.80	-3.43	-5.57	2.14	0.06
PBTI5	-3.72	-5.49	1.77	-3.48	-5.55	2.08	

[a]Electrochemically determined vs Fc/Fc$^+$. E_{LUMO} = - (E_{red}^{onset} + 4.80). [b]E_{HOMO} = E_{LUMO} − E_g^{opt}.

4.2.2. Intramolecular reorganization energy calculations

The intramolecular reorganization energies values for PBTI1-PBTI5 dimeric models, calculated at the B3LYP/6-31G** level, are collected in Table 4.2.

Table 4.2. DFT-calculated of intramolecular reorganization energies for holes (λ_h) and electrons (λ_e) at B3LYP/6-31G** level.

Molecules	λ (meV)	
	Electron transport (λ_e)	Hole transport (λ_h)
PBTI1	280	290
PBTI2	200	220
PBTI3	150	170
PBTI4	120	130
PBTI5	100	110

The λ values, shown in Table 4.2, decrease upon increasing the building block unit. Ongoing from PBTI1 to PBTI2 and PBTI3 the λ_e shows a significant reduction, however this is less accentuated in the longer systems, PBTI4 and PBTI5. This reduction in the λ values upon increasing

the chain length is reasonable, if we consider that it is easier to delocalize the charge in sistems with a larger number of alternated C-C/C=C bones.

These results are in consonance with the previously obtained data, where the topology of the frontier molecular orbitals, indicates that the charge is delocalized in the central part for PBTI4 and PBTI5 polymers, having a similar extension to that observed for PBTI3.

4.2.3. Optical properties and TD-DFT vertical transition energies

The optical properties of PBTI1-PBTI5 polymers were investigated by measuring their UV-Vis absorption spectra both in solution at different temperatures and as thin films (Figure 4.5), which provide direct evidence of the aggregation process depending on the building block molecular size.
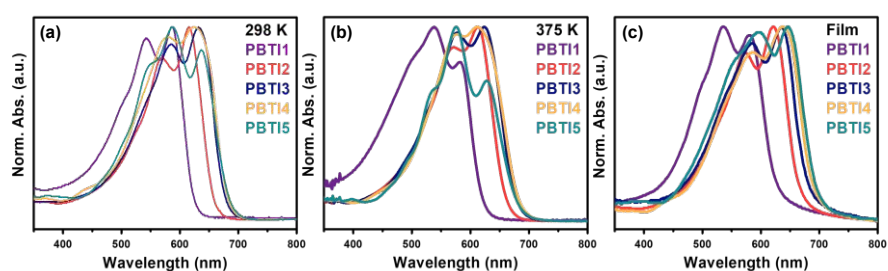
Figure 4.5. UV-Vis absorption spectra of PBTI1-PBTI5 polymers (a) in chlorobenzene solutions at 298 K and (b) 373 K, and (c) as-cast thin films.

In comparison to the small molecules (BTI2-BTI5, Figure 1.4(a)), PBTI1-PBTI5 polymers are strongly aggregated in solution at room temperature (Figure 4.5(a)), but also in heated chlorobenzene solutions at 373 K (Figure 4.5(b)), showing strong 0-0/0-1 vibronic transitions.

On the other hand, by comparing the absorption spectra of PBTI1-PBT5 in solution (Figures 4.5(a) and (b)) and thin film (Figure 4.5(c)), a minimal, red-shifted maximum absorption (~ 10 nm) was observed for the thin film maximum absorptions, which further validate the strong interchain aggregation of these homopolymers in solution.

In the spectra of the PBTI1-PBTI5 thin films (Figure 4.5(c)), the absorption onsets show a gradual bathochromic shift from 626 nm for PBTI1 to 700 nm for PBTI5 and based on these values the optical HOMO-LUMO energy gaps (E_g^{opt} in Table 4.3) were estimated to be 1.98 eV (PBTI1), 1.86 eV (PBTI2), 1.82 eV (PBTI3), 1.80 eV (PBTI4) and 1.77 eV (PBTI5). The optical E_g values, then, decrease 0.12 eV from PBTI1 to PBTI2, however this reduction is much smaller ongoing from PBTI2 to PBTI5 (~ 0.03 eV), suggesting in this case similar level of electron delocalization in the larger homopolymers.

These experimental results are supported by TD-DFT theoretical calculations at the B3LYP/6-31G** level (Figure 4.6). Both experimental and theoretical data are summarized in Table 4.3.
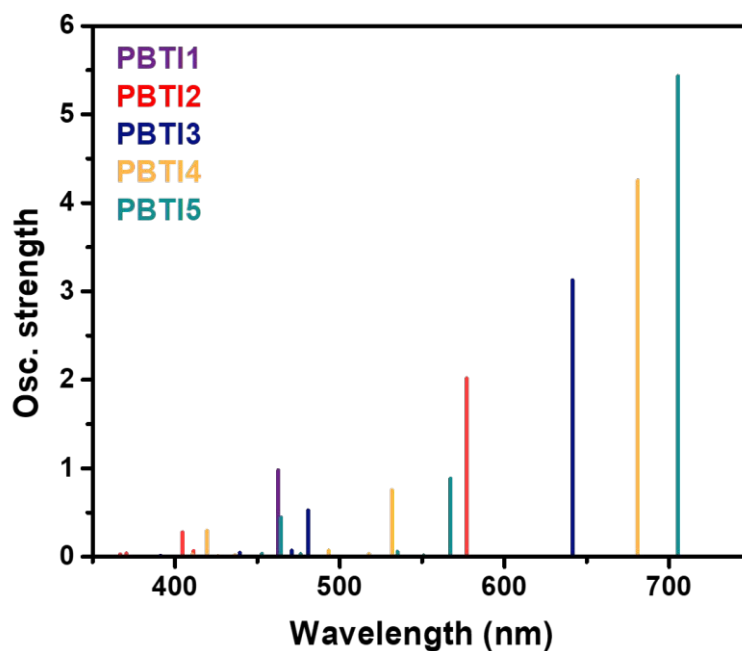
Figure 4.6. TD-DFT calculated vertical transition energies for PBTI1-PBTI5 at the B3LYP/6-31G** level.

As can be seen in Figure 4.6 and Table 4.3, TD-DFT calculated vertical transition energies for neutral PBTI1-PBTI5 are in good agreement with the experimental data (Figure 4.5(a)), predicting the existence of one intense transition that is bathochromically shifted ongoing from PBTI1 to PBTI5. This transition implies the promotion of one electron from the HOMO to the LUMO orbital (see OMs topologies in Figure 4.3).

Table 4.3. Photophysical properties of the PBTI1-PBTI5 homopolymers and the TD-DFT calculated vertical transition energies at B3LYP/6-31G** level.

Experimental data				
Molecules	λ_{abs}^{max} **ClBz at 300 K (nm)**	λ_{abs}^{max} **ClBz at 373 K (nm)**	λ_{abs}^{max} **film (nm)[a]**	λ_{abs}^{onset} **film (nm)[a]**
PBTI1	587	538	535	626
PBTI2	615	612	621	667
PBTI3	632	624	636	680
PBTI4	624	612	638	687
PBTI5	588	576	645	700
Theoretical data				
	λ (nm)	**f**	**Description**	
PBTI1	463	0.98	HOMO → LUMO (100%)	
PBTI2	577	2.02	HOMO → LUMO (99%)	
PBTI3	641	3.13	HOMO → LUMO (96%)	
PBTI4	681	4.25	HOMO → LUMO (93%)	
PBTI5	705	5.43	HOMO → LUMO (88%)	
[c]From as-cast films.				

4.3. Raman spectroscopy

4.3.1. Non-resonant Raman spectroscopy

FT-Raman spectra (λ_{exc}= 1064 nm) of the samples PBTI1-PBTI5 as bulk materials are shown in Figure 4.7.

1513 **1475**   **1453**
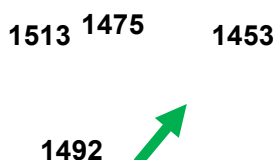
1492

Figure 4.7. FT-Raman spectra (λ_{exc} = 1064 nm) of PBTI1-PBTI5 as powder samples.

As can be seen in Figure 4.7, the spectral profile of the polymer PBTI1 (red curve) is rather simple, and it is dominated by only one intense Raman band at 1492 cm^{-1}, which is assigned to a collective C=C/C-C vibration localized over the whole conjugated skeleton (see eigenvectors in Figure 4.8). However, the spectral profile becomes more complicated as

the chain length of the monomeric units increases ongoing from PBTI2 to PBTI5. The collective C=C/C-C vibration is now splitted into two bands located at 1475 cm^{-1} and 1453 cm^{-1}. Both of them are delocalized over the whole conjugated skeleton, but the former one shows larger contribution on the external BTI units (see eigenvectors in Figure 4.8).

PBTI1
1502 (1492) cm^{-1}

PBTI2
1539 (1513) cm^{-1}

PBTI2
1480 (1475) cm^{-1}
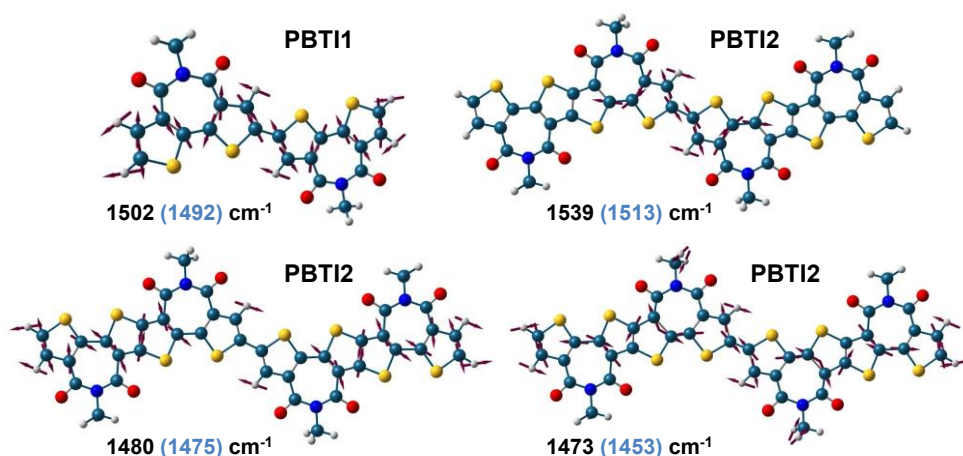
PBTI2
1473 (1453) cm^{-1}

Figure 4.8. Eigenvectors, calculated at B3LYP/6-31** level, of the vibrational Raman normal mode corresponding to the most intense Raman bands for PBTI1 and PBTI2.

These two bands, at 1475 and 1453 cm^{-1}, for PBTI2 are significantly downshifted compared to the most intense Raman band recorded for PBTI1, indicating an increase in the π-conjugation extension. Nevertheless, the position of these two bands experiments only a slight downshift (1-4 cm^{-1}) when the building block extension further increases, indicating similar π-conjugation lengths for PBTI2-PBTI5. These results suggest that the conjugation limit is reached for the BTI2 monomeric building block, which is in good agreement with the polymer band gaps.

In relation to these two bands (1475 and 1453 cm^{-1}), we can also notice a significant change in the relative intensities; that is, the Raman

vibration located at 1475 cm^{-1} loses intensity respect to the one recorded at 1453 cm^{-1}, on increasing the monomers length. This is understandable considering that upon lenghtening of the building block conjugated skeleton, the weigth of external BTI moieties is diminished respect to the whole conjugated skeleton.

Finally, the Raman band appearing at higher wavenumbers (1513 cm^{-1} for PBTI2) is assigned to an asymmetric stretching vibration focused on the C=C bonds of the external thiophene rings of the BTI unit (see eigenvector in Figure 4.8). Therefore, this Raman vibration is highly sensitive to changes in the dihedral angle between two consecutive building blocks and thus can offer information on the molecular ordering in thin film, as demonstrated theretically by predicting the dispersion of this band with the intermonomer dihedral angle, θ (Figure 4.9).
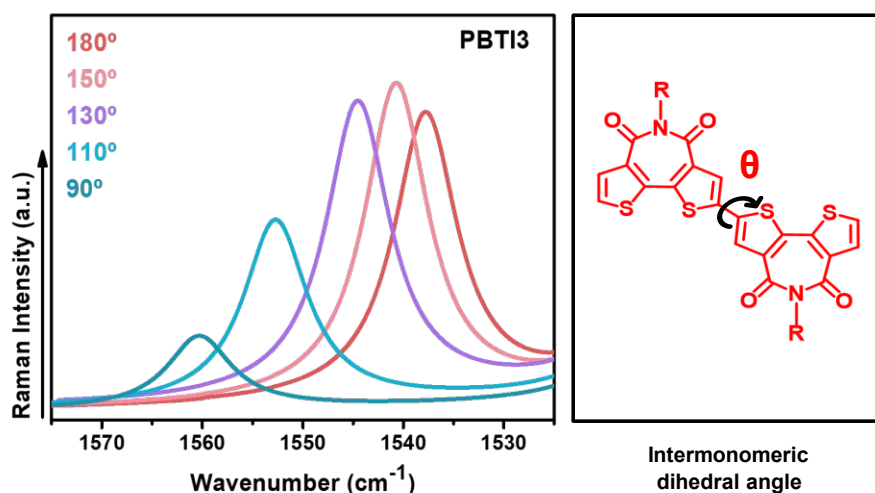
Figure 4.9. Predicted B3LYP/6-31G** dispersion of the PBTI3 v_{asymm} (C=C) vibration mode located on the external thiophene ring of the BTI unit with the variation of the inter monomeric dihedral angle (θ).

This Raman vibration is thus, very interesting since its trend from PBTI2 to PBTI5 is quite informative on the backbone planarity (Figure 4.10). For PBTI2 and PBTI3 (Figure 4.10) we can see a quite narrow band located at 1513 cm^{-1}, which starts to substantially widen for PBTI4 and PBTI5, showing two peaks overlapping below the same band; one that can be ascribed to an ordered phase which appears at lower wavelengths (salmon color in Figure 4.10) and the other one related to a disordered phase, appearing at higher wavelengths (aquamarine color in Figure 4.10). This first fact envisages that for polymers built from longer building blocks, PBTI4 and PBTI5, the supramolecular organization may be more disordered than for polymers PBTI1-PBTI3. This is likely attributed to the reduced motion freedom of the building blocks and the whole polymer chains as the building block becomes larger.
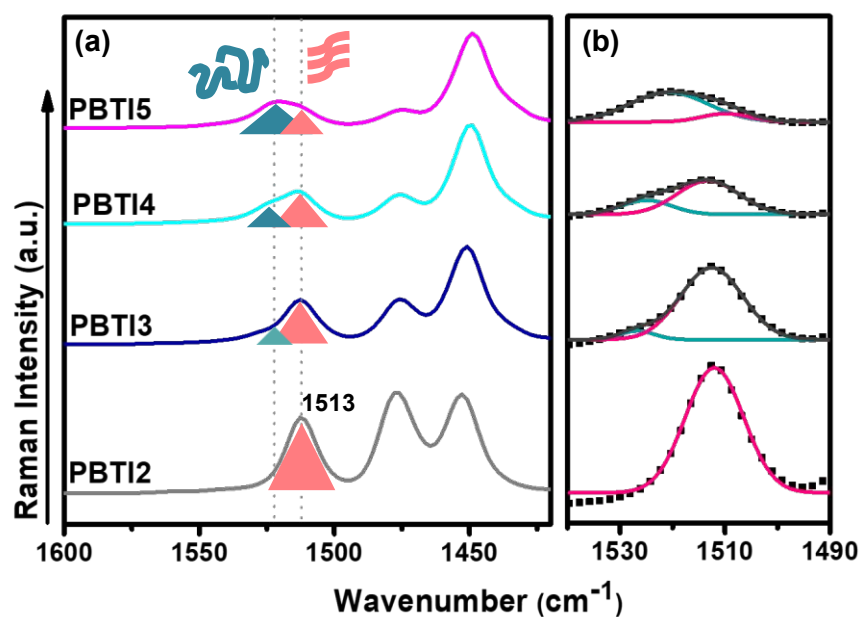
Figure 4.10. (a) FT-Raman spectra indicating the appearance of ordered (salmon color) and disordered (aquamarine color) phases in PBTI2-PBTI5 bulk samples. (b) Deconvolution of the v_{asymm} (C=C/C-C) of the external thiophenes of BTI units into ordered and disordered contributions based on fitting (pink solid line, ordered phase; cyan solid line, disordered phase; dark gray solid line, total fit; black dotted line, experimental data).

4.3.2. Resonant Raman spectroscopy

To further analyze the presence of disordered phases as the building block becomes larger, we exploited the sensitivity of resonant Raman spectroscopy to the molecular order, as previously described by Kim et al.[26–33] Thus, the Raman spectra of the PBTI1-PBTI5 homopolymers as thin films were recorded under 488, 514 and 785 nm excitations. The more energetic laser lines (488 and 514 nm) coincide with the more energetic part of the electronic absorption band of the polymers under study, and therefore, by exciting with these laser lines, we are in

resonance with the more disordered or less conjugated phases of the sample (Figure 4.11). On the contrary, by using the 785 nm excitation wavelength, the resonant conditions apply with the more ordered or more conjugated phases of the samples (Figure 4.11).
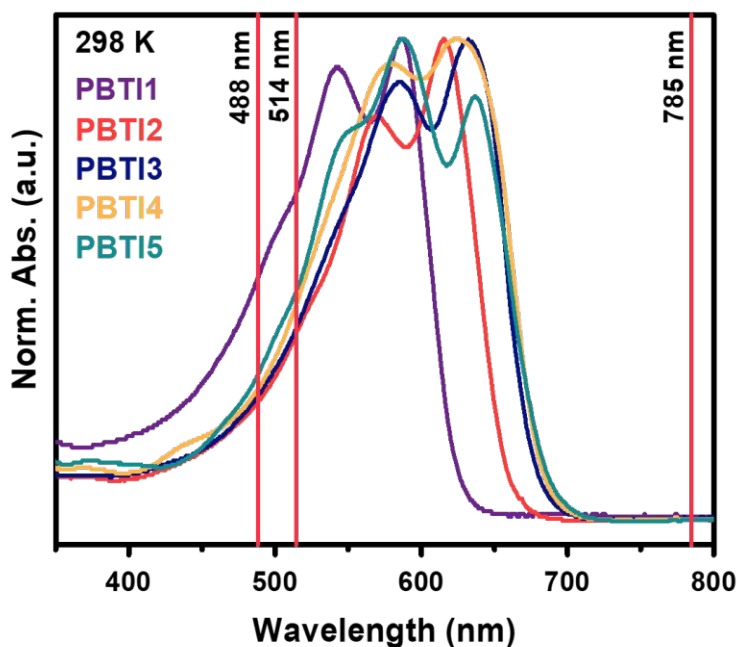
Figure 4.11. UV-Vis absorption spectra of homopolymers PBTI1-PBTI5 thin films indicating the laser wavelengths used for resonance Raman studies.

Now, we will focus on the Raman band appearing at ~ 1513-1520 cm^{-1} for PBTI2-PBTI5 homopolymers, which is very interesting for the study of ordered and disorder phases in the PBTI2-PBTI5 thin films, since as we have already seen in Figure 4.6, this Raman vibration can offer information on the molecular ordering in these homopolymer thin films. Thus, Figure 4.12 shows the different contributions under the broad Raman band between 1513-1520 cm^{-1} for PBTI2-PBTI5 homopolymers. As seen previously, two distinct peaks can be detected in some cases

corresponding to the ordered (centered at ~ 1513 cm^{-1}; salmon color) and disordered (centered at ~ 1520 cm^{-1}; aquamarine color) phases.
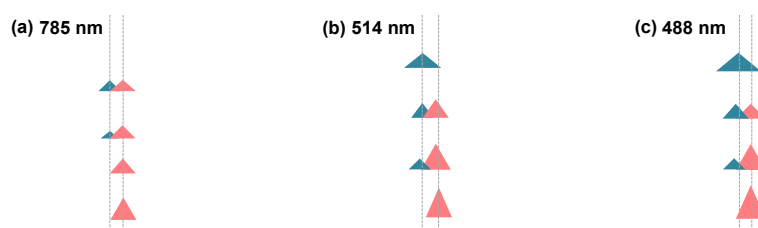
Figure 4.12. Resonance Raman spectra of PBTI2-PBTI5 thin films under (a) 785 nm excitation, (b) 514 nm excitation, and (c) 488 nm excitation. The triangles indicate the proportion and evolution of ordered (salmon color) and disordered (aquamarine color) phases with monomer lengthening.

In the case of PBTI2 (Figure 4.12) and regardless of the excitation wavelength used, the Raman band located at 1513 cm^{-1} is quite narrow, indicating the appearance of a single ordered phase. A similar situation is found for PBTI3 resonance Raman spectrum under 785 nm (Figure 4.12(a)), which also shows a sharp peak, pointing out a more ordered phase. However, the resonance Raman spectra under 514 and 488 nm (Figure 4.12(b) and (c)) envisage the coexistence of two different phases, one ordered phase (salmon color) at around 1511 cm^{-1} and another disordered phase at higher wavenumbers (aquamarine color). By exciting with these two more energetic laser lines, resonance conditions apply with more disordered phases, nonetheless, the more ordered phase is still the most abundant in the PBTI3 film, which is also notable under non-resonant conditions (see Section 4.3.1).

The situation reverses on going from PBTI4 to PBTI5. In the case of PBTI4, two phases coexist regardless of the laser wavelengths used,

261

thus we have a consistent mixture of ordered and disordered phases within the film. On the contrary, for PBTI5 the disordered phase is clearly the most abundant one. This disordered phase is the only one registered under 488 and 514 nm resonant conditions, and it is more evident in the 785 nm spectrum by the broadening of the 1513-1520 cm^{-1} Raman band. Thus, the Raman spectra point out the appearance of more disordered phases in the longest PBTIn systems, which may hinder charge transport.

The results obtained above indicate that in terms of molecular order, increasing the building block conjugated lengths may be not desirable for charge transport since film self-assembly into ordered structures can be hindered due to the reduced mobility of building blocks and polymer chains.

4.4. Electrical characterization

4.4.1. Organic Field Effect Transistors

In order to evaluate the charge transport properties of PBTI1-PBTI5 homopolymers, OFETs with a BCTG configuration were fabricated. For their fabrication, Cr and Au layers were used as contact electrodes, which were previously defined by photolithography onto borosilicate glass. On top of the contact electrodes, a thin layer of cesium fluoride (CsF) was deposited from solution to reduce contact resistance and to facilitate electron injection[34]. Afterwards, the PBTI1-PBTI5 semiconductors were deposited, followed by the CYTOP dielectric layer, both of them from solution by spin-coating, and were subsequently thermally annealed. Finally, Al was thermally evaporated as gate contact to complete the device fabrication. The transistor fabrication and characterization were carried out in a nitrogen-filled glovebox. The representative transistor

curves of the OFETs fabricated under the optimal conditions ($T_{anneal.}$ = 160 °C) are illustrated in Figure 4.13, and their performance parameters are summarized in Table 4.4.
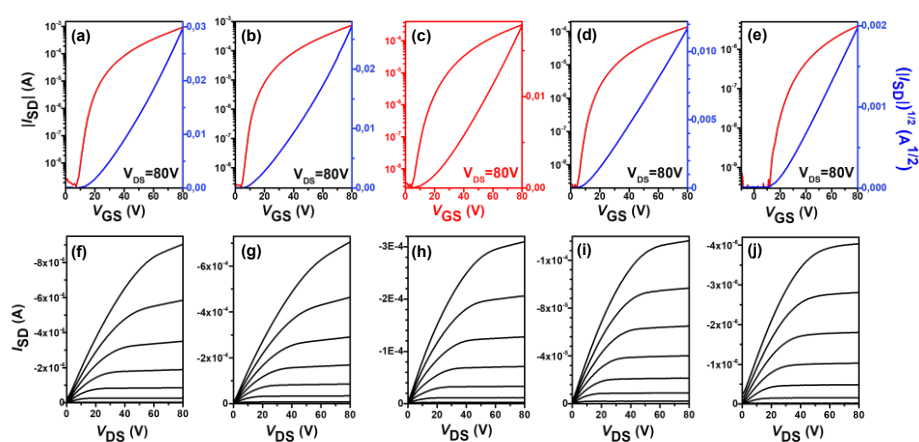
Figure 4.13. Output and transfer characteristics of OFET devices based on (a,f) PBTI1, (b,g) PBTI2, (c,h) PBTI3, (d,i) PBTI4, (e,j) PBTI5. The gate voltage range in the output plots is 0-80 V with 10 V intervals. The channel length and width are 50 µm and 5 mm, respectively, for all devices.

As shown in Figure 4.13, the PBTI1 homopolymer with the shortest building block exhibits the best OFET performance with the highest μ_e of 1.53 cm^2 V^{-1} s^{-1}, however this value drops by 2 orders to 0.014 cm^2 V^{-1} s^{-1} as the monomer size increases to PBTI5 (see reported values in Table 4.4).

Based on the results shown in Table 4.4, all PBTI1-PBTI5 homopolymers exhibit unipolar n-type behavior in transistors with nearly ideal device performance characteristics, accompanied by small I_{OFF} (10^{-9}-10^{-10} A), high I_{ON}/I_{OFF} (10^5-10^6), low V_{ON} (5-10 V), and small V_T (~15-25 V). These data differ from many high-performance D-A copolymers which

show kink-like transfer characteristics with high I_{OFF}, small I_{ON}/I_{OFF}, large V_{TH}, and ambipolarity. Such OFET characteristics of PBTI1-PBTI5 homopolymers are attributed to the A-A-type polymer backbones, which lead to low-lying HOMOs and greatly suppressed doping by air.

Table 4.4. BCTG OFET performance parameters of the PBTI1-PBTI5 homopolymers, fabricated under the optimal conditions. The semiconductor layers were spin-coated with on-center method, unless otherwise specified. The average mobility values from at least 5 devices are given in the parenthesis.

Semiconductor	T_{anneal} (°C)	$\mu_{e,sat}$ (cm^2 V^{-1} s^{-1})[a]	V_{TH} (V)	I_{ON}/I_{OFF}
PBTI1 (off-center)	160	3.71[b] (2.67)	30	10^6
PBTI1	160	1.53 (1.19)	25	10^6
PBTI2	160	1.34 (1.07)	21	10^6
PBTI3	120	0.53 (0.44)	22	10^6
PBTI4	160	0.21 (0.16)	14	10^6
PBTI5	160	0.014 (0.013)	26	10^5
[a]The mobilities were calculated with the average slop within V_{GS} = 70–80 V.. [b]Peak mobility at V_{GS} = 80 V.				

In principle, one may expect that the increase of the π-conjugation length should facilitate the intramolecular charge transport and consequently lead to improved mobility in OFET devices. However, in our case, as the monomer size increases the molecular ordering is disrupted[35] and the intermolecular charge transport is, as a consequence, hindered. As a result, the gain of intramolecular charge transport is largely offset or even completely overwhelmed by the reduced intermolecular charge transport which leads to decreased mobility in OFET devices.

The decreasing trend of charge carrier mobility in the studied polymers is then explained considering that the appearance of disordered

phases is more likely in homopolymers with more extended monomer sizes and in presence of long and branched side chains.

The PBTI1 device performance was further optimized by using the off-center spin-coating method (Figure 4.14). This method, which consists in placing the samples several centimeters away from the center which increase the spin-casting speed, is well known that effectively induces polymer chain alignment along the flow coating direction, enhancing the charge carrier mobility along that direction[26,27]. Moreover, the use of high boiling point solvent and high spin-casting temperature, provides sufficient time for the polymers to crystallize, which greatly improves the transistor performance. The representative transistor curves are shown in Figure 4.14 and the corresponding data are summarized in Table 4.4.
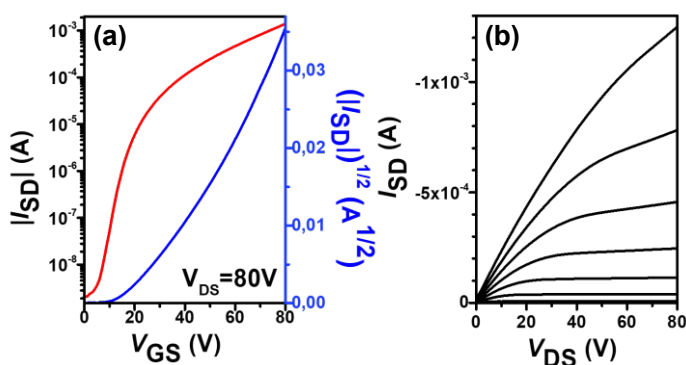
Figure 4.14. a) Output and b) transfer characteristics of OFET devices based on PBTI1 off-centered deposited semiconductor. The gate voltage range in the output plots is 0-80 V with 10 V intervals. The channel length and width are 50 μm and 5 mm, respectively, for all devices.

Electron mobilities up to 3.7 $cm^2 V^{-1} s^{-1}$ were recorded for PBTI1, by using this method, being these remarkable electron mobilities the highest values reported for all-acceptor-type polymer semiconductors,[22,36] and among the highest values for unipolar n-type polymer transistors. This can

be understood considering that PBTI1, having short repeating units, possess high motion of freedom which, by thermal annealing (160 ºC), leads to a better polymer chain alignment.

This is evidenced by Raman spectroscopy where the PBTI1 spectrum shows a well-defined band corresponding to the presence of only ordered phases. Nonetheless, for polymers with larger building blocks it is difficult to form high-quality π-aggregates and ordered microstructures due to the reduced molecular mobility. This is also evidenced by Raman spectroscopy where a higher proportion of disordered phases can be detected. Therefore, developing more extended ladder-type building blocks does not necessarily improve charge carrier mobility.

4.5. Morphological characterization of thin films

4.5.1. 2D-GIWAXS and AFM measurements

In order to better understand the mobility trend in this series of homopolymers, we studied the molecular packing as well as the morphologies of PBTI1-PBTI5 thin films prepared under the same conditions used for the optimal OFET fabrication. To this end, 2D-GIWAXS and AFM measurements were carried out (Figure 4.15 and 4.16, respectively).
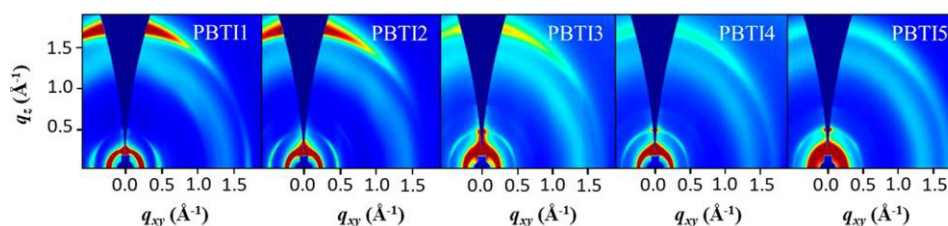
Figure 4.15. 2D-GIWAXS images of the thin film of PBTI1-PBTI5 prepared under the optimal device fabrication conditions.

All PBTI2-PBTI5 polymers exhibit similar lamellar d-spacing of ~ 26 Å (q_z (100) ≈ 0.25 Å^{-1}), with a close π-π stacking distance of 3.7 Å (q_z (010) ≈ 1.72 Å^{-1}), which is shorter than for BTI2-BTI5 small molecules.

By comparing the PBTI2 polymer with the BTI2 small molecule (Section 1.4.1 in Chapter 1), in the case of the PBTI2 polymer, a lamellar scattering up to (200) in the in-plane (IP) direction and a strong out-of-plane (OOP, 010) scattering was observed, suggesting a predominant face-on orientation for PBTI2. An interesting change in the intermolecular orientation from predominantly edge-on to face-on orientation was observed after the polymerization of BTI2-BTI5 molecules. However, it is worth mentioning that the face-on orientation does not necessarily lead to low charge carrier mobility[37].

Nevertheless, the enhanced chain rigidity as the building block increases leads to reduced molecular mobility, which hinders the self-assembly of polymer chains and results in decreased film crystallinity.
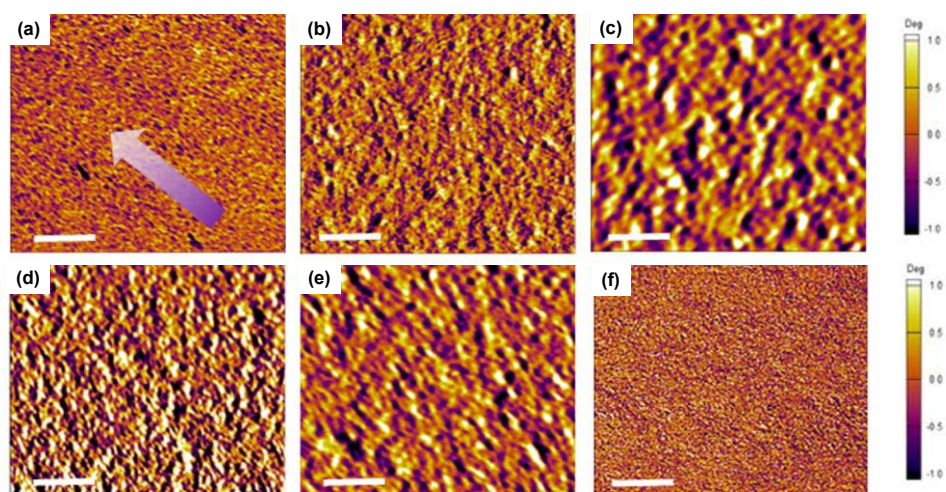
Figure 4.16. AFM phase images of thin films of (a) PBTI1 off-center (b-f) PBTI1-PBTI5 on-center homopolymers prepared under the optimal device fabrication conditions (scale bar: 1μm).

The AFM measurements (Figure 4.16) reveal that PBTI1-PBTI5 on-center spin-coated films are surprisingly rough with RMS between 2 and 4 nm, except for the largest building block (PBTI5), which exhibits much smaller RMS, below 1 nm, indicative of weak film crystallinity. As the monomer extension increases from PBTI2 to PBTI4, larger grain boundaries are observed, resulting in poorer film quality. The crystalline character in combination with the minimized grain boundaries leads to the largest mobility for PBTI1 in the polymer series. Conversely, the film of polymer PBTI5 shows featureless microstructure, indicative of its lowest ordering, which results in the smallest mobility.

By comparing the off-center (Figure 4.16(a)) and on-center (Figure 4.16(b)) spin-coated PBTI1 films, we observed that the former clearly shows highly interconnected and densely packed fibrils extended over

several microns, which leads to the superior charge transport performance in off-center spin-coated PBTI1 films.

4.6.   References

[1]   Letizia, J. A.; Salata, M. R.; Tribout, C. M.; Facchetti, A.; Ratner, M. A.; Marks, T. J. N-Channel Polymers by Design: Optimizing the Interplay of Solubilizing Substituents, Crystal Packing, and Field-Effect Transistor Characteristics in Polymeric Bithiophene-Imide Semiconductors. *J. Am. Chem. Soc.* **2008**, *130*, 9679–9694.

[2]   Guo, X.; Ortiz, R. P.; Zheng, Y.; Hu, Y.; Noh, Y.-Y.; Baeg, K.-J.; Facchetti, A.; Marks, T. J. Bithiophene-Imide-Based Polymeric Semiconductors for Field-Effect Transistors: Synthesis, Structure−Property Correlations, Charge Carrier Polarity, and Device Stability. *J. Am. Chem. Soc.* **2011**, *133*, 1405–1418.

[3]   Guo, X.; Kim, F. S.; Seger, M. J.; Jenekhe, S. A.; Watson, M. D. Naphthalene Diimide-Based Polymer Semiconductors: Synthesis, Structure–Property Correlations, and n-Channel and Ambipolar Field-Effect Transistors. *Chem. Mater.* **2012**, *24*, 1434–1442.

[4]   Guo, X.; Zhou, N.; Lou, S. J.; Smith, J.; Tice, D. B.; Hennek, J. W.; Ortiz, R. P.; Navarrete, J. T. L.; Li, S.; Strzalka, J.; Chen, L. X.; Chang, R. P. H.; Facchetti, A.; Marks, T. J. Polymer Solar Cells with Enhanced Fill Factors. *Nat. Photonics* **2013**, *7*, 825–833.

[5]   Wang, Y.; Guo, H.; Ling, S.; Arrechea-Marcos, I.; Wang, Y.; López Navarrete, J. T.; Ortiz, R. P.; Guo, X. Ladder-Type Heteroarenes: Up to 15 Rings with Five Imide Groups. *Angew. Chemie Int. Ed.* **2017**, *56*, 9924–9929.

[6]   Wang, Y.; Yan, Z.; Guo, H.; Uddin, M. A.; Ling, S.; Zhou, X.; Su, H.; Dai, J.; Woo, H. Y.; Guo, X. Effects of Bithiophene Imide Fusion on the Device Performance of Organic Thin-Film Transistors and All-Polymer Solar Cells. *Angew. Chemie Int. Ed.* **2017**, *56*, 15304–15308.

[7]   Chen, J.; Yang, K.; Zhou, X.; Guo, X. Ladder-Type Heteroarene-Based Organic Semiconductors. *Chem. Asian J.* **2018**, *13*, 2587—2600.

[8]   Kim, G.; Han, A.-R.; Lee, H. R.; Lee, J.; Oh, J. H.; Yang, C. Acceptor–Acceptor Type Isoindigo-Based Copolymers for High-Performance n-Channel Field-Effect Transistors. *Chem. Commun.* **2014**, *50*, 2180–2183.

[9]   Yuan, Z.; Fu, B.; Thomas, S.; Zhang, S.; DeLuca, G.; Chang, R.; Lopez, L.; Fares, C.; Zhang, G.; Bredas, J.-L.; Reichmanis, E. Unipolar Electron Transport Polymers: A Thiazole Based All-Electron Acceptor

Approach. *Chem. Mater.* **2016**, *28*, 6045–6049.

[10]   Saito, M.; Osaka, I.; Suda, Y.; Yoshida, H.; Takimiya, K. Dithienylthienothiophenebisimide, a Versatile Electron-Deficient Unit for Semiconducting Polymers. *Adv. Mater.* **2016**, *28*, 6921–6925.

[11]   Shi, Y.; Guo, H.; Qin, M.; Zhao, J.; Wang, Y.; Wang, H.; Wang, Y.; Facchetti, A.; Lu, X.; Guo, X. Thiazole Imide-Based All-Acceptor Homopolymer: Achieving High-Performance Unipolar Electron Transport in Organic Thin-Film Transistors. *Adv. Mater.* **2018**, *30*, 1705745.

[12]   Wang, Y.; Hasegawa, T.; Matsumoto, H.; Michinobu, T. Significant Improvement of Unipolar N-Type Transistor Performances by Manipulating the Coplanar Backbone Conformation of Electron-Deficient Polymers via Hydrogen Bonding. *J. Am. Chem. Soc.* **2019**, *141*, 3566–3575.

[13]   Durban, M. M.; Kazarinoff, P. D.; Luscombe, C. K. Synthesis and Characterization of Thiophene-Containing Naphthalene Diimide n-Type Copolymers for OFET Applications. *Macromolecules* **2010**, *43*, 6348–6352.

[14]   Jung, I. H.; Lo, W.-Y.; Jang, J.; Chen, W.; Zhao, D.; Landry, E. S.; Lu, L.; Talapin, D. V; Yu, L. Synthesis and Search for Design Principles of New Electron Accepting Polymers for All-Polymer Solar Cells. *Chem. Mater.* **2014**, *26*, 3450–3459.

[15]   Usta, H.; Risko, C.; Wang, Z.; Huang, H.; Deliomeroglu, M. K.; Zhukhovitskiy, A.; Facchetti, A.; Marks, T. J. Design, Synthesis, and Characterization of Ladder-Type Molecules and Polymers. Air-Stable, Solution-Processable n-Channel and Ambipolar Semiconductors for Thin-Film Transistors via Experiment and Theory. *J. Am. Chem. Soc.* **2009**, *131*, 5586–5608.

[16]   Sun, H.; Wang, L.; Wang, Y.; Guo, X. Imide-Functionalized Polymer Semiconductors. *Chem. – A Eur. J.* **2019**, *25*, 87–105.

[17]   Lee, J.-K.; Gwinner, M. C.; Berger, R.; Newby, C.; Zentel, R.; Friend, R. H.; Sirringhaus, H.; Ober, C. K. High-Performance Electron-Transporting Polymers Derived from a Heteroaryl Bis(Trifluoroborate). *J. Am. Chem. Soc.* **2011**, *133*, 9949–9951.

[18]   Stalder, R.; Mei, J.; Subbiah, J.; Grand, C.; Estrada, L. A.; So, F.; Reynolds, J. R. N-Type Conjugated Polyisoindigos. *Macromolecules* **2011**, *44*, 6303–6310.

[19]   Takeda, Y.; Andrew, T. L.; Lobez, J. M.; Mork, A. J.; Swager, T. M. An Air-Stable Low-Bandgap n-Type Organic Polymer Semiconductor Exhibiting Selective Solubility in Perfluorinated Solvents. *Angew. Chemie Int. Ed.* **2012**, *51*, 9042–9046.

[20]   Zhao, X.; Wen, Y.; Ren, L.; Ma, L.; Liu, Y.; Zhan, X. An Acceptor-Acceptor Conjugated Copolymer Based on Perylene Diimide for High Mobility n-Channel Transistor in Air. *J. Polym. Sci. Part A Polym. Chem.* **2012**, *50*, 4266–4271.

[21]   Yuen, J. D.; Wudl, F. Strong Acceptors in Donor–Acceptor Polymers for High Performance Thin Film Transistors. *Energy Environ. Sci.* **2013**, *6*, 392–406.

[22]   Guo, X.; Facchetti, A.; Marks, T. J. Imide- and Amide-Functionalized Polymer Semiconductors. *Chem. Rev.* **2014**, *114*, 8943–9021.

[23]   Wu, Y.; Han, J.-M.; Hong, M.; Krzyaniak, M. D.; Blackburn, A. K.; Fernando, I. R.; Cao, D. D.; Wasielewski, M. R.; Stoddart, J. F. X-Shaped Oligomeric Pyromellitimide Polyradicals. *J. Am. Chem. Soc.* **2018**, *140*, 515–523.

[24]   Wang, Y.; Guo, H.; Harbuzaru, A.; Uddin, M. A.; Arrechea-Marcos, I.; Ling, S.; Yu, J.; Tang, Y.; Sun, H.; López Navarrete, J. T.; Ortiz, R. P.; Woo, H. Y.; Guo, X. (Semi)Ladder-Type Bithiophene Imide-Based All-Acceptor Semiconductors: Synthesis, Structure-Property Correlations, and Unipolar n-Type Transistor Performance. *J. Am. Chem. Soc.* **2018**, *140*, 6095–6108.

[25]   Guo, X.; Zhou, N.; Lou, S. J.; Smith, J.; Tice, D. B.; Hennek, J. W.; Ortiz, R. P.; Navarrete, J. T. L.; Li, S.; Strzalka, J.; Chen, L. X.; Chang, R. P. H.; Facchetti, A.; Marks, T. J. Polymer Solar Cells with Enhanced Fill Factors. *Nat. Photonics* **2013**, *7*, 825–833.

[26]   Yuan, Y.; Giri, G.; Ayzner, A. L.; Zoombelt, A. P.; Mannsfeld, S. C. B.; Chen, J.; Nordlund, D.; Toney, M. F.; Huang, J.; Bao, Z. Ultra-High Mobility Transparent Organic Thin Film Transistors Grown by an off-Centre Spin-Coating Method. *Nat. Commun.* **2014**, *5*, 3005.

[27]   Kim, N.-K.; Jang, S.-Y.; Pace, G.; Caironi, M.; Park, W.-T.; Khim, D.; Kim, J.; Kim, D.-Y.; Noh, Y.-Y. High-Performance Organic Field-Effect Transistors with Directionally Aligned Conjugated Polymer Film Deposited from Pre-Aggregated Solution. *Chem. Mater.* **2015**, *27*, 8345–8353.

[28]   Tsoi, W. C.; James, D. T.; Kim, J. S.; Nicholson, P. G.; Murphy, C.

E.; Bradley, D. D. C.; Nelson, J.; Kim, J.-S. The Nature of In-Plane Skeleton Raman Modes of P3HT and Their Correlation to the Degree of Molecular Order in P3HT:PCBM Blend Thin Films. *J. Am. Chem. Soc.* **2011**, *133*, 9834–9843.

[29]   Tsoi, W. C.; James, D. T.; Domingo, E. B.; Kim, J. S.; Al-Hashimi, M.; Murphy, C. E.; Stingelin, N.; Heeney, M.; Kim, J.-S. Effects of a Heavy Atom on Molecular Order and Morphology in Conjugated Polymer:Fullerene Photovoltaic Blend Thin Films and Devices. *ACS Nano* **2012**, *6*, 9646–9656.

[30]   Kim, J.; Baeg, K.-J.; Khim, D.; James, D. T.; Kim, J.-S.; Lim, B.; Yun, J.-M.; Jeong, H.-G.; Amegadze, P. S. K.; Noh, Y.-Y.; Kim, D.-Y. Optimal Ambipolar Charge Transport of Thienylenevinylene-Based Polymer Semiconductors by Changes in Conformation for High-Performance Organic Thin Film Transistors and Inverters. *Chem. Mater.* **2013**, *25*, 1572–1583.

[31]   Wood, S.; Kim, J.-H.; Hwang, D.-H.; Kim, J.-S. Effects of Fluorination and Side Chain Branching on Molecular Conformation and Photovoltaic Performance of Donor–Acceptor Copolymers. *Chem. Mater.* **2015**, *27*, 4196–4204.

[32]   Wood, S.; Kim, J.-H.; Wade, J.; Park, J. B.; Hwang, D.-H.; Kim, J.-S. Systematic Control of Heteroatoms in Donor–Acceptor Copolymers and Its Effects on Molecular Conformation and Photovoltaic Performance. *J. Mater. Chem. C* **2016**, *4*, 7966–7978.

[33]   Razzell-Hollis, J.; Fleischli, F.; Jahnke, A. A.; Stingelin, N.; Seferos, D. S.; Kim, J.-S. Effects of Side-Chain Length and Shape on Polytellurophene Molecular Order and Blend Morphology. *J. Phys. Chem. C* **2017**, *121*, 2088–2098.

[34]   Baeg, K.-J.; Kim, J.; Khim, D.; Caironi, M.; Kim, D.-Y.; You, I.-K.; Quinn, J. R.; Facchetti, A.; Noh, Y.-Y. Charge Injection Engineering of Ambipolar Field-Effect Transistors for High-Performance Organic Complementary Circuits. *ACS Appl. Mater. Interfaces* **2011**, *3*, 3205–3214.

[35]   Niimi, K.; Shinamura, S.; Osaka, I.; Miyazaki, E.; Takimiya, K. Dianthra[2,3-b:2′,3′-f]Thieno[3,2-b]Thiophene   (DATT):   Synthesis, Characterization, and FET Characteristics of New π-Extended Heteroarene with Eight Fused Aromatic Rings. *J. Am. Chem. Soc.* **2011**, *133*, 8732–8739.

[36]   Shi, Y.; Guo, H.; Qin, M.; Wang, Y.; Zhao, J.; Sun, H.; Wang, H.;

Wang, Y.; Zhou, X.; Facchetti, A.; Lu, X.; Zhou, M.; Guo, X. Imide-Functionalized Thiazole-Based Polymer Semiconductors: Synthesis, Structure–Property Correlations, Charge Carrier Polarity, and Thin-Film Transistor Performance. *Chem. Mater.* **2018**, *30*, 7988–8001.

[37]   Rivnay, J.; Toney, M. F.; Zheng, Y.; Kauvar, I. V; Chen, Z.; Wagner, V.; Facchetti, A.; Salleo, A. Unconventional Face-On Texture and Exceptional In-Plane Order of a High Mobility n-Type Polymer. *Adv. Mater.* **2010**, *22*, 4359–4363.

IV. SUMMARY AND CONCLUSIONS

In this thesis, we have studied a series of ladder-type heteroarenes systems containing π-conjugated fused rings. We have focused on how molecular and supramolecular properties of the π-conjugated fused molecules, both in solution and in the solid state, influence charge transport mechanisms, by using different spectroscopic techniques supported by theoretical calculations at DFT level.

In **Chapter 1** a series of fused ladder-type heteroarenes based on bithienoimide units, with increasing chain length from two to five fused BTI units (BTI2-BTI5) has been selected to analyze the significant decrease of the charge transport properties upon increasing their building block length, which was previously observed in our research group. To this end, we investigated the influence of the molecular structure and length of these semiconductors on charge stabilization in solution and charge transport mechanism in the OFET device.

The results suggested that these small molecules show enhanced molecular aggregation in solution upon increasing the BTIn chain length, both in neutral and charged states. In the case of charged species, while both radical anion and dianion π-dimers were easily observed for BTI3-BTI5 semiconductors, only π-dimer radical anions were registered for BTI2, which in this case is related to the delocalization of the injected charge over the two neighboring molecules, thus preventing the introduction of an extra electron due to the increased electrostatic repulsion.

In good agreement with this result, in the solid state, the injected negative charge in BTI2 is also stabilized through-space between two adjacent molecules. This through-space charge delocalization, evidenced by CMS experiments and supported by quantum chemical calculations, does not apply to BTI3-BTI5, where charges seem to be localized on

single BTI molecules. Thus, the more efficient charge transport process found in BTI2, with an electron field effect mobility ∼40x times higher than BTI5, which has been previously ascribed to enhanced thin film crystallinity, is also related to charge relaxation over two molecules, in a π-dimer configuration.

In **Chapter 2**, two novel fused quinoidal oligothiophene imides (BTICN and QTICN) with increasing conjugation length from 3 to 5 fused rings and end-caped with strongly electron-withdrawing dicyanomethylene groups have been studied. These quinoidal systems present highly stable open-shell ground states and substantial electrical conductivity without doping.

The results suggested that the high conductivities of these quinoidal thiophene imides were found to be related to a cross-conjugation assisted self-doping process, in which a positively charged radical cation and a negatively charged radical anion were formed, as revealed by the XPS results and Raman spectra. A high diradical character was also found to be essential for this self-doping mechanism. Therefore, while BTICN displayed a relatively poor conductivity, the quaterthiophene imide based QTICN film exhibited a remarkable electrical conductivity, as a result of its high degree of diradical character and enhanced molecular packing in film state.

In addition, the excellent half-lives of over 60 days achieved for these fused organic biradicaloids based on quinoidal oligothiophenes were correlated to its deeply-lying LUMO energy levels due to the attachment of the strong electron-withdrawing imide group onto the tetracyano quinoidal frameworks.

In **Chapter 3**, a series of nitrogen-doped aromatic polycyclic mono and dicarboximide (PADI) have been studied. The interest of these

systems lies on the fact that, unlike other PADI systems, this new family of nitrogen-doped PADIs was synthesized by an innovative procedure that avoids metal-based cross-coupling reactions. In addition, these molecules are able to stabilize multiple redox processes, making them attractive for future electronic devices and batteries applications.

Specifically, in this chapter we investigated the interplay of different effects such as (i) the type of solubilizing chains, (ii) the all-acceptor vs donor-acceptor nature of the novel systems and (iii) the molecular ordering on the organic field effect transistor (OFET) device response characteristics.

The results suggested that all-acceptor systems (naft-2-4) based solely on naphthalimide units show multiple reduction processes, in which up to tetranion species were stabilized, while the donor-acceptor derivative (naft-1) containing naphthalimide and pyrene units shows amphoteric redox behavior, in which only up to dianion species were obtained. This lately is in good agreement with the ambipolar mobilities observed for naft-1 in OFETs, while only electron mobilities were registered for naft-2-4 systems.

In **Chapter 4**, an in-depth study of a series of (semi)ladder-type homopolymers based on BTI units, with increasing conjugation length from 3 to 15 fused rings per building block, respectively, has been performed. As in the case of BTIn small molecules, in this case a monotonic decrease in electron mobility was also observed with increasing the monomer size.

The results suggested that the reduction trend of the electron mobility is attributed to the reduced flexibility and degree of motion of the building block as the monomer size increases. By using resonance Raman spectroscopy and X-ray diffraction measurements we could

demonstrate that, as the monomer size becomes larger, a negative effect on the π-stacking quality was observed, with more disordered phases within the film, which are detrimental for charge transport. These negative effects are not fully compensated by the fast intramolecular charge transport along the ladder-type fused structure and polymer backbone, leading to gradually reduced mobility as the monomer size increases.

V. RESUMEN Y CONCLUSIONES

V.I. Introducción y Objetivos

La presente Tesis Doctoral se centra en el estudio de sistemas orgánicos semiconductores, de tipo escalera, funcionalizados con grupos imida. Las moléculas tipo escalera son sistemas compuestos de anillos aromáticos fusionados conectados mediante dos o más átomos adyacentes[1], que aportan diversas ventajas con respecto a los sistemas con mayor libertad conformacional. Entre las ventajas podemos mencionar la planaridad del esqueleto conjugado, lo que implica mayor longitud de la conjugación efectiva, y por lo tanto una reducción del gap HOMO-LUMO[2]. Además, dada la planaridad de estos sistemas, se obtienen bajos valores de energía de reorganización, así como un apilamiento π de moléculas adyacentes más cercano lo que se traduce en un transporte de carga más efectivo[3,4]. De ahí que estos sistemas tipo escalera están recibiendo un enorme interés como semiconductores moleculares o como unidades constituyentes de polímeros para dispositivos electrónicos de alto rendimiento.

Hay muchos ejemplos de sistemas tipo escalera, implementados en dispositivos orgánicos como los transistores de efecto de campo de base orgánica (OFETs, Organic Field Effect Transistors) que presentan movilidades comparables con los del silicio amorfo[5], sin embargo, la mayoría de estas moléculas son semiconductores de tipo p (transportadores de huecos), mientras que la síntesis de análogos transportadores de electrones (tipo n) es mucho más tediosa debido a la presencia de la nube de electrones π de alta densidad dentro del esqueleto aromático que lleva a que estos sistemas presenten baja estabilidad en condiciones ambientales.

No obstante, el desarrollo de sistemas π-conjugados de tipo escalera deficientes en electrones es esencial para obtener

semiconductores dador-aceptor que presenten transporte ambipolar (tanto de huecos como electrones) necesarios para la fabricación de circuitos orgánicos complementarios de bajo consumo (CMOS, Complemetary Organic Circuits).

En búsqueda de nuevos materiales orgánicos transportadores de electrones y altamente estables, se ha llegado a la síntesis de materiales basados en unidades de perilendiimida (PDI) y naftalendiimida (NDI)[6].

Otro ejemplo de heteroarenos funcionalizados con grupos imida son los sistemas bitienoimida (BTI)[7], los cuales combinan la planaridad y el apilamiento π-π efectivo de las unidades de tiofeno con la capacidad electro-aceptora del grupo imida. Estos sistemas se han empleado como unidades constituyentes para la síntesis de polímeros, obteniéndose una serie de semiconductores poliméricos con altas movilidades en dispositivos OFETs[8] y OPV (Organic Photovoltaics)[9] para dispositivos electrónicos de alto rendimiento.

Concretamente, en esta Tesis Doctoral se ha llevado a cabo el estudio de cuatro familias de semiconductores orgánicos tipo escalera funcionalizados con grupos imida, tres familias basadas en unidades de bitienoimida, y otra familia basada en unidades de naftalenodiimida y pireno.

Con este estudio se pretende establecer relaciones estructura-propiedad, con el fin de optimizar el funcionamiento de dispositivos electrónicos orgánicos, y particularmente en OFETs, cuya implementación también se ha llevado a cabo para los distintos materiales a estudio propuestos. Para ello nos centramos en el estudio de las estructuras electrónicas y moleculares de los sistemas orgánicos a estudio, así como las propiedades ópticas y electrónicas, y finalmente su uso en OFETs. Más concretamente analizamos cómo varían estas propiedades con el

aumento de la longitud de la cadena conjugada en los sistemas basados en unidades de BTI, mientras que en los sistemas basados en unidades de NDI y pireno, nos centramos en investigar el efecto que tienen los sustituyentes alquílicos del átomo de nitrógeno del grupo imida tanto en la solubilidad como en el empaquetamiento molecular, así como la naturaleza completamente aceptora *versus* dador-aceptor de estos sistemas.

V.II. Metodología

Para llevar a cabo este estudio, se han empleado técnicas espectroscópicas de absorción electrónica UV-Vis/NIR y Raman, resonante y no resonante, tanto a temperatura ambiente como a temperatura variable. Los resultados obtenidos se han apoyado en cálculos químico-cuánticos a nivel DFT. En algunos casos concretos, se han usado técnicas alternativas como son la espectroscopía de modulación de cargas (CMS, Charge Modulation Spectroscopy), resonancia electrónica de espín (ESR), Microscopia de fuerza atómica (AFM, Atomic Force Microscopy), difracción de rayos X con incidencia rasante bidimensional (2D-GIWAXS), difracción de rayos X (XRD, X-Ray Diffraction), espectroscopia fotoelectrónica de rayos X (XPS, X-Ray Photoelectron Spectroscopy) y medidas de conductividad eléctrica.

V.III. Resultados

A continuación, pasamos a detallar los resultados más relevantes obtenidos de las cuatro familias de semiconductores orgánicos estudiados en esta Tesis Doctoral.

1. Sistemas fusionados tipo escalera basados en unidades de BTI

En el primer capítulo de resultados se lleva a cabo el estudio de una serie de heteroarenos fusionados basados en unidades bitienoimida con longitud de cadena desde 2 hasta 5 unidades de BTI (Figura V.1). Más concretamente se analiza el efecto del aumento de la longitud de la cadena conjugada en el transporte de carga. En una publicación previa[10], habíamos comprobado que estos sistemas basados en unidades BTI, experimentan una disminución de la movilidad de electrones al aumentar la longitud de la cadena conjugada. Esta diminución inesperada de la movilidad de electrones podría estar relacionada con la reducida movilidad molecular en el estado sólido que lleva a un empaquetamiento molecular menos eficaz y por tanto a un bajo grado de cristalinidad de la lámina semiconductora. Sin embargo, con el objetivo de ir más allá, y obtener más información en cuanto al mecanismo de transporte de carga en estos sistemas, analizamos el efecto que la longitud y estructura molecular en i) la estabilización de cargas en disolución y ii) la estabilización de cargas en la interfase dieléctrico/semiconductor orgánico de un dispositivo OFET en funcionamiento.
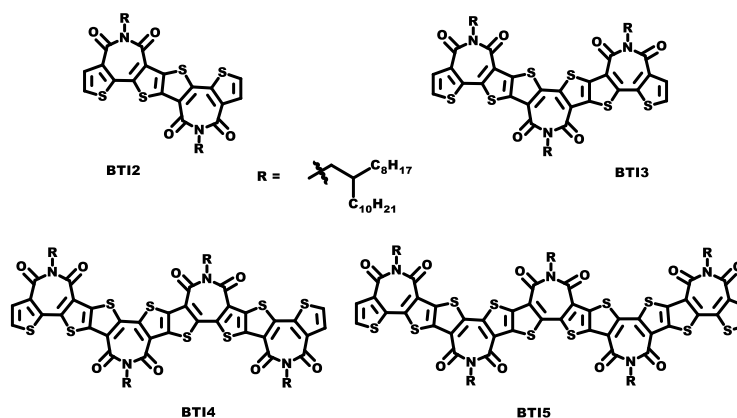
Figura V.1. Estructuras químicas de los heteroarenos bajo estudio basados en unidades BTI (BTI2-BTI5).

También se llevó a cabo el estudio de agregados supramoleculares en las especies cargadas de BTI2-BTI5 tanto en disolución como en el estado sólido. Esto nos permite analizar cómo las interacciones intra- e intermoleculares entre sistemas π cargados se ven afectadas por la longitud de la unidad BTI y de esta manera entender la naturaleza de los portadores de carga en el dispositivo. Las reacciones de π-dimerización de iones han despertado recientemente un gran interés dado que se ha comprobado que influyen fuertemente en los mecanismos de transporte de carga, y por lo tanto son muy adecuadas como modelos para estudiar la deslocalización de carga intermolecular en materiales π-conjugados[11–14]. Hasta ahora se han estudiado mucho las reacciones de π-dimerización de radicales cationes[15–18], sin embargo, son limitados los estudios que se encontraron en la literatura relacionados con la dimerización de radicales aniones[19–21].

Para llevar a cabo este estudio, hemos usado una combinación experimental/teórico que vincula las técnicas espectroscópicas y electroquímicas con cálculos químico-cuánticos con el fin de analizar la inyección de cargas, tanto en disolución como en el estado sólido en el dispositivo OFET activo. Más concretamente se utiliza la técnica de absorción electrónica UV-Vis, la espectroelectroquímica UV-Vis/NIR *in situ* y la espectroscopía de modulación de carga (CMS, Charge Modulation Spectroscopy) combinados con cálculos DFT y TD-DFT.

2. Sistemas quinoides fusionados basados en unidades de BTI con alta conductividad eléctrica

En el segundo capítulo de resultados se analiza una serie de moléculas orgánicas con carácter diradical, basadas en bitienoimida, con longitud de cadena creciente y que presentan alta conductividad eléctrica.

Resulta bien conocido que las moléculas diradicales orgánicas basadas en derivados oligotiofénicos son semiconductores prometedores en OFETs de tipo n[22,23] y en termoeléctricos orgánicos[24]. Estos derivados oligotiofénicos quinoides con HOMO-LUMO gap relativamente pequeños presentan reactividad química extremadamente alta, ya que los electrones pueden ser fácilmente promovidos desde el nivel energético HOMO al LUMO[25]. Como consecuencia de ellos, los sistemas quinoides presentan carácter dirradical que aumenta conforme el gap energético disminuye[26,27]. Así, la estructura electrónica del estado fundamental de estos sistemas puede ser representado mediante el equilibrio entre dos estructuras resonantes, una estructura singlete de capa cerrada (quinoide) y otra singlete de capa abierta (dirradical), siendo la proporción relativa de estas dos estructuras será la que determine la contribución diradical en el estado electrónico fundamental. Para explicar las propiedades magnéticas de estos sistemas, es necesario considerar la existencia del estado triplete magnéticamente activo el cual se encuentra en equilibrio térmico con el estado singlete de capa abierta, por lo tanto, se podría poblar energéticamente a temperatura ambiente. Este hecho proporciona a los sistemas quinoides propiedades optoelectrónicas y magnéticas únicas[28,29].

La gran desventaja de los diradicales moleculares es la baja estabilidad ambiental, que necesita ser abordada adecuadamente. Sin embargo, la presencia de electrones desapareados en moléculas diradicales de capa abierta les proporciona la capacidad de presentar alta conductividad eléctrica sin necesidad de dopaje químico[24]. Por lo tanto, los materiales conductores basados en diradicaloides no dopados (o los denominados semiconductores auto-dopados) pueden eliminar los inconvenientes del método tradicional de dopaje químico, como la baja eficiencia del dopado, la gran dependencia de las condiciones de

procesamiento y el deterioro de la estabilidad del material o del dispositivo, que proporcionan un camino alternativo prometedor para lograr materiales conductores orgánicos más avanzados[30]. Además, la presencia de los electrones desapareados en la forma diradical de capa abierta puede inducir un transporte de carga intramolecular con interacciones intermoleculares espin-espin[31]. La transferencia de electrones intermoleculares entre las estructuras de capa abierta (forma canónica diradical) y de capa cerrada (forma quinoide) podría dar lugar a un autodopado característico con la generación de portadores de carga libres que conducen una alta conductividad eléctrica sin dopado[32].

Así en este capítulo, inspirados por los excelentes resultados obtenidos con sistemas quinoides hasta la fecha, se llevó a cabo el estudio de dos sistemas quinoides orgánicos basados en unidades bitienoimida fusionados (BTICN y QTICN), así como sus homólogos aromáticos (BTI y QTI) (Figura V.2).
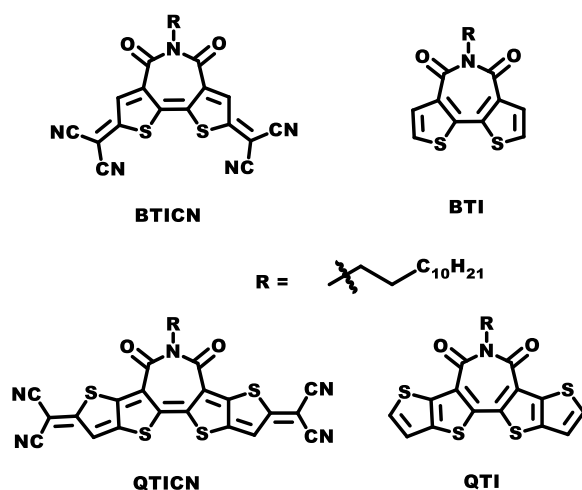
Figura V.2. Estructuras químicas de sistemas quinoides bajo estudio (BTICN y QTICN) y sus homólogos aromáticos (BTI y QTI).

Estos sistemas quinoides, con una longitud de cadena que aumenta de tres a cinco anillos fusionados, y funcionalizados con grupos dicianometilenos terminales, son sistemas muy prometedores en la búsqueda de materiales eficientes sin necesidad de dopantes para dispositivos electrónicos de tipo n con alta capacidad de transporte de electrones y estabilidad ambiental superior.

Para llevar a cabo este estudio, usamos una combinación experimental/teórica que vincula las técnicas espectroscópicas y electroquímicas con cálculos químico-cuánticos con el fin de analizar el efecto de la longitud de cadena sobre el carácter diradical y el transporte de carga. Más concretamente se utiliza la técnica de absorción electrónica UV-Vis, la espectroelectroquímica UV-Vis/NIR *in situ*, la voltametría cíclica (CV, cyclic voltammetry) en disolución, así como la espectroscopía vibracional Raman a temperatura ambiente y a temperatura variable, usando diferentes líneas excitatrices en condiciones de resonancia y no resonancia, para todos los sistemas a estudio tanto en muestras en estado sólido como en forma de películas delgadas. Todo ello, combinado con cálculos DFT y TDDFT. Además, las propiedades eléctricas de estos sistemas fusionados se han examinado en dispositivos electrónicos OFETs.

3. Dicarboximidas policíclicas aromáticas dopadas con nitrógeno

En el tercer capítulo de resultados se estudia una familia de sistemas policíclicos aromáticos capaces de estabilizar múltiples cargas.

Se conoce que los sistemas basados en dicarboximidas policíclicas aromáticas (PADIs)[33] y sus análogos dopados con heteroátomos son clases emergentes de materiales semiconductores derivados de la conocida familia de hidrocarburos policíclicos (PAHs)[34]. Estos materiales se han aplicado con éxito en dispositivos de

almacenamiento de energía debido a su notable comportamiento redox[35]. Entre varios PADIs, los compuestos π-conjugados que contienen grupo imida[36], como las perilenodiimidas (PDI) y las naftalenodiimidas (NDI)[37], son los semiconductores de tipo n más estudiados. Esto se debe a varios factores como: i) la presencia de grupos imida con fuerte carácter atrayente de electrones, lo que reduce los niveles de energía LUMO del semiconductor y facilita la inyección de electrones y la estabilización de carga a través de los sistemas π-conjugados[38,39]; ii) esqueletos conjugados que pueden ser modificados químicamente, ofreciendo la posibilidad de afinar los potenciales redox y promover la generación de especies polianiónicas reversibles, para su uso como materiales de electrodos en baterías[40]; y iii) la solubilidad y procesabilidad, que se pueden modular fácilmente mediante la selección apropiada de cadenas alquílicas en el átomo de nitrógeno del grupo imida. Por lo tanto, las cadenas alquílicas largas proporcionan una buena capacidad de formación de películas delgadas a través de una solubilidad mejorada, incluso en grandes sistemas planos π-conjugados con muchos anillos fusionados, mientras que las interacciones intermoleculares pueden promoverse por la ausencia de sustituyentes laterales, para aplicaciones como electrodos.

La desventaja que presentan es que la mayoría de los sistemas PADIs π-conjugados se obtienen a través de reacciones de arilación C-H o acoplamiento cruzado a base de metales, siendo la síntesis de dicarboximidas policíclicas aromáticas π-extendidas, mediante reacciones libres de metales relativamente inexplorada.

Por lo tanto, inspirados por las excelentes propiedades de estos semiconductores orgánicos y por la relativa escasez de reacciones libres de metales para su síntesis, una familia de mono- y dicarboximidas policíclicas aromáticas dopadas con nitrógeno fueron (Figura V.3) han

sido estudiadas en este capítulo. Estos sistemas han sido sintetizados por el grupo del profesor José Luis Segura de la Universidad Complutense de Madrid mediante reacciones de autocondensación y condensación cruzada libres de metales, entre unidades de pireno[41] y 1,8-naftalenoimida[42] dotados con funcionalidades 1,2-dicetona[43].

Estos compuestos se dividen en dos grupos, el primero basado en unidades de naftalimida y pireno (naft-1, Figura V.3) que presenta una forma de T, y un segundo grupo donde se incluyen 3 moléculas basadas en unidades naftalenoimida (naft-2-4, Figura V.3), que tienen forma linear y se diferencian únicamente en las cadenas alquílicas solubilizantes en el átomo de nitrógeno del grupo imida, lo cual puede llevar a diferentes agregaciones supramoleculares, solubilidad y capacidad de formación de películas delgadas. Más concretamente se busca analizar el papel que tienen diferentes efectos tales como: i) el tipo de cadena solubilizante, ii) la naturaleza completamente aceptora frente a naturaleza dador-aceptor de estos sistemas y iii) el papel que desempeña el ordenamiento molecular sobre la capacidad de estabilizar múltiples cargas, así como sobre su funcionamiento en dispositivos electrónicos OFETs.

Figura V.3. Estructuras químicas de naft-1, sistema con forma cruzada o T formado por un grupo naftalimida y otro grupo pireno, y naft-2-4, sistemas con forma linear formados por dos unidades naftalimida.

Para llevar a cabo este estudio, usamos una combinación experimental/teórica que vincula técnicas espectroscópicas y electroquímicas con cálculos químico-cuánticos con el fin de analizar el efecto de las cadenas alquílicas solublizantes y la naturaleza electroactiva de los grupos constituyentes, en la estabilización y transporte de carga en OFETs. Más concretamente se utiliza la técnica de absorción electrónica UV-Vis, la espectroelectroquímica UV-Vis/NIR *in situ*, la voltametría cíclica (CV) en disolución combinados con cálculos DFT y TD-DFT. Además, las propiedades eléctricas de estos sistemas fusionados se han examinado en dispositivos electrónicos OFETs utilizando películas depositadas en fase vapor que se caracterizaron mediante técnicas XRD y AFM.

4. Semiconductores poliméricos basados en unidades de bitienoimida

Para concluir, el cuarto capítulo de resultados se centra en el estudio de una serie de polímeros (PBTI1-PBTI5, Figura V.4) construidos a partir de monómeros fusionados, basados en unidades bitienoimida con longitud de cadena desde 1 unidad hasta 5 unidades de BTI.
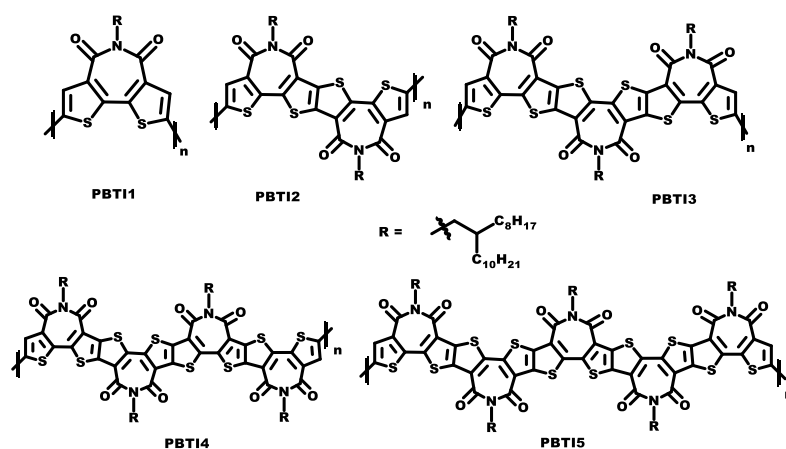
Figura V.4. Estructuras químicas de los homopolímeros semiconductores bajo estudio basados en unidades BTI (PBTI1-PBTI5).

Los sistemas basados en BTI[44] son una de las unidades constituyentes más prometedoras para la síntesis de polímeros de tipo aceptor-aceptor (A-A) de alto rendimiento[45–47], cuyo desarrollo sigue siendo un gran desafío. Los polímeros A-A tienen interés ya que pueden alcanzar bajos valores de energía del LUMO, facilitándose la inyección de electrones, así como bajos valores de energía del HOMO, necesarios para suprimir la acumulación de huecos, con el fin de lograr semiconductores unipolares tipo n.

Las moléculas conjugadas de tipo escalera basadas en unidades BTI son una estructura eficaz para explorar materiales que presenten alta movilidad de electrones, ya que combinan características como rigidez, esqueleto conjugado plano y, por lo tanto, apilamiento π-π mejorado, con la deficiencia de electrones de las unidades BTI[44,46,48]. De hecho, la incorporación de estas unidades monoméricas en la síntesis de polímeros proporcionó una gran batería de semiconductores con altos rendimientos en OFETs (movilidades de hasta 0.2 cm^{2}V^{-1}s^{-1})[49] y en OPVs (con factores de llenado de 76-80%)[50,51].

Por tanto, inspirados por las excelentes propiedades de los polímeros basados en unidades BTI, en el presente capítulo hemos estudiado una serie de homopolímeros tipo semi-escalera basados en unidades BTI, con longitud de cadena creciente de 3 a 15 anillos aromáticos fusionados por monómero, (PBTI1-PBTI5, Figura V.4)

En el caso de estos polímeros, al igual que en el caso de las moléculas pequeñas (BTI2-BTI5) estudiados en el capítulo 1, se ha observado una disminución de la movilidad de electrones al aumentar la longitud de la cadena conjugada del monómero.

Para analizar el origen de esta disminución de las propiedades eléctricas con la longitud de la cadena, usamos una combinación

experimental/teórica que vincula técnicas espectroscópicas con cálculos químico-cuánticos con el fin de analizar el impacto de las interacciones intra- e intermoleculares en el transporte de carga. Más concretamente se utiliza la técnica de absorción electrónica UV-Vis en disolución a temperatura ambiente y temperatura variable, así como la espectroscopía vibracional Raman a temperatura ambiente, usando diferentes líneas excitatrices en condiciones de resonancia y no resonancia, de los sistemas a estudio tanto en estado sólido como en películas delgadas. Todo ello combinado con cálculos DFT y TD-DFT. Además, las propiedades eléctricas de estos polímeros se han analizado en OFETs.

V.IV. Conclusiones

En esta tesis, hemos estudiado una serie de heteroarenos tipo escalera que contienen anillos fusionados π-conjugados funcionalizados con grupos imida. Nos hemos centrado en cómo las propiedades moleculares y supramoleculares de los sistemas a estudio, tanto en disolución como en estado sólido, influyen en los mecanismos de transporte de carga, mediante el uso de diferentes técnicas espectroscópicas apoyadas en cálculos teóricos a nivel de DFT y TD-DFT.

En la primera familia de sistemas a estudio (**Capítulo 1**), los resultados obtenidos sugieren que los semiconductores BTIn muestran una mayor agregación molecular en disolución al aumentar la longitud de la cadena de BTI, tanto en estado neutro como especies cargadas. Con relación a las especies cargadas, en el caso de los semiconductores BTI3-BTI5 se observaron tanto π-dímeros aniones radicales y dianiones, mientras que en el caso del sistema más corto (BTI2) solo se aislaron π-dímeros aniones radicales, el cual está relacionado con la deslocalización de la carga inyectada sobre las dos moléculas vecinas, evitando así la

introducción de un electrón extra debido al aumento de la repulsión electrostática.

De acuerdo con este resultado, hemos demostrado que, en el estado sólido, la carga negativa inyectada en el sistema BTI2 también se estabiliza entre dos moléculas adyacentes. Esta deslocalización de carga, evidenciada por experimentos de CMS y respaldada por cálculos químicos cuánticos, no se aplica a los sistemas de mayor tamaño BTI3-BTI5, donde las cargas parecen estar localizadas en moléculas BTI individuales. Por tanto, el proceso de transporte de carga más eficiente que se encuentra en BTI2, con una movilidad de efecto de campo de electrones ~40 veces superior a la del BTI5, y la cual se ha atribuido previamente a una cristalinidad mejorada en la película delgada, también está relacionado con la relajación de carga sobre dos moléculas adyacentes, formando un agregado de tipo π- dímero.

En la segunda familia de sistemas a estudio (**Capítulo 2**), los resultados obtenidos sugieren que las altas conductividades de moléculas basadass en BTI están relacionadas con un proceso de autodopado asistido por conjugación cruzada, en el que se forma un catión radical cargado positivamente y un anión radical cargado negativamente, estando evidenciado por XPS y espectroscopía Raman. También se encontró que el alto carácter diradical es esencial para el mecanismo de autodopado. Por lo tanto, mientras que el sistema quinoide más corto (BTICN) mostró una conductividad relativamente pobre, la película delgada del sistema quinoide más largo (QTICN) exhibió una conductividad eléctrica notable, como resultado de su alto grado de carácter diradical y un empaquetamiento molecular mejorado.

Además, los excelentes valores de vida media de más de 60 días obtenidos para estos biradicaloides orgánicos fusionados basados en

bitienoimida quinoides se correlacionaron con sus bajos niveles de energía LUMO debido a la unión del grupo imida, fuertemente atrayente de electrones, a estructuras tetracianoquinoidales.

En la tercera familia de sistemas a estudio (**Capítulo 3**) los resultados obtenidos sugieren que los sistemas con solo grupos aceptores (naft-2-4), basados únicamente en unidades de naftalenoimida, muestran múltiples procesos de reducción, en los que se estabilizaron hasta especies tetraniónicas, mientras que el derivado dador-aceptor (naft-1) que contiene unidades de naftalenoimida y pireno, muestra un comportamiento redox anfótero, en el que sólo se aislaron especies aniónicas y dianiónicas. Esto último, está en consonancia con las movilidades ambipolares observadas para naft-1 en OFETs, mientras que solo se registraron movilidades de electrones para los sistemas naft-2-4.

Además, se comprobó que mientras que las propiedades ópticas y electroquímicas (en disolución) de naft-2-4 eran muy similares, en el caso de la caracterización eléctrica de OFETs (en estado sólido), el naft-2 funcionaba mucho peor que naft-4, lo cual se debe a las diferencias en los grupos laterales que presentan estos dos compuestos lo que lleva a un peor empaquetamiento molecular, y por consiguiente induce un peor funcionamiento del dispositivo, debido a un transporte de carga entre moléculas más ineficaz. Por otro lado, los sustituyentes tan voluminosos en el naft-3, hace que este empaquete peor al formar las láminas delgadas, lo que implica la ausencia de actividad eléctrica en OFETs.

En la cuarta familia de sistemas a estudio (**Capítulo 4**), los resultados obtenidos sugieren que la disminución en la movilidad de electrones de estos sistemas poliméricos al aumentar la longitud de la unidad monomérica se atribuye a la reducción de la flexibilidad y el grado de movimiento de los constituyentes que forman la cadena polimérica a

medida que aumenta el tamaño del monómero. Mediante el uso de espectroscopia Raman resonante y mediciones de difracción de Rayos X, apoyados por cálculos teóricos a nivel DFT, pudimos demonstrar que, a medida que aumenta la longitud del monómero se observa un efecto negativo en la calidad del apilamiento π, con la aparición de fases más desordenadas dentro de la película delgada de polímero, que son perjudiciales para el transporte de carga. Por lo tanto, en términos de orden molecular, aumentar la longitud de la cadena conjugada de unidades monoméricas puede no ser deseable para el transporte de carga, ya que el empaquetamiento supramolecular en estructuras ordenadas puede verse impedido debido a la movilidad reducida de las cadenas de polímeros.

V.V. Referencias

[1]   Cai, Z.; Awais, M. A.; Zhang, N.; Yu, L. Exploration of Syntheses and Functions of Higher Ladder-Type π-Conjugated Heteroacenes. *Chem* **2018**, *4*, 2538–2570.

[2]   Tsuda, A.; Osuka, A. Fully Conjugated Porphyrin Tapes with Electronic Absorption Bands That Reach into Infrared. *Science* **2001**, *293*, 79 LP – 82.

[3]   Prins, P.; Grozema, F. C.; Schins, J. M.; Patil, S.; Scherf, U.; Siebbeles, L. D. A. High Intrachain Hole Mobility on Molecular Wires of Ladder-Type Poly(p-Phenylenes). *Phys. Rev. Lett.* **2006**, *96*, 146601.

[4]   Casado, J.; Katz, H. E.; Hernández, V.; López Navarrete, J. T. Spectroelectrochemical Raman Study of Two End-Capped Sexithiophenes with Applications as Electroactive Molecular Materials. *J. Phys. Chem. B* **2002**, *106*, 2488–2496.

[5]   Schweicher, G.; Garbay, G.; Jouclas, R.; Vibert, F.; Devaux, F.; Geerts, Y. H. Molecular Semiconductors for Logic Operations: Dead-End or Bright Future? *Adv. Mater.* **2020**, *32*, 1905909.

[6]   Feng, J.; Jiang, W.; Wang, Z. Synthesis and Application of Rylene Imide Dyes as Organic Semiconducting Materials. *Chem. – An Asian J.* **2018**, *13*, 20–30.

[7]   Letizia, J. A.; Salata, M. R.; Tribout, C. M.; Facchetti, A.; Ratner, M. A.; Marks, T. J. N-Channel Polymers by Design: Optimizing the Interplay of Solubilizing Substituents, Crystal Packing, and Field-Effect Transistor Characteristics in Polymeric Bithiophene-Imide Semiconductors. *J. Am. Chem. Soc.* **2008**, *130*, 9679–9694.

[8]   Xue, Q.; Xie, G. Thermally Activated Delayed Fluorescence beyond Through-Bond Charge Transfer for High-Performance OLEDs. *Adv. Opt. Mater.* **2021**, *n/a*, 2002204.

[9]   Wang, Y.; Yan, Z.; Guo, H.; Uddin, M. A.; Ling, S.; Zhou, X.; Su, H.; Dai, J.; Woo, H. Y.; Guo, X. Effects of Bithiophene Imide Fusion on the Device Performance of Organic Thin-Film Transistors and All-Polymer Solar Cells. *Angew. Chemie Int. Ed.* **2017**, *56*, 15304–15308.

[10]   Wang, Y.; Guo, H.; Ling, S.; Arrechea-Marcos, I.; Wang, Y.; López Navarrete, J. T.; Ortiz, R. P.; Guo, X. Ladder-Type Heteroarenes: Up to 15 Rings with Five Imide Groups. *Angew. Chemie Int. Ed.* **2017**, *56*, 9924–9929.

[11]   Zheng, T.; Cai, Z.; Ho-Wu, R.; Yau, S. H.; Shaparov, V.; Goodson, T.; Yu, L. Synthesis of Ladder-Type Thienoacenes and Their Electronic and Optical Properties. *J. Am. Chem. Soc.* **2016**, *138*, 868–875.

[12]   Jones, B. A.; Facchetti, A.; Wasielewski, M. R.; Marks, T. J. Tuning Orbital Energetics in Arylene Diimide Semiconductors. Materials Design for Ambient Stability of n-Type Charge Transport. *J. Am. Chem. Soc.* **2007**, *129*, 15259–15278.

[13]   Payne, M. M.; Parkin, S. R.; Anthony, J. E.; Kuo, C.-C.; Jackson, T. N. Organic Field-Effect Transistors from Solution-Deposited Functionalized Acenes with Mobilities as High as 1 Cm2/V·s. *J. Am. Chem. Soc.* **2005**, *127*, 4986–4987.

[14]   Nishinaga, T.; Komatsu, K. Persistent π Radical Cations: Self-Association and Its Steric Control in the Condensed Phase. *Org. Biomol. Chem.* **2005**, *3*, 561–569.

[15]   Rizalman, N. S.; Ferrón, C. C.; Niu, W.; Wallace, A. L.; He, M.; Balster, R.; Lampkin, J.; Hernández, V.; López Navarrete, J. T.; Ruiz Delgado, M. C.; Hartl, F. Radical Cations of End-Capped Tetrathienoacenes and Their π-Dimerization Controlled by the Nature of α-Substituents and Counterion Concentration. *RSC Adv.* **2013**, *3*, 25644–25647.

[16]   Mayorga Burrezo, P.; Pelado, B.; Ponce Ortiz, R.; De la Cruz, P.; López Navarrete, J. T.; Langa, F.; Casado, J. Robust Ethylenedioxythiophene–Vinylene Oligomers from Fragile Thiophene–Vinylene Cores: Synthesis and Optical, Chemical and Electrochemical Properties of Multicharged Shapes. *Chem. – A Eur. J.* **2015**, *21*, 1713–1725.

[17]   Ferrón, C. C.; Delgado, M. C. R.; Hernández, V.; Navarrete, J. T. L.; Vercelli, B.; Zotti, G.; Cortada, M. C.; Novoa, J. J.; Niu, W.; He, M.; Hartl, F. Substituent and Counterion Effects on the Formation of π-Dimer Dications of End-Capped Heptathienoacenes. *Chem. Commun.* **2011**, *47*, 12622–12624.

[18]   Ferrón, C. C.; Capdevila-Cortada, M.; Balster, R.; Hartl, F.; Niu, W.; He, M.; Novoa, J. J.; López Navarrete, J. T.; Hernández, V.; Ruiz Delgado, M. C. Multistep π Dimerization of Tetrakis(n-Decyl)Heptathienoacene Radical Cations: A Combined Experimental and Theoretical Study. *Chem. – A Eur. J.* **2014**, *20*, 10351–10359.

[19]   Dunsch, L.; Rapta, P.; Schulte, N.; Schlüter, A. D. Structural Dependence of Redox-Induced Dimerization as Studied by In Situ

ESR/UV/Vis-NIR Spectroelectrochemistry: The Fluoranthenopyracylene Oligomers. *Angew. Chemie Int. Ed.* **2002**, *41*, 2082–2086.

[20]   Wu, Y.; Frasconi, M.; Gardner, D. M.; McGonigal, P. R.; Schneebeli, S. T.; Wasielewski, M. R.; Stoddart, J. F. Electron Delocalization in a Rigid Cofacial Naphthalene-1,8:4,5-Bis(Dicarboximide) Dimer. *Angew. Chemie Int. Ed.* **2014**, *53*, 9476–9481.

[21]   Mani, T.; Grills, D. C. Probing Intermolecular Electron Delocalization in Dimer Radical Anions by Vibrational Spectroscopy. *J. Phys. Chem. B* **2017**, *121*, 7327–7335.

[22]   Zeng, Z.; Shi, X.; Chi, C.; López Navarrete, J. T.; Casado, J.; Wu, J. Pro-Aromatic and Anti-Aromatic π-Conjugated Molecules: An Irresistible Wish to Be Diradicals. *Chem. Soc. Rev.* **2015**, *44*, 6578–6596.

[23]   Zhang, C.; Zang, Y.; Zhang, F.; Diao, Y.; McNeill, C. R.; Di, C.; Zhu, X.; Zhu, D. Pursuing High-Mobility n-Type Organic Semiconductors by Combination of "Molecule-Framework" and "Side-Chain" Engineering. *Adv. Mater.* **2016**, *28*, 8456–8462.

[24]   Yuan, D.; Guo, Y.; Zeng, Y.; Fan, Q.; Wang, J.; Yi, Y.; Zhu, X. Air-Stable n-Type Thermoelectric Materials Enabled by Organic Diradicaloids. *Angew. Chemie Int. Ed.* **2019**, *58*, 4958–4962.

[25]   Kubo, T.; Sakamoto, M.; Nakasuji, K. Biradicaloid Character of Phenalenyl-Based Aromatic Compounds with a Small HOMO–LUMO Gap. *Polyhedron* **2005**, *24*, 2522–2527.

[26]   Ponce Ortiz, R.; Casado, J.; Hernández, V.; López Navarrete, J. T.; Viruela, P. M.; Ortí, E.; Takimiya, K.; Otsubo, T. On the Biradicaloid Nature of Long Quinoidal Oligothiophenes: Experimental Evidence Guided by Theoretical Studies. *Angew. Chemie Int. Ed.* **2007**, *46*, 9057–9061.

[27]   Ponce Ortiz, R.; Casado, J.; Rodríguez González, S.; Hernández, V.; López Navarrete, J. T.; Viruela, P. M.; Ortí, E.; Takimiya, K.; Otsubo, T. Quinoidal Oligothiophenes: Towards Biradical Ground-State Species. *Chem. – A Eur. J.* **2010**, *16*, 470–484.

[28]   Huang, Y.; Egap, E. Open-Shell Organic Semiconductors: An Emerging Class of Materials with Novel Properties. *Polym. J.* **2018**, *50*, 603–614.

[29]   Ray, S.; Sharma, S.; Salzner, U.; Patil, S. Synthesis and Characterization of Quinoidal Diketopyrrolopyrrole Derivatives with Exceptionally High Electron Affinities. *J. Phys. Chem. C* **2017**, *121*,

16088–16097.

[30]   Russ, B.; Robb, M. J.; Popere, B. C.; Perry, E. E.; Mai, C.-K.; Fronk, S. L.; Patel, S. N.; Mates, T. E.; Bazan, G. C.; Urban, J. J.; Chabinyc, M. L.; Hawker, C. J.; Segalman, R. A. Tethered Tertiary Amines as Solid-State n-Type Dopants for Solution-Processable Organic Semiconductors. *Chem. Sci.* **2016**, *7*, 1914–1919.

[31]   Shimizu, A.; Uruichi, M.; Yakushi, K.; Matsuzaki, H.; Okamoto, H.; Nakano, M.; Hirao, Y.; Matsumoto, K.; Kurata, H.; Kubo, T. Resonance Balance Shift in Stacks of Delocalized Singlet Biradicals. *Angew. Chemie Int. Ed.* **2009**, *48*, 5482–5486.

[32]   Zhang, Y.; Zheng, Y.; Zhou, H.; Miao, M.-S.; Wudl, F.; Nguyen, T.-Q. Temperature Tunable Self-Doping in Stable Diradicaloid Thin-Film Devices. *Adv. Mater.* **2015**, *27*, 7412–7419.

[33]   Seifert, S.; Schmidt, D.; Shoyama, K.; Würthner, F. Base-Selective Five- versus Six-Membered Ring Annulation in Palladium-Catalyzed C–C Coupling Cascade Reactions: New Access to Electron-Poor Polycyclic Aromatic Dicarboximides. *Angew. Chemie Int. Ed.* **2017**, *56*, 7595–7600.

[34]   Shi, Q.; Shi, X.; Feng, C.; Wu, Y.; Zheng, N.; Liu, J.; Wu, X.; Chen, H.; Peng, A.; Li, J.; Jiang, L.; Fu, H.; Xie, Z.; Marder, S. R.; Blakey, S. B.; Huang, H. Synthetic Routes for Heteroatom-Containing Alkylated/Arylated Polycyclic Aromatic Hydrocarbons. *Angew. Chemie Int. Ed.* **2021**, *60*, 2924–2928.

[35]   Murata, T.; Koide, T.; Nobukuni, H.; Tsuji, R.; Morita, Y. 2D Coordination Network of Trioxotriangulene with Multiple Redox Abilities and Its Rechargeable Battery Performance. *Int. J. Mol. Sci.* **2020**, *21*.

[36]   Wang, R.; Shi, K.; Cai, K.; Guo, Y.; Yang, X.; Wang, J.-Y.; Pei, J.; Zhao, D. Syntheses of Polycyclic Aromatic Diimides via Intramolecular Cyclization of Maleic Acid Derivatives. *New J. Chem.* **2016**, *40*, 113–121.

[37]   Ledwon, P.; Ovsiannikova, D.; Jarosz, T.; Gogoc, S.; Nitschke, P.; Domagala, W. Insight into the Properties and Redox States of N-Dopable Conjugated Polymers Based on Naphtalene Diimide Units. *Electrochim. Acta* **2019**, *307*, 525–535.

[38]   Di Donato, E.; Fornari, R. P.; Di Motta, S.; Li, Y.; Wang, Z.; Negri, F. N-Type Charge Transport and Mobility of Fluorinated Perylene Bisimide Semiconductors. *J. Phys. Chem. B* **2010**, *114*, 5327–5334.

[39]   Ortiz, R. P.; Herrera, H.; Blanco, R.; Huang, H.; Facchetti, A.;

Marks, T. J.; Zheng, Y.; Segura, J. L. Organic N-Channel Field-Effect Transistors Based on Arylenediimide-Thiophene Derivatives. *J. Am. Chem. Soc.* **2010**, *132*, 8440–8452.

[40]   Merz, J.; Steffen, A.; Nitsch, J.; Fink, J.; Schürger, C. B.; Friedrich, A.; Krummenacher, I.; Braunschweig, H.; Moos, M.; Mims, D.; Lambert, C.; Marder, T. B. Synthesis, Photophysical and Electronic Properties of Tetra-Donor- or Acceptor-Substituted Ortho-Perylenes Displaying Four Reversible Oxidations or Reductions. *Chem. Sci.* **2019**, *10*, 7516–7534.

[41]   Hu, J.; Zhang, D.; Harris, F. W. Ruthenium(III) Chloride Catalyzed Oxidation of Pyrene and 2,7-Disubstitued Pyrenes: An Efficient, One-Step Synthesis of Pyrene-4,5-Diones and Pyrene-4,5,9,10-Tetraones. *J. Org. Chem.* **2005**, *70*, 707–708.

[42]   de Echegaray, P.; Mancheño, M. J.; Arrechea-Marcos, I.; Juárez, R.; López-Espejo, G.; López Navarrete, J. T.; Ramos, M. M.; Seoane, C.; Ortiz, R. P.; Segura, J. L. Synthesis of Perylene Imide Diones as Platforms for the Development of Pyrazine Based Organic Semiconductors. *J. Org. Chem.* **2016**, *81*, 11256–11267.

[43]   Richards, G. J.; Cador, A.; Yamada, S.; Middleton, A.; Webre, W. A.; Labuta, J.; Karr, P. A.; Ariga, K.; D'Souza, F.; Kahlal, S.; Halet, J.-F.; Hill, J. P. Amphiprotism-Coupled Near-Infrared Emission in Extended Pyrazinacenes Containing Seven Linearly Fused Pyrazine Units. *J. Am. Chem. Soc.* **2019**, *141*, 19570–19574.

[44]   Chen, J.; Yang, K.; Zhou, X.; Guo, X. Ladder-Type Heteroarene-Based Organic Semiconductors. *Chem. Asian J.* **2018**, *13*, 2587—2600.

[45]   Shi, Y.; Guo, H.; Qin, M.; Zhao, J.; Wang, Y.; Wang, H.; Wang, Y.; Facchetti, A.; Lu, X.; Guo, X. Thiazole Imide-Based All-Acceptor Homopolymer: Achieving High-Performance Unipolar Electron Transport in Organic Thin-Film Transistors. *Adv. Mater.* **2018**, *30*, 1705745.

[46]   Sun, H.; Wang, L.; Wang, Y.; Guo, X. Imide-Functionalized Polymer Semiconductors. *Chem. – A Eur. J.* **2019**, *25*, 87–105.

[47]   Wang, Y.; Hasegawa, T.; Matsumoto, H.; Michinobu, T. Significant Improvement of Unipolar N-Type Transistor Performances by Manipulating the Coplanar Backbone Conformation of Electron-Deficient Polymers via Hydrogen Bonding. *J. Am. Chem. Soc.* **2019**, *141*, 3566–3575.

[48]   Wang, Y.; Guo, H.; Harbuzaru, A.; Uddin, M. A.; Arrechea-Marcos, I.; Ling, S.; Yu, J.; Tang, Y.; Sun, H.; López Navarrete, J. T.; Ortiz, R. P.;

Woo, H. Y.; Guo, X. (Semi)Ladder-Type Bithiophene Imide-Based All-Acceptor Semiconductors: Synthesis, Structure-Property Correlations, and Unipolar n-Type Transistor Performance. *J. Am. Chem. Soc.* **2018**, *140*, 6095–6108.

[49]   Guo, X.; Ortiz, R. P.; Zheng, Y.; Hu, Y.; Noh, Y.-Y.; Baeg, K.-J.; Facchetti, A.; Marks, T. J. Bithiophene-Imide-Based Polymeric Semiconductors for Field-Effect Transistors: Synthesis, Structure−Property Correlations, Charge Carrier Polarity, and Device Stability. *J. Am. Chem. Soc.* **2011**, *133*, 1405–1418.

[50]   Razzell-Hollis, J.; Fleischli, F.; Jahnke, A. A.; Stingelin, N.; Seferos, D. S.; Kim, J.-S. Effects of Side-Chain Length and Shape on Polytellurophene Molecular Order and Blend Morphology. *J. Phys. Chem. C* **2017**, *121*, 2088–2098.

[51]   Guo, X.; Zhou, N.; Lou, S. J.; Smith, J.; Tice, D. B.; Hennek, J. W.; Ortiz, R. P.; Navarrete, J. T. L.; Li, S.; Strzalka, J.; Chen, L. X.; Chang, R. P. H.; Facchetti, A.; Marks, T. J. Polymer Solar Cells with Enhanced Fill Factors. *Nat. Photonics* **2013**, *7*, 825–833.

Appendix A: List of Abbreviations and symbols

Abbreviations

AFM   Atomic Force Microscopy

BCBG   Bottom-Contact Bottom-Gate

BCTG   Bottom-Contact Top-Gate

BTI   Bithienoimide

CV   Cyclic Voltammetry

D-A   Donor-Acceptor

DCM   Dichloromethane

DFT   Density Functional Theory

DRX   X-Ray Diffraction

ECC   Effective Conjugation Coordinate

Fc/Fc+   Ferrocene/Ferrocenium Redox Couple

FT   Fourier Transform

GIWAXs   Grazing-Incidence Wide-Angle X-ray scattering

HF   Hartree Fock

HMDS   Hexamethyldisilaxane

HOMO   Highest Occupied Molecular Orbital

ICT   Intramolecular Charge Transfer

LUMO   Lowest Unoccupied Molecular Orbital

NDI   Naphthalene diimide

NIR   Near Infrared

OFET   Organic Field-Effect Transistor

OLED   Organic Light-Emitting Diode

OPV   Organic Photovoltaic

OSC   Organic Semiconductor

OTS   Octadecylthrichlorosilane

PDI   Perylene diimide

SAM   Self-Assembled Monolayer

TD-DFT   Time Dependent Density Functional Theory

TCBG   Top-Contact Bottom-Gate

UV-Vis   Ultra-Violet Visible

Symbols

V_{GS} Gate-source voltage

V_{DS} Drain-source voltage

I_{DS} Drain-source current

V_{Th} Threshold voltage

E_F Fermi level

W   Channel Width

L   Channel Length

μ   Field-effect mobility

C_i Gate capacitance

P   Pinch off

I_{ON}/I_{OFF} on/off current ratio

ε_0 vacuum permittivity

ε_r Relative permittivity

e   elementary charge

N_A Avogadro's number

n   Charge carrier density

Appendix B: List of Publications

The research work developed in this Doctoral Thesis has resulted in 9 publications, four of them directly related to the Thesis and the other five related to parallel works.

Publications directly related to this Doctoral Thesis

Each chapter of this Thesis is found in each of the publications shown below, respectively.

1. *Ladder-type bithiophene imide-based organic semiconductors: understanding charge transport mechanisms in organic field effect transistors;* Alexandra Harbuzaru, Iratxe Arrechea-Marcos, Alberto D. Scaccabarozzi, Yingfeng Wang, Xugang Guo, Mario Caironi, J. Teodomiro López Navarrete, M. Carmen Ruiz Delgado and Rocío Ponce Ortiz; *J. Mater. Chem. C* **2020**, 8, 15759-15770.

2. *Stable Organic Diradicals Based on Fused Quinoidal Oligothiophene Imides with High Electrical Conductivity*; Kun Yang, Xianhe Zhang, Alexandra Harbuzaru, Lei Wang, Yang Wang, Changwoo Koh, Han Guo, Yongqiang Shi, Jianhua Chen, Huiliang Sun, Kui Feng, M. Carmen Ruiz Delgado, Han Young Woo, Rocio Ponce Ortiz, and Xugang Guo; *J. Am. Chem. Soc.* **2020**, 142, 4329-4340.

3. *Synthesis and electronic properties of nitrogen-doped π-extended polycyclic aromatic dicarboximides with multiple redox processes;* Alexandra Harbuzaru, Matías J. Alonso-Navarro, Marcos Martínez-Fernández, Paula Pérez Camero, J. Teodomiro López Navarrete, M. Mar Ramos, Rocío Ponce Ortiz and José L. Segura; *J. Mater. Chem. C* **2021**, 9, 7936-7949.

4. *(Semi)ladder-type Bithiophene Imide-Based All-Acceptor Semiconductors: Synthesis, Structure-Property Correlations, and Unipolar n-Type Transistor Performance*; Yingfeng Wang, Han Guo, Alexandra

Harbuzaru, Mohammad Afsar Uddin, Iratxe Arrechea-Marcos, Shaohua Ling, Jianwei Yu, Yumin Tang, Huiliang Sun, J. Teodomiro López Navarrete, Rocío Ponce Ortiz, Han Y. Woo, Xugang Guo. *J. Am. Chem. Soc*. **2018**, 140, 6095-6108.

Other publications:

1. *Closely packed, low reorganization energy pi-extended postfullerene acceptors for efficient polymer solar cells;* Steven M. Swick, Weigang Zhu, Micaela Matta, Thomas J. Aldrich, Alexandra Harbuzaru, J. Teodomiro Lopez Navarrete, Rocio Ponce Ortiz, Kevin L. Kohlstedt, George C. Schatz, Antonio Facchetti, Ferdinand S. Melkonyan, and Tobin J. Marks; *PNAS* **2018**, 115, E8341-E8348.

2. *High Electron Mobility in [1]Benzothieno[3,2-b][1]benzo-thiophene-Based Field-Effect Transistors: Toward n-Type BTBTs;* Hakan Usta, Dojeon Kim, Resul Ozdemir, Yunus Zorlu, Sanghyo Kim, M. Carmen Ruiz Delgado, Alexandra Harbuzaru, Seonhyoung Kim, Seonhyoung Kim, Gökhan Demirel, Jongin Hong, Young-Geun Ha, Kilwon Cho, Antonio Facchetti, Myung-Gil Kim; *Chem. Mater*. **2019**, 31, 5254-5263.

3. *Effective interplay of donor and acceptor groups for optoelectronic properties tuning in Oligothiophene-Naphtalimide Assemblies*; Alexandra Harbuzaru, Matías J. Alonso-Navarro, Paula de Echegaray, Iratxe Arrechea-Marcos, Albert-Harillo Baños, Alejandro de la Peña, M. Mar Ramos, J. Teodomiro López Navarrete, Mariano Campoy-Quiles, Rocío Ponce Ortiz and José L. Segura; *J. Mater. Chem. C* **2020**, 8, 15277-1529.

4. Processable High Electron Mobility π-Copolymers via Mesoscale Backbone Conformational Ordering; Brian J. Eckstein, Ferdinand S. Melkonyan, Gang Wang, Binghao Wang, Eric F. Manley,

Simone Fabiano, Alexandra Harbuzaru, Rocio Ponce Ortiz, Lin X. Chen, Antonio Facchetti, and Tobin J. Marks; *Adv. Funct. Mater*. **2021**, 31, 2009359.

5. *Alkoxy functionalized benzothiadiazole based donor–acceptor conjugated copolymers for organic field-effect transistors*; Marc Comí, Dhananjaya Patra, Rui Yang, Zhihui Chen, Alexandra Harbuzaru, Yiming Wubulikasimu, Sarbajit Banerjee, Rocío Ponce Ortiz, Yao Liu and Mohammed Al-Hashimi; *J. Mater. Chem. C* **2021**, 9, 5113-5123.